NORTHWESTERN UNIVERSITY

Investigation of the Effect of Ferroelectric Domain Structure and Dynamics on the Electro-Optic Properties of Polydomain Epitaxial Barium Titanate Thin Films

A DISSERTATION

SUBMITTED TO THE GRADUATE SCHOOL
IN PARTIAL FULFILMENT OF THE REQUIREMENTS

for the degree

DOCTOR OF PHILOSOPHY

Field of Materials Science and Engineering

By

Anthony L Meier

EVANSTON, ILLINOIS

June 2007

© Copyright by Anthony L Meier 2007

All Rights Reserved

ABSTRACT

Investigation of the Effect of Ferroelectric Domain Structure and Dynamics on the Electro-Optic Properties of Polydomain Epitaxial Barium Titanate Thin Films

Anthony L. Meier

The dependence of the electro-optic (EO) properties on the field-dependent domain structure in epitaxial polydomain $BaTiO_3$ thin films was investigated. Models of both the field-dependent electronic polarization and the EO response and their dependence on domain structure were developed. The agreement of these models with measured polarization and EO data demonstrates their efficacy. The measured domain dtructure and remnant polarization were both in agreement with those predicted by the polarization model. The hysteretic EO response was well described by a model based on the E-field dependent intrinsic electro-optic response and the E-field dependent domain structure. In the model of the hysteretic EO response, the functional form of the field-dependent domain structure was that of the field-dependent polarization due to ferroelectric switching ($P_{ferro}(E)$). Effects due to 90^o domain switching were incorporated into the model by inclusion of elasto-optic contributions to the optical response.

Measurements of the effective electro-optic coefficient were made in waveguide and transmission geometries under both in-plane <110> and <100> E-fields. The field dependence of the electro-optic response (r_{eff}) for both <110> and <100> E-fields is dominated by the r_{51}-contributing domains. The <110> field act to pole these domains, resulting in larger effective electro-optic coefficient (r_{eff}) values and a hysteretic response whereas a <100> field does not pole these domains, resulting in a lower r_{eff} and no hysteresis. Average effective electro-optic coefficient (r_{eff}) values at 633 nm under <110> and <100>

fields were 247 and 5.6 pm/V, respectively. Average r_{eff} values at 1550 nm under <110> and <100> fields were 132 and 14 pm/V, respectively.

Domain dynamics were studied as a function of the applied bias based on the assumption of a distribution of relaxation times within the film. The distribution of relaxation times is tentatively attributed to a distribution of domain sizes. The transient 90^{o} domain relaxation was examined as a function of the poling field. The time response was well described by the Koulraush-Williams-Watts function, with the relaxation time constant linearly proportional to the poling field. The transient amplitude likewise increased with the poling field.

Approved:_____

Professor Bruce W. Wessels

ACKOWLEDGMENTS

First, I would like to thank my advisor, Professor Bruce Wessels for his continued support and guidance over the last five years. I would also like to thank my thesis committee, Prof. Michael Bedzyk, Prof. Thomas Mason, and Prof. Selim M. Shahriar for taking the time to critically evaluate this dissertation. This work was funded in part through a National Science Foundation, Division of Electrical and Communications Systems grant (NSF ECS-0457610). Additionally, extensive use was made of Central Facilities supported by the NSF MRSEC grant (DMR-0076097).

Special thanks are given to the Tobin Marks group and especially Dr. Lian Wang and Prof. Tobin Marks for the development and synthesis of the barium MOCVD precursor used in our MOCVD growth systems. Special thanks likewise go to Dr. David J. Towner for providing $BaTiO_3$ samples used in this research. Additional collaborators I would like to thank include Prof. Zolotoyabko of the Technion Technical Institute in Israel and Amit Desai formerly of North Carolina State University.

I would like to thank the current and former members of the Wessels group for their support over the years. I would like especially to thank Dr. David J. Towner, Dr. Pingsheng Tang, Dr. Feng Niu, Pao Tai Lin and Dr. Tetze Hamano for all of the insightful conversations and ideas they shared with me over the years. I would also like to thank the other member of the Wessels groups that I pestered over the years including Dr. Bing Han, Dr. Kipyung Ahn, Dr. Anil Dhote, Dr. Steve May, Dr. Philip Chiu, George Sterbinsky, Nidhi Parashar, Aaron Ji Cheng and Nikhil Ranjaraju. I would also like to thank Dr. Jerry Carsello for all of his assistance throughout the course of this research.

Lastly I am most thankful to and for my wife Mary Beth. She has been my constant supporter, companion and fellow adventurer as I dragged her from the Midwest to the West coast, back to the Midwest and next on to the East coast. I am likewise grateful for my two incredible little men John Riley and Jackson Bradley. Mary Beth and the boys remind me constantly of what really matters in life. I would like to thank my mom/soccer-coach/basketball-coach who has always believed in me and was

always the one telling me to “go for it”. I would like to thank all the rest of my family and Mary Beth’s family for all of their love and support.

TABLE OF CONTENTS

Abstract 3

Ackowledgments 5

Table of contents 7

List of Figures 9

List of Tables 24

1 Introduction 25

2 Background and Literature Survey 28
2.1 Introduction 28
2.2 Electronic polarization 28
2.2.1 Ferroelectric and dielectric contributions to electronic polarization 28
2.2.2 Polarization in thin films and ceramics verses bulk single crystals 32
2.3 Temporal response of domain dynamics 36
2.3.1 Introduction 36
2.3.2 Ferroelectric relaxation ($E_{applied} = 0$) 37
2.3.3 Ferroelastic switching and strain 48
2.4 Electro-optic properties of ferroelectric thin films 49
2.4.1 Hysteretic electro-optic response 49
2.4.2 Models of domain structure dependent electro-optic response 54

3 Experimental and analytic techniques 56
3.1 Growth of $BaTiO_3$ thin films by metal-organic chemical vapor deposition 56
3.2 Post growth annealing of $BaTiO_3$ thin films 57
3.3 Thin film characterization 58
3.3.1 X-ray diffraction 58
3.3.2 Prism coupling 58
3.4 Device fabrication 58
3.4.1 Transmission electro-optic device 58
3.4.2 Waveguide electro-optic modulator 59
3.5 Electronic polarization measurements 60
3.6 Electro-optic measurements 63
3.6.1 Electro-optic measurements in the transmission geometry 65
3.6.1.1 The Senarmont polariscope 65
3.6.1.2 Transmission geometry electro-optic measurement apparatus 71
3.6.1.3 Electro-optic coefficient measurement apparatus 74
3.6.1.4 Electro-optic coefficient measurement procedure 76
3.6.1.5 Electro-optic coefficient analysis 78
3.6.1.6 Measurement of electro-optic response to unbiased voltage pulse 82
3.6.2 Electro-optic measurements in the waveguide geometry 83
3.6.2.1 Waveguide geometry electro-optic measurement apparatus 83
3.6.2.2 Electro-optic coefficient measurement procedure 84

4 Electro-optic Theory of polydomain $BaTiO_3$ thin films 89
4.1 Background and introduction 89
4.1.1 Optical indicatrix an the linear electro-optic tensor 89
4.1.2 Domain structure and EO tensor in polydomain $BaTiO_3$ thin films 92
4.2 Effects of $BaTiO_3$'s large off-diagonal electro-optic coefficient 94
4.2.1 Propagation in the plane of rotation of the index ellipsoid 96
4.2.2 Propagation perpendicular to the plane of rotation of the index ellipsoid 103
4.2.2.1 E-field dependence of birefringence under constraint $\vec{k} \| \left(\vec{E} \times \vec{P} \right)$ 105
4.2.2.2 Combined effect of indicatrix rotation and $\delta\Delta n$ on EO response 108

5 Ferroelectric Properties of $BaTiO_3$ Thin Films 121
5.1 Electronic polarization of polydomain thin films 121
5.1.1 Model of domain structure dependence of in-plane polarization 121
5.1.2 In-plane polarization along <100> and <110> directions 138
5.1.3 Analysis of remnant and non-remnant contributions to the polarization 144
5.1.4 E-field dependent polarization (unsaturated hysteresis loops) 154
5.1.5 Summary of in-plane electronic polarization measurements 169
5.2 Electro-optic measurements of polydomain $BaTiO_3$ thin films 171
5.2.1 Introduction 171
5.2.2 EO coefficient measurements of epitaxial polydomain thin films 173
5.2.3 Effect of field on the EO response 190
5.2.3.1 EO pulse response under in-plane <100> oriented E-field 193
5.2.3.2 Modeling the hysteretic EO pulse response under an in-plane <110> oriented E-field 197
5.2.4 Extrinsic EO effect and its frequency dependence 231
5.2.4.1 Slow f-response /large extrinsic EO effect due to significant 90^o domain flipping 231
5.2.4.2 Transient analysis of the extrinsic EO effect due to 90^o domain switching 241
5.2.4.3 Extrinsic EO effect due to 180^o domain flipping 259
5.3 Summary of ferroelectric properties of $BaTiO_3$ thin films 261

6 Summary and Conclusions 264

7 Suggestions for future work 269
7.1 Effect of point defect structure and oxygen vacancies on the EO response 269
7.2 Domain dynamics 269
7.3 Epitaxial Si-integrated $BaTiO_3$ EO modulators 270

References 271

Appendix I 284

Appendix II 288

LIST OF FIGURES

Figure 2-1. The total polarization (P_{tot}) and the dielectric polarization determined from the integrated small-signal capacitance (P_{diel}) of a (111) oriented PZT thin film are shown along with the ferroelectric contribution to the polarization determined by subtracting P_{diel} from P_{tot} [Gerber et al. 2005][77]..... 30

Figure 2-2. The measured total polarization and non-remnant polarization hysteresis loops of a 0.19 μm^2 PZT memory cell capacitor are shown. Also shown is the remnant hysteresis loop determined by subtracting the non-remnant loop from the total polarization hysteresis loop. The inset shows the modified drive profile that allows for the measurement of both the total and non-remnant hysteresis loops [Jung et al.][80]..... 31

Figure 2-3. P-E hysteresis loop of a virgin single-domain bulk single-crystal $BaTiO_3$ sample adapted from Glower and Hester (1965)[83] 33

Figure 2-4. Strain limits on switching in polycrystalline ceramics and polydomain epitaxial thin films limit the total achievable ferroelectric switching. Furthermore as non-180^o domains are both ferroelastic and ferroelectric, the coupling of the polarization to the elastic strain results in significant back switching of the flipped non-180^o domains [Cao 2005] [86]. 33

Figure 2-5. Surface-normal P-V hysteresis loops of epitaxial PZT thin films. The remnant polarization in the a-oriented film on Si is just 25% of that of the c-oriented film on MgO [Tsukada et al.][90]..... 34

Figure 2-6. Power-law transient electro-optic response of a $KNbO_3$ thin film observed by Hoerman et al.[66] 38

Figure 2-7. Pareto probability distributions of relaxation times given by equation (2-9) are shown for a τ_P value of 5 ms and *m* values ranging from 0.9 to 0.1. For $\tau < \tau_P$ the probability equals zero..... 39

Figure 2-8. The normalized Levy α-stable distributions are shown for β values ranging from 0.9 to 0.1 on both linear and log time scales[148]..... 41

Figure 2-9. A typical Levy α-stable distribution of relaxation times corresponding to the KWW parameters $\beta = \frac{1}{2}$ and $\tau_{KWW} = 4$ ms is shown. 41

Figure 2-10. Distribution of relaxation times in a ferroelectric single crystal MAPBB sample determined using polarized light video microscopy [Matyjasek & Rogowski Cryst. Res. Technol. 2006][121]. 42

Figure 2-11. A KWW stretched exponential fit to measured polarization relaxation in PZT thin films is shown [Gruverman et al. APL 1997] [119]. 43

Figure 2-12.Polarization relaxation subsequent to poling is shown for MAPBB [Matyjasek & Rogowski JAP 2006](a), and TAAP (b) organic ferroelectric samples. The relaxation time is observed to increase with increasing magnitude of the poling field[Matyjasek & Rogowski J. Phys.-Condes. Matter 2006]... 45

Figure 2-13. Experimental setup for ferroelastic relaxation measurements made by Fu et al.[118] and Koval et al.[124] using the direct piezoelectric effect..... 46

Figure 2-14. Transient charge due to ferroelastic switching in (a) 70 nm and (b) 700 nm thick PZT thin films. Color was added for clarity due to the poor quality of the electronic reproduction of the manuscript.[Koval et al. 2005][124]..... 47

Figure 2-15. The KWW stretching exponent β is plotted verses the applied load in PZT films due to Koval et al. The β values were taken from the tabulated results [Koval et al. 2005][124]..... 47

Figure 2-16. The KWW characteristic time constant τ is plotted verses the applied load for the 70 nm PZT thin film (a), and the 700 nm PZT thin film (b). The τ values were taken from the tabulated results [Koval et al. 2005][124]..... 48

Figure 2-17. (a) Theoretical stress Vs E-field phase diagram for c- and a-domains in a single crystal $BaTiO_3$ sample. Both E-field and compressive stress were applied parallel to the surface normal of a thin plate $BaTiO_3$ single crystal. The grey regions surrounding the c-domain/a-domain phase boundary represents the hysteresis of the non-remnant switching due to the kinetic nature of the switching.(b)Experimentally determined stress Vs. E-field phase diagram for c- and a-domains in a bulk single crystal $BaTiO_3$[Burcsu et al. 2004][156]..... 49

Figure 2-18. Hysteretic EO response reported by Kim and Kwok for $BaTiO_3$ thin films on MgO(001) substrates by PLD. Using coplanar strip electrodes, the applied field was along an in-plane <110> direction. 52

Figure 2-19. Hysteretic EO response of BST thin films due to Li et al[168]. In spite of the labeling of the axes it is believed that what is recorded is Γ_ω / E_{DC} rather than Γ_ω / E_{AC} 53

Figure 3-1. Schematic of transmission electro-optic device 59

Figure 3-2. Waveguide electro-optic modulator device schematic. The SiO_2 layer is optional and if omitted electrodes are deposited directly on the $BaTiO_3$ film. 60

Figure 3-3. Electrical connections used for wire-bonded samples when making electronic polarization measurements..... 61

Figure 3-4. Driving profile used to generate both the full hysteresis loop as well as the two non-switching half loops..... 62

Figure 3-5. Device geometry showing the orientation of the applied electric field (E) to the Poynting vector of the optical mode (S) in the a.) waveguide and b.) transmission geometries..... 64

Figure 3-6. the Senarmont polariscope, also referred to as PSCA setup, is used for measurement of EO properties in the transmission geometry. 66

Figure 3-7. Transmission curve of a Senarmont PSCA polariscope. The maximum linearity point (m_1) and null transmission point (m_o) are labeled..... 67

Figure 3-8. 2D map of equation (3-1) . Darkest regions correspond to I_{min} while brightest regions correspond to $I_{min}+I_{max}$. 68

Figure 3-9. The effective signal-to-noise ratio as a function of analyzer angle β is plotted a.) for the theoretically perfect polariscope (i.e. $I_{min} = 0$) and b.) for a polariscope with a finite I_{min}. 69

Figure 3-10. Plot of (3-1) and the 1st and 2nd derivatives of (3-1) with respect to the analyzer angle β. The rate of change of the modulation depth is largest at the null transmission point and is approximately linear as seen from $d^2I/d\beta^2$ and dI/db respectively. 70

Figure 3-11. Schematic of mounted and connectorized sample for transmission electro-optic measurement 72

Figure 3-12. Schematic optical sub-system consisting of transmission polariscopes for measurement at (a) 632.8 nm and (b) 1561 nm 73

Figure 3-13. Schematic of electrical subsystem used for measurement of electro-optic coefficient. Setup used for sample bias voltages of 9 V or less. For higher bias voltages the system in Figure 3-14 was employed. 75

Figure 3-14. Schematic of electrical subsystem used for measurement of electro-optic coefficient with sample bias voltages as high as ±40V. For bias voltages of 9V or less the setup in Figure 3-13 was normally used. 75

Figure 3-15. The transmitted intensity at different analyzer angles with a 1kHz sinusoidal driving voltage (10Vpp +5V DC bias) applied to the EO device. The open symbols are the points where $\delta_{AC} = 0$ used to determine the value of I_{amp} 79

Figure 3-16. The transmitted intensity at the point where δ_{AC} is zero is plotted verses the analyzer angle. The solid line shows the fit to the measured data using (3-3) with $\delta_{AC} = 0$. The I_{amp} value determined from fitting is given on the figure. 80

Figure 3-17. Schematic showing the modulation depth due to δ_{AC} for a discrete range of analyzer angles 81

Figure 3-18. Normalized measured modulation depth and theoretical modulation depth for a retardation amplitude of 7.2 mRad. 81

Figure 3-19. Schematic of electrical subsystem used in measurement of EO response to square-wave voltage pulse. 82

Figure 3-20. Schematic of optical subsystem of waveguide EO measurement apparatus 84

Figure 3-21. Image of lens-tipped fiber at the 4 μm working distance from the endface of the waveguide. Inset shows schematic of CCD microscope used to position the lens-tipped fiber. 84

Figure 3-22. Map of the (β,δ) parameter-space of equation (3-6) 85

Figure 3-23. Theoretical transmitted intensity of PSA polariscope. By overdriving the sample V_π is determined directly from the measured data. Note the Senarmont PSCA polariscope with the analyzer angle fixed at zero has the same transmission curve as the PSA polariscope 86

Figure 3-24. Theoretical transmission of PSA polariscope with $\delta_{AC} = 0$. The transmission curve of the Senarmont polariscope operated at the maximum linearity point is shown for comparison. In order to determine V_π when $\delta_{AC} = 0$, the PSA requires twice the applied voltage of the Senarmont operated at M_1. 87

Figure 4-1. schematic of the six stable domain variants in the tetragonal phase of $BaTiO_3$. The EO tensors of all six domain variants are given after transformation of coordinates to those of variant (1). ... 93

Figure 4-2 Schematic of opto-geometric configurations employed in the study of the electro-optic properties of BaTiO3 thin films.(a) and (b) show the configurations employed in the transmission geometry while (c) and (d) show configurations used in the waveguide geometry. The field direction (E) and Poynting vector (S) of the optical mode are shown as well as the orientation of the six allowed domain variants. ... 94

Figure 4-3. Schematic showing plane view of indicatrix. Large grey arrow indicates orientation of the polar axis. The central elliptical cross-section of the optical indicatrix is shown as a function of the propagation direction in the xz-plane (a) in the absence of an applied E-field and (b) with an applied E-field in the xz-plane perpendicular to the propagation direction. ... 97

Figure 4-4. Dependence of $\delta\Delta n$ due to domain variant 5 from Figure 4-2(c) and (d) on the in-plane propagation direction with an in-plane orthogonal E-field. The angle θ is defined in Figure 4-3. ... 99

Figure 4-5. $\delta\Delta n$ due to 180° domain variants is seen to cancel for all θ where θ is defined in Figure 4-3. 99

Figure 4-6. Combined effect of domain types 5 and 3 from Figure 4-2(c) and (d) on the in-plane directional dependence of $\delta\Delta n$. The angle θ is defined in Figure 4-3 ... 100

Figure 4-7. $\delta\Delta n$ is plotted as a function of the in-plane E-field direction and the in-plane propagation direction for: (a) domain variant 5, (b) domain variant 3, (c)(d) equal volume fractions of variants 5 and 3. The scale bar give $\delta\Delta n$ for (a)-(c). For clarity the film average is shown on a finer scale in (d). The angle θ is defined in Figure 4-3. The lines correspond to the $\delta\Delta n$ when k is orthogonal to E and therefore correspond to the relevant plots in Figure 4-6. ... 102

Figure 4-8. Schematic showing orientation of the eigenmodes. For $\vec{k} \,||\, \left(\vec{E} \times \vec{P}\right)$ where *P* is the polarization vector, the orientation and magnitude of the eigenmodes is identical to that of the semiaxes of the indicatrix in the plane defined by *E* and *P*. ... 104

Figure 4-9. Schematic of indicatrix and unit cell. The indicatrix is isotropic in the plane normal to the optic axis such that for propagation normal to the plane defined by the optic axis and the E-field vector, the coordinate system can always be defined such that $\vec{k}$ is along the y-axis and the rotation of the indicatrix is confined in the xz-plane making equations (4-8) - (4-10),(4-13) completely general for the case where $\vec{k} \,||\, \left(\vec{E} \times \vec{P}\right)$ where $\vec{P}$ is the optical axis shown in blue in the figure. ... 104

Figure 4-10. Ratio of coefficients *b* and *c* from (4-16) as a function of θ. At $\theta = 0°$ the coefficient *b* is identically zero and the $\delta\Delta n\left(E\right)$ is purely quadratic. At 90° it is highly linear ... 106

Figure 4-11. $\delta\Delta n(E)$ and $\Delta\eta(E)$ for three different E-field orientations (see Figure 4-8). The point at which $\delta\Delta n + 0$ for a finite negative field results from offsetting contributions to the birefringence from the r_{13} and r_{33} and the r_{51} EO coefficients ... 107

Figure 4-12. $\delta\Delta n(E,\theta)$ for the domain variant shown in the figure. At θ = 0° $\delta\Delta n(E)$ is quadratic while at θ = 90° $\delta\Delta n(E)$ is linear. The black contour lines demark a region where $\delta\Delta n(E) \approx 0$ ($\delta\Delta n(E) = \pm 2.5\times10^{-6}$). The points at finite negative E where $\delta\Delta n(E) = 0$ result from offsetting contributions from r_{51} and (r_{13}, r_{33}) 107

Figure 4-13. E-field and θ dependence of the rotation of the indicatrix. θ gives the orientation of the E-file to the polar axis of the domain as in Figure 4-8 108

Figure 4-14. PSCA polarimeter. The EO sample is modeled as an arbitrary linear retarder with its slow axis at some angle θ to the x-axis. An applied E-field perpendicular to the polar axis causes a non-trivial rotation of the principle indices by ±α degrees..... 109

Figure 4-15. ΔI transmitted for a-domain variants from Figure 4-2(b): (a) domain variant 5, (b) domain variant 6 (c) average ΔI due to equal volume fractions of T5 and T6 (rendered on a scale of just 5% of that in (a) and (b)). (d) shows the ΔI due to variant 3 and (e) shows the average ΔI due to equal volume fractions of T5 and T3 on the same scale as (a) and (d). (f) shows the ΔI due to T5 when the rotation is artificially set to zero. The scale in (f) is just 10% of that in (a) and the inset in the upper right corner of (f) shows the result rendered on the same scale as (a). 113

Figure 4-16. The theoretical field dependent change in the transmitted intensity for the domain variants from Figure 4-2(b) when $\vec{k} \,||\, (\vec{E}\times\vec{P})$. The operating point used in the simulated theoretical $\Delta I(E)$ was $\theta = 0^\circ$ and $\beta = 3^\circ$ (see Figure 4-14) This typifies the operating points employed for transmission EO measurements with a <110>-oriented E-field. At the operating point the response due to domain variant 5 is the same as that due to variant 3. The incomplete cancelation of 180° domain variants is reflected in the finite average transmitted intensity with equal volume fractions of variants 5 and 6 or 3 and 4..... 114

Figure 4-17. The theoretical change in the transmitted intensity of domain variants T6 and T4 from Figure 4-2b are shown. The solid red line was calculated using the Jones Calculus as given by equation (4-26). The blue circles show the change in transmitted intensity calculated using equations(4-28) and (4-29) in which the result of the Jones calculus is simplified using the small angle approximation. 116

Figure 4-18. The theoretical transmitted intensity of domain variants T6 and T4 as given by equation (4-30) is plotted along with the result using the exact Jones calculus given by equation (4-26)..... 116

Figure 4-19. Theoretical change in the transmitted intensity for propagation perpendicular to the plane of rotation of the indicatrix when the applied field is along a crystallographic <110> direction. The results using the un-simplified Jones calculus expression given by equation (4-26) are shown (solid lines) along with the results in which small angle approximations were made for the parameters α, θ and β (see Figure 4-14) as given by equation (4-31). 117

Figure 4-20. ΔI(θ,β) in the waveguide geometry with a <110> oriented E-field and orthogonal propagation direction for four different assumed domain structures. A reduced θ dependence is evident. The assumed domain variants are listed in the insets in the lower right of each image in the order transited by the propagating mode (refer to Figure 4-2(d)). In (a) both the a- and c-domain are assumed to be 1.5

mm thick. In (b) c-domain is 2.25 mm while the a-domain is 0.75 nm thick (75% c-domain). In (c) c-domain is 100 nm a-domain is 33 nm thick. In (d) c-domains are (100) nm thick and a-domain is 66 nm thick. 119

Figure 5-1. a) The c-up domain with is polar axis pointing out of the plane of the film is shown along with the associated coordinate system. The coordinate system of this domain variant serves as the reference coordinate system in which the polarization contributions from all six of the domain variants (shown in (b)) are reported. In (b) the c-domains are shown in blue and the a-domains are shown in gold. 123

Figure 5-2. Two different theoretical coercivity distributions are shown. A Dirac delta function distribution and a Weibull distribution. Both CDFs and PDFs are shown. 126

Figure 5-3. Theoretical polarization due to domain switching along an in-plane <100> direction. The polarization was determined using equation (5-15) after substituting a Weibull CDF (red) or a Heaviside CDF (blue). 127

Figure 5-4. The theoretical [100] and [010] polarizations given by equation (5-15) for an in-plane field at 30^o with respect to the [100] direction. The polarizations are plotted verses the components of the applied field along the corresponding axis. 128

Figure 5-5. The theoretical [100] and [010] polarizations given by equation (5-15) for an in-plane field at 30^o with respect to the [100] direction. The polarizations are plotted verses the applied field E. 129

Figure 5-6. Schematic showing the relationship between the [100] and [010] polarization vectors and their components parallel to the applied field direction. 129

Figure 5-7. The theoretical polarizations for an applied in-plane field direction at 30^o to the [100] axis. (a) show the result for a delta function distribution of coercivities from Figure 5-2 while (b) shows the result for the Weibull distribution of coercivities shown in Figure 5-2. 131

Figure 5-8. Two Weibull coercivity distributions are shown. The narrow distribution characterized by the solid lines corresponds to Weibull parameters of (8. 0.92). The wider distribution characterized by dashed lines corresponds to Weibull parameters of (2.2, 0.92) 132

Figure 5-9. In-plane directional dependence of the maximum polarization due to domain flipping for a range of maximum applied fields. A Weibull distribution of coercivities with Weibull parameters (8, 0.92) is assumed (see Figure 5-8). 133

Figure 5-10. In-plane directional dependence of the maximum polarization due to domain flipping for a range of maximum applied fields. A Weibull distribution of coercivities with Weibull parameters (2.2, 0.92) is assumed (see Figure 5-8). 133

Figure 5-11. The three coercivity distributions used to model the electronic polarization of sample DT443 are shown. The distribution parameters for the Weibull and gamma distributions are given in Table 5-1 below. The lower right figure shows the measured dP/dV and the corresponding fit from which both PDF and CDF were calculated. 136

Figure 5-12. Fits to the measured polarization of sample DT443 were made using the thin-film polarization model given by equations (5-19), (5-16) and (5-15). Fits were made using the three different coercivity distributions from Figure 5-11. 137

Figure 5-13. Electronic polarization hysteresis loops measured in the plane of the films using coplanar strip electrodes. 139

Figure 5-14. Box and scatter plots of the measured maximum polarization under a maximum applied voltage of 19.9 V. Summary statistics are provided to the right of the plots. 140

Figure 5-15. Electronic polarization hysteresis loop of bulk $BaTiO_3$ crystal taken from Wieder[195] shows that when full remnant switching occurs the remnant polarization is approximately the same as the saturation polarization of 26 $\mu C/cm^2$. 142

Figure 5-16. The drive profile used to determine the remnant and non-remnant components of the polarization is shown along with a typical example of the resulting polarization measured (sample HR24a). 145

Figure 5-17. The measured full hysteresis loop and the two non-switching half-loops are used to determine the remnant polarization loop (sample DT443). 145

Figure 5-18. Remnant, non-remnant, and full electronic polarization hysteresis loops for sample HR24a. 146

Figure 5-19. Full uncompensated (○) as well as remnant (solid line) and non-remnant (+) electronic polarization hysteresis loops of a 0.19 μm^2 PZT memory cell are shown [Jung et al.][80] 146

Figure 5-20. Full and remnant electronic polarization loops of sample HR24a are shown along with the field dependent capacitance (dP/dV) of the full loop. The maximum capacitance of the full loop occurs at fields that corresponds to the coercive fields of the remnant polarization loops 148

Figure 5-21. The temporal evolution of the full, remnant, and non-remnant electronic polarization of sample HR24a under the driving voltage shown in the upper plot are given 149

Figure 5-22. The temporal evolution of the switching current densities associated with the full, remnant and non-remnant electronic polarization of sample HR24a under the driving voltage shown in the upper plot are given. 150

Figure 5-23. The temporal evolution of the full, remnant, and non-remnant electronic polarization of sample DT443 under the driving voltage shown in the upper plot are given 150

Figure 5-24 The temporal evolution of the switching current densities associated with the full, remnant and non-remnant electronic polarization of sample DT443 under the driving voltage shown in the upper plot are given. 151

Figure 5-25. Electronic polarization measurements on PZT thin films reported by Wang and Chang[81]. The temporal evolution of the switching current is shown along with the triangle wave driving voltage in the upper figure. From the upper figure the applied voltages temporally coincident with the peaks in the switching current are just less than 2 and -2 V respectively (red lines). From the full uncompensated hysteresis loop shown in the lower figure it is evident that these voltages correspond to the points at which dP/dE of the full uncompensated loop are maximized. Additionally, the values of the fields at which dP/dE is maximized are larger than the coercive fields of the full uncompensated hysteresis loop consistent with the result measured on our polydomain $BaTiO_3$ thin films. 152

Figure 5-26. Compensated remnant hysteresis loop of a PVDF sample reproduced from Dickens et al.[69]. The peak in the total current density occurs at an applied field equal to the coercive field of the *compensated* remnant hysteresis loop, consistent with the observations in our polydomain $BaTiO_3$ thin films 153

Figure 5-27. The field dependence of (1) the total current density, (2) the non-remnant current density and (3) the remnant current density of a PVDF sample are reproduced from Dickens et al.[69]. 153

Figure 5-28. The full uncompensated hysteresis loop as well as the remnant hysteresis loop generated by subtracting the non-remnant dielectric component of the polarization from the full loop. The coercive fields of the resulting remnant polarization loop are observed to be larger than those of the full uncompensated hysteresis loop, consistent with the observed behavior in our polydomain $BaTiO_3$ thin films. Data shown is for a $SrBi_2(Ta,Nb)_2O_9$ thin film and is reproduced from Bhattacharyya et al.[203] 154

Figure 5-29. a. series of unsaturated full hysteresis loops; b. series of unsaturated remnant hysteresis loops generated by subtraction the measured non-switching half-loops from the full loops; c. the field dependent capacitance or dP/dV of the full loops [sample DT443]. 156

Figure 5-30. Coercive fields of the full and remnant hysteresis loops for a series of unsaturated hysteresis loops for sample DT443 are shown. Also shown is the value of the applied field at which $(dP/dE)_{max}$ of the full hysteresis loop occurs. As seen in the figure the coercive fields of the remnant hysteresis loops correspond to the fields at which the maxima of dP/dE of the full hysteresis loops occur for the entire series of unsaturated loops. 156

Figure 5-31. The field-dependent coercive field along with the measured cumulative distribution function of coercivities derived in Section are shown to be reasonably well correlated. At the inflection point of the field-dependent coercive fields at 0.9 MV the CDF would indicate that ~65% of the switchable volume fraction has undergone a 180^o domain reversal [sample DT443]. 157

Figure 5-32. The evolution of the coercive field of full polarization hysteresis loops are shown for a number of samples. The measurements were made from series of unsaturated hysteresis loops measured for each sample. 158

Figure 5-33. The evolution of the remnant polarization of full polarization hysteresis loops are shown for a number of samples. The measurements were made from series of unsaturated hysteresis loops measured for each sample. 159

Figure 5-34. The evolution of the maximum polarization of full polarization hysteresis loops are shown for a number of samples. The measurements were made from series of unsaturated hysteresis loops measured for each sample. 160

Figure 5-35. As seen in the figure, the non-remnant half-loop polarization exhibits an approximately linear dependence on the applied electric field with very little hysteresis observed relative to that in the full hysteresis loop included for comparison. 161

Figure 5-36. The small signal capacitance and dielectric constants calculated from the non-remnant polarization half-loops are plotted verses the maximum applied field of the non-remnant half-loop in the lower plot. The upper plot shows the full hysteresis loop capacitance measured under the maximum available test voltage (19.9V). As seen in the figure the small signal capacitance is maximized at

approximately the same field value where the maximum capacitance of the full hysteresis loop is observed. The dashed green lines in the lower figure are included as a guide to the eye. 163

Figure 5-37. The upper plot shows the measured small signal capacitance of a $SrBi_2(Ta_{0.5},Nb_{0.5})_2O_9$ thin film[203]. The lower figure from the same reference shows the capacitance calculated from the full polarization hysteresis loop of the film. As seen the small signal capacitance is maximized at the same field for which the capacitance of the full hysteresis loop is maximized. 164

Figure 5-38. The reversible polarization of sample DT443 determined from a standard small signal capacitance measurement is nearly identical to that of the portion of the non-remnant half-loops that correspond to increasing magnitude of the applied field. 165

Figure 5-39. The full hysteresis loop of sample DT443 is shown (black squares) along with the remnant loop determined by subtracting out the reversible dielectric contributions determined from a small-signal capacitance measurement (red circles) and the remnant loop determined by subtracting the non-switching half-loops from the full loop (green upright triangles). Because the non-remnant half-loops include contributions from both the dielectric constant and non-remnant ferroelectric contributions, this represents the true remnant loop. The difference between these two remnant loops or equivalently the difference between the non-remnant half-loops and the dielectric contributions determined from the small signal capacitance measurement gives the non-remnant ferroelectric contributions to the polarization (blue inverted triangles). 166

Figure 5-40. The temporal evolution of the current densities of the non-remnant components of the electronic polarization are shown for three samples. DT443 and HR24a exhibit the characteristically flat non-remnant current densities, while that of sample AM069b is highly peaked reminiscent of the remnant current densities normally observed in our films. 167

Figure 5-41. The non-remnant half-loops of samples DT443, HR24a and AM069b are shown. The nearly liner dP/dE with modest hysteresis observed in samples DT443 and HR24a is characteristic of our samples. In contrast a more clearly non-linear dP/dE and enhanced hysteresis is observed in the non-remnant half-loops of AM069b 168

Figure 5-42. The series of unsaturated hysteresis loops of sample AM069b are shown. The upper figure shows the full hysteresis loops. The lower figure shows the non-remnant half loops. The pinching off of the full loop and the significant non-linear hysteresis of the non-remnant loops are believed to be due to 90^o-degree domain flipping 169

Figure 5-43. Schematic of the a-domains along with an applied (a) <100>, or (b) <110> E-field vector. 172

Figure 5-44. Schematic of typical transmission geometry EO measurement 174

Figure 5-45. Sample DT443 measured response voltage due to the EO effect for a range of analyzer angles. As shown in the upper plot, the sample was driven with a 1kHz 10 V_{pp} sinusoidal driving voltage with a 20 V DC bias voltage. The legend refers to the response in the lower figure at the given analyzer angle. Note the characteristic frequency doubling at the null transmission point. 174

Figure 5-46. Sample DT443 response voltage measured at points where the AC amplitude of the applied voltage goes to zero plotted for a range of analyzer angles. From a fit to the data using equation (5-28) the response voltage corresponding to I_{amp} was found to be ~390V 176

Figure 5-47. (DT443 20V bias 10Vpp 1kHz). Normalized measured modulation depth and theoretical modulation depth for a retardation amplitude of 7.2 mRad. 177

Figure 5-48 Data for three additional EO coefficient analyses are presented. As in Figure 5-46, the fit to the measured data in the figures at left is used to determine the value of I_{amp} that is subsequently used to normalize the measured modulation depth. The figures at right show the resulting normalized modulation depth (unitless) as a function of the analyzer angle as well as the fit using equation (5-30). The values of δ_{amp} corresponding to the fits to the data are given in the figures at right. 179

Figure 5-49. Figures at left show optimal fit to equation (5-28) as well as those for ±10% error in the estimate of I_{amp}. The figure at right shows the resulting percentage error in the calculated r_{eff} value due to error in the estimate of I_{amp} 181

Figure 5-50. Electro-optic response and a I kHz driving voltage of sample DT446 measured in the waveguide geometry. Measurement was made at a bias voltage of 10 V. From the measured V_π of 3.3 V and the geometry of the modulator, the effective electro-optic coefficient under the 10 V bias was 162 pm/V at λ_o of 1561 nm. 182

Figure 5-51. Scatter and box plots of the effective electro-optic coefficients measured with in-plane electric field oriented along <110> and <100> directions respectively. The two samples marked by green crosses in the left figure are the two <100> samples that were annealed in air at 1100 ^oC prior to measurement. The median r_{eff} values for measurement under <110> and <100> fields were 153 pm/V and 12.5 pm/V respectively. 183

Figure 5-52. Bias dependence of r_{eff} under in-plane <110> oriented E-fields are shown for samples DT446, DT443 and AM040b. Foe each sample, the measurement geometry is indicated. 184

Figure 5-53. Bias dependence of r_{eff} under in-plane <100> oriented E-fields are shown for samples AM033 and DT454, measured in the waveguide and transmission geometries respectively. 185

Figure 5-54. X-ray diffraction analysis of domain structure. Surface normal Bragg reflections for a number of samples are shown along with the corresponding EO coefficients measured under an in-plane <100> oriented electric field. Significant increases in the c-domain fractions were observed for the two annealed films in which relatively large EO coefficients were measured. However several of the as-grown samples such as DT454 and DT394 have fairly large c-domain fractions and yet their EO coefficients are rather modest. 189

Figure 5-55. Schematic of the a-domains along with an applied (a) <100>, or (b) <110> E-field vector. 191

Figure 5-56.**a**. shows the resulting hysteretic EO response observed when the response is due to domain variants subject to poling by the applied field. **b**. shows the cycling of the voltage pulse train amplitude and polarity along with the resulting EO response. In **c**. a stylistic representation of the monopolar voltage pulse trains of varying amplitude and polarity is shown. The result shown here are from sample DT443 measured with an in-plane E-field along a <110> direction. 192

Figure 5-57. EO response verses the E-field associated with the application of a monopolar continuous voltage pulse train. Hysteresis is observed in (a) (DT443) where an in-plane <110> oriented E-field is applied, while no hysteresis is observed for an in-plane <100> oriented field for either propagation in transmission (b) (AM069a) or in a waveguide (c) (DT454). 193

Figure 5-58.(a) Theoretical E-field dependence of the film average δΔn due to domain variants 3 and 4 from Figure 5-55a.(b) theoretical relative volume fractions ΔA_{43} of anti-parallel domain variants 3 and 4 from Figure 5-55a. ΔA_{43} is expected to be proportional to the remnant polarization hysteresis loop defined in Section5.1. 195

Figure 5-59. Schematic showing the theoretical field dependent EO response(solid line) and a hypothetical attenuated response due to 90°-domain flipping of the r_{51} and r_{42} contributing domain variants. 196

Figure 5-60. Remnant hysteresis loop of sample DT443 and the corresponding fit to equation (5-38). The corresponding $\Delta A_{ij}(E)$ determined from equation (5-39) with *S* set to 1 is likewise shown. 199

Figure 5-61(a) a schematic representation of a typical "butterfly" EO hysteresis loop. (b) a schematic representation of the field-dependent relative domain volume fraction $\Delta A_{ij}(E)$ of the same form as the remnant polarization hysteresis loop. The $\Delta A_{ij}(E)$ values in a given quadrant in (b) correspond to the EO response in the like-numbered quadrant in (a). (c) Theoretical EO response of the four a-domain variants under a <110> field as shown in Figure 5-55b. Note the similarity of the intrinsic response in (c) to that of the in (a) in the regions where the domain structure is relatively stable (in red). 200

Figure 5-62. Remnant polarization loop and EO hysteresis loop of sample DT443. Coercive fields from both measurements are in good agreement. Theoretically the "coercive field" from the EO measurement should be somewhat smaller than that from the remnant polarization measurement due to the finite ΔI predicted for equal volume fractions of 180° a-domain variants. 202

Figure 5-63(a) schematic representation of intrinsic EO response satisfying the condition $\Delta I_i(E) = -\Delta I_j(E)$. The intrinsic response of domain variants 3 and 4 from Figure 5-55a under a <100> field will be of this form.(b) "butterfly" EO hysteresis loop generated using equation (5-41) with $\Delta I_3(E)$ from (a) and the simple $\Delta A_{34}(E)$ from (b). 203

Figure 5-64. In-plane electronic polarization measurement of DT443. The maximum applied fields employed were the same as those in the EO pulse response measurements from Figure 5-56a. As outlined in sections 3.5 and 5.1, the remnant polarization hysteresis loop is derived by subtracting the non-switching half loops from the full hysteresis loop. The four "sides" of the remnant hysterisis loop were fit to separate polynomial functions so as to generate analytic expressions with wich to represent the remnant hysterisis. For clarity, every other point of the remnant loop is shown. 206

Figure 5-65.Polarization Hysteresis measurement on sample DT443 under ±19V driving voltages. The remnant hysteresis loop derived from the full loop and the non-switching half loops is likewise shown. Also shown for comparison is the remnant hysteresis loop measured with maximum applied fields of ±0.8 MV/m. 207

Figure 5-66. Plot of the field-dependent hysteretic relative domain fraction ΔA_{ij} under the driving conditions employed in the pulse response EO measurements in Figure 5-56a. Where $\Delta A_{ij}(E) > 0$,

variants 3 and 5 are the predominant a-domain variants in the film. Where $\Delta A_{ij}(E) < 0$, variants 4 and 6 are the predominant a-domain variants in the film. 207

Figure 5-67. Hysteretic EO response of sample DT443 and the corresponding fit using equation (5-47) after plugging in equations (5-39) and (5-40) 209

Figure 5-68. Comparison of theoretical ΔI_{net} based on measured remnant polarization to the measured field-dependent EO response of DT443 210

Figure 5-69. E-field normalized theoretical ΔI_{net} and measured EO response of DT443. The finite linear slope upon reducing the field towards zero is due to the quadratic E-field dependence of $\delta\Delta n$ and therefore ΔI. 210

Figure 5-70. Fit of theoretical ΔI_{net} to the measured EO response of DT443 assuming that the domain structure is fully poled by the ±0.8 MV/m $|E_{MAX}|$ 211

Figure 5-71. Fit of field-normalized theoretical ΔI_{net} to field-normalized EO response data of DT443 assuming the domain structure is fully poled by the ±0.8 MV/m $|E_{MAX}|$ 211

Figure 5-72. EO hysteresis loops of sample DT443. (a) shows the EO response normalized with respect to the applied field which is proportional to the $r_{eff}(E)$ in the sample. The regions in red show where r_{eff} is inversely proportional to the applied field. (b) shows the "butterfly" EO hysteresis loop of the field dependent transmitted intensity. 213

Figure 5-73. EO hysteresis loops of sample AM040b. (a) shows the EO response normalized with respect to the applied field which is proportional to the $r_{eff}(E)$ in the sample. The regions in red show where r_{eff} is inversely proportional to the applied field. (b) shows the "butterfly" EO hysteresis loop of the field dependent transmitted intensity. 214

Figure 5-74. EO hysteresis loops of a polycrystalline PZT thin film. (a) shows $r_{eff}(E)$ in the sample. The regions in red show where r_{eff} is inversely proportional to the applied field(b) shows the "butterfly" EO hysteresis loop of the field dependent transmitted intensity.[Potter et al. 1993][165] 215

Figure 5-75. EO hysteresis loops of an epitaxial PLZT thin film. (a) shows $r_{eff}(E)$ in the sample. The regions in red show where r_{eff} is inversely proportional to the applied field (b) shows the "butterfly" EO hysteresis loop of the field dependent transmitted intensity.[Reitze et al. 1993][161] 216

Figure 5-76. EO hysteresis loop of an epitaxial BST thin film. The regions in red show where r_{eff} is inversely proportional to the applied field.[Li et al. 2000][168] 217

Figure 5-77. $BaTiO_3\{200\}$ Bragg reflections of sample DT443 at different applied electric fields 219

Figure 5-78. Schematic of geometry during field dependent lattice parameter measurements by x-ray diffraction. Given the theta angle of 22.5° and the slit width of 50 μm, the x-ray illuminated area is ~11x larger than that in the 12 μm electrode gap where the in-plane E-field is maximized. The measured lattice parameter represents the modal average of the entire illuminated area. 220

Figure 5-79. Surface normal lattice parameters and strain in sample DT443 are plotted verses the applied field. 221

Figure 5-80. Schematics showing stress and strain that results from 90° c-domain flipping. Left figure shows a single a-domain unit cell. Right figure shows plan view with equal number of 90° a-domain unit cells. Equal volume fractions of 90° a-domain variants are expected in the thin films. 222

Figure 5-81. Theoretical E-field dependent strains in the a-domains of sample DT443 due to 90° c-domain flipping. ε_{22} is gven by the emperical equation (5-51), while ε_{11} and ε_{33} are given by equation (5-53). 223

Figure 5-82. Theoretical EO response of a 650 nm thick $BaTiO_3$ thin film when the effect from strain due to 90° c-domain flipping is included. 224

Figure 5-83. Hysteretic EO response of sample DT443 under applied electric field of magnitudes as high as 3.5 MV/m. The "bending over" of the response as field magnitudes exceed ~1.5 MV/m is attributed to strain induced by 90° flipping of c-domains. The EO response under a maximum field amplitude of 0.8 MV/m is included for comparison. 225

Figure 5-84. Remnant hysteresis loop measured with a field magnitude of 0.8 MV/m. The remnant loop is normalized to 1 to reflect the assumption of full poling of the a-domains. The fit in red was used to model the difference in relative domain fractions of 180° a-domains, $\Delta A_{ij}(E)$, for the purpose of modeling the EO response shown in Figure 5-85. (DT443). 225

Figure 5-85. Theoretical EO response when the difference in relative volume fraction of 180° a-domains, $\Delta A_{ij}(E)$, is modeled using the remnant polarization loop measured at a maximum field amplitude of 0.8 MV/m. (DT443). 226

Figure 5-86. The original symmetric ΔA_{ij} function and the shifted function due to internal fields are shown. Both assume that poling is nearly complete at an applied field magnitude of 0.8 MV/m. 227

Figure 5-87. The asymmetry of the measured EO response is qualitatively reflected in the theoretical response under the assumption of a finite internal field (DT443). 227

Figure 5-88. The theoretical EO response assuming the same finite internal field as in Figure 5-87 but assuming the strain within the 12 μm gap between the electrodes is 10x that determined from the surface normal x-ray diffraction measurements (DT443). 229

Figure 5-89. Figure shows a hypothetical hysteretic dependence of the transmitted intensity of the various a-domain variants due to slow relaxation dynamics of some fraction of the flipped c-domains. 230

Figure 5-90. The resulting theoretical EO response under the assumption of a hysteretic dependence of the transmitted intensity due to the various a-domain variants, exhibits "cross over" at finite field of the ascending and descending branches of the response curve which is qualitatively similar to that observed in the measured EO response (DT443). 230

Figure 5-91. For 1 MV/m E-fields the change in birefringence due to both a.) the intrinsic EO effect and b.) the elasto-optic effect due to 90°-domain flipping a small domain volume fraction are on the order of 10^{-3}. That due directly to a 90°-domain flip c.) in which the ordinary and extraordinary axes effectively trade places is ~0.1 231

Figure 5-92. Frequency dispersion of the extrinsic electro-optic response of sample AM069b due to 90° domain flipping. 234

Figure 5-93. Frequency dependence of EO response from 1 kHz to 3 MHz 234

Figure 5-94. Extrinsic EO response of sample AM069b due to 90° domain flipping when operated near the null transmission point with zero bias voltage. Upper schematic shows section of the Senarmont transmission curve near the null transmission point. Lower schematic shows the elliptic cross-section of the negative uniaxial indicatrix of a $BaTiO_3$ domain and the associated orientation of the polar axis under different applied E-fields. 236

Figure 5-95. Extrinsic EO response of sample AM069b due to 90° domain flipping when operated approximately 4° away from the null transmission point with zero bias voltage. 237

Figure 5-96. Extrinsic EO response of sample AM069b due to 90° domain flipping when operated approximately 1° away from the null transmission point with a +1.5V bias voltage. 238

Figure 5-97. "Pinched" hysteresis loop of sample AM069b is consistent with the proposed 90° domain switching model. 240

Figure 5-98. The theoretical "pinched" hysteresis loop of a compressively loaded $BaTiO_3$ sample due to 90° domain flipping. Adapted from figure 4a of Soh, Song and Ni (2006)[206]. 240

Figure 5-99. Schematic showing the indicatrix cross-section of two anti-parallel domain variants both under field and in the absence of a field. The vertical transitions represent the intrinsic EO contributions of the domain variants while the horizontal transitions represent 180° domain flipping. While a finite extrinsic EO contribution results from a 180° reversal under a finite field (ΔI_3), a 180° reversal in the absents of a field makes no contribution to the EO response as the indicatrix cross-section is unchanged as a result of the flip. 242

Figure 5-100. Shown are a series of EO response curves of sample DT443 under the application of monopolar voltage pulse trains of different amplitude. 243

Figure 5-101.a. transient EO rise time when driven by an 11 V pulse (0.92 MV/m). The “ringing” in the response beginning at t=0 is due to channel crosstalk at the oscilloscope. The 10%-90% rise time is 28 ns. b. The transient response is well fit to a simple exponential with a time constant of 11 ns (DT443). 244

Figure 5-102, τ_{RC} as a function of load resistor determined from the measured 3dB cutoff frequency. Inset shows the frequency dependence of the EO response measured with different load resistors from which the relationship was derived. A 100 Ω load resistor corresponds to a τ_{RC} of ~10 ns in excellent agreement with the measured 11 ns τ_{RC} determined from the fit in Figure 5-101b. 244

Figure 5-103. Pareto probability distributions of relaxation times given by equation (2-9) are shown for a τ_P value of 5 ms and *m* values ranging from 0.9 to 0.1. For $\tau < \tau_P$ the probability equals zero. 246

Figure 5-104. The transient electro-optic decay observed in sample DT443 subsequent to removal of the applied 12 ms voltage pulse are shown on a semi-log plot along with the fits to the data using equation (2-11). 247

Figure 5-105. The dependence of the fitting parameters in equation (2-11) on the maximum applied field are shown for the transient EO measurements on sample DT443. 248

Figure 5-106. Comparison of the resulting scale parameters A_o and τ of equation (2-11) when the shape parameters given by the power exponent *m* and the stretching exponent β are left variable or fixed. 251

Figure 5-107. A typical Levy α-stable distribution of relaxation times corresponding to the KWW parameters $\beta = \frac{1}{2}$ and $\tau_{KWW} = 4$ ms is shown. 253

Figure 5-108. Stress-driven EO relaxation after removal of the applied 12 ms voltage pulse. For clarity only every 10th data point is shown. Solid lines show the KWW stretched exponential fit of equation (2-12) to the data (DT443) 255

Figure 5-109. The KWW fitting parameters for the stress-driven EO decay as given in equation (2-12) are plotted verses the maximum applied electric field (DT443). 256

Figure 5-110. The stress-driven EO decay upon removal of the applied voltage pulse is shown along with fits to equation (2-12) with β as a fitting variable and β fixed at 0.5. 256

Figure 5-111. The KWW fitting parameter A_o of equation (2-12) with $\beta = 0.5$ is plotted verses the maximum applied field (DT443). The solid blue line gives the fit to the data using a Weibull CDF function. The dashed orange line gives the associated Weibull probability density function. 257

Figure 5-112. The characteristic time constant KWW fitting parameter τ of equation (2-12) with $\beta = 0.5$ is plotted verses the maximum applied field (DT443). The solid red line gives the linear fit to the data. ... 257

Figure 5-113. Distributions of relaxation times for a range of E_{MAX} amplitudes rendered on both log and linear time scales. In all cases the voltage pulse was applied for 12 ms(DT443). 259

Figure 5-114. a.)EO response of sample DT443 when driven by the bi-polar square wave voltage shown in b. For comparison the EO response of the sample when driven by a mono-polar voltage pulse with the same maximum applied electric field is shown in c. 261

Figure 5-115. KWW stretched exponential fits to the transient EO response due to 180^o domain switching (sample DT443) 261

Figure 116 The field dependent change in birefringence of the a-domain variants when the elasto-optic as well as electro-optic effects are included is shown 289

Figure 117. Field induced rotation of the indicatrix of the a-domains when both EO and elasto-optic contributions are considered. 290

Figure 118. The theoretical change in the transmitted intensity of the a-domains when both the electro-optic and elasto-optic effects are considered. 292

LIST OF TABLES

Table 2-1. Dielectric constants for single-domain single crystal $BaTiO_3$ samples reported in the literature[56,91-98].(T) stress-free unclamped low frequency value. (S) strain-free clamped high frequency value. 35

Table 3-1. Typical MOCVD growth parameters for $BaTiO_3$ thin film growth 56

Table 3-2. Tabulated growth conditions and film properties for select films examined in this study 57

Table 3-3. Typical RT6000S test parameters when using the Charge4 application 63

Table 3-4. Typical RT6000S test parameters when using the Manual4 application 63

Table 5-1. Fitting parameters for polydomain thin-film polarization fitting model 137

Table 5-2. Tabulated electronic polarization hysteresis parameters for all samples measured 143

Table 5-3. Relevant parameters for the samples examined in demonstration of the efficacy of the method of determination of the effective electro-optic coefficient 180

Table 5-4. Effective electro-optic coefficient measurement results under an in-plane <100> oriented electric field 186

5-5 187

Table 5-6. Equation (5-38) fitting parameters assumed in the fit to the remnant hysteresis loop of Sample DT443 shown in Figure 3-4 198

Table 5-7. Tabulated fitting parameters of equation (2-11) for the range of applied voltages in sample DT443 249

Table 5-8. Field dependent KWW stretched exponential fitting parameters of fits shown in Figure 5-108. The field dependence of the fitting parameters from the 3rd through 5th column are given in Figure 5-109 in which all three fitting parameters were allowed to vary. The last two columns reflect the fit for a fixed β value of 0.5 (see Figure 5-111) [sample DT443]. 258

Table AI-1. Si_3N_4 PECVD deposition parameters on Oxford Plasmalab80 RIE/PECVD 285

Table AI-2. Si_3N_4 RIE etch recipe parameters on Oxford Plasmalab80 RIE/PECVD 286

1 INTRODUCTION

Ferroelectric oxides represent a broad class of multi-functional materials with a wide range of applications[1-4]. Their tunable dielectric constant makes ferroelectric thin films suitable for use in tunable microwave filters and varactors[5-10] including thin-film $BaTiO_3$ tunable microwave devices[11,12]. In thin film ferroelectrics, the piezoelectric and pyroelectric properties have been utilized to fabricate a host of sensor, actuator and microelectromechanical systems (MEMS) devices[13-15]. These include ultrasonic micro-motors, micro-pumps and micro-valves[1] as well as infrared (IR) optical sensors[16-18]. $Ba_{x-1}Sr_xTiO_3$ and $BaTiO_3$ thin films likewise show promise for a range of sensor applications including gas, humidity and liquid-phase ion sensors[19-23].

The use of ferroelectrics and ferroelectric thin films for non-volatile ferroelectric random access memory (FRAM or FeRam) applications has been widely studied[3,24-30]. There are already several commercially available lead zirconium titanate (PZT) based FRAM memory products currently avalible[3,31] and many of the major memory manufacturers are actively developing FRAM based memory products[32].

Ferroelectrics likewise exhibit excellent non-linear optical properties which have been widely studied. These include second harmonic generation (SHG)[33-38] as well as the Pockels linear electro-optic effect. While bulk single-crystal lithium niobate is the standard commercial ferroelectric employed in electro-optic modulators[39], electro-optic modulators based on a wide range of ferroelectric thin films have been reported[40-45] including $BaTiO_3$ thin film modulators[12,37,46-54]. Several of these ferroelectrics have bulk electro-optic properties far superior to the 30 pm/V electro-optic coefficient of $LiNbO_3$[39,55]. In comparison bulk $BaTiO_3$ has a clamped high-frequency electro-optic coefficient of 730 pm/V[56].

There are several advantages that thin film ferroelectrics provide as compared to bulk ferroelectrics. For example, one of the primary limitations of bandwidth in electro-optic modulators is the velocity mismatch between the optical and microwave fields[39]. For thin film ferroelectric modulators deposited on low-κ substrates, this velocity mismatch can be significantly reduced[46,57] and through the use

of low-κ buffer layers even eliminated[46]. Additionally integration on a silicon platform has been key to the success of FRAM[26-30], and Si-integration of ferroelectric thin films opens the way for the development of monolithically integrated opto-electronic devices[58-61].

In spite of these advantages ferroelectric thin films have not been commercialized for non-linear optical applications. This is due in part to the fact that the non-linear optical properties in ferroelectric thin films are frequently well below those of their bulk counterparts[53,54]. However, more recently non-linear optical properties of $BaTiO_3$ thin films have been reported that approach[12,47,48] and even match or exceed[36,52] those of their bulk counterparts. The reduced non-linear optical response often observed in ferroelectric thin films relative to bulk ferroelectrics has been attributed to the polydomain ferroelectric domain structure in the epitaxial thin films[12,36-38].

In previous work by Hoerman[12], a model of the dependence of the electronic polarization and the electro-optic response on the domain structure in polydomain ferroelectric thin films was developed. This model was used to assess the degree of poling achieved in the films based on the known bulk properties of the given ferroelectric material. The model however was limited to the prediction of the polarization along a principle <100> axis in the sample. Further development of this polarization model should consider polarization for any in-plane direction of the applied field.

In Hoerman's model of the electro-optic response, the intrinsic response was modeled using approximate expressions whose application is limited to on-diagonal EO coefficients. While this approach allows one to determine effective electro-optic coefficients, it can not be used to accurately *model* the hysteretic EO response that is often observed in polydomain ferroelectric thin films. In order to model the hysteretic electro-optic response, the model must be extended by including the effects of the large off-diagonal r_{51} coefficient, including the quadratic field-dependence of the birefringence as well as the rotation of the indicatrix.

Domain switching as fast as 280 ps (36 MHz) has been reported in the literature[62]. High frequency domain dynamics are expected to effect the high-frequency operation of EO

modulators, and as such characterization of the domain dynamics of any ferroelectric material being considered for use in the next generation of high-bandwidth EO modulator is essential. Previous work by Hoerman examined the dynamic response of relaxing ferroelastic domains in polydomain $BaTiO_3$ thin films[12]. Very short poling times of 1 μs or less and very long poling times of ~100 s were employed in these studies. As such there is an eight orders of magnitude gap between the short and long poling times examined by transient EO analysis. No systematic study of the magnitude of the poling field on the transient response was made in this earlier work. As such, a systematic analysis of the field dependence of the transient EO response at intermediate poling times would extend the earlier work of Hoerman. Pursuant to this, the field dependence of the transient EO response for poling times on the order of ms (midway between the 1 μs and 100 s poling times employed by Hoerman) will be studied.

In this study Hoerman's model is extended to facilitate the modeling of the hysteretic polarization and electro-optic response for any in-plane applied E-field. A polarization model is developed in which the polarization along the principle in-plane <100> directions is determined by the distribution of coercivities of the domain variants whose polar axes are parallel to the given <100> direction. The theoretical measured polarization for any in-plane field direction is then given by the sum of the projection of the two in-plane <100> polarization vectors onto the applied E-field vector.

A model of the field-dependent EO response is developed that includes the effects due to $BaTiO_3$'s large off-diagonal r_{51} electro-optic coefficient. These include the rotation of the indicatrix and the quadtratic field-dependence of the change in the birefringence. Consideration of these effects in the theoretical intrinsic response allows for the accurate modeling of the hysteretic electro-optic response.

Measured electronic polarization and electro-optic data will be analyzed in the context of these models to provide insight into the domain structure dependence of both the electronic polarization and the electro-optic response.

2 BACKGROUND AND LITERATURE SURVEY

2.1 Introduction

The domain structure of a ferroelectric has a profound effect on its measured macroscopic ferroelectric and non-linear optical properties[12,36-38]. A ferroelectric is defined as a material with two or more identical (or enatniomorphic) polar states[2,63]. Each of these states defines a particular domain variant. In the room temperature tetragonal phase of $BaTiO_3$ there are six such domain variants with their polar axes parallel or anti parallel to one of the three <100> crystallographic axes[64]. Non-linear optical coefficients (d_{ij}, r_{ij}) of the oppositely oriented (180^o) domain variants are of opposite sign[12,36-38]. In polydomain ferroelectrics this can result in a non-linear optical response that is significantly smaller than that in bulk single-domain single crystals[12,36-38]. This includes non-linear optical properties such as the Pockels linear electro-optic effect[12,37] and second harmonic generation (SHG)[36,38]. As such an understanding of the domain structure and its dynamics under poling fields are essential in characterizing the non-linear electro-optic properties of polydomain ferroelectric thin films. In particular the non-linear optical properties in polydomain ferroelectrics can be modeled as a function of the relative volume or areal fractions of the different domain variants[12,36-38]. Conversely, because the domain structure effects the nonlinear optical properties of the ferroelectric, measurement of the transient non-linear optical response including the linear electro-optic response[12,65-67] and the second harmonic generation response[36,68] can be used as a means of assessing the temporal evolution of the domain structure.

2.2 Electronic polarization

2.2.1 Ferroelectric and dielectric contributions to electronic polarization

Electronic polarization measurements are one of the primary means of characterizing the domain structure and domain dynamics of ferroelectrics. However, the electronic polarization of a ferroelectric consists of contributions due to both the spontaneous polarization of the ferroelectric domains and their switching under an applied field as well as field-dependent dielectric contributions as given by[69-73]

$$P_{tot} = P_{ferro} + P_{diel} \Rightarrow P_{ferro} = P_{tot} - P_{diel} \qquad (2\text{-}1).$$

Because the ferroelectric component of the polarization is by definition proportional to the switched domain volume fraction[74-76], it is this component of the polarization that is relevant for the determination of the hysteretic field dependence of the non-linear optical properties of ferroelectric thin films. As indicated by equation (2-1) the ferroelectric contributions to the polarization can be determined by subtracting the dielectric polarization contributions from the total polarization[70,77].

The dielectric contribution to the polarization is given by[72]

$$P_{diel} = \frac{1}{A}\int C(V)\ \delta V \tag{2-2}$$

where A is the capacitor plate area of the ferroelectric capacitor and $C(V)$ is the voltage-dependent small-signal capacitance. The dielectric contribution to the total polarization expressed in terms of the applied field and the electronic susceptibility is given by[78]

$$P_{i_{diel}} = \varepsilon_{\circ}\chi_{ij}E_j \tag{2-3}$$

where the electronic susceptibility χ is related to the relative permittivity by $\varepsilon = 1 + \chi$.

For the single domain variant of $BaTiO_3$ with its polar c-axis parallel to the z-axis of the reference coordinate system, equation (2-3) takes the form

$$P_{1_{diel}} = \varepsilon_{\circ}\chi_a E_1 \quad P_{2_{diel}} = \varepsilon_{\circ}\chi_a E_2 \quad P_{3_{diel}} = \varepsilon_{\circ}\chi_c E_3 \tag{2-4}$$

where the values of the susceptibility are given by[79]

$$\chi_a = (\varepsilon_a - 1) \quad \chi_c = (\varepsilon_c - 1) \tag{2-5}$$

As indicated by equation (2-2), the dielectric contribution to the polarization can be determined by integrating the measured small-signal capacitance with respect to the applied voltage and normalizing the result by the capacitor plate area[72]. In Figure 2-1 taken from Gerber et al. 2005[77] the large-signal or total polarization of a (111)-oriented lead zirconium titanate (PZT) thin film is shown along with the dielectric polarization determined from the integrated small-signal capacitance. Also shown in the figure is the ferroelectric contribution to the polarization determined by subtracting the dielectric polarization from the total polarization.

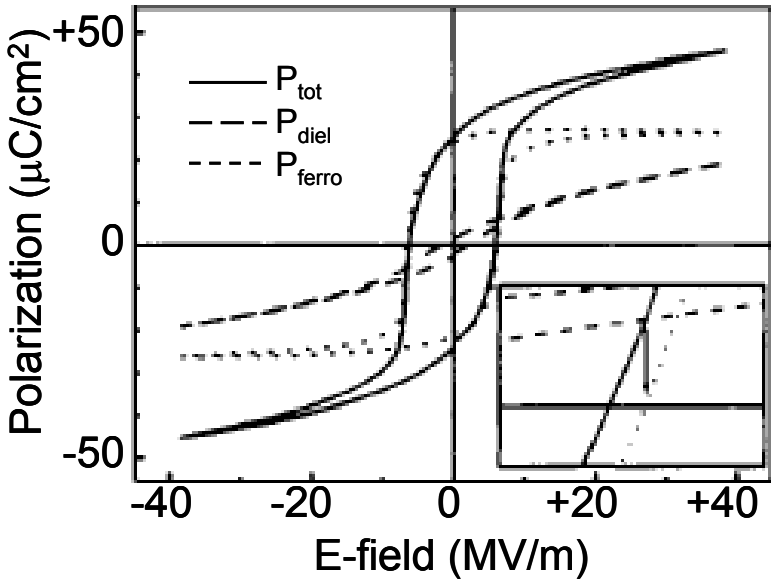

Figure 2-1. The total polarization (P_{tot}) and the dielectric polarization determined from the integrated small-signal capacitance (P_{diel}) of a (111) oriented PZT thin film are shown along with the ferroelectric contribution to the polarization determined by subtracting P_{diel} from P_{tot} [Gerber et al. 2005][77].

By using an appropriate driving voltage, it is possible to measure both the total polarization and the non-remnant polarization from standard large-signal P-V or P-E measurements; from these the remnant polarization loop can be determined[72,74,80]. Polarization hysteresis loops such as that shown in Figure 2-1 are typically measured by driving the sample with a symmetric bipolar triangle wave driving voltage[76,81]. Figure 2-2 shows the polarization loops for a 0.19 μm^2 PZT memory cell capacitor due to Jung et al.[80]. Figure 2-2 illustrates a method that allows one to distinguish the remnant and non-remnant contributions to the polarization by employing the modified driving voltage shown in the inset[72,74,80]. By first applying one cycle of a symmetric bipolar triangle wave voltage, one half of the *total* polarization (including both remnant and non-remnant polarization contributions) is measured as usual. This corresponds to segments ① and ② of the driving voltage in the inset of Figure 2-2. By then repeating the last half cycle as shown by segment ③ in the inset, only the non-remnant components of the polarization are measured. The second half of both the total and non-remnant polarization hysteresis loop is measured by employing a second drive profile of the same form as that in the inset in Figure 2-2 but of opposite

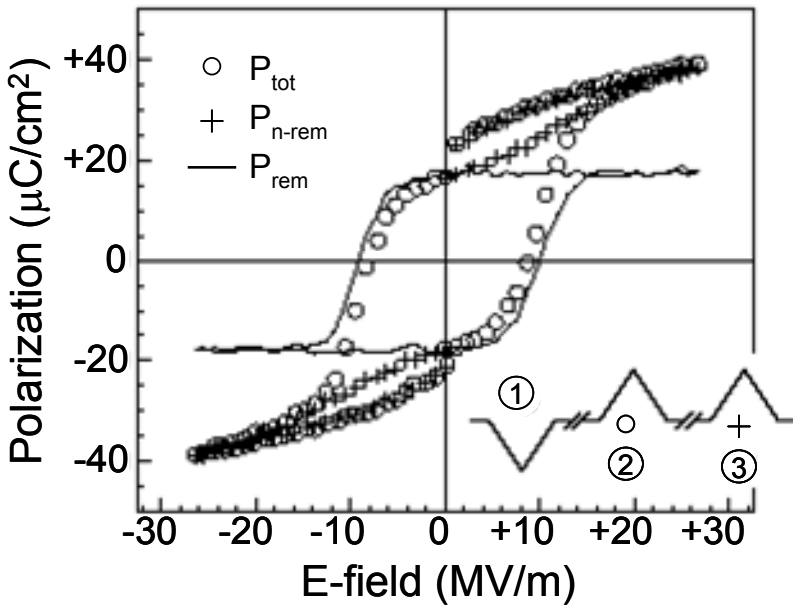

Figure 2-2. The measured total polarization and non-remnant polarization hysteresis loops of a 0.19 μm^2 PZT memory cell capacitor are shown. Also shown is the remnant hysteresis loop determined by subtracting the non-remnant loop from the total polarization hysteresis loop. The inset shows the modified drive profile that allows for the measurement of both the total and non-remnant hysteresis loops [Jung et al.][80].

polarity. The remnant hysteresis loop in Figure 2-2 (due strictly to remnant ferroelectric domain switching) is determined by subtracting the non-remnant hysteresis loop from the total hysteresis loop[*]. An important distinction between the method demonstrated in Figure 2-2 and that shown in Figure 2-1 is that the non-remnant polarization in Figure 2-2 will include any non-remnant ferroelectric contributions to the polarization. In contrast the "reversible" or non-remnant dielectric polarization in Figure 2-1 does not include any non-remnant ferroelectric contributions to the polarization and represents strictly the dielectric polarization. In Figure 2-2 the remnant loop is perfectly flat upon reducing the applied field back to zero because *all* of the non-remnant contributions have been subtracted out of this remnant loop. In contrast, in Figure 2-1 the polarization of the ferroelectric hysteresis loop decreases slightly as the field

[*] As show in Figure 2-2 the non-remnant half-loops are biased by the remnant polarization P_r. In order to determine the remnant hysteresis loop, this bias must be subtracted out of the non-remnant loops *prior* to subtracting the non-remnant hysteresis from the total polarization hysteresis loop.

is reduced to zero. This is because this ferroelectric hysteresis includes *all* of the ferroelectric contributions including the non-remnant ferroelectric contributions due to back switching[†].

The inclusion of the dielectric contributions in the total polarization results in a smaller coercive field (E_C) for the total polarization hysteresis loop than for the remnant hysteresis loops as seen in the inset in Figure 2-1 and in Figure 2-2. Due to the inclusion of the dielectric polarization in the total polarization loop, the coercive field of the total polarization loop does not correspond to the point at which equal volume fractions of 180^o domains exist in the film[77]. Rather the coercive fields of the remnant hysteresis loop corresponds to the point at which equal 180^o domain volume fractions exist in the film[77] which likewise corresponds to the inflection point of the total polarization loop where dP/dE attains its maximum value[73,80].

2.2.2 Polarization in thin films and ceramics verses bulk single crystals

In single-domain bulk single crystals of $BaTiO_3$ full poling or complete alignment of the domains along an applied field direction is possible[‡]. The resulting "square" P-E hysteresis loops typically exhibit a saturation polarization[§] equivalent to the bulk single-crystal spontaneous polarization value of $BaTiO_3$ of 26 $\mu C/cm^2$ [(64)] as seen in Figure 2-3[83]. In polycrystalline samples or polydomain thin films, the existence of non-180^o domains that are both ferroelectric and ferroelastic[84,85] can significantly affect the hysteretic behavior. Coupling between the elastic strain and the polarization leads to incomplete domain alignment and significant back switching of non-180^o domains. As a result of the incomplete domain alignment and back switching, the saturation polarization in thin films and polycrystalline samples can be significantly less than that in bulk single-domain single-crystals[86] as shown in Figure 2-4.

[†] Back switching is the reversal of a domain upon reducing the applied field prior to the change in polarity of the applied field.

[‡] This is not true of all bulk single crystal ferroelectrics. The large tetragonality or self-strain of $PbTiO_3$ for example prevent full poling of $PbTiO_3$ to a single domain state by application of an electric-field alone[Lines and Glass 1977].

[§] The saturation polarization is determined from an extrapolation to V= 0 of the polarization at the maximum applied voltage along a line with a slope equal to dP/dV at the maximum applied voltage. For a background discussion of the electronic polarization hysteresis loop refer to [82] D. Damjanovic, in *The Science of Hysteresis, Volume 3*, edited by I. Mayergoyz and G. Bertotti (Elsevier, 2005), Vol. Volume 3, pp. 337-465.

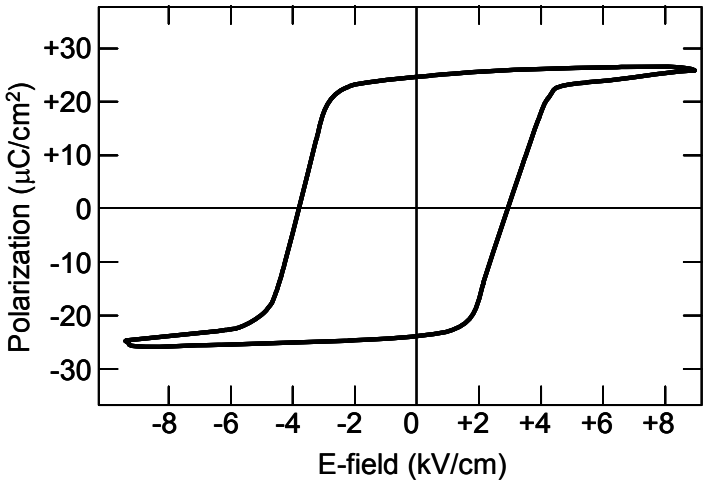

Figure 2-3. P-E hysteresis loop of a virgin single-domain bulk single-crystal $BaTiO_3$ sample adapted from Glower and Hester (1965)[83]

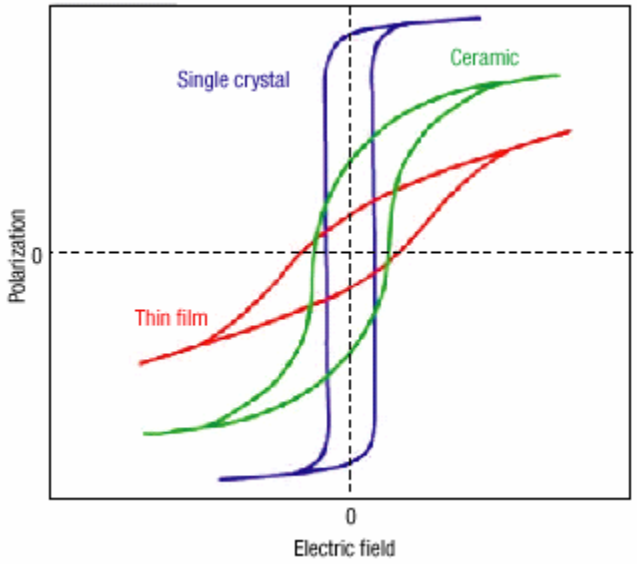

Figure 2-4. Strain limits on switching in polycrystalline ceramics and polydomain epitaxial thin films limit the total achievable ferroelectric switching. Furthermore as non-180° domains are both ferroelastic and ferroelectric, the coupling of the polarization to the elastic strain results in significant back switching of the flipped non-180° domains [Cao 2005] [86].

In polydomain epitaxial thin films the strain limits on non-180° degree domain switching result in a positive correlation between the remnant polarization (P_r)** and the volume fraction of domains susceptible to 180° switching for an applied field direction[87-90]. Figure 2-5 shows standard P-V hysteresis

** The remnant polarization is that measured at V = 0 after reducing the voltage from the maximum applied voltage of either polarity. For a background discussion of the electronic polarization hysteresis loop refer to [82] Ibid.

loops for two different epitaxial PZT thin films grown on MgO and Si substrates, respectively[90]. The film grown on the MgO substrate is predominantly c-oriented while that grown in the Si substrate is predominantly a-oriented. The hysteresis loops were measured in the surface normal direction. The authors attribute the smaller remnant polarization in the a-oriented film to limited alignment of the predominant a-domains along the out-of-plane direction of the applied field. In addition to its higher remnant polarization the highly c-oriented PZT film on the MgO substrate shows almost no indication of

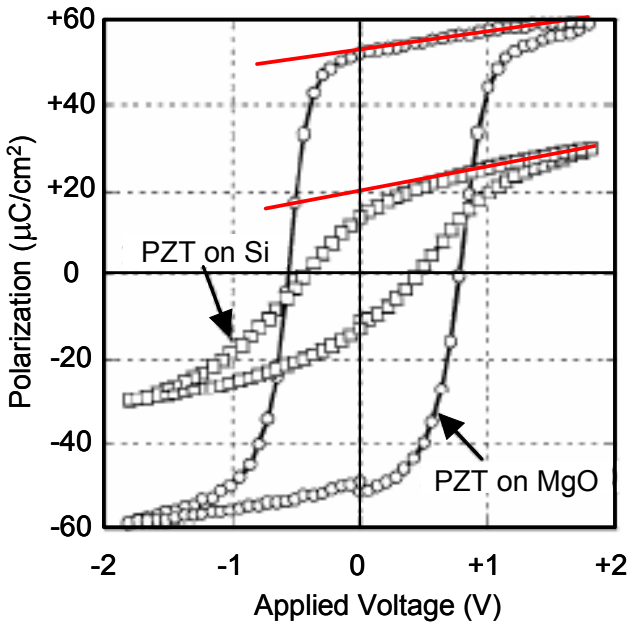

Figure 2-5. Surface-normal P-V hysteresis loops of epitaxial PZT thin films. The remnant polarization in the a-oriented film on Si is just 25% of that of the c-oriented film on MgO [Tsukada et al.][90].

back switching upon reducing the applied voltage back to zero. This is evidenced by the linear decrease in the polarization while decreasing the applied voltage towards zero. In contrast, the PZT film on the Si substrate with its higher volume fraction of ferroelastic a-domains shows signs of significant back switching. This is evidenced by the difference between the remnant polarization (P(V=0)) and the saturation polarization given by the intercept of the red line with the polarization axis. Similarly in surface normal P-V hysteresis loops on ferroelectric $Bi_{3.15}Nd_{0.85}Ti_3O_{12}$ thin films Hu reports a P_r of 28 $\mu C/cm^2$ for films with the polar axis predominantly parallel to the surface normal verses a P_r of just $7\mu C/cm^2$ for films with the polar axis predominantly in the plane of the film[87]. In highly textured

$KSr_2Nb_5O_{15}$ ferroelectric ceramics a P_r of 18 $\mu C/cm^2$ was measured for applied fields parallel to the polar axis of the preferred orientation[88]. In contrast a P_r of just 3 $\mu C/cm^2$ was measured for applied fields perpendicular to the polar axis of the preferred orientation.

In addition to its effect on the remnant polarization, the domain structure in polydomain thin films likewise has a pronounced effect on the dielectric contributions to the measured polarization as a result of the anisotropic nature of the dielectric constant in ferroelectrics. $BaTiO_3$ has a large dielectric anisotropy with the dielectric constant parallel to the polar axis (ε_c) of approximately 130 and a dielectric constant perpendicular to the polar axis (ε_a) of between 2000 to 4800[56,91-98]. The range of the reported value of ε_a for single domain single crystal samples is rather large. The assumed value of ε_a has a pronounced effect on the predicted dielectric contributions to the polarization as seen from equations (2-4) and (2-5). Table 2-1 summarizes the reported values from the literature of the dielectric constants in single-domain single crystal $BaTiO_3$ samples.

Table 2-1. Dielectric constants for single-domain single crystal $BaTiO_3$ samples reported in the literature[56,91-98].(T) stress-free unclamped low frequency value. (S) strain-free clamped high frequency value.

ε_a	ε_c	Ref.	comment
4400 (T)	130 (T)	Merz 1949	measured
3640 (T) 600 (S)		Devonshire 1951	theoretical
2000 (S)		Benedict & Durand 1958	measured
2200 (S)		Merten 1968	measured
1850 (S)		Tominaga & Nakamura 1975	measured
4100 - 4300 (T) 2100 -2250 (S)	170-190 (T) 110 (S)	Turik & Shevchenko 1979	measured
3500 - 4800 (T)	120 - 160 (T)	Nakao et al. 1992	measured
4400±400 (T) 2180±300 (S)	130 (T) 56 (S)	Zgonik et al. 1994	measured

For polarization measurements on single domain single crystals, the hysteresis loops are often very "square" with a relatively small slope in the saturation region as seen in Figure 2-3. Because in these cases the measurement is made along the polar axis of the single domain, the dielectric contribution is solely that due to the relatively small ε_c (~130) as seen from equation (2-4) and (2-5). In polydomain thin films, the existence of non-180^o domains that are not aligned with the field direction result in relatively large ε_a dielectric polarization contributions, which as seen from equation (2-4) and (2-5) act to increase the slope of the total polarization P-E loop[69-72,76].

2.3 Temporal response of domain dynamics

2.3.1 Introduction

It is generally accepted that ferroelectric domain reversal occurs through a nucleation and growth process[1,2,99]. It has been widely observed that the domain growth process consists of an initial rapid forward growth of needle like domains followed by a slower sideways domain growth [2,25,100-106]. With regard to the nucleation process, Landauer[107] showed that the thermal activation energies for random homogeneous nucleation of reversed domains were greater than $10^8 k_B T$ all but precluding the possibility of homogeneous domain nucleation during domain switching[63,105,107]. Because these activation energies can be greatly reduced at interfaces and defect sites, nucleation is generally assumed to be heterogeneous occurring at preferred nucleation sites[2,99] Piezoforce microscopy studies of PZT thin films have demonstrated that the nucleation is heterogeneous occurring preferentially at 90^o domain walls[108,109]. Similarly nanosecond time resolved synchrotron x-ray microdiffraction studies of PZT thin films have likewise found nucleation to be highly deterministic repeatedly occurring at the same preferential sites over repeated switching cycles[110].

In spite of its long history, the kinetics of domain switching remains an area of active research and inquiry. The conditions under which domain switching is nucleation limited and under which it is growth limited remain an open question which is actively debated[2,4,80,111,112]. The growth-limited (or domain-wall limited) Kolmogorov-Avrami-Ishibashi (KAI) model[99,113] has been widely used to

characterize the switching kinetics of ferroelectric domains in bulk samples as well as thin films since its introduction in 1970. Under a square wave or step voltage the KAI model predicts switching currents and transient polarization are given by[114]

$$j(t) = (2P_s n/\tau)\left(t/\tau\right)^{n-1} \exp\left[-\left(t/\tau\right)^n\right]$$
$$P(t) = P_s \exp\left[-\left(t/\tau\right)^n\right] \quad (2\text{-}6)$$

were n is the dimensionality of the domain growth limited to values between 1 and 3 and τ is a characteristic relaxation time constant. However in many cases nucleation-limited models such as those due to Du and Chen[73,115] have been found to better describe the switching kinetics in ferroelectric thin films[111]. Similarly a nucleation-limited switching model due to Tagantsev et al.[116] was found to describe the switching kinetics of a 130 nm PZT thin film better than the KAI model. As the lateral size (or effective plate area) of the ferroelectric capacitor becomes smaller the switching kinetics are predicted to necessarily become nucleation limited due to the limited number of nucleation sites[4]. Scott predicts that this area will range between 1 to 100 μm^2 depending upon the particular ferroelectric material[4].

2.3.2 Ferroelectric relaxation ($E_{applied}$ = 0)

Ferroelectric relaxation results from domain switching that occurs in the absence of an externally applied electric field. Ferroelectric relaxation is a widely studied phenomenon and occurs due to internal depolarizing fields and internal stress in the ferroelectric[78,82]. Typically the observed temporal responses does not follow a simple Debye-like exponential decay. A wide range of temporal responses have been observed including stretched exponential relaxation ($\Delta P(t) \propto \exp\left(-(t/\tau)^{\beta}\right)$)[117-135], logarithmic relaxation ($\Delta P(t) \propto \ln(t)$)[136,137] and power-law relaxation ($\Delta P(t) \propto t^{\alpha}$)[12,65,66,131,138,139]. In previous ferroelectric relaxation studies in the Wessels group, Hoerman found that both the electro-optic response and the polarization exhibited a power law relaxation where the temporal response was given by[12,66]

$$\Phi(t) \propto t^{-m} \quad (2\text{-}7).$$

The values of the exponent *m* were between 0.2 to 0.3 for the transient electro-optic measurements and between 0.2 and 0.001 for the transient polarization measurements. The differences in the values of *m* were attributed to different magnitudes and durations of the poling voltages. These differences result in different initial non-equilibrium domain structures from which relaxation proceeds back towards equilibrium. Figure 2-6 shows the power-law transient electro-optic response of a $KNbO_3$ film due to Hoerman et al.[66]. From the fit to the data using equation (2-7) the power-law exponent *m* was found to be 0.2.

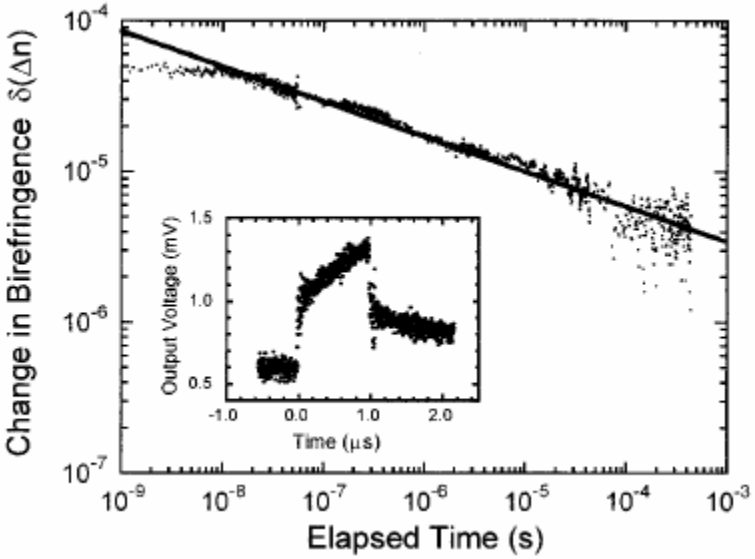

Figure 2-6. Power-law transient electro-optic response of a $KNbO_3$ thin film observed by Hoerman et al.[66]

The power-law relaxation observed by Hoerman was attributed to a fractal ferroelectric domain structure in the films. It was assumed that the relaxation time was proportional to the domain volume ($\tau_i(V_i) = \tau_P V_i$) where τ_P is a constant scaling factor[66]. It was likewise assumed that the distribution of domain volumes was given by a power law distribution consistent with a fractal domain structure according to[66]

$$N(V) = N_\circ V^{-\gamma} \tag{2-8}$$

where $N_\circ$ is a constant scaling factor. Because equation (2-8) gives the number density of domains by volume, (2-8) is multiplied by the volume V to get the distribution of relaxation times (DRT) $\Pi(\tau)$ given by

$$\Pi(V) = N_\circ V^{2-\gamma} \Leftrightarrow \Pi(\tau) = N_\circ \left(\frac{\tau}{\tau_P}\right)^{2-\gamma} = N_\circ \left(\frac{\tau}{\tau_P}\right)^{-m} \tag{2-9}$$

For which the response is given by equation (2-7) or equivalently[66,140]

$$\Phi(t) \propto \left(\frac{t}{\tau_P}\right)^{(2-\gamma)} = \left(\frac{t}{\tau_P}\right)^{-m} \tag{2-10}.$$

The right side of equation (2-9) is equivalent to a Pareto distribution[140,141]. It is known that a Pareto DRT gives rise to a power-law transient response of the form given in equation (2-10)[140]. The Pareto probability distribution given on the right in equation (2-9) is equal to zero for $\tau < \tau_P$ as shown in Figure 2-7 where, for illustration purposes, equation (2-9) is plotted for $\tau_P = 5$ ms and *m* ranges from 0.9 to 0.1.

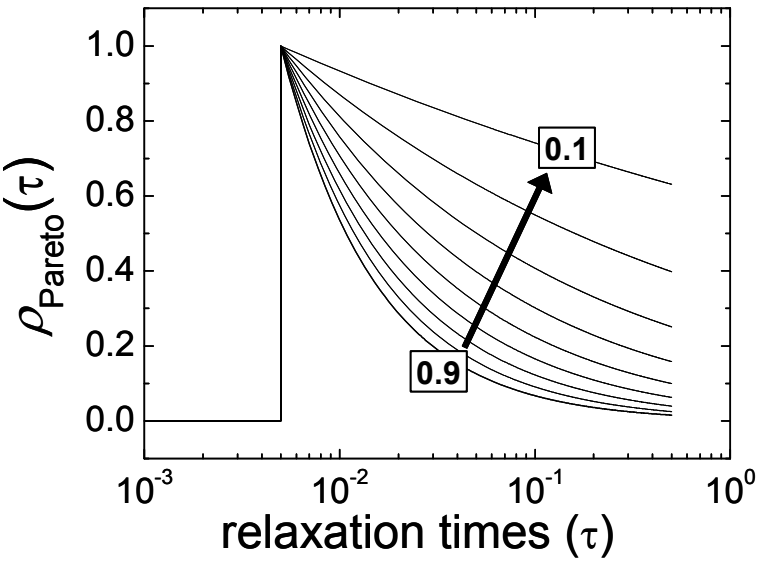

Figure 2-7. Pareto probability distributions of relaxation times given by equation (2-9) are shown for a τ_P value of 5 ms and *m* values ranging from 0.9 to 0.1. For $\tau < \tau_P$ the probability equals zero.

In the long time limit, which in the films studied by Hoerman corresponded to $t \geq 3$ s, the relaxation was found to be better characterized by a modified stretched exponential given by

$$\Phi(t) = At^{-m} \exp\left[-\left(\frac{t}{\tau}\right)^{\beta}\right] \tag{2-11}.$$

A is a constant and the exponential in equation (2-11) is of the form of the Kohlraush-Williams-Watts (KWW) stretched exponential[140,142,143].

The well known Kohlraush-Williams-Watts (KWW) stretched exponential function has been used extensively to model the relaxation of ferroelectric domains[117-135]. The KWW stretched exponential is given by

$$\Phi(t) = 1 - \exp\left[-\left(\frac{t}{\tau}\right)^{\beta}\right] \tag{2-12}$$

where τ is a characteristic relaxation time of the system and β is referred to as the stretching exponent. When β equals 1, equation (2-12) reduces to a simple exponential and for small β of approximately 0.1 or less equation (2-12) predicts a logarithmic time dependence[144]. Non exponential relaxation is typically assumed to result from a population of independent relaxing elements with distinct relaxation times[140,142,143,145-147]. The relaxation of the individual elements is assumed to be simple Debye-like exponential relaxation. Under these assumptions, the observed macroscopic non-Debye-like relaxation results from the superposition of all of the relaxing elements. There is therefore a distribution of relaxation times associated with the ensemble of relaxing elements that make up the system. It has been well established that a relaxation process that is properly characterized by the Kohlrausch-Williams-Watts stretched exponential function, is characterized by a distribution of relaxation times that correspond to a Levy α-stable distribution[140,142,143,145-147]. The general form of the Levy α–stable distribution is given by[140,142,145]

$$\rho_{KWW}(\tau) = \frac{-\tau_{KWW}^{\,2}}{\pi\tau}\sum_{k=0}^{\infty}\left[\frac{(-1)^k}{k!}\sin(\pi\beta k)\Gamma(\beta k+1)\left(\frac{\tau}{\tau_{KWW}}\right)^{(\beta k+1)}\right] \tag{2-13}$$

where $\Gamma(n)$ is the Gamma function. For the purposes of plotting $\rho_{KWW}(\tau)$ is frequently normalizing with respect to τ_{KWW} such that $G_{KWW}(\tau/\tau_{KWW}) = \tau_{KWW}\rho_{KWW}(\tau)$. In Figure 2-8 the resulting $G_{KWW}(\tau/\tau_{KWW})$ for β values ranging from 0.1 to 0.9 are shown on both linear and log scales[148].

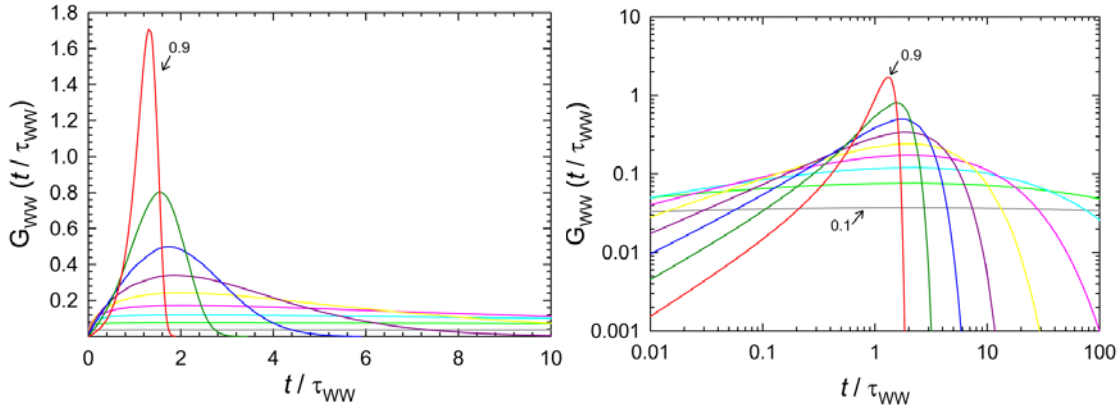

Figure 2-8. The normalized Levy α-stable distributions are shown for β values ranging from 0.9 to 0.1 on both linear and log time scales[148].

For $\beta = ½$, equation (2-13) takes the closed analytic form[142,145]

$$\rho_{KWW}(\tau) = \frac{1}{2}\sqrt{\frac{\tau}{\pi\tau_{KWW}}}\exp\left[\frac{-\tau}{4\tau_{KWW}}\right] \tag{2-14}$$

In Figure 2-9 equation (2-14) is plotted for τ_{KWW} equal to 4 ms.

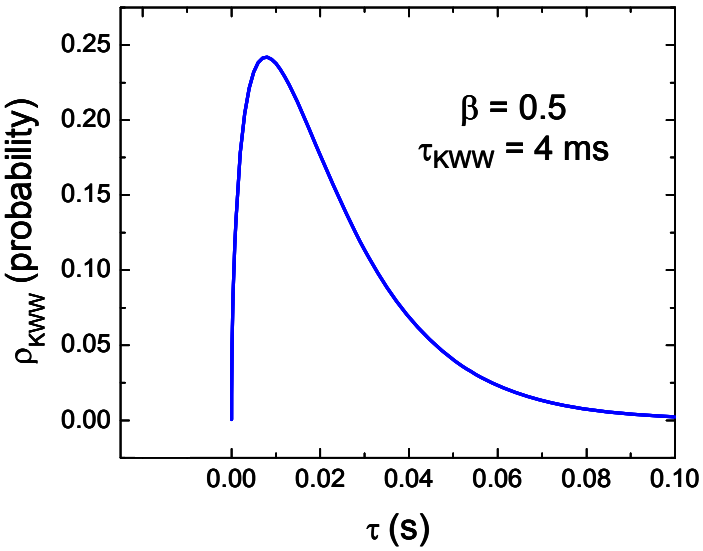

Figure 2-9. A typical Levy α-stable distribution of relaxation times corresponding to the KWW parameters $\beta = \frac{1}{2}$ and $\tau_{KWW} = 4$ ms is shown.

Recently Matyjasek and Rogowski have estimated a distribution of switching times in ferroelectric methylammonium bromobismuthate (MAPBB) single crystals very similar in appearance to the Levy distribution shown in Figure 2-9[121]. The authors used polarized-light video microscopy to monitor the relaxation in a 1mm^2 region of the sample. Forty frames of video per second were recorded and each frame was divided into a 7x9 grid. The relaxation time within each of the 63 grid elements was

recorded and from this, the distribution of relaxation times of the 63 grid elements was constructed as shown in Figure 2-10.

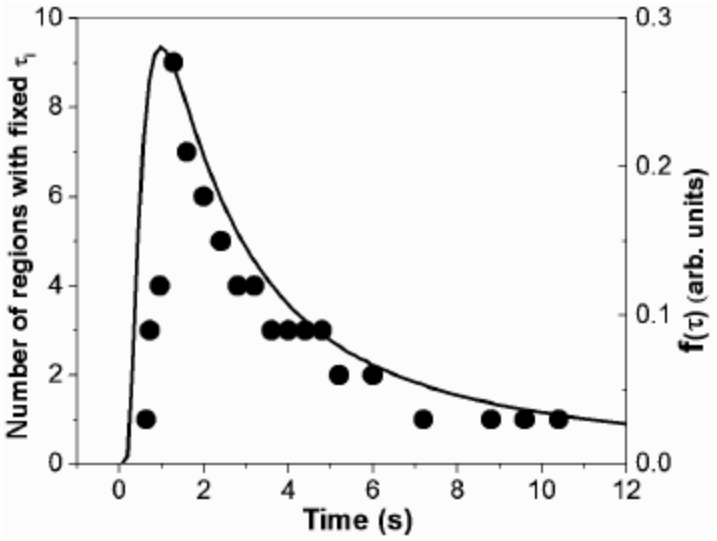

Figure 2-10. Distribution of relaxation times in a ferroelectric single crystal MAPBB sample determined using polarized light video microscopy [Matyjasek & Rogowski Cryst. Res. Technol. 2006][121].

As mentioned previously, the Kohlraush-Williams-Watts (KWW) stretched exponential function has been used extensively to model the relaxation of ferroelectric domains[117-132,149,150]. Relaxation in PZT has been most widely modeled using the KWW function[118-120,124-127,149,150]. However the relaxation in other ferroelectrics have likewise been modeled using the KWW function[117,121-123,128-130]. Many of these studies involved poling the samples by applying a poling voltage and then monitoring the polarization retention verses time using either piezoforce microscopy (PFM) or electrostatic force microscopy (EFM)[119,120,125-127]. In several others the change in polarization during the relaxation was determined by integrating the measured transient current with respect to time[118,124]. Results from several of these domain relaxation studies will be reviewed in the following discussion.

Gruverman et al.[119] studied the relaxation of the polarization in polycrystalline PZT thin films subsequent to the removal of a poling voltage. The transient polarization subsequent to removal of a 5 V poling voltage is given in Figure 2-11. In Figure 2-11 the authors plot $-\ln\left(P(t)\right)$ rather than $P(t)$ verses time. In this case the time dependence of $-\ln\left(P(t)\right)$ is given by

$$-\ln\left(P(t)\right) = At^{\beta} \tag{2-15}$$

where β is the same stretching exponent given in equation (2-12) and A is related to the fitting parameters in equation (2-12) by

$$A = \left(\frac{1}{\tau}\right)^{\beta} \tag{2-16}.$$

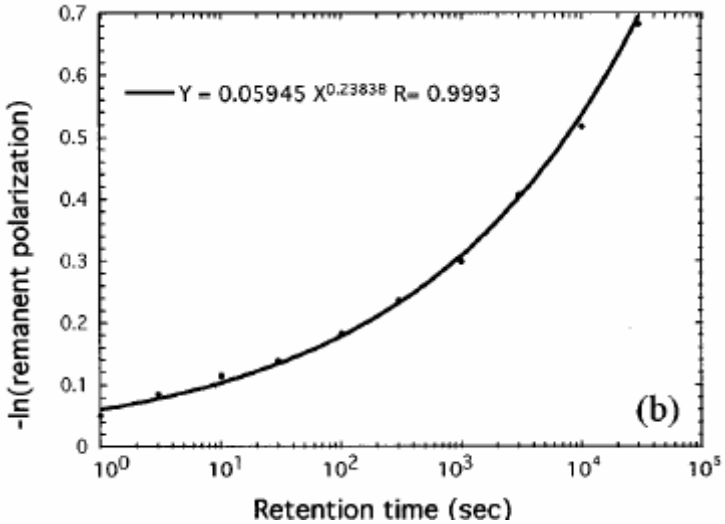

Figure 2-11. A KWW stretched exponential fit to measured polarization relaxation in PZT thin films is shown [Gruverman et al. APL 1997] [119].

Figure 2-11 shows the film-average macroscopic relaxation of the sample for which the stretching exponent β was found to be 0.24. In the same study, PFM analysis of the relaxation of a single grain in the polycrystalline sample determined a β value of 0.69. Similarly in measurements on polycrystalline PZT thin films by Song et al.[126] the macroscopic value of β was found to be between 0.26 to 0.28 whereas from EFM analysis of the relaxation of single domains within the samples, the β values were consistently found to be 1. This indicates that the individual domains were characterized by a single relaxation time exhibiting normal Debye-like relaxation. From Figure 2-8 it is apparent that the width of the distribution of relaxation times is inversely proportional to β.

There have been some interesting recent studies by Matyjasek and Rogowski on relaxation in organic ferroelectrics including telluric acid ammonium phosphate (TAAP) crystals[122] and methylammonium bromobismuthate (MAPBB) crystals[121,123]. These material systems are certainly less well known and of less general interest than PZT of other well known ferroelectrics. However in these

studies by Matyjasek and Rogowski[121-123] the authors look at the effect of both the magnitude and duration of the poling voltage on the subsequent relaxation. They find that upon increasing magnitude and duration of the poling voltage a longer relaxation time is observed. This is consistent with the hypothesis that the under larger and longer poling voltages the domains grow to larger final sizes under the applied field. Upon removing the field the larger domains relax more slowly.

There have been several reports that the relaxation of a ferroelectric domain is inversely proportional to the domain size[126,149,150]. Figure 2-12a and b show the relaxation of poled TAAP and MAPBB ferroelectric samples, respectively. In both cases the relaxation for two different poling voltages is shown and as noted above, the relaxation is slower when a larger poling voltage is employed. Nagarajan et al. observed a similar increase in the relaxation time with an increase in the poling voltage in polycrystalline PZT thin films[127]. In a poled MAPBB sample Matyjasek and Rogowski[123] observe a relaxation of the polarization for which the relaxation time constant is inversely proportional to the poling time. Given that domain switching occurs through a nucleation and growth process[2,99,100], it is reasonable to assume that a longer poling time results in larger average domains which are more stable and decay more slowly[126,149,150]. Consistent with this hypothesis, both Song et al.[126] and Agronin et al.[151] observed a linear dependence of the final domain size on the magnitude of the applied poling field. This is the domain size at the end of the poling cycle prior to the relaxation. Agronin et al. likewise observed a logarithmic increase in the domain size with increasing duration of the poling voltage.

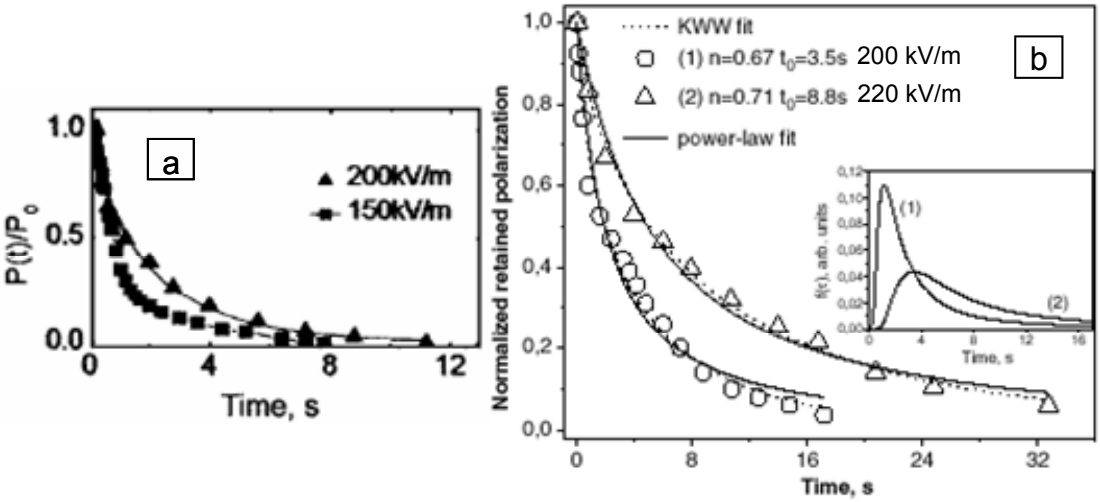

Figure 2-12.Polarization relaxation subsequent to poling is shown for MAPBB [Matyjasek & Rogowski JAP 2006](a), and TAAP (b) organic ferroelectric samples. The relaxation time is observed to increase with increasing magnitude of the poling field[Matyjasek & Rogowski J. Phys.-Condes. Matter 2006].

Polarization retention studies such as those described in the preceding paragraph describe the combined effects of both 180° and non-180° domain relaxation as both domain types can be flipped by the poling field and both may relax due to strain fields and depolarization fields. The ferroelastic relaxation due to non-180° domains flipping can be isolated from that due to 180° flipping by mechanically loading or "poling" the sample. Because the strain state is unaffected by a 180° domain reversal, the application of a mechanical load provides no driving force for 180° domain reversal. Thus through mechanical loading, the relaxation of the ferroelastic domains may be studied in isolation. Both Fu et al.[118] and Koval et al.[124] have studied the relaxation of ferroelastic domains in PZT thin films using the piezoelectric effect. The voltage resulting from the application of a constant mechanical load gives rise to a transient current as the ferroelastic domains relax towards a new equilibrium domain structure under the applied load. The integrated current yields an accumulated charge that is proportional to the change in polarization due to the ferroelastic domain switching. Similarly upon removal of the applied load the ferroelastic domains relax back towards the initial equilibrium domain structure[††]. A schematic of the experimental setup used by both Fu and Koval is shown in Figure 2-13.

[††] Both 180° and non-180° domain walls are generally mobile during either 180° or non-180° domain reversal. What is preserved in the non-switching domains is their *net* volume fraction. Their size and shape may change during the reversal of the actively switching domains. Similarly upon unloading the domain structure relaxes back towards the

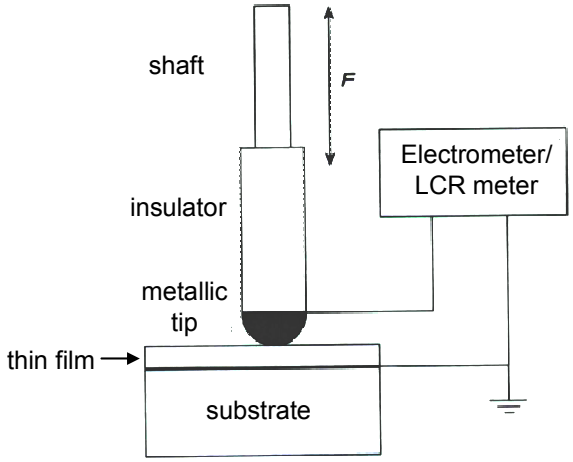

Figure 2-13. Experimental setup for ferroelastic relaxation measurements made by Fu et al.[118] and Koval et al.[124] using the direct piezoelectric effect

Koval et al.[124] made measurements of the relaxation for a range of applied loads on both a 70 nm and 700 nm thick polycrystalline PZT thin films. Figure 2-14a and b show the transient accumulated charge in the 70 and 700 nm films respectively along with the fits to the KWW stretched exponential of the form

$$Q_{tot} = Q_{int} + Q_{ext}\left(1 - \exp\left[-\left(\frac{t}{\tau}\right)^{\beta}\right]\right) \tag{2-17}$$

where Q_{int} is the instantaneous *intrinsic* piezoresponse of the initial domain structure and Q_{ext} is the transient *extrinsic* contribution due to ferroelastic domain switching. Figure 2-15 and Figure 2-16 show the tabulated KWW fitting parameters β and τ verses the applied load given by Koval et al.[124]. In both films measured by Koval et al., the β values were approximately independent of the applied load as seen in Figure 2-15. As seen in Figure 2-16, the KWW relaxation time constant τ_{KWW} increases with increasing applied load. That of the 700 nm film shown in Figure 2-16b increases linearly with the applied load.

---

initial *volume fractions* of the various domain variants, not an identical domain structure. The position of the domain walls may well change.

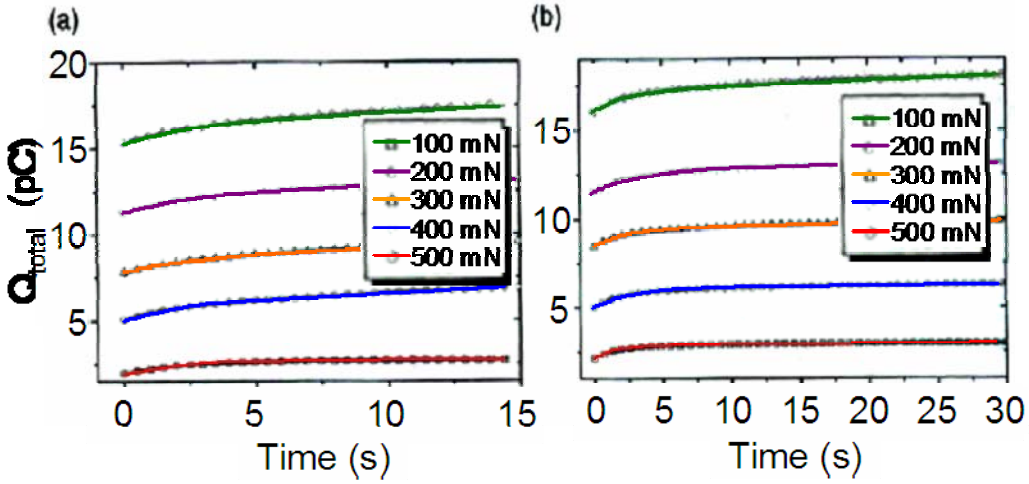

Figure 2-14. Transient charge due to ferroelastic switching in (a) 70 nm and (b) 700 nm thick PZT thin films. Color was added for clarity due to the poor quality of the electronic reproduction of the manuscript.[Koval et al. 2005][124].

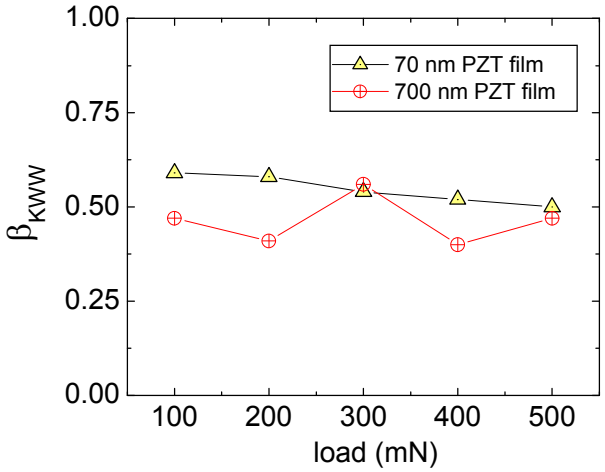

Figure 2-15. The KWW stretching exponent β is plotted verses the applied load in PZT films due to Koval et al. The β values were taken from the tabulated results [Koval et al. 2005][124].

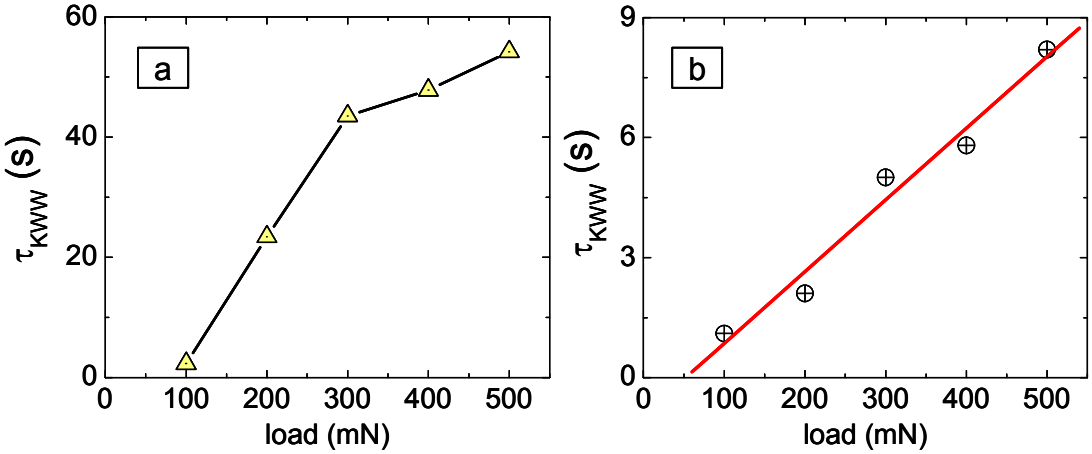

Figure 2-16. The KWW characteristic time constant τ is plotted verses the applied load for the 70 nm PZT thin film (a), and the 700 nm PZT thin film (b). The τ values were taken from the tabulated results [Koval et al. 2005][124].

2.3.3 Ferroelastic switching and strain

Ferroelastic non-180° domain switching gives rise to stresses thereby changing the strain state in the ferroelectric. Bhattacharya's research group at Cal Tech has investigated ferroelastic switching in bulk $BaTiO_3$ under combined electro-mechanical loading[152-156]. Figure 2-17a shows a theoretical stress versus E-field phase diagram for tetragonal c- and a- domains in a thin-plate single crystal $BaTiO_3$ sample due to Burcsu et al.[156] In the study by Burcsu et al. the applied stress and the applied E-field were both parallel to the surface normal of a thin-plate single crystal $BaTiO_3$ sample. From the phase diagram it is evident that increasing compressive stresses stabilize the a-domains in the film. The coercive field for 90° switching from an a- to a c-domain ($E_{c\,(90^\circ)}$) increases linearly with the applied stress. The grey region around the c-domain/a-domain phase boundary represents the hysteresis of the non-remnant switching due to the kinetic nature of the switching.

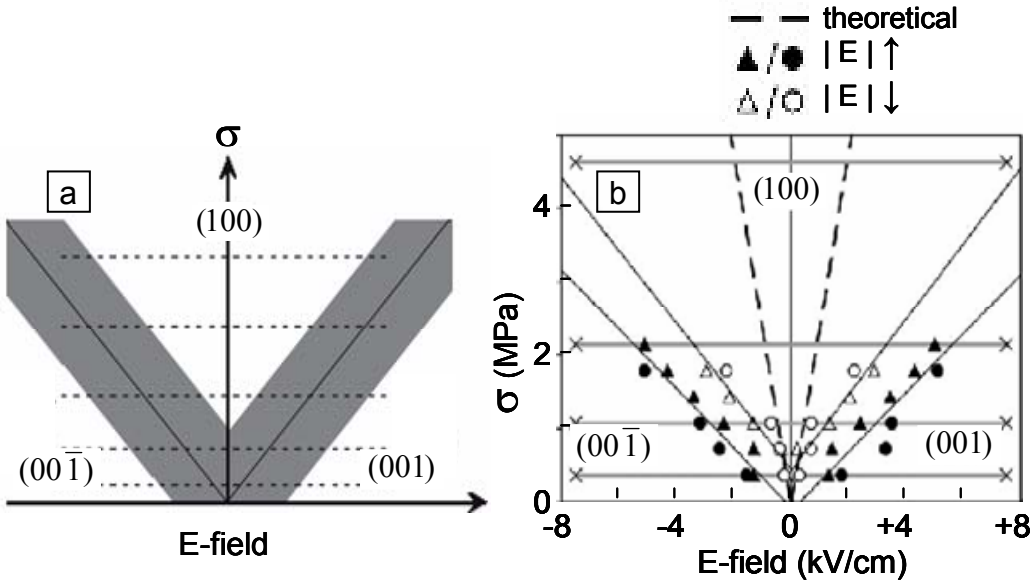

Figure 2-17. (a) Theoretical stress Vs E-field phase diagram for c- and a-domains in a single crystal $BaTiO_3$ sample. Both E-field and compressive stress were applied parallel to the surface normal of a thin plate $BaTiO_3$ single crystal. The grey regions surrounding the c-domain/a-domain phase boundary represents the hysteresis of the non-remnant switching due to the kinetic nature of the switching.(b)Experimentally determined stress Vs. E-field phase diagram for c- and a-domains in a bulk single crystal $BaTiO_3$[Burcsu et al. 2004][156]

The experimental results reported by Burcsu et al.[156] are in general agreement with their theoretical predictions as shown in Figure 2-17b. However, the experimentally observed dependence of the coercive field for 90° switching on the applied stress is significantly greater than the theoretical prediction. The dependence is linear consistent with the theoretical prediction. Furthermore due to the kinetic nature of switching, the coercive field for a-to-c switching is larger than that at which the c-to-a relaxation occurs while reducing the applied E-field.

2.4 Electro-optic properties of ferroelectric thin films

2.4.1 Hysteretic electro-optic response

The hysteretic electronic polarization of ferroelectrics due to the field-dependent configuration of the domain structure can give rise to hysteresis of the electro-optic properties of ferroelectrics as well[‡‡]. Hysteresis of the electro-optic response of ferroelectric thin films is a widely reported phenomenon. Much of the previously reported work has been for lead-lanthanum zirconium titanate (PLZT) thin

[‡‡] As a detailed discussion of the Pockels linear electro-optic effect is given in Chapter 4 it is not discussed here.

films[157-164] or lead zirconium titanate (PZT) thin films[165,166]. Hysteretic electro-optic response has likewise been reported for $Bi_4Ti_3O_{12}$ thin films[167], barium-lead titanate ($Ba_{1-x}Pb_xTiO_3$) thin films[41] and barium-strontium titanate (BST) thin films[168-170]. In previous work in the Wessels research group by Nystrom[37] and Hoerman[12] observed hysteretic EO response in strontium-barium niobate ($Sr_xBa_{1-x}NbO_3$) [37], potassium niobate ($KNbO_3$) [12,37] and barium titanate ($BaTiO_3$) [12] thin films. Several other researchers have likewise reported hysteretic EO response for $BaTiO_3$ [171,172] and $KNbO_3$ [173] thin films.

In many of the reports of hysteretic electro-optic response, a "quadratic" field dependence is likewise reported. A quadratic electro-optic coefficient is often extracted when a "quadratic" field dependence is observed[41,160,161,166-169]. In most instances the "quadratic" field dependence of the EO response is clearly due to extrinsic contributions due to the evolution of the domain structure under the applied field[174]. As Gopalan et al. point out in the CRC Handbook of Photonics[174], a quadratic electro-optic response can result from several distinct mechanisms. These include the intrinsic Kerr quadratic electro-optic response that exists in all materials and is described by the fourth-ranked Kerr EO tensor R_{ijkl}. Another source of a quadratic field dependence of the birefringence arises as a result of finite off-diagonal components in the intrinsic third-ranked Pockels linear electro-optic tensor. It is well documented that a large off-diagonal Pockels linear electro-optic coefficient in conjunction with an appreciable natural birefringence results in a quadratic field dependence of the change in birefringence ($\delta\Delta n(E) \propto E^2$)[52,174-177]. Lastly, the non-linear domain switching in a polydomain ferroelectric can likewise give rise to a quadratic EO response[174]. As Gopalan et al. point out[174], what is observed in this case is the film-average intrinsic linear EO response of a polydomain structure that is evolving with the change in the applied field. Furthermore, it is only this last source of a quadratic EO response that can give rise to hysteresis in the EO response. Neither the intrinsic Pockels or Kerr EO effects give rise in and of themselves to a hysteretic EO response[178,179].

Recently an empirical model of the hysteretic EO response based on the reversible electronic polarization was developed by Chen and Phillips[180] who note that due to the polarization reversal the

linear electro-optic effect in ferroelectrics can exhibit a "pseudo-quadratic" field dependence of the change in birefringence. They therefore caution that careful interpretation of the field-induced change in the birefringence is required to avoid misleading conclusions.

In some instances of reported quadratic EO response in ferroelectric thin films the authors explicitly refer to the calculated linear and quadratic EO coefficients as "effective" coefficients[63,173]. Graettinger et al. explicitly indicate that their effective quadratic EO coefficient is due to domain reconfiguration under the applied field. In the previous work in the Wessels group due to Nystrom[37] and Hoerman[12] the hysteretic EO response was modeled in terms of the evolution of the field dependent domain structure within the film. Despite the observed hysteresis in several previous reports of the hysteretic electro-optic response, the "quadratic" field dependence was attributed to an intrinsic Kerr quadratic electro-optic effect[41,160,161,168]. Several of the reports of hysteretic electro-optic response will be addressed in detail in the following paragraphs.

Kim and Kwok observed a hysteretic "quadratic" electro-optic response for $BaTiO_3$ thin films deposited by pulsed laser deposition (PLD) as shown in Figure 2-18. The change in birefringence of the transmitted optical mode was measured while cycling an applied DC bias field. The applied in-plane E-field direction for the EO measurement reported in Figure 2-18 was along an in-plane <110> direction. The authors indicate that no significant electro-optic response was measured for other in-plane field directions.

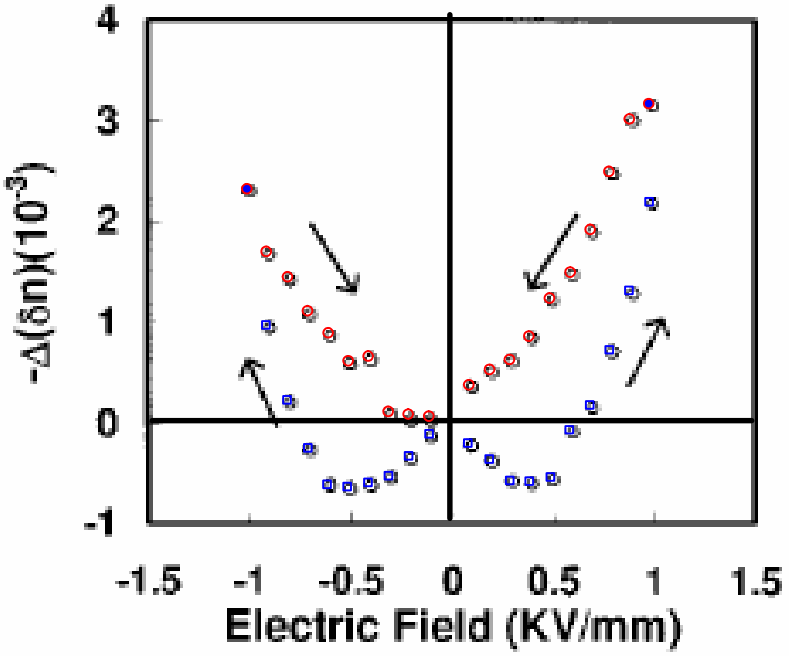

Figure 2-18. Hysteretic EO response reported by Kim and Kwok for $BaTiO_3$ thin films on MgO(001) substrates by PLD. Using coplanar strip electrodes, the applied field was along an in-plane <110> direction.

The most obvious "quadratic" dependence in Figure 2-18 is in the troughs of the butterfly loop. These sections of the hysteresis loop (shown in blue) are dominated by extrinsic effects due to the rapidly evolving domain structure subsequent to the change in the polarity of the applied voltage. In contrast, in those sections of the hysteresis loop shown in red, the domain structure is typically more stable as the applied field is decreasing from a maximum but has not yet switched polarity.

Kim and Kwok indicate that the applied field at the troughs of the EO hysteresis loop (~|0.5| kV/mm) corresponds to the coercive field of the D-E hysteresis loop. This is incorrect. In spite of the similar appearance of the "butterfly" EO hysteresis loop in Figure 2-18 to "butterfly" capacitance verses voltage (C-V) hysteresis loops typical of ferroelectrics, they are not analogous. Because the capacitance is proportional to dP/dV, the peak of the C-V loop corresponds to the point at which the slope of the P-E hysteresis loop is maximized. As was shown in Section 2.2.1 this corresponds to the coercive fields of the remnant P-E hysteresis loop. As indicated in Section 2.1 the EO response due to equal volume

fractions of oppositely oriented domains largely cancel[§§]. As such it is the points at finite field where δΔn goes to zero that approximately equal volume fractions of oppositely oriented domains exist in the sample and as was shown in Section 2.2.1 these points define the coercive field of the remnant hysteresis loop.

Li et al.[168] observed hysteretic electro-optic response in BST thin films of various compositions. Figure 2-19 shows the hysteretic electro-optic response for BST thin films of two different compositions measured using a circular polariscope[181]. The measurements were made by applying a small fixed-amplitude AC voltage while varying the applied DC voltage. Measurements of the retardation due to the AC voltage (Γ_ω) at different applied DC bias voltages are recorded. In their analysis of the EO results

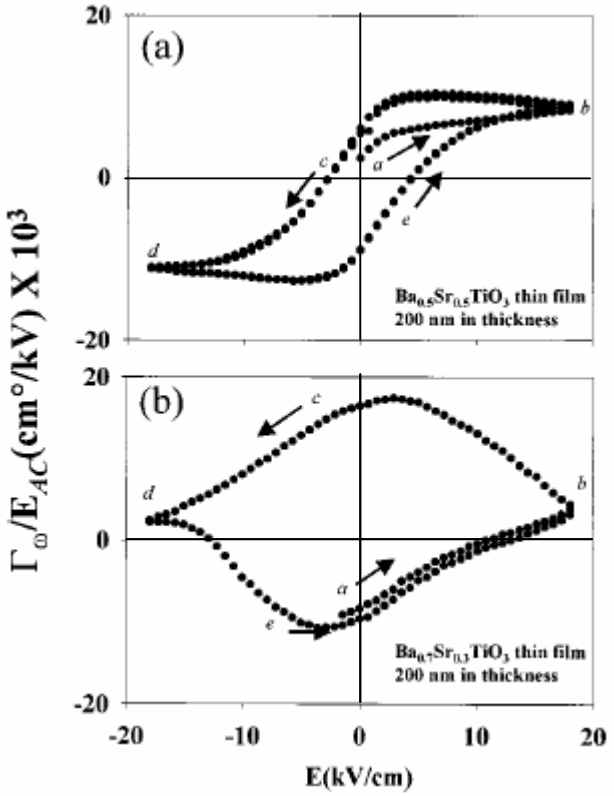

Figure 2-19. Hysteretic EO response of BST thin films due to Li et al[168]. In spite of the labeling of the axes it is believed that what is recorded is Γ_ω/E_{DC} rather than Γ_ω/E_{AC}

[§§] As pointed out in chapters 4 and 5 the asymmetry of the field dependent EO response due to $BaTiO_3$'s large off-diagonal EO coefficient means that the theoretical point at which δΔn or the change in transmitted intensity (δΔI) goes to zero does not correspond exactly to the point at which equal volume fractions of oppositely oriented contributing domains exist in the film.

shown in Figure 2-19 the author do not include the extrinsic contributions due to the evolution of the domain structure and instead extract effective Pockels and Kerr electro-optic coefficients from the hysteretic EO data in Figure 2-19. In the subsequent discussion the authors indicate that the relative magnitudes of these effective Pockels and Kerr EO coefficients is indicative of coexistence of cubic and ferroelectric phases. This indicates that they do not simply intend to model what they recognize as extrinsic domain related contributions to the EO response with contributions with linear and quadratic dependencies on the applied field. Rather they mistake the extrinsic contributions due to the evolution of the domain structure for a convolution of linear and quadratic intrinsic contributions. Such a convolution of intrinsic linear and quadratic EO effects could not possibly account for the observed hysteresis.

2.4.2 Models of domain structure dependent electro-optic response

Few attempts have been made to model the domain structure dependence of the electro-optic response in polydomain ferroelectric thin films. The prior work in this area is briefly reviewed. As previously mentioned Chen and Phillips[180] have recently developed an empirical model of the hysteretic EO response based on the reversible electronic polarization. The field dependence of the electro-optic effect is developed in the context of the theory due to DiDomenico and Wemple[182] in which the Pockels coefficient is considered to be the quadratic polarization optic coefficient biased by the spontaneous polarization. Some of the shortcomings of the model due to Chen and Phillips are as follows. The model considers only linear electro-optic effects under an applied field parallel to the polar axis. As such the effect due to the large off diagonal EO coefficient of $BaTiO_3$ is not included in the model. In their model, hysteretic effects due to the field dependence of the ferroelectric domain structure are empirically fit by a hyperbolic tangent function. The hyperbolic tangent function is chosen simply because it yields the correct "shape" for the P-E hysteresis loops and it has no physical significance. A constant multiplier is used to give the correct saturation polarization.

In the previous work in the Wessels group Nystrom[37] modeled the hysteretic electro-optic response of polydomain $BaTiO_3$ thin films as a function of the areal fraction of each of the domain

variants. Nystrom's method is an extension of that developed by Gopalan[38] for the analysis of second harmonic generation in polydomain ferroelectric thin films. In Nystrom's model the areal domain fractions served as semi-empirical fitting functions that were modified as necessary to fit the observed EO hysteresis. The semi-empirical areal fractions were modeled as linear function differing in slope for different ranges of the applied field.

Hoerman[12] extended the work by Nystrom, identifying the correct functional form for the differential domain areal fraction as that of the ferroelectric contributions to the electronic polarization. However, Hoerman did not attempt to model the measured hysteretic EO response based on the theoretical EO response and the ferroelectric component of the polarization. In his model Hoerman employs approximate expressions for the change in birefringence which are only valid when the off diagonal electro-optic coefficients are negligible. Additionally Hoerman's model does not consider the effect due to the rotation of the principle indices under the applied field. While these simplifying assumptions presents no obstacle for the determination of effective electro-optic coefficients, it precludes the accurate modeling of the theoretical field dependent EO response.

3 EXPERIMENTAL AND ANALYTIC TECHNIQUES

3.1 Growth of $BaTiO_3$ thin films by metal-organic chemical vapor deposition

Epitaxial $BaTiO_3$ thin films were deposited by low pressure metal organic chemical vapor deposition (MOCVD). Deposition was typically on MgO(100) substrates or Si(100) substrates with a $SrTiO_3$(100)//MgO(100) integration heterostructure. A two-stage growth process developed by Towner was employed[36,183]. A more detailed description of the two-stage growth procedure is given by Towner[36,183]. The two-stage growth process involves an initial low-temperature (750 ^oC) nucleation phase followed by a high temperature growth stage (900 ^oC). Standard MOCVD bubblers were employed for precursor transport with 5N purity Ar used as the carrier gas. Bubbler temperatures were maintained using aluminum sleeves in conjunction with heater cartridges. These were controlled with a temperature controller and a solid state relay. This allowed for temperature control to less than ±0.3 ^oC The precursors used were 5N purity titanium tetraisopropoxide (TTIP) for Ti and a custom Ba precursor, $Ba(hfa)_2$ pentaethyleneglycol ethylbutylether ($Ba(hfa)_2$·PEB). Ba precursors were prepared by Professor T. Marks group at Northwestern University. Growth temperature and pressure were 900 ^oC and 10 Torr, respectively. The growth system, based on a horizontal quartz reactor is described in detail in the recent dissertation by Towner[36]. In total, one hundred and twenty $BaTiO_3$ films were gown on the horizontal MOCVD reactor. Typical growth parameters are given in Table 3-1. Table 444 lists the growth conditions and select film properties for a number of the more significant films examined in this study.

Table 3-1. Typical MOCVD growth parameters for $BaTiO_3$ thin film growth

Parameter		Parameter	
Ba Source	$Ba(hfa)_2$ PEB	Ba Source Temperature (^oC)	128 - 130
Ti Source	Ti-tetraisopropoxide	Ti Source Temperature (^oC)	27
H_2O Carrier Gas/Flow Rate (sccm)	128 - 130	H_2O Source Temperature (^oC)	0
Ba Carrier Gas/Flow Rate (sccm)	Ar / 110-114	Base Pressure (Torr)	~ 0.1 - 0.2
Ti Carrier Gas/Flow Rate (sccm)	Ar / 20	O_2 Partial Pressure (Torr)	2.6
Ti Diluent Gas/Flow Rate (sccm)	Ar / 37-39	System Growth Pressure (Torr)	8
Manifold Push Gas/Flow Rate (sccm)	O_2 / 271-297	Growth Temperature (^oC)	750 (Nuc.) 900 (Growth)

In table 444 the SiO_2 layer column indicates whether an SiO_2 buffer layer was deposited on the $BaTiO_3$ thin film. All films were grown using the two-stage growth method and in all cases a 3-6 minute nucleation phase at 750 ^oC was employed. Some films were annealed in atmospheric conditions post growth as indicated in the last column.

Table 3-2. Tabulated growth conditions and film properties for select films examined in this study

Film ID	Substrate	SiO_2 Layer (nm)	thickness (nm)	T_{growth} (^oC)	BTO{200} ω-FWHM (degrees)	n (@ 633 nm)	annealed (^oC)
AM003	MgO(100)	no	769	894	0.37	2.404	no
AM009	MgO(100)	400	730	912	0.57	2.364	no
AM016	MgO(100)	no	701	916	0.47	2.350	no
AM018	MgO(100)	no	592	899	0.61	2.374	no
AM033	MgO(100)	yes	627	891	0.33	2.396	4hr 1100
AM039	MgO(100)	400	624	917	0.39	2.374	no
AM040b	MgO(100)	no	524	900	0.30	2.384	10hr 1100
AM047	MgO(100)	200	600	875	0.52	2.384	no
AM055	MgO(100)	no	540	933	0.32	2.397	5.5hr 1100
AM069a	MgO(100)	no	404	910	0.28	2.389	10hr 1100
AM069b	MgO(100)	no	404	910	0.31	2.391	no
DT443	MgO(100)	no	640	900	0.43	2.365	no
DT454	MgO(100)	yes	615	880	0.40	2.389	no
HR24a	MgO(100)	no	454	900	0.33	2.358	no
HR24b	MgO(100)	no	454	900	0.32	2.360	10hr 1100
HR26	Si(100)	no	550	900	0.84	2.414	no

3.2 Post growth annealing of $BaTiO_3$ thin films

Several films were annealed after growth in a Thermodyne 59300 high temperature tube furnace. Annealing was in air under atmospheric conditions. The films were loaded into the tube furnace at room temperature and ramped at 10 ^oC per minute to between 1100 to 1200 ^oC where the were held for between

1.5 to 12 hours. The films were then either air quenched by removal from the furnace at temperature or they were left in the furnace as it was ramped down to room temperature at 10 ^{o}C per minute.

3.3 Thin film characterization

3.3.1 X-ray diffraction

Surface normal θ–2θ and ω x-ray diffraction measurements were made on all films investigated. The relative domain fractions, phase purity and epitaxial quality of the films were assessed from these surface normal measurements. Measurements of the MOCVD grown $BaTiO_3$ thin films were typically made on a General Electric XRD-5 diffractometer with LiF Cu-kα_1 focusing monochrometer. For measurement of the MBE gown $SrTiO_3$(100)//MgO(100) integration layers either of two diffractometers was used. These included a Rigaku ATX-G, and a 4-circle 12 kW diffractometer with a rotating Cu anode. Phi-scan measurements on the 4-circle diffractometer were made to assess the quality of the in-plane epitaxy of both the $BaTiO_3$ thin films and the MBE grown buffer layers.

3.3.2 Prism coupling

Film thickness, refractive index and optical loss measurements of the $BaTiO_3$ thin films were measured using a Metricon 2010 prism coupler. All measurements were made at λ = 632.8 nm. Index and loss measurements were made for both the TE and TM modes. The manufacturer's specifications indicate accuracies for the index and thickness measurements of ±0.001 and ±0.5% respectively.

3.4 Device fabrication

3.4.1 Transmission electro-optic device

The fabrication of transmission electro-optic devices consists of standard contact photolithography to create the pattern for the coplanar electrodes followed by deposition of either Cr/Au or Ti/Au electrodes by electron beam evaporation. The device consists simple of two coplanar electrodes with a 5 μm electrode gap deposited directly on the $BaTiO_3$ film. Figure 3-1 shows a schematic of the resultant device. The step by step process flow is provided in Appendix I.

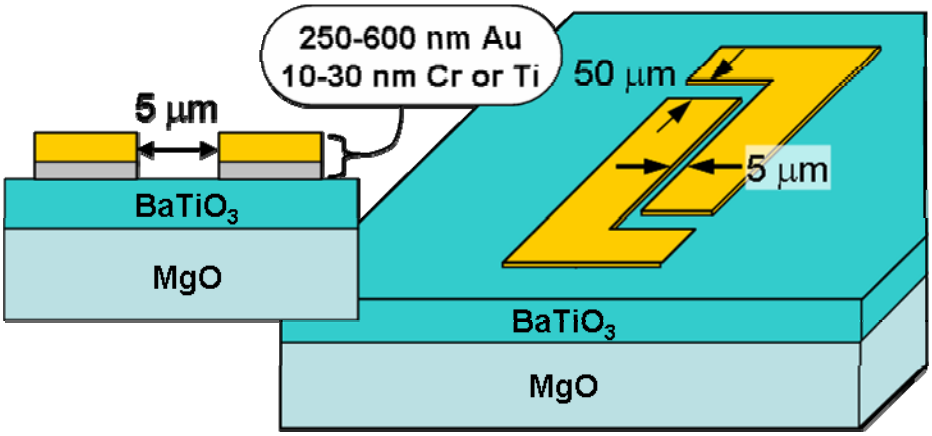

Figure 3-1. Schematic of transmission electro-optic device

3.4.2 Waveguide electro-optic modulator

The waveguide electro-optic modulator device structure, as shown in Figure 3-2, is considerably more complex than the simple transmission electro-optic device discussed in 3.4.1. The device process flow, in summary, consists of the following. A Si_3N_4 layer is first deposited on the $BaTiO_3$ thin film. The strip-loaded waveguides are fabricated by first defining the waveguide patterns using contact lithography, and then forming the waveguides through an RIE etch of the Si_3N_4. At this point, if desired, an optional SiO_2 buffer layer is deposited by e-beam evaporation. Next, photolithography is used to define the electrode pattern, taking care to align the pattern with the underlying waveguides. Finally the electrodes are deposited by e-beam evaporation and, subsequent to a lift-off process, the device is complete. A detailed description of the fabrication process is given in Appendix I.

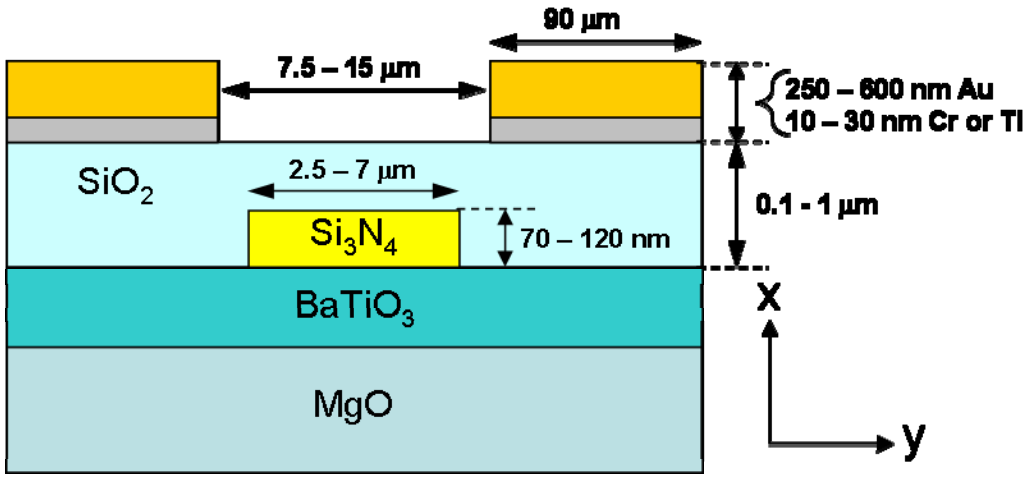

Figure 3-2. Waveguide electro-optic modulator device schematic. The SiO_2 layer is optional and if omitted electrodes are deposited directly on the $BaTiO_3$ film.

3.5 Electronic polarization measurements

In-plane electronic polarization measurements were made using the waveguide device structures described in the preceding Section 3.4.2. A Radiant Technologies RT6000S apparatus was employed in the measurements. BNC cables were run from the supply and return lines on the RT6000S into a stainless steel enclosure with electrical feedthroughs to insure proper electromagnetic shielding. A probe station inside the E-M shielding enclosure was used to make contacts to the coplanar electrodes on the sample. Alternatively if the samples were already connectorized, contacts were made using BNC-to-(test clip) adaptors as shown in Figure 3-3. The probe station was equipped with a heated stage to facilitate temperature dependent polarization measurements.

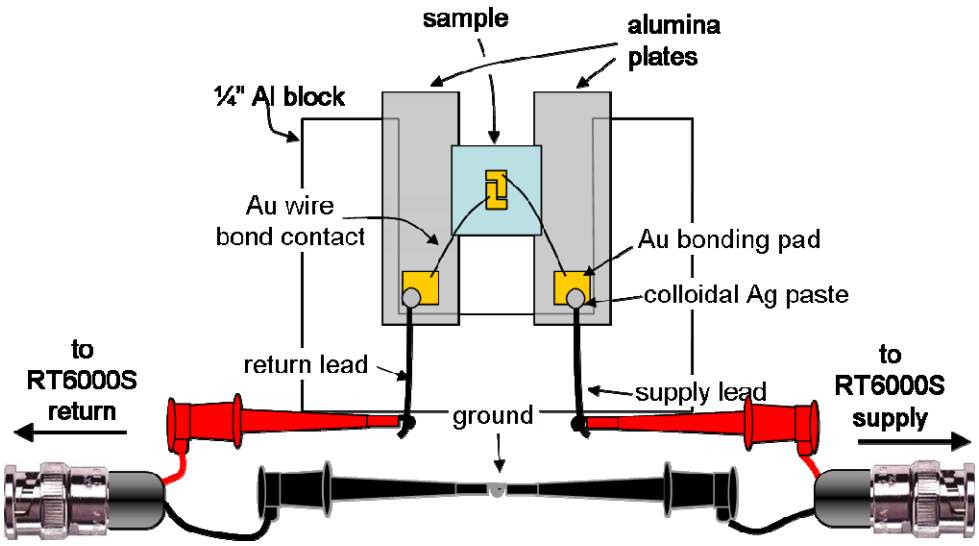

Figure 3-3. Electrical connections used for wire-bonded samples when making electronic polarization measurements

The RT6000S was used in the "virtual ground" mode rather than the Sawyer-Tower mode. Advantages of the virtual ground mode over the Sawyer-Tower mode are as follows. In the Sawyer-Tower mode, the sense capacitor gives rise to a "back voltage" which reduces the measured voltage and therefore the calculated polarization. While careful selection of the sense capacitor can reduce the back voltage, no back voltages are present for measurements in the virtual ground mode. Additionally, in the Sawyer-Tower mode, the parasitic capacitance adds directly to the sense capacitance and thus again gives rise to back voltages leading again to calculated polarizations lower than the actual value. In contrast, in the virtual ground mode the return terminal is maintained at zero potential such that no parasitic voltages arise.

The RT6000S programs Charge4 or Manual4 were used to make the electronic polarization measurements[76]. For standard full hysteresis loops, Charge4 was employed. Manual4 allows one to employ custom driving voltage profiles. As such, Manual4 was used to measure the two non-switching half-loops in addition to the full hysteresis loop in order to derive the remnant hysteresis loop. Figure 3-4 shows a custom drive profile used to generate both the full hysteresis loop as well as the non-switching half-loops. Because the non-switching half-loops are immediately preceded by identical preset loops, no

180° domain switching is expected during the non-switching half-loop (hence the name). As such the non-switching half-loop allows one to isolate the polarization contributions due to dielectric polarization as well as that due to 90° domain switching and then subtract this from the full hysteresis loop to derive the remnant hysteresis loop. Table 3-3 and Table 3-4 give the standard test parameters employed in the Charge4 and Manual4 programs, respectively.

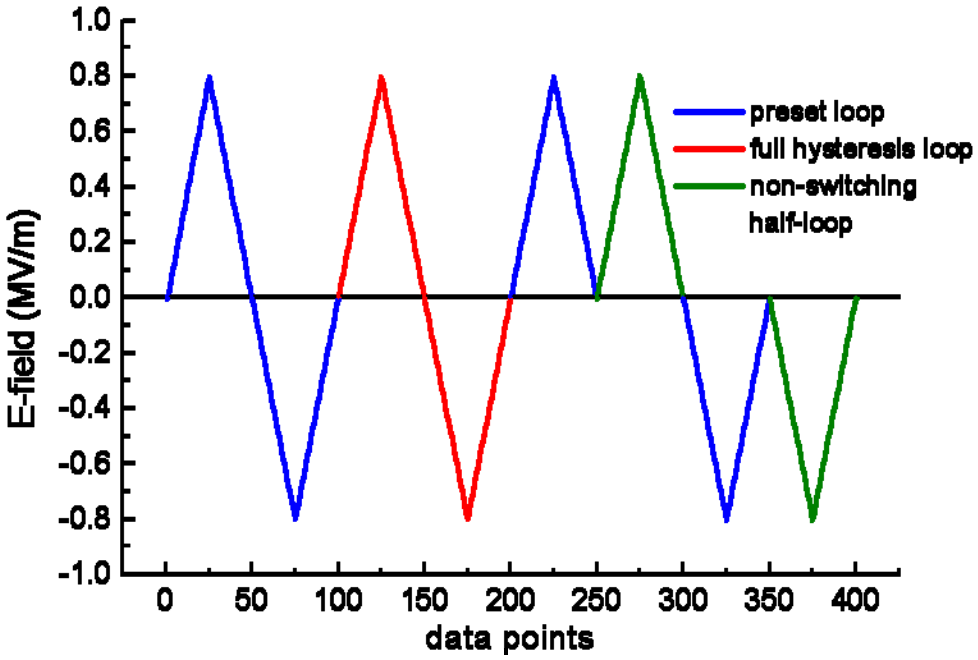

Figure 3-4. Driving profile used to generate both the full hysteresis loop as well as the two non-switching half loops.

For the purpose of calculating the in-plane polarization, devices were modeled as parallel plate capacitors. The plate area corresponds to the product of the $BaTiO_3$ film thickness and the overall device length while the plate separation corresponds to the electrode gap. The large dielectric constant of the $BaTiO_3$ film relative to that of the MgO substrate justifies adoption of such a model.[184] While the parallel plate approximation is known to underestimate the polarization, it has been shown that for films with dielectric constants in excess of 1000 and film thicknesses in excess of 600 nm the error introduced by using the parallel plate approximation rather than the full Farnell equation is less than 6%[12]. While automated routines exist for the RT6000S tester that measured and then eliminate both the parasitic

capacitance and leakage from the measured polarization, the leakage current compensation is limited in its capacity. In films with excessive leakage ($R<10^{-9}\ \Omega$) distorted hysteresis loops were observed.

Table 3-3. Typical RT6000S test parameters when using the Charge4 application

RT6000S Charge4 settings	Value
Voltage Mode	LOW Voltage (only option)
Maximum drive voltage (V)	1 - 19.99
Number of test points	100-500 (default 100)
Hardware Mode	Virtual Ground Mode
Test Mode	Hysterisis
Time between hysteresis points (ms)	0.17
Current vs. Voltage measurement delay (ms)	100 (minimum)
Measurement pulse step rate (ms)	2 (default)

Table 3-4. Typical RT6000S test parameters when using the Manual4 application

RT6000S Manual4 settings	Value
Voltage Mode	LOW Voltage (only option)
Maximum drive voltage (V)	1 - 19.99
Number of test points	500
Hardware Mode	Virtual Ground Mode
Test Mode	Hysterisis
Drive Profile Type	Custom Inflection
Time between hysteresis points (ms)	0.17
Current vs. Voltage measurement delay (ms)	100 (minimum)
Measurement pulse step rate (ms)	2 (default)
Remove offset from hysteresis data	Yes
RT6000 internal amplification factor	16.2

3.6 Electro-optic measurements

Measurements of the electro-optic properties of epitaxial $BaTiO_3$ thin films were made in either the waveguide geometry or the transmission geometry as shown in

Figure 3-5. In both geometries, the applied electric field is in the plane of the film typically along either a <100> or a <110> direction. In the transmission geometry the Poynting vector $\bar{S}$ of the optical mode is parallel to the surface normal of the film and orthogonal to the applied electric field. In the waveguide geometry the Poynting vector $\bar{S}$ of the optical mode lies in the plane of the film, and is orthogonal to the applied electric field.

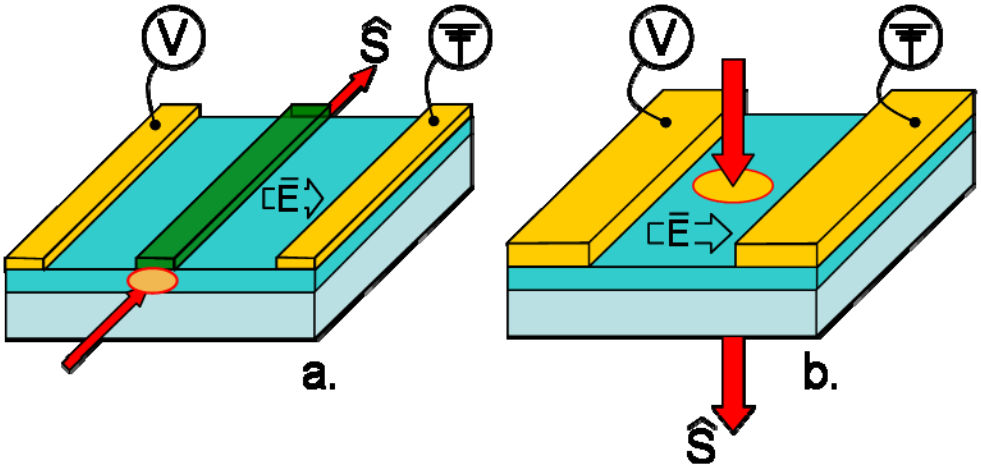

Figure 3-5. Device geometry showing the orientation of the applied electric field (E) to the Poynting vector of the optical mode (S) in the a.) waveguide and b.) transmission geometries.

Both measurement geometries have their advantages and disadvantages. The transmission geometry has the advantages of simple device fabrication and ease of coupling. The primary disadvantage of the transmission geometry is that the interaction length between the optical mode and the modulating electric field is limited to the thickness of the film – typically between 400 to 1000 nm. As such V_π can not be directly measured and determination of r_{eff} is indirect. In the waveguide geometry the long interaction lengths (2 – 10 mm typically) allow for the direct measurement of V_π and straight forward calculation of r_{eff}. Additionally, the waveguide geometry is the relevant geometry for

commercial applications of $BaTiO_3$ thin film electro-optic modulators. However, the device fabrication process required for waveguide measurements is significantly more complicated and time consuming. Additionally, cleaved endfaces are required. Cleaving has a success rate of at best 60% per attempt. The particulars of the measurements methods in the two geometries will be discussed separately in the following sections.

3.6.1 Electro-optic measurements in the transmission geometry

3.6.1.1 The Senarmont polariscope

A polariscope or polarimeter configured to employ the Senarmont compensation method[181] was used for the electro-optic measurements in the transmission geometry (see Figure 3-6). The Senarmont setup is also commonly referred to as the polarizer-sample-compensator-analyzer or PSCA setup[175]. The primary advantage of the Senarmont polariscope over the polarizer-sample-analyzer or PSA setup is that the presence of the compensator, in the form of a quarter wave plate, allows one to select the operating point and likewise compensate for any natural birefringence of the sample by adjusting the analyzer angle. With reference to the coordinate system from Figure 3-6, we designate the y-axis as the origin of azimuth, and set the input polarizer at an angle $\theta = 90^\circ$ (the sample is oriented such that the field induced principle axes are at $\pm 45^\circ$). The compensator consists of a quarter-wave plate with one of its principle axis aligned with the optical axis of the input polarizer (90°). In this configuration it can be shown[181] that light emerging from the compensator is linearly polarized at an angle $\theta - \delta/2$ where δ is the retardation induced by the sample.

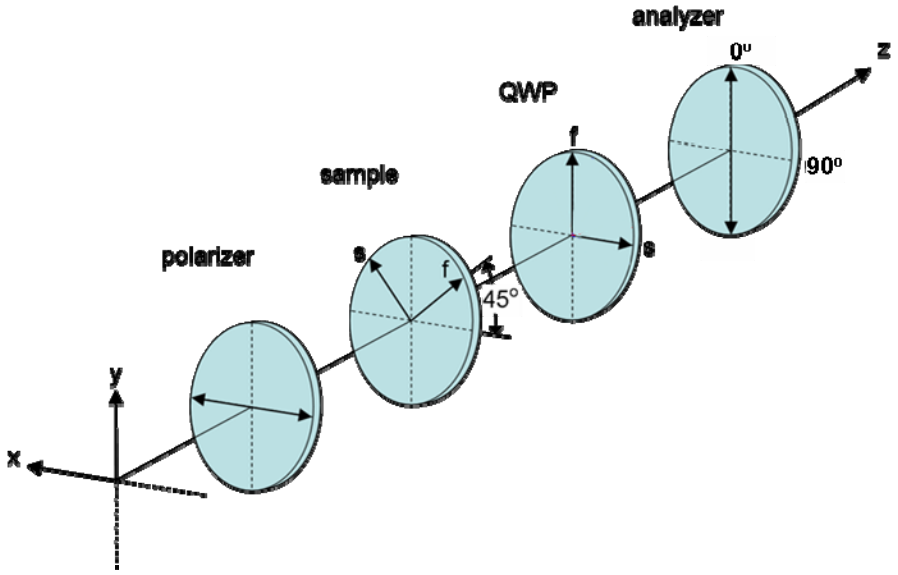

Figure 3-6. the Senarmont polariscope, also referred to as PSCA setup, is used for measurement of EO properties in the transmission geometry.

The transmitted intensity in the PSCA setup as a function of analyzer angle (β) and the retardation induced by the sample (δ) is given by the expression[175]

$$I = I_{\min} + I_{amp} \sin^2\left[\left(\delta/2\right) - \beta\right] \tag{3-1}$$

where I_{amp} is the peak-to-peak amplitude of the transmission curve, and I_{min} is the finite intensity reaching the detector at the null transmission point due to non-ideality and imperfect alignment of the optical elements of the polariscope as well as stray ambient light entering the detector. Figure 3-7 shows the transmitted intensity through the polariscope as a function of the analyzer angle β, and the retardation introduced by the sample δ.

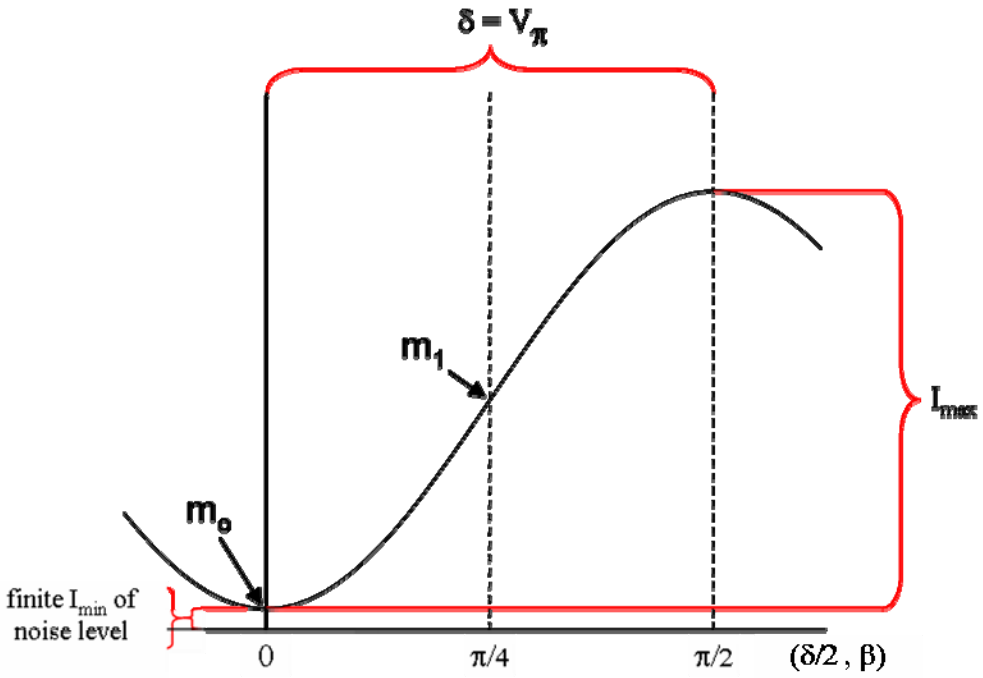

Figure 3-7. Transmission curve of a Senarmont PSCA polariscope. The maximum linearity point (m_1) and null transmission point (m_o) are labeled.

As written, δ includes all contributions to the retardation induced by the sample. These include any fixed or static retardation associated with natural birefringence or the application of a DC bias voltage or both. It likewise includes any dynamic retardation associated with the application of an AC voltage to the sample. In the case where static retardation is present due either to the application of a DC bias or to natural birefringence, the analyzer is simply adjusted to compensate for the static birefringence such that the argument of the $\sin^2$ term in (3-1) corresponds to the desired operating point on the transmission curve. Figure 3-8 shows a map of equation (3-1) in the 2D (β,δ)-space.

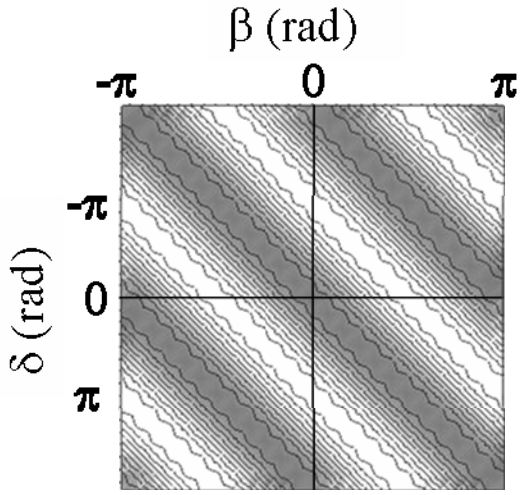

Figure 3-8. 2D map of equation (3-1) . Darkest regions correspond to I_{min} while brightest regions correspond to $I_{min}+I_{max}$.

In Figure 3-7, the points on the curve labeled M_1 and M_o represent two important operating points of the Senarmont polariscope. M_1 is referred to as the maximum linearity point as $\Delta I/\Delta\delta$ is approximately linear for small $\Delta\delta$ in the vicinity of M_1 as seen in Figure 3-7, and Figure 3-10. However, there are a number of advantages in operating at M_o or the null transmission point.

The ratio of the amplitude of the dynamic response (I_{AC}) due to the application of an AC voltage signal, and the static level of the transmitted intensity (I_{DC}) is maximized in the vicinity of the null transmission point. While the theoretical I_{AC}/I_{DC} ratio is divergent at the null transmission point as shown in Figure 3-9a, the finite intensity measured at the null transmission point (I_{min}) results in a maximum I_{AC}/I_{DC} ratio as some small angle away from the null transmission point as seen in Figure 3-9b. Typical measured I_{AC}/I_{DC} ratios at the null transmission point range from the low 10^{-3} to the low 10^{-2} range. An I_{AC}/I_{DC} ratio at the null transmission point of $6.3\text{x}10^{-3}$ was assumed in Figure 3-9b.

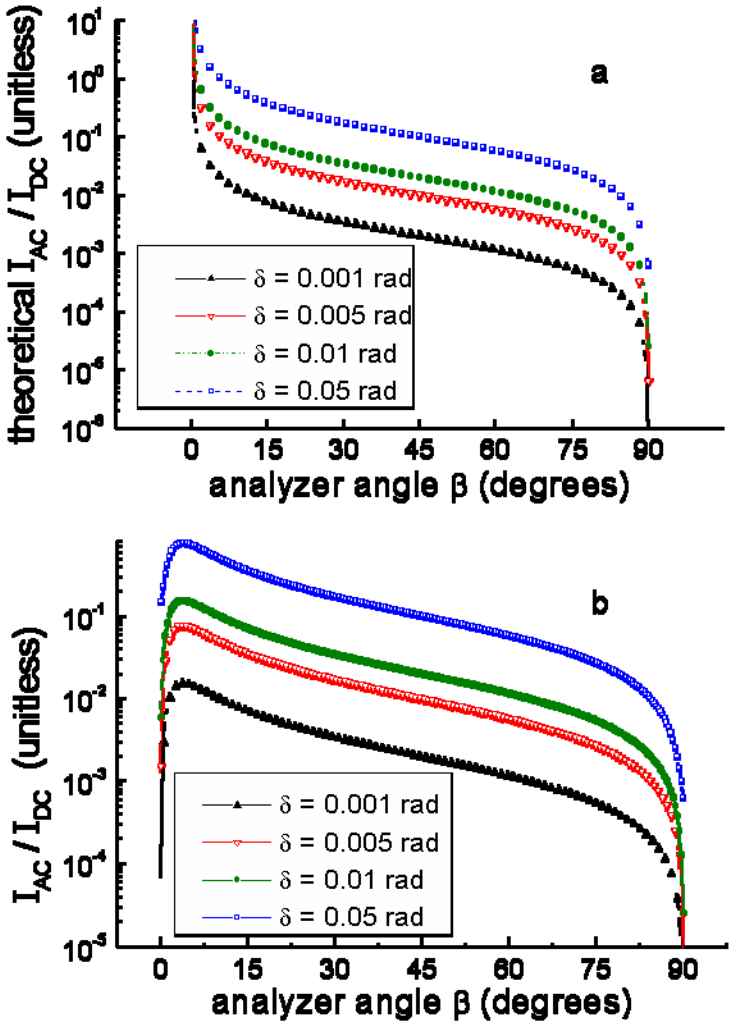

Figure 3-9. The effective signal-to-noise ratio as a function of analyzer angle β is plotted a.) for the theoretically perfect polariscope (i.e. $I_{min} = 0$) and b.) for a polariscope with a finite I_{min}.

Additionally, at the null transmission point, the rate of change of I_{AC} with analyzer angle β $\left[\Delta\left(dI/d\beta\right)/\Delta\beta\right]$ is maximized and approximately linear as seen from the plot of $\delta^2 I/\delta\beta^2$ and $\delta I/\delta\beta$ in Figure 3-10. The large I_{AC}/I_{DC} ratio, as well as the linearity and maximized slope of $\delta I/\delta\beta$ vs. β all make EO data collection and analysis more robust in the vicinity of the null transmission point.

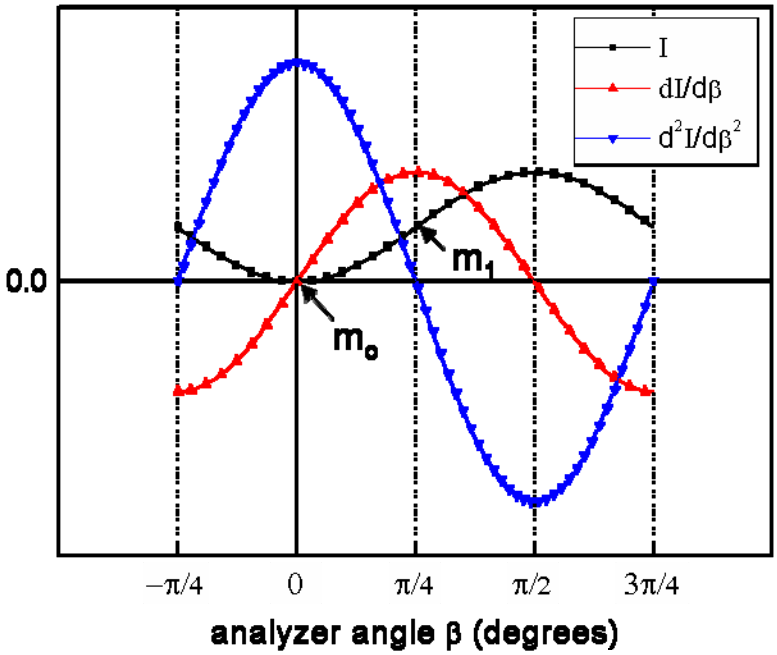

Figure 3-10. Plot of (3-1) and the 1st and 2nd derivatives of (3-1) with respect to the analyzer angle β. The rate of change of the modulation depth is largest at the null transmission point and is approximately linear as seen from $d^2I/d\beta^2$ and dI/db respectively.

Lastly, as a result of the symmetry of the transmission curve about the null transmission point, driving the sample to $\pm\delta/2$ results in a response frequency double that of the driving frequency. The minimum of the transmission curve along with this "characteristic frequency doubling"[175] of the response, facilitate precise determination of the null transmission point. In contrast the very linearity of $\Delta I/\Delta\delta$ at M_1 which makes it a desirable operation point likewise makes it quite difficult to precisely identify. All measurements in the transmission geometry were made in the vicinity of the null transmission point M_o. In addition to the aforementioned positive reasons for choosing to operate at the null transmission point, limitations of the photo detectors necessitated operation near the null transmission point. At the gain settings or incident intensities necessary to observe the AC-modulated response of the film, the photo detectors employed for transmission measurements at both λ = 633 nm (Hamamatsu R928 PMR) and 1561 nm (New Focus 2033) became saturated at analyzer angles outside a range of no greater than β = ±15°. Neutral density filters can not be employed to overcome this limitation as they attenuate the signal as well as the background level.

3.6.1.2 Transmission geometry electro-optic measurement apparatus

The device structures tested in the transmission geometry included both the waveguide devices and the transmission EO test structures described previously in Section 3.4. The schematic in Figure 3-11 shows the typical manner in which the samples were mounted as well as how the electrical contacts to the samples were made. Thin 1mm alumina substrates with 2.5 mm^2 gold bonding pads are secured with epoxy to a ¼" thick U-shaped aluminum block. The aluminum block provides mechanical stability and is taped to accept a mounting post. The sample is mounted across the gap between the two alumina substrates using a medium-tack adhesive. In addition to providing electrical isolation, the thin alumina substrates allow for the close approach of coupling and decoupling optics on both sides of the sample.

Gold lead wires are soldered to a female BNC bulkhead terminal. The other ends of the lead wires are electrically and mechanically connected to the 2.5 mm^2 Au bonding pads using a silver colloidal paste. Prior to making these contacts with the Ag paste, the lead wires are secured with epoxy to the alumina substrate and the Al block for improved mechanical stability. Gold contacts are then made from the 2.5 mm^2 Au bonding pads to the Au electrodes on the sample using a wire bonder (West-Bond 7476E).

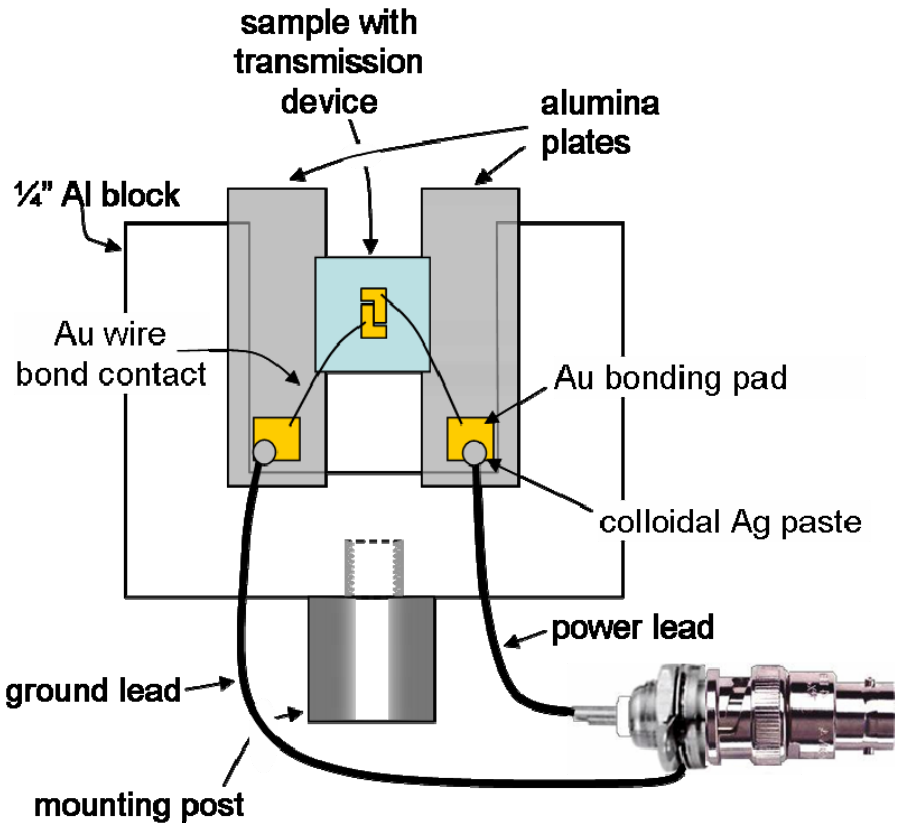

Figure 3-11. Schematic of mounted and connectorized sample for transmission electro-optic measurement

With the sample so prepared, it is mounted in the optical path between the coupling and decoupling optics. Figure 3-12 a and b show the Senarmont polariscopes used to measure the electro-optic properties of the $BaTiO_3$ thin films in the transmission geometry at λ = 632.8 nm and 1561 nm respectively. Many of the elements are common to measurements at both wavelengths. A 10x objective is used to collect and collimate the light as it exits the sample and a Glan Thompson polarizer (Thorlabs GTH10M) is used as the analyzer at both 632.8 and 1561 nm. The analyzer was mounted in a high precision rotation stage (Thorlabs PRM1) with better than 2.4 arc minute angular resolution. Positioning of the coupling and decoupling optics is accomplished using 3-axis precision flexure stages (Elliot-Martock MDE122) that provide 20 nm resolution and a 2 mm range for all three axes. To facilitate

positioning of the sample, each flexure stage is mounted on a translation stage (Elliot-Martock 889-60) that provides a 6 cm translation range along the optical axis of the measurement system.

For measurement at 632.8 nm, a 22.5 mW He-Ne laser source (JDS Uniphase 1145P) was oriented with its plane of polarization parallel to that of the Glan Thompson input polarizer. A 20x objective was used to couple light to the sample. For investigation of the polarization dependence of the EO coefficient, a half-wave plate was positioned between the source and the input polarizer to facilitate alignment of the plane of polarization of the source with that of the input polarizer. The measured extinction ratio with the Glan Thompson polarizers was approximately -40 bB. The input polarizer and the multiple-order quartz quarter-wave plate (Edmund Scientific D43698) were both mounted in standard rotation stages. A photomultiplier tube (PMT) (Hamamatsu R928) was used to detect the transmitted intensity for measurements at λ = 632.8 nm. The PMT was mounted in a shielded housing and powered by a low-noise high-voltage power supply (Keithley 247). Supply voltages of between 300 to 450V were typically employed.

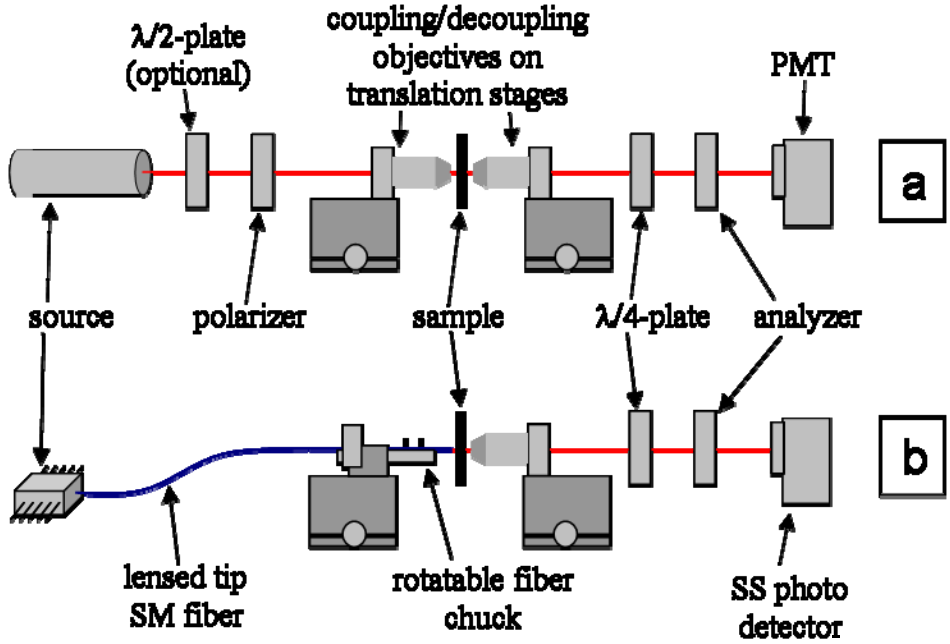

Figure 3-12. Schematic optical sub-system consisting of transmission polariscopes for measurement at (a) 632.8 nm and (b) 1561 nm

For measurements at 1561 nm, a zero-order quarter wave plate (Newport 10RP04-40) and a solid state Ge photo detector (New Focus 2033) are used on the output side. A temperature controlled (Wavelength Electronics HTC-1500) 20mW FC connectorized pigtailed DFB laser diode (ThorLabs) was used for the source. An FC-connectorized patch cord was spliced to a single mode lens-tipped fiber with a 2μm spot size and a 4μm working distance (Nanonics Imaging, Ltd.) and connected to the pigtailed DFB laser. A video microscope consisting of a CCD camera and a long working distance objective is mounted above the sample and used to facilitate the positioning of the lens tipped fiber at the required 4 μm working distance. With the FC patch cord connected to the pigtailed DFB laser, the extinction ratio at the output of the lens-tipped fiber was approximately -16 dB. The polarized output from the DFB laser acquires a finite ellipticity by the time it exits the lens-tip of the fiber resulting in the lower extinction ratio realized with the fiber-based system. When the input is slightly elliptical, the amplitude of the Senarmont transmission curve is reduced with an increase in I_{min} and a decrease in maximum transmitted intensity ($I_{min}+I_{max}$). As the period of the transmission curve is unaffected, no error is introduced in the analysis of r_{eff} due to a slightly elliptical input.

In addition to quantitative measurement of the effective electro-optic coefficient, r_{eff}, measurements of the frequency dependence of the electro-optic response and the electric field dependence of the electro-optic response were made. The optical apparatus described in this section is common to all transmission geometry electro-optic measurements. The nature of the electrical subsystem employed depends upon the wavelength, the frequency and the type of electro-optic measurement being made.

3.6.1.3 Electro-optic coefficient measurement apparatus

A schematic of the electrical subsystem employed for transmission measurements of the electro-optic coefficient at λ = 632.8 and 1561 nm are shown in Figure 3-13 and Figure 3-14. The setups shown in Figure 3-13 and Figure 2-14 are capable of measurement of the electro-optic coefficient from

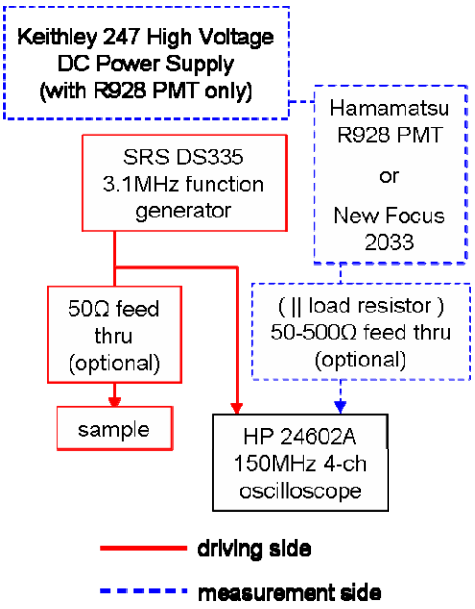

Figure 3-13. Schematic of electrical subsystem used for measurement of electro-optic coefficient. Setup used for sample bias voltages of 9 V or less. For higher bias voltages the system in Figure 3-14 was employed.

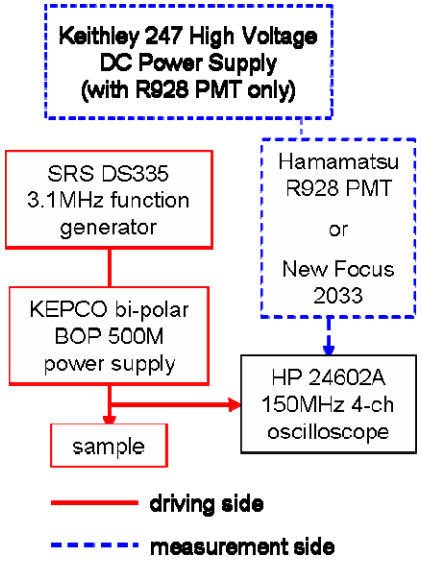

Figure 3-14. Schematic of electrical subsystem used for measurement of electro-optic coefficient with sample bias voltages as high as ±40V. For bias voltages of 9V or less the setup in Figure 3-13 was normally used.

DC up to 3.1MHz at λ = 632.8 nm and from DC up to approximately 10kH at 1561 nm, respectively. The 30kHz 3dB bandwidth of the New Focus 2033 photoreciever at the medium and high gain settings required for the transmission EO measurement limits the upper frequency limit for measurement at 1550

nm. In addition to the bandwidth limitations of the New Focus 2033, photocurrent noise increases sharply at frequencies in excess of 5kHz. As such, measurements at 1561 nm were made at 1 kHz in both the transmission and waveguide geometries, regardless of the bias voltages employed.

For measurements at 632.8 nm, with no load resistor between the PMT and the HP oscilloscope (Z_{input} =1 MΩ), the measured 3 dB bandwidth of the measurement system in Figure 3-13a was 10.3 kHz, with the response being flat out to slightly over 1 kHz. With a 500Ω load resistor in parallel with the oscilloscope on the detection side and the 50Ω feedthrough on the driving side, electro-optic measurements can be made out to the 3.1MHz limit of the SRS DS335 function generator. Typically, because of the much larger signal strength realized with no load resistor on the detector side, EO coefficient measurements were made at 1kHz with no load resistor (a 50 Ω load resistor typically attenuated the response by more than an order of magnitude). The frequency response of the electro-optic effect was then separately measured out to 3MHz using a 50 to 500Ω load resistor on the detector side.

The bias voltage of the SRS DS335 function generator is limited such that $\left|V_{AC-peak}\right|+\left|V_{DC}\right|\leq 10V$ into a high impedance load. As such the system in Figure 3-13b is used when higher bias voltages are desired. The output of the SRS DS335 function generator is connected to the voltage programmable input channel on the Kepco BOP-500 power supply. The built in operational amplifier of this supply provides a gain of 50 at its output. As such, care must be taken in setting amplitude of V_{AC} and V_{DC} from the SRS DS335 function generator so as not to exceed the breakdown voltage of the sample. The frequency response of the Kepco power supply remains flat to just past 1kHz with a 3dB cutoff of 20kHz. As such electro-optic measurements with the setup shown in Figure 3-13b are limited to frequencies of 1 kHz or less. Measurements employing this setup were typically made at 1kHz.

3.6.1.4 Electro-optic coefficient measurement procedure

The electro-optic coefficient measurement procedure is similar to that described by Hoerman.[12] For EO measurements, frequencies from DC up to 3 MHz were employed. Bias voltages ranged from 0

up to ±40V corresponding to bias fields as high as ±8 MV/m across electrode gaps ranging from 5 to 15 μm. Applied AC voltages ranged from 2 to 20 V_{pp} with 10 V_{pp} being most commonly used.

The procedure for measuring the EO coefficient at $\lambda = 632.8$ nm is as follows. Prior to mounting the sample in the optical path, the quarter wave plate is removed from the polariscope. The Hamamatsu R928 PMT supply voltage is set at ~200V and the output of the PMT is connected directly to either channel 1 or 2 of the scope with DC coupling selected. While monitoring the PMT signal on the scope, the analyzer angle is adjusted to the null transmission point. The null transmission point is uniquely identified by a frequency doubling of the modulated transmitted intensity. It is likewise identified by minima in both the time average transmitted intensity and the amplitude of modulation of the transmitted intensity. The high resolution micrometer on the analyzer's rotation stage is used to minimize the transmitted intensity. The quarter wave plate is reinserted in the system and the angle of the quarter wave plate is adjusted to minimize the transmitted intensity. Subsequent to this alignment, the angles of the input polarizer and the quarter wave plate should not be adjusted. Next, prior to coupling to the sample, the analyzer angle is adjusted ~1 to 2^{o} away from the null transmission point, as the EO signal to noise ratio is optimized at a small angle away from the null transmission point.

With the sample mounted in the optical path (Figure 3-12) the electrical subsystem is configured in a manner appropriate for the measurement conditions (see previous section). The Hamamatsu R928 PMT supply voltage is then set at between 300 to 500V on the Keithley 247 high voltage power supply. The output from the PMT is connected to channel 2 of the HP oscilloscope with AC-coupling selected for channel 2. Using a BNC tee, the driving voltage (sinusoidal + optional DC bias) is connected to channel 1 of the scope and simultaneously applied to the sample under test. The scope's trigger is set to channel 1 and DC-coupling is selected for channel 1 on the scope. DC coupling allows one to measure both the AC and DC components of the signal. With an AC voltage signal applied to the sample, adjust the coupling and decoupling optics until a detectable signal is measured on channel 2 of the scope. Fine tune the position of the coupling and decoupling optics to optimize the EO signal.

Once the EO signal from the PMT is optimized, switch channel 2 on the scope from AC to DC coupling and monitor the PMT signal while adjusting the analyzer angle to find the null transmission point. In addition to minimization of the transmitted intensity, one looks for the characteristic frequency doubling that occurs at the null transmission point. Again, the micrometer on the analyzer rotation stage is used to accurately identify the null transmission point. The signal averaging function on the HP 24602A scope is used to improve the signal to noise ratio of the measured EO response. The signal-averaged EO response is then captured and saved to a computer using a GPIB interface in conjunction with the HP Scopelnk 2.01 software. Next, using the micrometer on the analyzer, adjust the analyzer angle and repeat the process of capturing the signal-averaged EO response to the computer. The analyzer's micrometer is graduated in 2.4 arc minute increments and typically measurements were made in steps of 12 to 24 arc minutes (0.2 – 0.4^{o}) out to between 1 to 3^{o}. For films in which the EO coefficient is small, it is sometimes necessary to connect the PMT output to both channel 2 and channel 3 using a BNC tee. Channel 2 is then set to AC coupling to monitor just the AC component of the transmitted intensity while channel 3, which is strictly DC coupled, gives the DC component of the transmitted intensity. The procedure is otherwise the same with signal averaged data from channels 1 through 3 being captured and saved to the computer at each increment of the analyzer angle.

3.6.1.5 Electro-optic coefficient analysis

For an applied AC voltage of frequency ν, the AC component of the induced phase change in the electro-optic device under test will have the same functional form as that of the driving voltage assuming the electro-optic response is linear over the range of the applied voltage (3-2).

$$V_{AC} = V_{amp} \sin(t\omega) \quad \rightarrow \quad \delta_{AC} = \delta_{amp} \sin(t\omega) \tag{3-2}$$

Any DC component of δ in equation (3-1) associated with the application of a DC bias voltage is compensated for when one adjusts the analyzer angle to the null position with driving voltage (including

bias) applied to the sample as per the procedures outlined in 3.6.1.4. Substituting (3-2) into (3-1) the transmitted intensity as a function of δ_{AC} and β is

$$I = I_{\min} + I_{amp} \sin^2 \left[\left(\frac{\delta_{amp}}{2} \sin(t\omega) \right) - \beta \right] \tag{3-3}$$

In equation (3-3) the zero of β is redefined as that of the null transmission point under the applied bias voltage. Equation (3-3) is used to fit the measured data.

Figure 3-15 shows some typical data measured using the procedure outlined in 3.6.1.4. The upper portion of the figure shows the driving voltage (1kHz $10V_{pp}$ $+5V_{DC\ bias}$) while the lower portion of the figure shows the transmitted intensity measured by the PMT at five different analyzer angles ranging from 0 to 0.8°. For clarity, only every 20th data point is shown. From the measured data the value of I_{min}, which corresponds to the minimum transmitted intensity at the null transmission point ($\beta = 0^\circ$), can de directly measured. By plotting the transmitted intensity at $\delta_{AC} = 0$ verses the analyzer angle β and fitting to (3-3) with $\delta_{AC} = 0$, the value of I_{amp} can be determined.

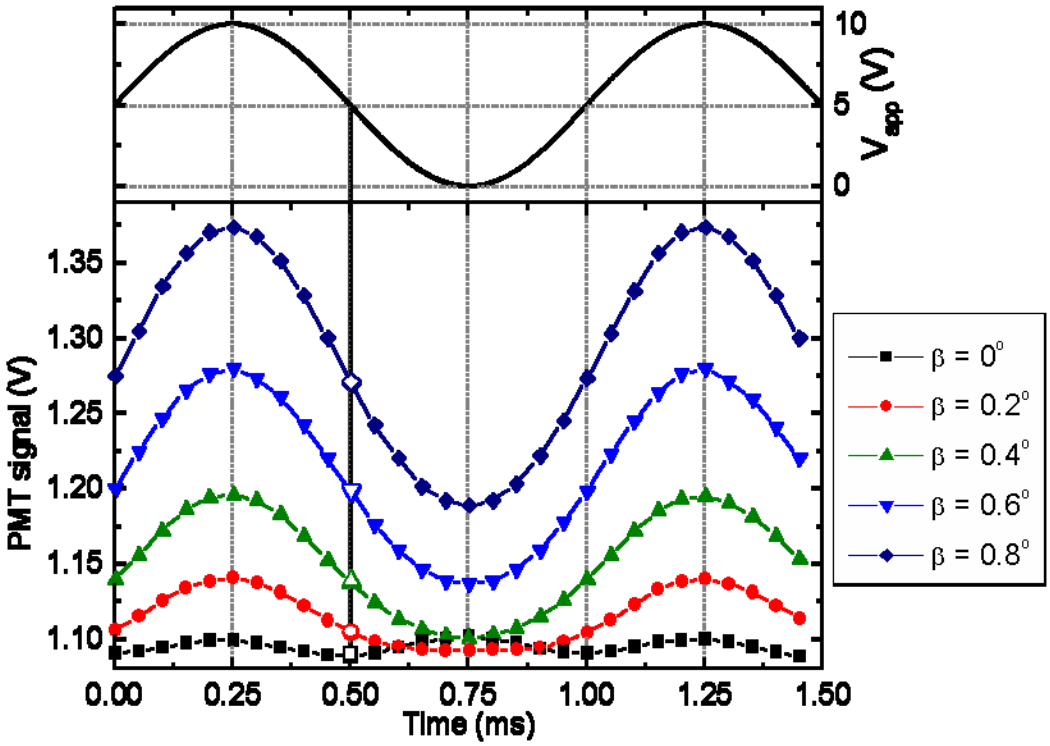

Figure 3-15. The transmitted intensity at different analyzer angles with a 1kHz sinusoidal driving voltage (10Vpp +5V DC bias) applied to the EO device. The open symbols are the points where $\delta_{AC} = 0$ used to determine the value of I_{amp}

In Figure 3-15 the open symbols correspond to the point at which the AC component of the applied voltage is zero and therefore δ_{AC} is zero. Figure 3-16 shows the transmitted intensity verses analyzer angle at this point as well as the fit to the data using (3-3) with δ_{AC} set to zero. From the fit, the value of I_{amp} is determined.

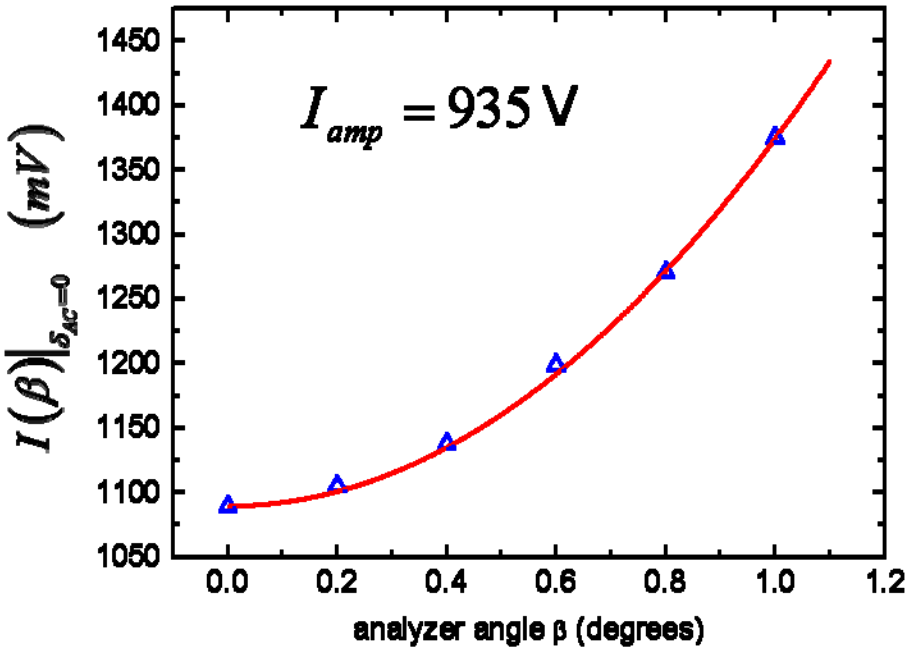

Figure 3-16. The transmitted intensity at the point where δ_{AC} is zero is plotted verses the analyzer angle. The solid line shows the fit to the measured data using (3-3) with $\delta_{AC} = 0$. The I_{amp} value determined from fitting is given on the figure.

As previously mentioned, for an ideal polariscope I_{min} is zero. Dropping I_{min} and dividing (3-3) by I_{amp} yields an expression for the normalized transmitted intensity of an ideal polariscope as a function of δ_{amp} and β.

$$I_N = I/I_{amp} = \sin^2\left[\left(\frac{\delta_{amp}}{2}\sin(t2\pi\nu)\right) - \beta\right] \tag{3-4}$$

The measured modulation depth ($\Delta\tilde{I}_{mod}$) is shown schematically in Figure 3-17 . If the measured modulation depth is normalized by dividing by the previously determined I_{amp} value, and then plotted verses the analyzer angle, the data may be fit using equation (3-4) with δ_{amp} being the sole fitting

parameter as shown in Figure 3-18. From the δ_{amp} value determined from fitting $\Delta\tilde{I}_{\mathrm{mod}}(\beta)$ with equation (3-4), r_{eff} can be directly determined by[175]

$$r_{eff} = \frac{2\delta_{amp}\lambda_o}{\pi n_{avg}^3 t}\left(\frac{g}{V_{pp}}\right) \tag{3-5}$$

where λ_o is the free space wavelength, n_{avg} is the average refractive index in the film at λ_o, g is the electrode gap and t is the film thickness.

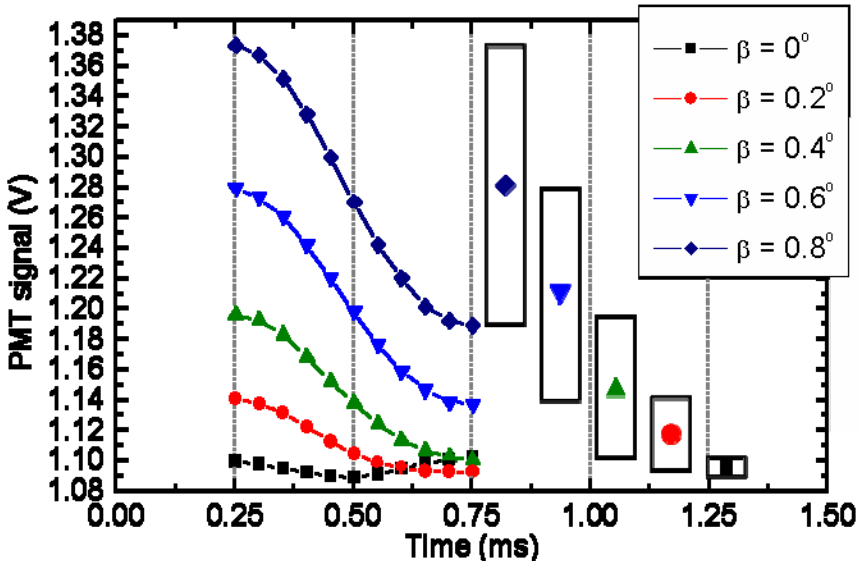

Figure 3-17. Schematic showing the modulation depth due to δ_{AC} for a discrete range of analyzer angles

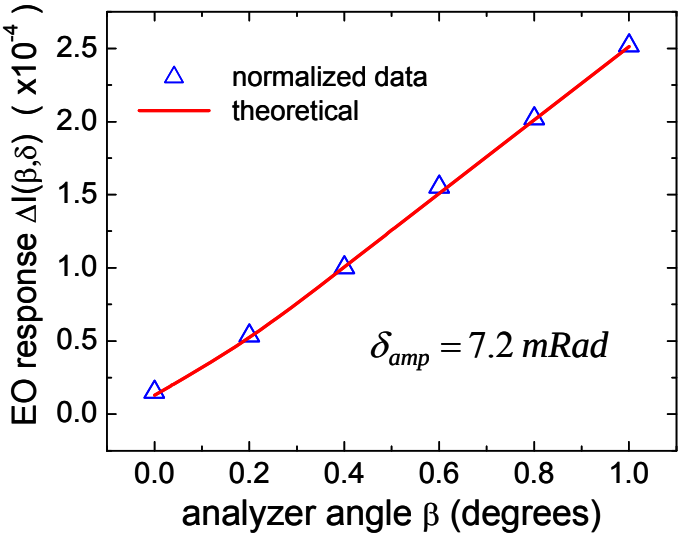

Figure 3-18. Normalized measured modulation depth and theoretical modulation depth for a retardation amplitude of 7.2 mRad.

3.6.1.6 Measurement of electro-optic response to unbiased voltage pulse

Unbiased square-wave voltage pulses were used to study the transient electro-optic properties of $BaTiO_3$ thin films as well as examining the domain structure dependent hysteresis of the electro-optic response. When measuring the electro-optic response to a square-wave voltage pulse, the optical setup is the same as that used in the measurement of the r_{eff} shown in Figure 3-12. The electrical subsystem employed is shown in Figure 3-19 .

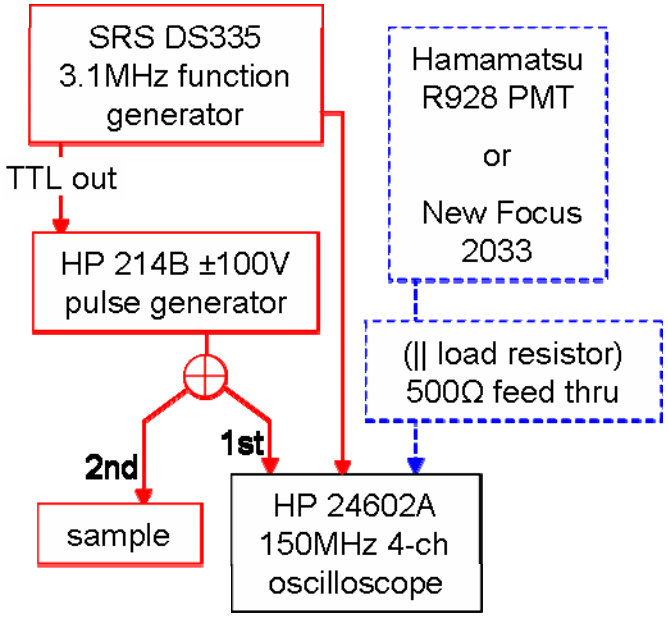

Figure 3-19. Schematic of electrical subsystem used in measurement of EO response to square-wave voltage pulse.

The HP 214B pulse generator was used in external trigger mode with the TTL output from the SRS function generator acting as the trigger source. A square wave from the primary output channel from the SRS function generator is connected to channel 1 of the HP 24602A scope. The scopes trigger is set to channel 1 and DC coupling is selected for channel 1. The output from the HP 214B pulse generator is connected to channel 2 of the scope through a 50Ω feed thru. DC coupling is selected for channel 2. The pulse delay on the HP 214B is adjusted such that the pulse from the HP214b is delayed 20 ms relative to the step edge of the square wave from the SRS function generator on channel 1. This prevents the appearance of channel cross-talk during the measurement of the transient EO response. The pulse width

from the HP 214B can be adjusted from 25ns up to 10 ms. For most measurements a 10 ms pulse width was employed. The pulse amplitude can be adjusted from 0.3 up to 50V with both source and load impedance of 50Ω. When the high-Z source impedance is selected the HP 214B provides from 0.3 up to 100V into a 50Ω load. The source impedance was always set to 50Ω as voltages in excess of 50V were not employed. Once the pulse amplitude is adjusted the pulse signal is captured and saved to the computer as per the procedure in 3.6.1.4. The HP 214B output is then disconnected from Channel 2 of the HP scope. With a PMT supply voltage of between 300 to 500V, the PMT output is connected to channel 2 of the scope. The HP 214B output is then connected to the sample. The signal averaging function of the HP scope is used to improve the signal to noise ratio of the EO response measured by the PMT. This signal-averaged EO response is then captured and saved to the computer using the HP Scopelnk 2.01 software.

3.6.2 Electro-optic measurements in the waveguide geometry

3.6.2.1 Waveguide geometry electro-optic measurement apparatus

Measurements in the waveguide geometry are made using a fiber-based coupling system very similar to that used for transmission measurements at 1561 nm. Figure 3-20 shows a schematic of the waveguide electro-optic measurement apparatus. The physical setup is the same as that shown in Figure 3-12b except that the quarter wave-plate on the output side is removed and the sample is now mounted on a waveguide translation stage (Elliot Martock MDE 883) positioned between the two flexure stages. A video microscope consisting of a CCD camera (Watec LLC-903K) and a long working distance objective is mounted above the sample and used to facilitate the positioning of the lens tipped fiber at the required 4 μm working distance. Figure 3-21 shows a captured image from the video microscope of the lens-tipped fiber at the 4 μm working distance from the cleaved endface of the waveguide electro-optic modulator. The electrical subsystems employed for waveguide EO measurements are identical to those used for transmission measurements at 1561 nm, from Figure 3-13,Figure 3-19.

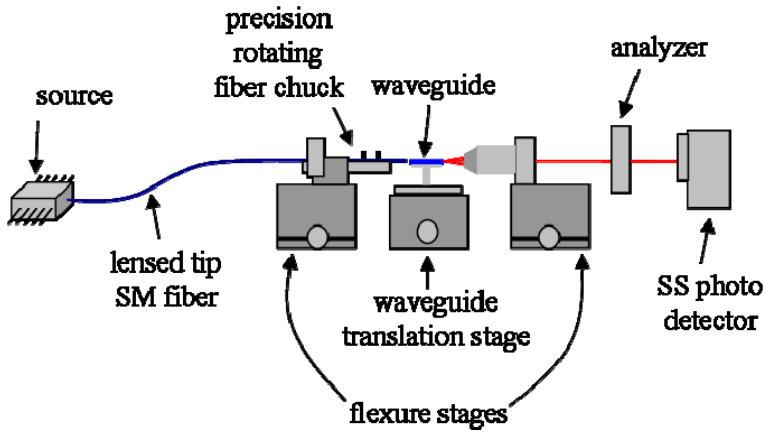

Figure 3-20. Schematic of optical subsystem of waveguide EO measurement apparatus

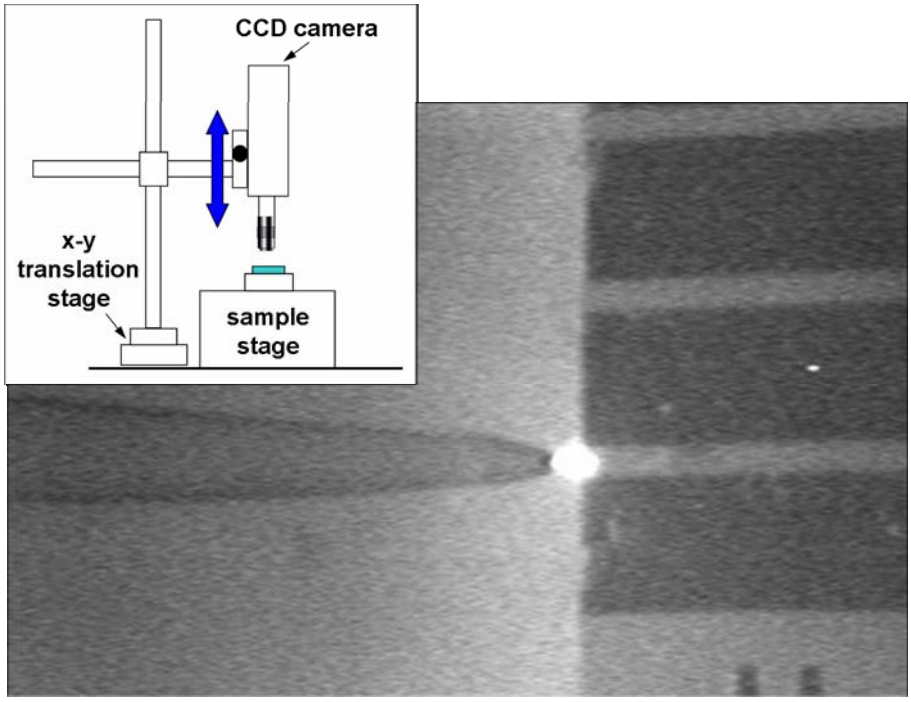

Figure 3-21. Image of lens-tipped fiber at the 4 μm working distance from the endface of the waveguide. Inset shows schematic of CCD microscope used to position the lens-tipped fiber.

3.6.2.2 Electro-optic coefficient measurement procedure

As mentioned previously, the long interaction lengths realized in the waveguide geometry allow for the direct measurement of V_π and from the measured V_π the effective electro-optic coefficient (r_{eff}) can be directly determined. For the simple polarizer-sample-analyzer (PSA) plane polariscope realized by removing the quarter wave plate in Figure 3-6, the transmission equation is given by

$$I = I_{\min} + I_{amp}\left[\frac{1}{2} - \cos^2(\beta)\cos(\delta) + \frac{1}{2}\cos(\delta)\right] \tag{3-6}$$

where δ is the total retardation induced in the sample, I_{amp} is the peak-to-peak amplitude of the transmission curve, and I_{min} is the finite intensity reaching the detector at the null transmission point due to non-ideality and imperfect alignment of the optical elements of the polariscope as well as stray ambient light entering the detector. Figure 3-22 shows a map of equation (3-6) in the 2D (β,δ)-space.

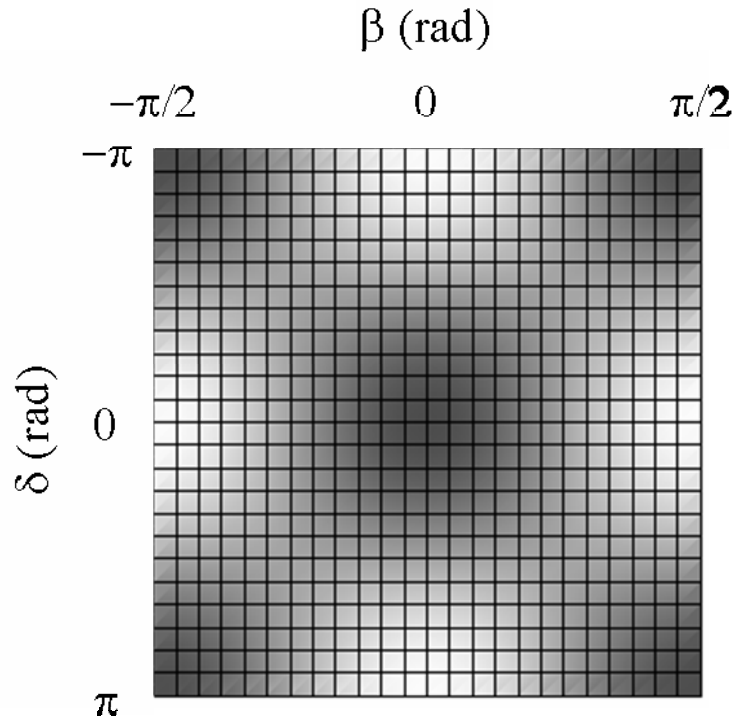

Figure 3-22. Map of the (β,δ) parameter-space of equation (3-6)

When the analyzer is crossed with respect to the input polarizer (i.e. β = 0), equation (3-6) reduces to[175]

$$I = I_{\min} + I_{amp}\sin^2\left(\delta/2\right) \tag{3-7}$$

By applying a triangle wave voltage to the sample of sufficiently large amplitude, the V_π voltage can be read directly as shown in Figure 3-23[47] . It should be noted that for a PSA polariscope, the form of the EO signal shown in Figure 3-23

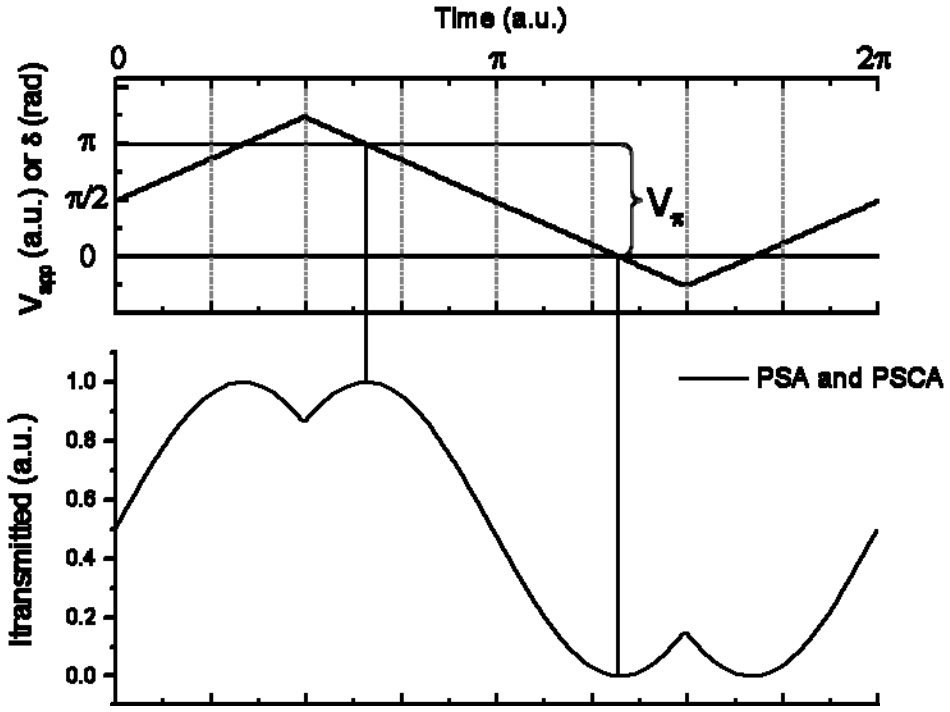

Figure 3-23. Theoretical transmitted intensity of PSA polariscope. By overdriving the sample V_π is determined directly from the measured data. Note the Senarmont PSCA polariscope with the analyzer angle fixed at zero has the same transmission curve as the PSA polariscope

is only possible when there is a static component of retardation due either to the natural birefringence of the sample or application of a DC bias voltage. In Figure 3-23, a δ_{DC} of $\pi/2$ is assumed. In the absence of any δ_{DC} component, V_π can be determined from the transmitted intensity as shown in Figure 3-24. In Figure 3-24 the transmission of the Senarmont polariscope with the analyzer at 45^o (i.e. maximum linearity point M_1) is shown along with the PSA transmission curve. It is obvious from the figure that in the absence of any δ_{DC} contribution to δ_{Total}, the measurement of V_π requires the application of a larger V_{AC} with the PSA polariscope as compared to the Senarmont polariscope. This is because by operating at the maximum linearity point the total δ_{AC} required to overdrive the sample and measure V_π is just over π, while for the PSA polariscope a δ_{AC} in excess of 2π is required to measure V_π. Unlike the Senarmont polariscope the operating point of the PSA polariscope can not be biased by adjusting the analyzer angle as evidenced by a comparison of Figure 3-8 and Figure 3-22.

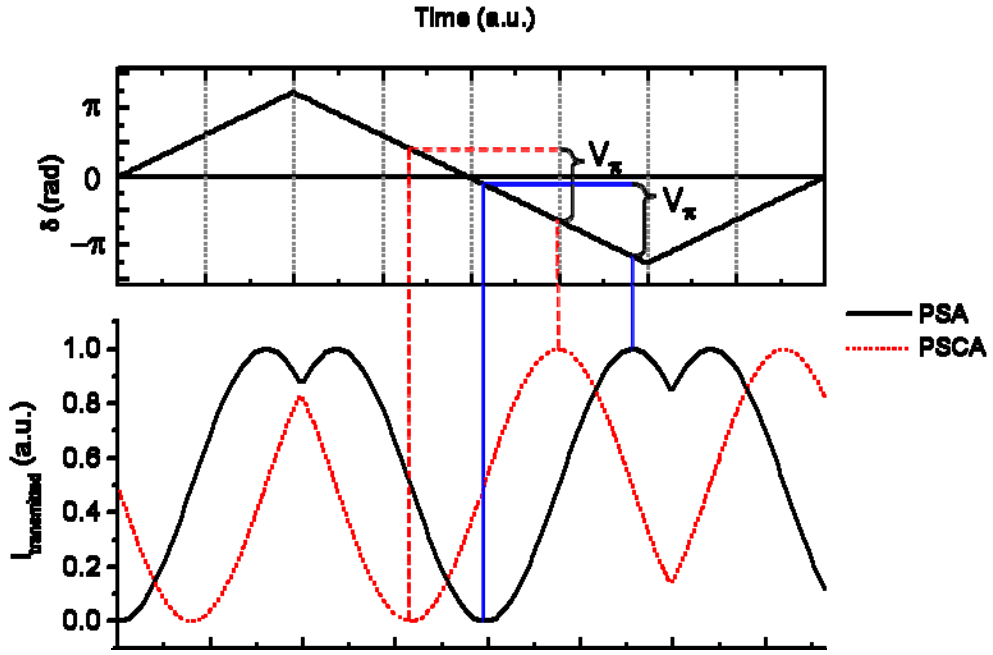

Figure 3-24. Theoretical transmission of PSA polariscope with $\delta_{AC} = 0$. The transmission curve of the Senarmont polariscope operated at the maximum linearity point is shown for comparison. In order to determine V_π when $\delta_{AC} = 0$, the PSA requires twice the applied voltage of the Senarmont operated at M_1.

Having determined V_π directly from the modulation of the transmitted intensity, the effective electro-optic coefficient can be directly calculated from

$$r_{eff} = \frac{\lambda g}{n_{avg}^3 \ell V_\pi \Gamma \phi} \tag{3-8}$$

where λ is the free space wavelength, g is the electrode gap, n_{avg} is the average index of refraction of the film, and ℓ is the interaction length which in this case is the device length. Γ is the overlap integral of the optical and microwave modes given by

$$\Gamma = \frac{g}{V} \frac{\iint E_m |E_o|^2 \, dxdy}{\iint |E_o|^2 \, dxdy} \tag{3-9}$$

where V is the applied voltage, E_m is the microwave field determined using the conformal-mapping technique[47,185] and E_o is the optical field calculated by the effective-index method. Lastly ϕ in (3-8) is an attenuation factor due to the presence of the SiO_2 buffer layer, given by

$$\phi \approx \frac{g}{\left(\frac{2t\varepsilon_{comp}}{\varepsilon_{SiO_2}} + g \right)} \tag{3-10}$$

where t is the SiO_2 buffer layer thickness, and ε_{comp} is the composite microwave dielectric constant of the $BaTiO_3$ thin film on the MgO substrate measured with a vector network analyzer[186].

4 ELECTRO-OPTIC THEORY OF POLYDOMAIN $BATIO_3$ THIN FILMS

4.1 Background and introduction

4.1.1 Optical indicatrix an the linear electro-optic tensor

The electro-optic effect is a nonlinear optical property involving a change in the refractive index of a material upon application of a low frequency or RF electric field. Specifically, the electro-optic effect is the change in the permittivity tensor at optical frequencies due to application of a low frequency electric field. In an anisotropic material, the relationship between the material response in the form of the electric displacement or electric flux density D and E the complex amplitude of the electric field of an optical mode propagating in the material is given by

$$D_i = \varepsilon_{ij} E_j = \varepsilon_o \varepsilon_{r(ij)} E_j = \varepsilon_o \left(1 + \chi_{(ij)}\right) E_j = \varepsilon_o E_j + P_i \tag{4-1}$$

The tensor nature of the permittivity ε_{ij} in an anisotropic material results in birefringence such that for an arbitrary propagation direction in the material two orthogonal plane-polarized eigenmodes are supported, which together with the propagation direction form an orthogonal triplet. In a uniaxial material such as $BaTiO_3$, the phase velocities of the two eigenmodes are distinct for any propagation direction not coincident with the optic axis. The optical indicatrix or index ellipsoid is used to determine the orientation and associated refractive indices of the eigenmodes given an arbitrary propagation direction. The index ellipsoid represents an iso-surface of electric energy density ($\frac{1}{2} D \bullet E$) in D-space[178]. The semiaxes of the index ellipsoid corresponds to directions in which $\boldsymbol{D}$ and $\boldsymbol{E}$ are parallel, and in the principle axis system the indicatrix is given by

$$\frac{x^2}{\varepsilon_{xx}} + \frac{y^2}{\varepsilon_{yy}} + \frac{z^2}{\varepsilon_{zz}} = 1 \quad or \quad \frac{x^2}{n_x^2} + \frac{y^2}{n_y^2} + \frac{z^2}{n_z^2} = 1 \tag{4-2}$$

In a coordinate system other than the principle axis system, the off diagonal terms of the symmetric permittivity tensor are non-vanishing and the equation for the indicatrix will contain up to three additional cross terms. The inverse of the permittivity tensor is called the impermeability tensor ($\bar{\bar{\eta}} = \bar{\bar{\varepsilon}}^{-1}$) and using Voight notation one can write the general equation for the optical indicatrix as

$$\eta_1 x^2 + \eta_2 y^2 + \eta_3 z^2 + 2\eta_4 yz + 2\eta_5 xz + 2\eta_6 xy = 1 \tag{4-3}$$

The change in the impermeability tensor upon application of an electric field is given by

$$\Delta\eta_{ij} = r_{ij\mathbf{k}}\mathbf{E}_{\mathbf{k}} + s_{ij\mathbf{kl}}\mathbf{E}_{\mathbf{k}}\mathbf{E}_{\mathbf{l}} \tag{4-4}$$

where $r_{ij\mathbf{k}}$ and $s_{ij\mathbf{kl}}$ are third and fourth rank tensors giving the linear electro-optic and quadratic electro-optic coefficients respectively. In equation (4-4) and subsequent equations in this chapter, all terms and subscripts associated with E-fields or material properties at optical frequencies are shown in italics while those associated with the low frequency applied E-field are shown in bold non-italic type. In non-centrosymmetric materials such as tetragonal $BaTiO_3$ where the second order electronic susceptibility $\chi^{(2)}$ is non-vanishing it is sufficient to consider the Pockels linear electro-optic effect, as the Kerr effect is several orders of magnitude smaller[55].

Symmetry in the first two indices of the $r_{ij\mathbf{k}}$ tensor (reflective of the symmetry of the permittivity tensor) allows it to be written as a 6×3 matrix. Considering only the linear electro-optic coefficient, equation (4-4) can be rewritten as

$$\begin{bmatrix}\Delta\eta_{11}\\ \Delta\eta_{22}\\ \Delta\eta_{33}\\ \Delta\eta_{23}\\ \Delta\eta_{13}\\ \Delta\eta_{12}\end{bmatrix} = \begin{bmatrix}\Delta\eta_{1}\\ \Delta\eta_{2}\\ \Delta\eta_{3}\\ \Delta\eta_{4}\\ \Delta\eta_{5}\\ \Delta\eta_{6}\end{bmatrix} = \begin{bmatrix}r_{11\mathbf{1}} & r_{11\mathbf{2}} & r_{11\mathbf{3}}\\ r_{22\mathbf{1}} & r_{22\mathbf{2}} & r_{22\mathbf{3}}\\ r_{33\mathbf{1}} & r_{33\mathbf{2}} & r_{33\mathbf{3}}\\ r_{23\mathbf{1}} & r_{23\mathbf{2}} & r_{23\mathbf{3}}\\ r_{13\mathbf{1}} & r_{13\mathbf{2}} & r_{13\mathbf{3}}\\ r_{12\mathbf{1}} & r_{12\mathbf{2}} & r_{12\mathbf{3}}\end{bmatrix}\begin{bmatrix}\mathbf{E}_1\\ \mathbf{E}_2\\ \mathbf{E}_3\end{bmatrix} = \begin{bmatrix}r_{\mathbf{11}} & r_{\mathbf{12}} & r_{\mathbf{13}}\\ r_{\mathbf{21}} & r_{\mathbf{22}} & r_{\mathbf{23}}\\ r_{\mathbf{31}} & r_{\mathbf{32}} & r_{\mathbf{33}}\\ r_{\mathbf{41}} & r_{\mathbf{42}} & r_{\mathbf{43}}\\ r_{\mathbf{51}} & r_{\mathbf{52}} & r_{\mathbf{53}}\\ r_{\mathbf{61}} & r_{\mathbf{62}} & r_{\mathbf{63}}\end{bmatrix}\begin{bmatrix}\mathbf{E}_1\\ \mathbf{E}_2\\ \mathbf{E}_3\end{bmatrix} \tag{4-5}$$

In (4-5), E-field induced changes of the diagonal components of the impermeability tensor are given by the $r_{ij\mathbf{k}}$ for which $i = j$ (or in the Voight notation the $r_{\mathbf{ij}}$ for which $i \le 3$). These components (shown in black in (4-5)) change the magnitude but not the orientation of the semiaxes of the indicatrix. The E-field induced changes to the off-diagonal components of the impermeability tensor are given by the $r_{ij\mathbf{k}}$ for which $i \ne j$ (or in the Voight notation the $r_{\mathbf{ij}}$ for which $i > 3$). These components (shown in blue in (4-5)) change both the magnitude and orientation of the semiaxes of the indicatrix. For materials of the 4mm crystal class such as $BaTiO_3$ the electro-optic tensor takes the form

$$r_{ij} = \begin{bmatrix} 0 & 0 & r_{13} \\ 0 & 0 & r_{23} \\ 0 & 0 & r_{33} \\ 0 & r_{42} & 0 \\ r_{51} & 0 & 0 \\ 0 & 0 & 0 \end{bmatrix} = \begin{bmatrix} 0 & 0 & r_{13} \\ 0 & 0 & r_{13} \\ 0 & 0 & r_{33} \\ 0 & r_{51} & 0 \\ r_{51} & 0 & 0 \\ 0 & 0 & 0 \end{bmatrix} \tag{4-6}$$

where the lines indicate equivalence of the connected components.

From equations (4-6) and (4-5) it is apparent that an applied E-field with components along the x or y direction, perpendicular to the optic axis, will result in a rotation of the indicatrix as evidenced by the presence of finite off-diagonal components in the impermeability tensor. It can be shown[175] that the rotation angle of the indicatrix in the ij-plane (α_{ij}) is given by

$$\tan\left(2\alpha_{ij}\right) = \frac{2\eta'_{ij}}{\eta'_{ii} - \eta'_{jj}} \tag{4-7}$$

Because the impermeability tensor is symmetric it can always be diagonalized to find the orientation and magnitude of the principle indices under the applied E-field. Consider the case where the E-field is confined in the xz-plane in which case the impermeability tensor under the E-field is of the form

$$\begin{bmatrix} \eta_1 + \Delta\eta_1 & 0 & \Delta\eta_5 \\ 0 & \eta_2 + \Delta\eta_2 & 0 \\ \Delta\eta_5 & 0 & \eta_3 + \Delta\eta_3 \end{bmatrix} = \begin{bmatrix} \eta'_{11} & 0 & \eta'_{13} \\ 0 & \eta'_{22} & 0 \\ \eta'_{31} & 0 & \eta'_{33} \end{bmatrix} = \begin{bmatrix} \eta'_1 & 0 & \eta'_5 \\ 0 & \eta'_2 & 0 \\ \eta'_5 & 0 & \eta'_3 \end{bmatrix} \tag{4-8}$$

The optical indicatrix under the applied field is found by solving for the general form of the eigenvalues and eigenvectors of (4-8).[178] The eigenvalues give the magnitude of the new principle indices under the applied electric field and the associated eigenvectors give the orientation of the indicatrix under the field. The eigenvalues or new principle indices of (4-8) take the general form

$$\begin{bmatrix} \eta''_1 \\ \eta''_2 \\ \eta''_3 \end{bmatrix} = \begin{bmatrix} \frac{1}{2}\left(\eta'_3 + \eta'_1 - \Theta\right) \\ \eta'_2 \\ \frac{1}{2}\left(\eta'_3 + \eta'_1 + \Theta\right) \end{bmatrix} \tag{4-9}$$

where

$$\Theta = \sqrt{\eta_3'^2 - 2\eta_1'\eta_3' + \eta_1'^2 + 4\eta_5'^2}$$

The corresponding eigenvectors are of the form

$$\begin{aligned} \bar{\eta}_1'' &= \left[\frac{1}{\eta_5'}\left(\eta_3'' - \eta_3'\right) \quad , \quad 0 \quad , \quad 1 \right] \\ \bar{\eta}_2'' &= \left[0 \quad , \quad 1 \quad , \quad 0 \right] \\ \bar{\eta}_3'' &= \left[\frac{1}{\eta_5'}\left(\eta_1'' - \eta_3'\right) \quad , \quad 0 \quad , \quad 1 \right] \end{aligned} \tag{4-10}$$

It should be noted that as written (4-10) constitutes an orthogonal (but not orthonormal) basis for the indicatrix under an applied field. These results will be used in the forthcoming analysis of the effect of the opto-geometric configuration on the theoretical electro-optic response.

4.1.2 Domain structure and EO tensor in polydomain $BaTiO_3$ thin films

In the tetragonal phase of $BaTiO_3$ there are six possible stable domain variants as shown in Figure 4-1. In Figure 4-1, the electro-optic tensors of all the domain variants are expressed in the coordinate system of variant (1). In th polydomain $BaTiO_3$ thin films examined in this study, all six variants are generally present. It should be noted that in analyzing the electro-optic response of a polydomain film, one is free to designate any of the domain variants as type (1), the EO tensors of the remaining five variants being then given as in Figure 4-1. The opto-geometric configurations employed in this study are shown in Figure 4-2. In all cases, the applied electric field is in the plane of the film typically along either a <100> or a <110> direction of the $BaTiO_3$ film. In the transmission geometry the Poynting vector of the optical mode is parallel to the surface normal of the film and orthogonal to the applied electric field. In the waveguide geometry the Poynting vector of the optical mode lies in the plane of the film, and is orthogonal to the applied electric field. In Figure 4-2 the domain variants labeled 1 and 2 represent the c-domains while the remainder (3 thru 6) represent the a-domains.

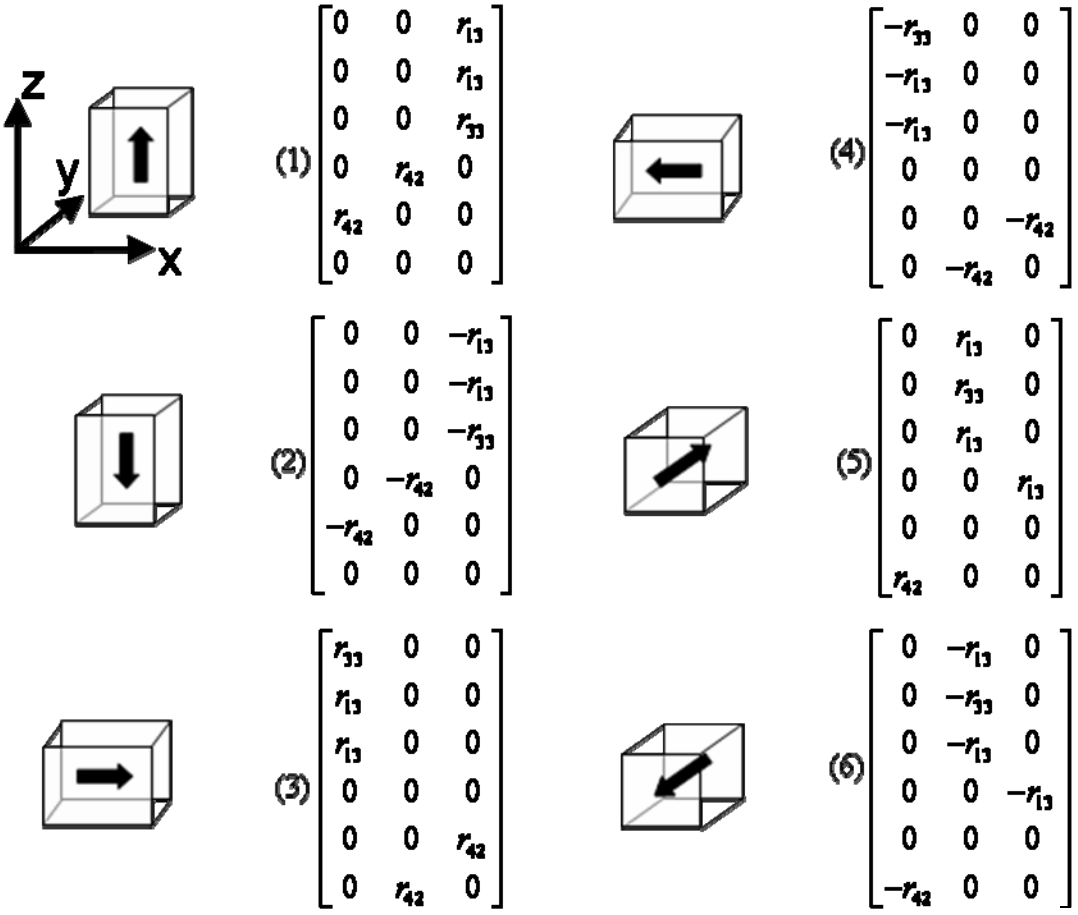

Figure 4-1. schematic of the six stable domain variants in the tetragonal phase of $BaTiO_3$. The EO tensors of all six domain variants are given after transformation of coordinates to those of variant (1).

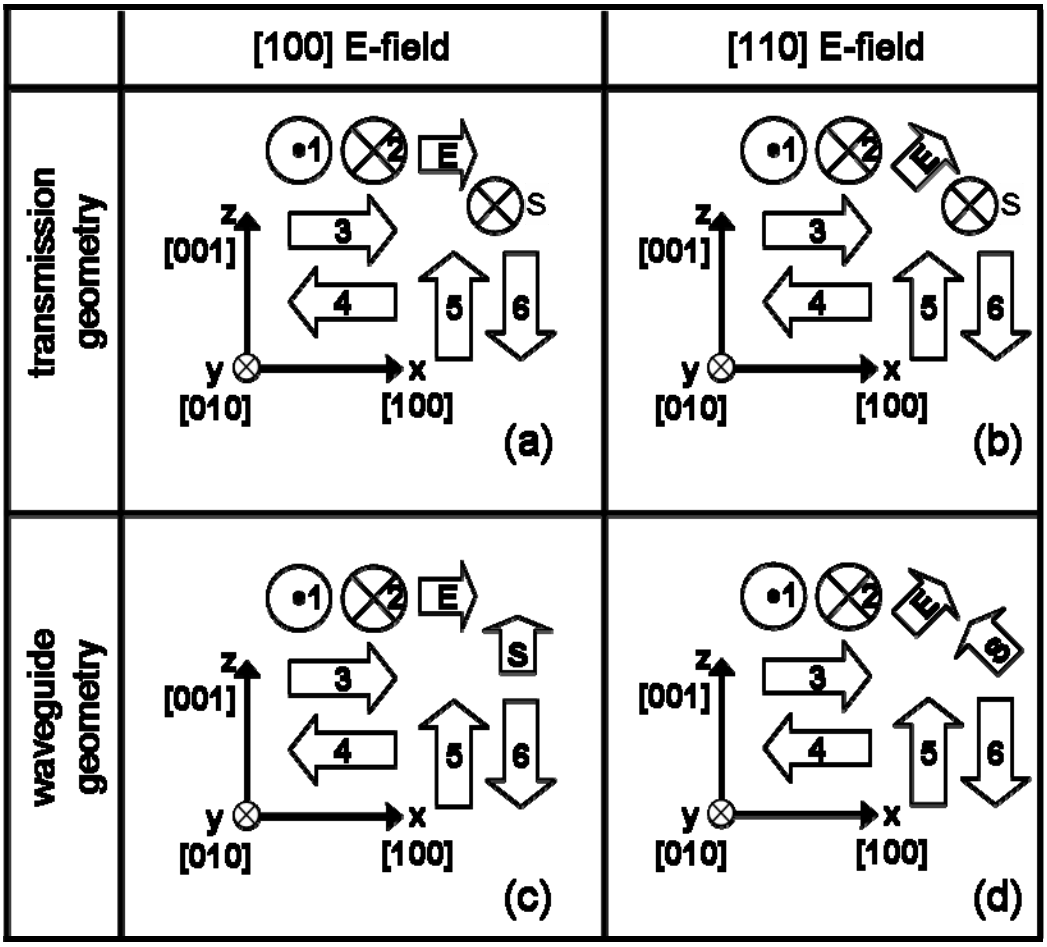

Figure 4-2 Schematic of opto-geometric configurations employed in the study of the electro-optic properties of BaTiO3 thin films.(a) and (b) show the configurations employed in the transmission geometry while (c) and (d) show configurations used in the waveguide geometry. The field direction (E) and Poynting vector (S) of the optical mode are shown as well as the orientation of the six allowed domain variants.

4.2 Effects of $BaTiO_3$'s large off-diagonal electro-optic coefficient

In general the tensor nature of the linear electro-optic effect necessitates careful consideration of the effect on the measured EO response of the particular opto-geometric configuration employed in any electro-optic measurement. This is particularly true for electro-optic materials with large off-diagonal linear electro-optic coefficients such as $BaTiO_3$. As noted previously, for ellipsometric measurements, an analyzer is generally used to convert the E-field induced change in the polarization state at the output of the sample into a change in the transmitted intensity. A number of parameters will effect the measured

change in the transmitted intensity δI. These include the orientation, with respect to that of the crystallographic domain structure, of both the propagation direction and the applied electric field[187].

In polydomain $BaTiO_3$ thin films it has generally been observed that the measured electro-optic coefficient varies considerably with the opto-geometric configuration of the modulator[12,169]. In particular, in both the transmission and the waveguide geometries, much larger electro-optic coefficients are on average measured when the modulating electric field is applied in an in-plane <110> direction as opposed to an in-plane <100> direction. While the effect of the in-plane E-field direction is due in part to the ability of the field to pole the domain structure[12], it is likewise due to the effects of the opto-geometry on the electro-optic response of the individual domains that are independent of the ability of the applied E-field to pole the domain structure.

Additionally, the azimuthal orientation of the sample within the polariscope can have a pronounced effect on the measured δI, particularly in the case where there is appreciable rotation of the indicatrix due to a large off-diagonal electro-optic coefficient. When a large off-diagonal electro-optic coefficient contributes to the EO response, both the rotation and the change in the principle indices must be considered.

An additional effect of the large off-diagonal electro-optic coefficients of $BaTiO_3$ is an appreciable quadratic component of the field induced birefringence for certain opto-geometric configurations[174,175]. Allerie et al.[175] show that for particular opto-geometric configurations, the E-field induced birefringence due solely to the linear electro-optic coefficient has both linear and quadratic dependences on the applied E-field. The quadratic E-field dependencies are those associated with the off-diagonal electro-optic coefficients and are therefore pronounced in $BaTiO_3$.

In the following sections the effect of different opto-geometric configurations on the theoretical electro-optic response of individual domain variants will be considered. Additionally the cumulative effects due to the various domain variants present in a polydomain film are likewise considered.

4.2.1 Propagation in the plane of rotation of the index ellipsoid

In $BaTiO_3$ the rotation of the indicatrix due to off-diagonal electro-optic coefficients is confined to the plane defined by the applied E-field vector and the polarization vector or optical axis of the given domain variant. In the waveguide geometry (Figure 4-2(c) and (d)), the propagation direction, the applied E-field, and the polar axis of all of the a-domain variants all lie within the plane of the film. Similarly, in the transmission geometry the plane-normal propagation direction lies in the same plane defined by the polar axis of the c-domains and the in-plane E-field vector. Therefore, in both instances, the propagation direction is in the plane of rotation of the indicatrix of the domain variants under consideration. When the propagation direction is confined within the plane of rotation of the indicatrix, the orientations of the two allowed optical modes for the given propagation direction do not change upon application of an external E-field. One optical mode always lies in the plane of rotation of the indicatrix and the other is always normal to the plane of rotation. In this case while the rotation of the indicatrix does not change the orientation of the eigenmodes, it does however contribute to the change in the indices of the eigenmodes as seen below in equation (4-12).

Consider domain variant 5 in Figure 4-2(c). If the in-plane electric field direction is adjusted to some angle θ while maintaining an orthogonal in-plane propagation direction, the birefringence both with and without an applied electric field can be determined as a function of θ. From these, the change in the birefringence as a function of θ can be determined. As the propagation direction is rotated in the plane of the film as shown schematically in Figure 4-3(a) the indices of the allowed modes in the absence of an applied electric field are given by

$$\begin{bmatrix} n_y(\theta) \\ n_{xz}(\theta) \end{bmatrix} = \begin{bmatrix} n_o \\ \left(\dfrac{\cos^2(\theta)}{n_o^2} + \dfrac{\sin^2(\theta)}{n_e^2} \right)^{-1/2} \end{bmatrix} \tag{4-11}$$

Under an in-plane orthogonal applied field as shown in Figure 4-3(b), the indices of the allowed optical modes are given by

$$\begin{bmatrix} n_y(\theta,E) \\ n_{xz}(\theta,E) \end{bmatrix} = \begin{bmatrix} n_o + r_{13}E\sin(\theta) \\ \left(\dfrac{\cos^2(\theta+\alpha_{ij})}{(n_x'')^2} + \dfrac{\sin^2(\theta+\alpha_{ij})}{(n_z'')^2} \right)^{-1/2} \end{bmatrix} \tag{4-12}$$

where α_{ij} is given by (4-7). n_x'' and n_z'' are defined by $n_i'' = 1/\sqrt{\eta_i''}$ where η_i'' is defined by (4-9). The components of the impermeability tensor (4-8), that appear in (4-7) and (4-9) being in this case defined as

$$\begin{bmatrix} \eta_{11}' \\ \eta_{33}' \\ \eta_{13}' \end{bmatrix} = \begin{bmatrix} \eta_1' \\ \eta_3' \\ \eta_5' \end{bmatrix} = \begin{bmatrix} \dfrac{1}{n_o^2} + r_{13}E\sin(\theta) \\ \dfrac{1}{n_e^2} + r_{33}E\sin(\theta) \\ r_{51}E\cos(\theta) \end{bmatrix} \tag{4-13}$$

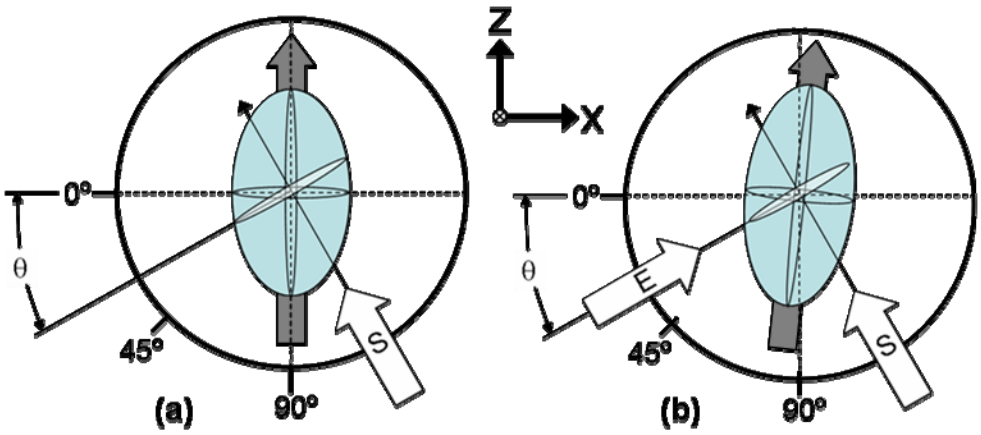

Figure 4-3. Schematic showing plane view of indicatrix[***]. Large grey arrow indicates orientation of the polar axis. The central elliptical cross-section of the optical indicatrix is shown as a function of the propagation direction in the xz-plane (a) in the absence of an applied E-field and (b) with an applied E-field in the xz-plane perpendicular to the propagation direction.

From (4-11) and (4-13) the change in the birefringence as a function of the propagation direction ($\delta\Delta n(\theta)$) can be determined. Figure 4-4 shows the result of numerical simulations of the $\delta\Delta n(\theta)$ for

[***] The indicatrix shown is for the positive uniaxial case. $BaTiO_3$ is negative uniaxial such that the semiaxis parallel to the polar axis is shorter than the two other axes. In introductory discussions of the indicatrix it is almost universally rendered for the positive uniaxial case. The analysis is in no way affected by this as all calculations and simulations reflect the negative uniaxial nature of $BaTiO_3$'s indicatrix

the domain variant 5 from Figure 4-2(c) and (d) assuming an applied electric field of 1MV/m with n_o and n_e of 2.412 and 2.360 at 633 nm[56] and assuming clamped bulk r_{ij} values (r_{13} = 10.2 pm/V, r_{33} = 40.6 pm/V, r_{51} = 730 pm/V)[56]. One can see that at θ = 0 when the propagation direction is parallel to the optic axis $\delta\Delta n(\theta)$ goes to zero. This is consistent with the predictions of coupled wave analysis based on perturbation theory[178,187]. Furthermore it implies that in the transmission geometry (Figure 4-2(a)(b)) the c-domains make no contribution to the measured EO response. In Figure 4-4 the maximum $\delta\Delta n(\theta)$ occurs at an angle of 35° and then drops off as θ goes to 90° where the EO response is due purely to the r_{13} and r_{33} contributions. In the waveguide geometry this implies that for a <100> oriented E-field, the a-domains make no r_{42} or r_{51} contribution to the EO response. In Figure 4-2(c) a-domain variants 5 and 6 make no contribution to the EO response while a-domain variants 3 and 4 make only r_{13} and r_{33} contributions to the EO response. Figure 4-5 shows $\delta\Delta n(\theta)$ due to variant 5 along with that due to variant 6. The theoretical $\delta\Delta n(\theta)$ for variant 6 is found by repeating the same simulation done for variant 5 after substituting the appropriate form of the EO tensor from Figure 4-1 into equation (4-5). In this case, with the EO tensor of variant 5 in the standard form ((4-6) or Figure 4-1(1)), the appropriate form of the EO tensor of for variant 6 is given by Figure 4-1(2) in which the finite components are the same as those of variant 5 but of opposite sign. It is therefore evident from (4-5) and (4-8) that the $\delta\Delta n(\theta)$ due to variant 6 for an applied E-field $\vec{E}$ is the same as that for variant 5 under an applied E-field of $-\vec{E}$. From the figure it is evident that for all θ the $\delta\Delta n(\theta)$ due to oppositely oriented domains ((5,6) or (3,4)) cancel.

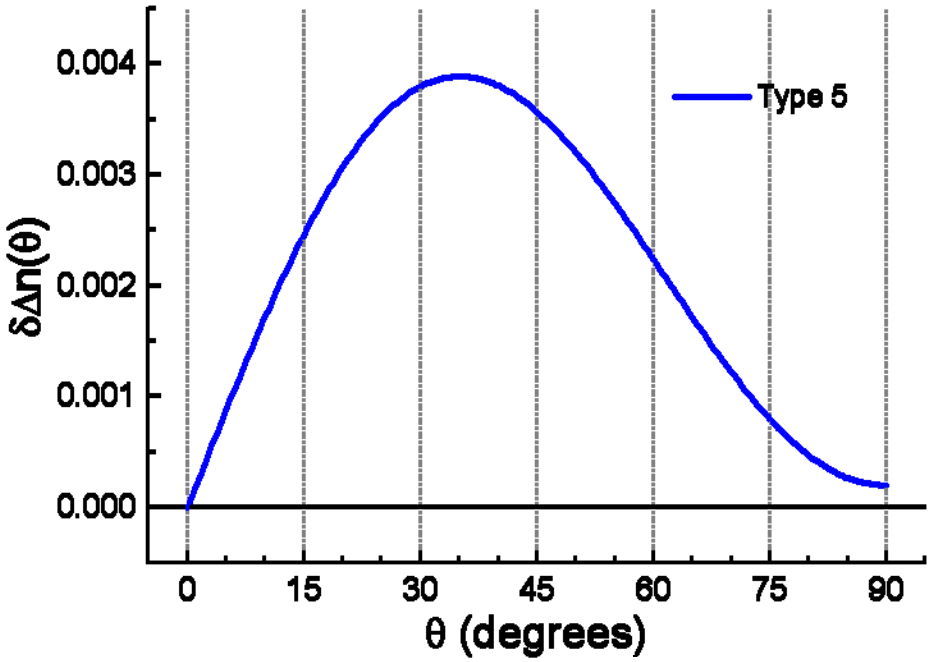

Figure 4-4. Dependence of δΔn due to domain variant 5 from Figure 4-2(c) and (d) on the in-plane propagation direction with an in-plane orthogonal E-field. The angle θ is defined in Figure 4-3.

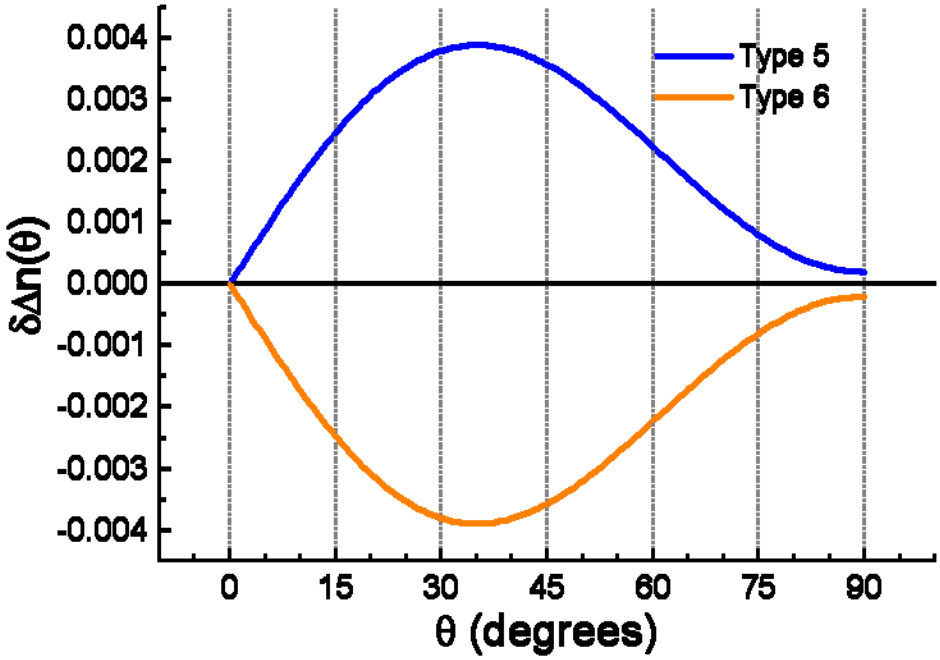

Figure 4-5. δΔn due to 180° domain variants is seen to cancel for all θ where θ is defined in Figure 4-3

As a consequence of the biaxial strain due to clamping by the substrate, the sum of the volume fractions of domain variants 5 and 6 are expected to be equal to the sum of the volume fractions of

domain variants 3 and 4. Figure 4-6 shows the theoretical $\delta\Delta n(\theta)$ for domain variant 5 plotted together with that due to domain variant 3. The $\delta\Delta n(\theta)$ due to variant 3 is found by repeating the same simulation done for variant 5 after substituting the appropriate form of the EO tensor (Figure 4-1(3)) into equation (4-5). For variant 3 the maximum $\delta\Delta n(\theta)$ occurs at $\theta = 55^{\circ}$. Also shown in the figure is the film average $\delta\Delta n(\theta)$ due to the presence of equal volume fractions of variants 3 and 5. From the figure, the film average $\delta\Delta n(\theta)$ when equal volume fractions of variants 3 and 5 are present is optimized when $\theta = 45^{\circ}$.

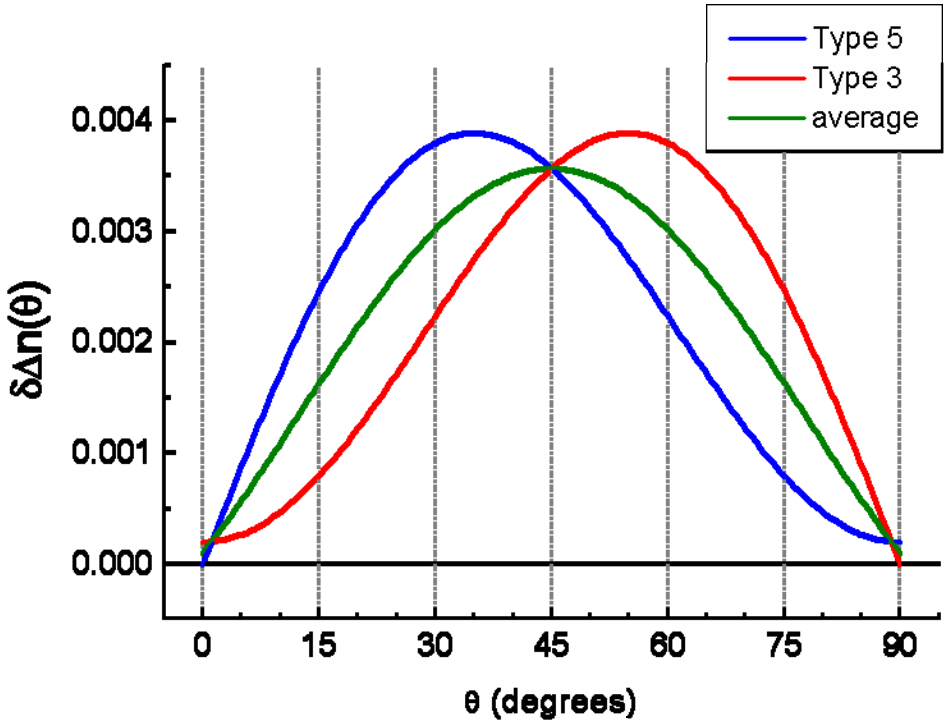

Figure 4-6. Combined effect of domain types 5 and 3 from Figure 4-2(c) and (d) on the in-plane directional dependence of δΔn. The angle θ is defined in Figure 4-3

The position of the maximum $\delta\Delta n(\theta)$ of variants 5 and 3 at 35° and 55° respectively is a result of the constraint of requiring the propagation direction to be orthogonal to the field direction. For the device geometries employed in this study this is a real constraint imposed by the device geometry. Figure 4-7(a) shows the numerical simulation of $\delta\Delta n$ due to domain variant 5 when the field direction and the propagation direction defined in Figure 4-3 are independently varied. The same 1MV/m field and bulk

material parameters assumed in the simulated results from Figure 4-4 through Figure 4-6 were assumed in the simulation shown in Figure 4-7. Figure 4-7(b) and (c) show the $\delta\Delta n$ due to variant 3 and the film average $\delta\Delta n$ for independent in-plane $\vec{E}$ and $\vec{k}$ orientations respectively. The scale bar gives the theoretical magnitude of $\delta\Delta n$ for Figure 4-7(a) thru (c). For clarity, Figure 4-7(d) shows the film average $\delta\Delta n$ on a different scale. The $\delta\Delta n(\theta)$ of variants 5 and 3 under the constraint of orthogonal $\vec{E}$ and $\vec{k}$ shown in Figure 4-6 represent the cross sections along the lines drawn in Figure 4-7(a) and (b) respectively. Similarly, the film average $\delta\Delta n(\theta)$ in Figure 4-6 represents the cross section along the line drawn in Figure 4-7(c) and (d).

From Figure 4-7 it is apparent that for a given domain variant, the maximum $\delta\Delta n$ occurs when the E-field is perpendicular to the optical axis (giving the maximum r_{51} contribution) and the propagation direction is at 45° to the optic axis. Again, this is consistent with the predictions of coupled wave analysis which for an E-field perpendicular to the optic axis predicts $\delta\Delta n \propto \cos(\theta)\sin(\theta)$ where θ is the angle between the propagation direction and the optic axis[187]. With equal volume fractions of 90° domain variants 5 and 3 the maximum $\delta\Delta n$ occurs when the E-field is at 45° (maximizing the net r_{51} contribution) and the propagation direction is orthogonal to the E-field (at 45° to the optic axis of both variant 5 and 3). This film average maximum $\delta\Delta n$ is ~72% of the maximum theoretical $\delta\Delta n$ due to either variant 5 or 3 individually when the E-field is perpendicular to the optic axis and $\vec{k}$ is at 45° to the optic axis.

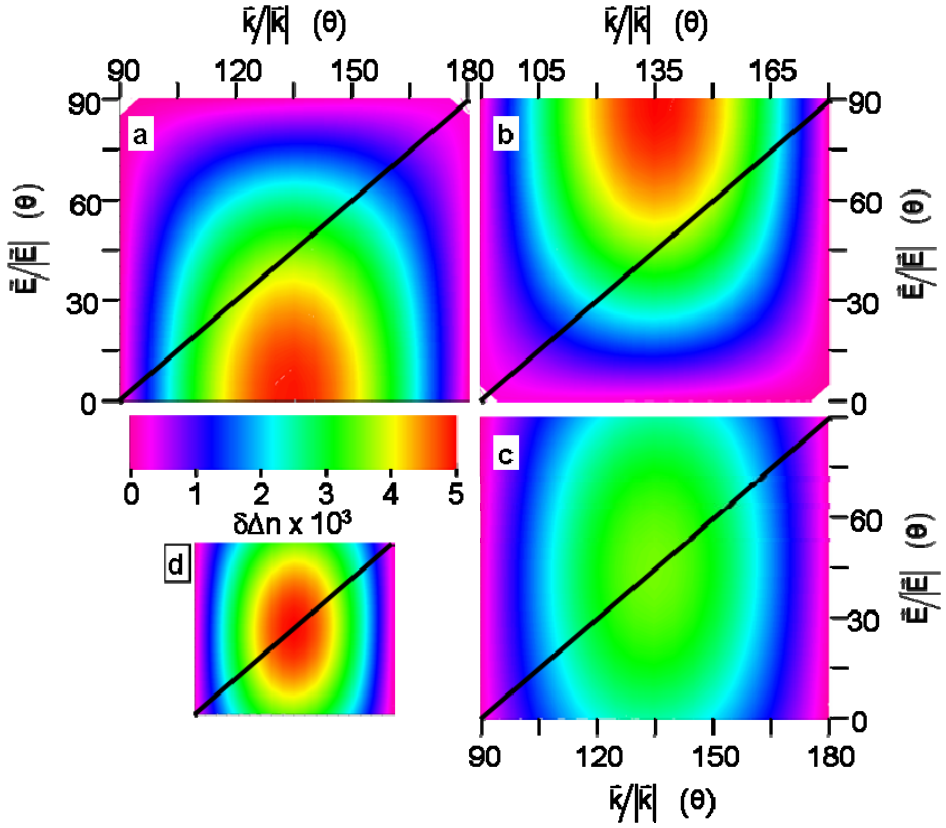

Figure 4-7. δΔn is plotted as a function of the in-plane E-field direction and the in-plane propagation direction for: (a) domain variant 5, (b) domain variant 3, (c)(d) equal volume fractions of variants 5 and 3. The scale bar give δΔn for (a)-(c). For clarity the film average is shown on a finer scale in (d). The angle θ is defined in Figure 4-3. The lines correspond to the δΔn when k is orthogonal to E and therefore correspond to the relevant plots in Figure 4-6.

For device geometries other than those considered here, larger film average $\delta\Delta n$ could be realized. For example, employing the Teng-Man reflectometry method[188] with the applied E-field parallel to the surface normal and in plane component of the propagation vector along a $BaTiO_3$<110> direction provides for a film average $\delta\Delta n$ due to the a-domains that is closer to the theoretical maxima from Figure 4-7(a) and (b). For an incident angle of 45° measured from the surface normal, the film average $\delta\Delta n$ due to variants 5 and 3 is 85% of the theoretical maximum, while for an incidents angle parallel to the $BaTiO_3$<111> direction (~55°) the film average $\delta\Delta n$ due to variants 5 and 3 is 95% of the theoretical maximum.

It is important to note that the dependence of $\delta\Delta n$ on the E-field and propagation directions discussed here is independent of the degree to which the domain structure is poled. Even assuming that

the film is fully poled such that domain variants 3 and 5 are the only a-domain variants present, the film average $\delta\Delta n$ along a <100> direction ($\theta = 0^o$ or 90^o) is just 3% of that along a <110> direction ($\theta = 45^o$).

4.2.2 Propagation perpendicular to the plane of rotation of the index ellipsoid

As noted previously, the rotation of the indicatrix is confined to the plane defined by the optical axis of the ferroelectric domain and the applied E-field vector. In the transmission geometry with an orthogonal in-plane E-field (Figure 4-2(a)(b)) the rotation of the a-domains is confined to the plane of the film, normal to the propagation direction. Similarly, in the waveguide geometry under the constraint of orthogonal $\vec{E}$ and $\vec{k}$ vectors, the indicatrix of the c-domains is confined in a plane perpendicular to the propagation direction. When propagation is normal to the plane of rotation of the indicatrix both the magnitude and the orientation of the eigenmodes change upon application of the E-field. The rotation of the eigenmodes is in this case equivalent to that of the indicatrix and is therefore directly determined from equation (4-7). Similarly if the field is confined in the xz-plane with propagation along y, then the magnitudes of the eigenmodes are simply the principle indices of the indicatrix under the applied E-field that lie in the xz-plane. These are equivalent to η_1'' and η_3'' from (4-9). The components of the impermeability tensor (4-8), that appear in (4-7) and (4-9) are as before defined in equation (4-13) where θ is again the angle between $\vec{E}$ and the xy-plane as shown in Figure 4-8 and Figure 4-9. The birefringence in the absence of an applied field in this case is simply $\Delta n = n_o - n_e$ where n_o and n_e are the ordinary and extraordinary refractive indices. This result is completely general for the case in which the propagation direction is normal to the plane defined by the E-field vector and the polar axis of the domain. Because the uniaxial indicatrix of $BaTiO_3$ is isotropic in the plane normal to the optic axis, one is free to define any arbitrary propagation direction in said plane as the y-direction such that the component of the E-field in that plane is parallel to the x-direction as shown in Figure 4-9. There is no reason to prefer the crystallographic axes by requiring x and y to lie along $BaTiO_3$<100> directions.

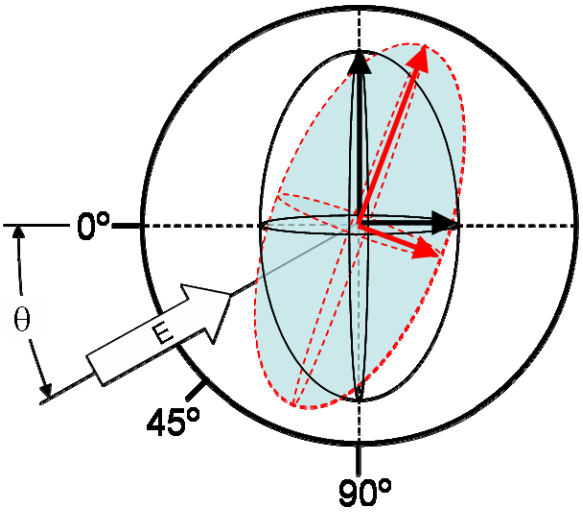

Figure 4-8. Schematic showing orientation of the eigenmodes. For $\vec{k} \| \left(\vec{E} \times \vec{P}\right)$ where P is the polarization vector, the orientation and magnitude of the eigenmodes is identical to that of the semiaxes of the indicatrix in the plane defined by E and P.

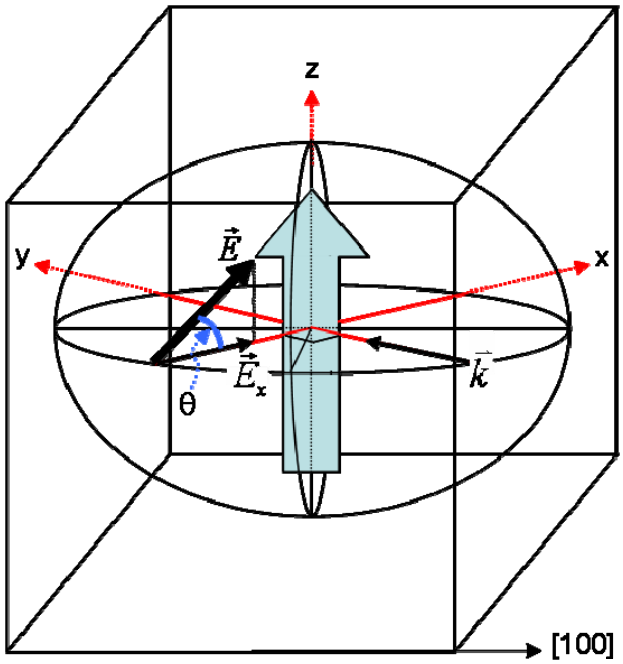

Figure 4-9. Schematic of indicatrix and unit cell. The indicatrix is isotropic in the plane normal to the optic axis such that for propagation normal to the plane defined by the optic axis and the E-field vector, the coordinate system can always be defined such that $\vec{k}$ is along the y-axis and the rotation of the indicatrix is confined in the xz-plane making equations (4-8) - (4-10),(4-13) completely general for the case where $\vec{k} \| \left(\vec{E} \times \vec{P}\right)$ where $\vec{P}$ is the optical axis shown in blue in the figure.

4.2.2.1 E-field dependence of birefringence under constraint $\vec{k} \,||\, \left(\vec{E} \times \vec{P}\right)$

When the propagation direction is normal to the plane of rotation of the indicatrix, the contribution to the E-field induced birefringence due to the off-diagonal EO coefficient r_{51} has a quadratic dependence on the applied E-field. That due to the r_{13} and r_{33} components is linearly dependent upon the applied E-field. As such the E-field dependence of the induced birefringence depends upon the relative degree of contribution from the r_{51} and the $\left(r_{13}, r_{33}\right)$ EO coefficients.

Substituting the values from (4-13) into equation (4-9), the general expression for the indices of the two eigenmodes under an applied E-field are given by

$$\begin{aligned} n_1' &= \left(\tfrac{1}{2}\left[\sin\left(\theta\right)\left(r_{33}+r_{13}\right)E+\eta_3+\eta_1-\Theta\right]\right)^{-\left(\frac{1}{2}\right)} \\ n_3' &= \left(\tfrac{1}{2}\left[\sin\left(\theta\right)\left(r_{33}+r_{13}\right)E+\eta_3+\eta_1+\Theta\right]\right)^{-\left(\frac{1}{2}\right)} \end{aligned} \tag{4-14}$$

where Θ from (4-9) can be rewritten as

$$\Theta = \sqrt{a+bE+cE^2} \tag{4-15}$$

After simplification, the general expressions for the coefficients in (4-15) are given by

$$\begin{aligned} a &= \left(\eta_3-\eta_1\right)^2 \\ b &= 2\sin\left(\theta\right)\left(r_{33}-r_{13}\right)\left(\eta_3-\eta_1\right) \\ c &= \sin^2\left(\theta\right)\left(r_{33}-r_{13}\right)^2+4r_{51}^2\cos^2\left(\theta\right) \end{aligned} \tag{4-16}$$

The change in the birefringence upon application of the E-field ($\delta\Delta n$) is then given by

$$\left(n_1'-n_3'\right)-\left(n_o-n_e\right) \tag{4-17}$$

where n_1' and n_3' are given by (4-14). While the expression in (4-17) is rather cumbersome after all the appropriate substitutions are made, the difference in the associated components of the impermeability tensor given by

$$\Delta\eta\left(E,\theta\right) = \eta_3''\left(E,\theta\right)-\eta_1''\left(E,\theta\right) = \Theta\left(E,\theta\right) \tag{4-18}$$

is roughly proportional to $\delta\Delta n$. As such inspection of (4-15) and (4-16) shows that when $\theta = 0^o$, $\Delta\eta$ and therefore $\delta\Delta n$ is strictly quadratic as long as $a \gg c$. This condition is always satisfied when

propagating perpendicular to the optical axis. When θ = 90°, the linear component of $\Delta\eta$ given by *b* in (4-16) is maximized. It should be noted that while *c* in (4-16) appears to indicate a finite quadratic dependence at θ = 90° due to the r_{33} and r_{13} coefficients, the coefficient *b* increases as θ goes from 0° to 90° as the coefficient *c* decreases such that the field dependence of $\delta\Delta n$ goes from quadratic at θ = 0° to linear at θ = 90°. Figure 4-10 shows the ratio of *b*/*c* as a function of θ.

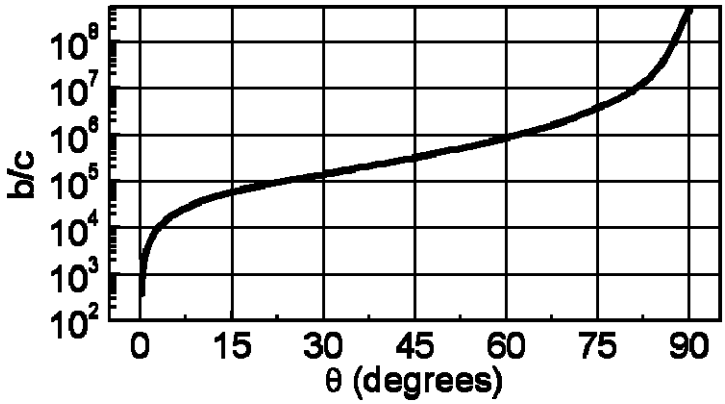

Figure 4-10. Ratio of coefficients *b* and *c* from (4-16) as a function of θ. At θ = 0° the coefficient *b* is identically zero and the $\delta\Delta n(E)$ is purely quadratic. At 90° it is highly linear

Figure 4-11 shows the E-field dependence of the change in birefringence ($\delta\Delta n$) of the domain from Figure 4-8 for E-field orientations of θ = 0°, 45°, and 90° where θ is defined as in Figure 4-8. The $\delta\Delta n$ is that derived from the analytic expressions in (4-14) through (4-17) assuming the same bulk EO coefficients and indices of refraction used previously. Also shown is the associated $\Delta\eta$ which as mentioned above is roughly proportional to $\delta\Delta n$.

$\delta\Delta n(E,\theta)$ for the domain in Figure 4-8 is shown in Figure 4-12 for the range E = -1 to 1 MV/m and θ = 0° to 90°. In Figure 4-12 the black contour lines demark the region where $\delta\Delta n(E,\theta) \approx 0$ ($\pm 1.5\times10^{-6}$). The points at which $\delta\Delta n(E,\theta) \approx 0$ for finite negative E correspond to points where the E-field induced birefringence due to the r_{51} EO coefficient is equal and opposite to that due to the r_{33} and r_{13} EO coefficients. In the case of measurements in the transmission geometry, the $\delta\Delta n(E,\theta)$ of the remaining 3 variants in the plane of the film can be inferred from symmetry.

$\delta\Delta n_{T6}(E,\theta) = \delta\Delta n_{T5}(-E,\theta)$, $\delta\Delta n_{T3}(E,\theta) = \delta\Delta n_{T5}(E, 90^{*} - \theta)$ and

$\delta\Delta n_{T4}(E,\theta) = \delta\Delta n_{T5}(-E, 90^{*} - \theta)$.

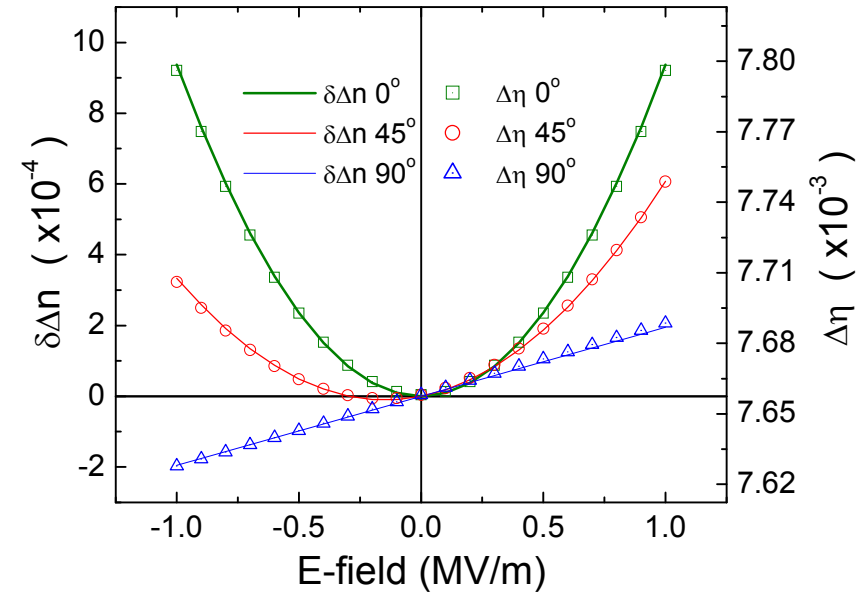

Figure 4-11. δΔn(E) and Δη(E) for three different E-field orientations (see Figure 4-8). The point at which δΔn + 0 for a finite negative field results from offsetting contributions to the birefringence from the r_{13} and r_{33} and the r_{51} EO coefficients

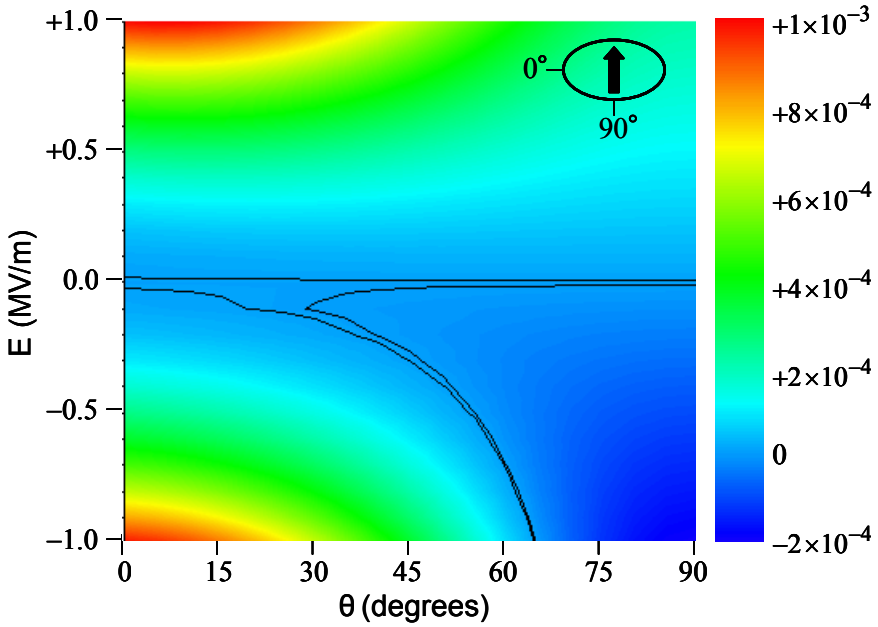

Figure 4-12. $\delta\Delta n(E,\theta)$ for the domain variant shown in the figure. At θ = 0° $\delta\Delta n(E)$ is quadratic while at θ = 90° $\delta\Delta n(E)$ is linear. The black contour lines demark a region where $\delta\Delta n(E) \approx 0$ ($\delta\Delta n(E) = \pm 2.5\times10^{-6}$). The points at finite negative E where $\delta\Delta n(E) = 0$ result from offsetting contributions from r_{51} and (r_{13}, r_{33}).

4.2.2.2 Combined effect of indicatrix rotation and $\delta\Delta n$ on EO response

When propagation is parallel to the plane of rotation of the indicatrix $\left(\vec{k} \,||\, \left(\vec{E} \times \vec{P}\right)\right)$ both the rotation of the indicatrix as well as the change in the birefingence have to be taken into account when modeling the theoretical change in the transmited intensity using the Jones calculus. The previous section treated the theoretical induced birefingence of $BaTiO_3$. Here we consider the combined effect of the $\delta\Delta n\left(E\right)$ as well as the rotation of the indicatrix and therefore the orientation of the eigenvectors of the two eigenmodes ($\alpha\left(E\right)$).

From (4-7) and (4-13) the rotation of the indicatrix can be written as

$$\alpha = \frac{1}{2}\arctan\left(\frac{2r_{51}E\cos\left(\theta\right)}{\eta_1 - \eta_3 + E\sin\left(\theta\right)\left(r_{13} - r_{33}\right)}\right) \tag{4-19}$$

where θ as before is as defined in Figure 4-8. The rotation of the indicatrix due to the r_{51} EO coefficient is linearly dependent on the applied field as seen in Figure 4-13. From (4-19) and Figure 4-13 the rotation α is maximum for a θ of 0° and decreases to zero as θ goes to 90°.

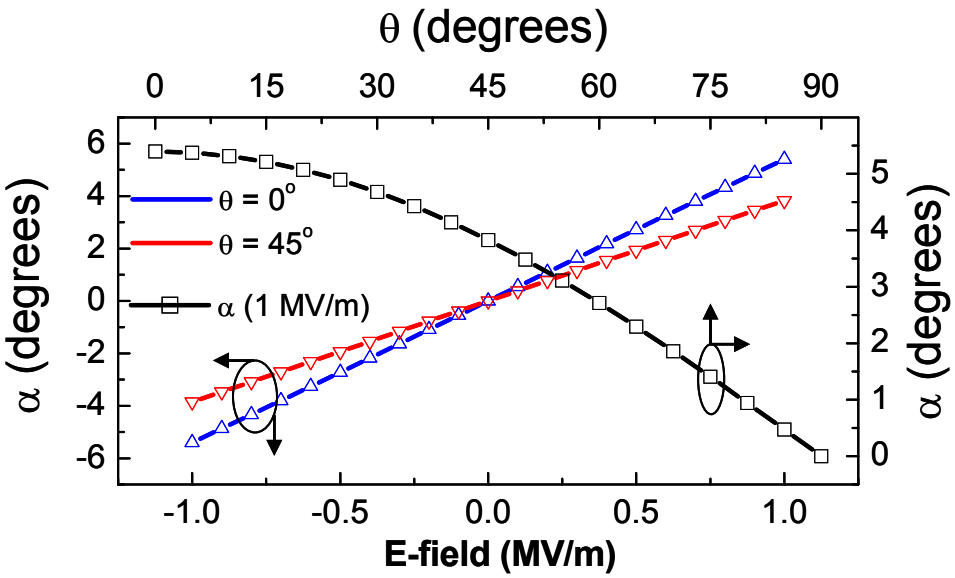

Figure 4-13. E-field and θ dependence of the rotation of the indicatrix. θ gives the orientation of the E-file to the polar axis of the domain as in Figure 4-8

Optimal polarimeter configuration

The effect on the transmitted intensity due to both the rotation of the index ellipsoid and the change in the indices of the two allowed optical modes is determined by use of the Jones calculus[181†††]. Figure 4-14 shows a PSCA polarimeter in which the EO sample is represented by an arbitrary linear retarder with its slow axis at an angle θ with respect to the x-axis. The compensator is a quarter wave-plate with its fast axis parallel to the x-axis and the analyzer's transmission axis is at some angle β to the x-axis. The input is assumed to be linearly polarized with propagation in the positive y direction and the plane of polarization parallel to the z-axis. The large r_{51} coefficient of $BaTiO_3$, results in a nontrivial rotation of the principle indices by an angle of ±α when a component of the applied field is perpendicular to the polar axis.

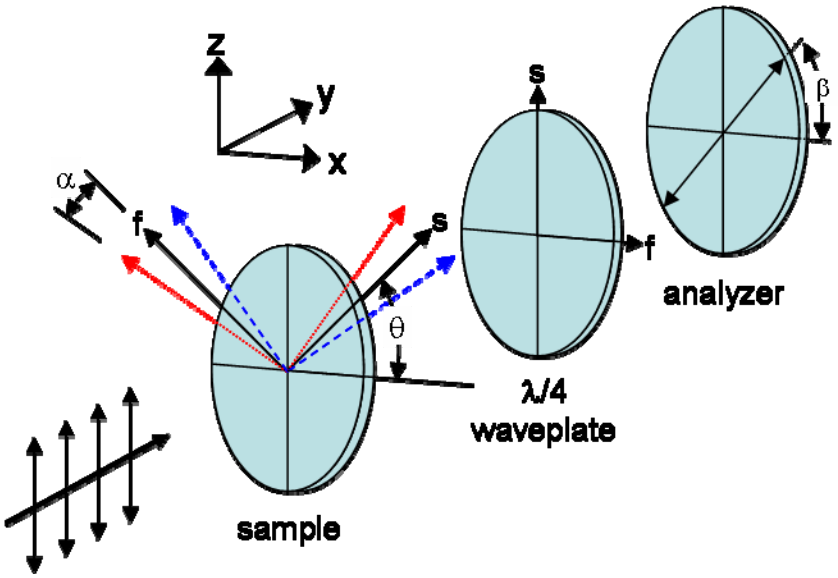

Figure 4-14. PSCA polarimeter. The EO sample is modeled as an arbitrary linear retarder with its slow axis at some angle θ to the x-axis. An applied E-field perpendicular to the polar axis causes a non-trivial rotation of the principle indices by ±α degrees.

††† The Jones calculus provides a means to characterize and analyze polarized light as it passes through optical elements such as wave-plates and retarders. The 2x1 Jones vector describes the polarization of the light and the 4x4 Jones matrices describe the transfer functions of the optical elements

The Jones matrix of the EO sample, which shall be referred to as ***R***, is given by[178,181]

$$\begin{bmatrix} e^{-i(\delta/2)}\cos^2(\theta+\alpha)+e^{i(\delta/2)}\sin^2(\theta+\alpha) & -i\sin\left(\delta/2\right)\sin\left(2(\theta+\alpha)\right) \\ -i\sin\left(\delta/2\right)\sin\left(2(\theta+\alpha)\right) & e^{-i(\delta/2)}\sin^2(\theta+\alpha)+e^{i(\delta/2)}\cos^2(\theta+\alpha) \end{bmatrix} \tag{4-20}$$

where δ is the retardation induced by the birefringence and $(\theta+\alpha)$ is the azimuthal angle of the slow axis with respect to the x-axis. With no E-field applied α is set to zero and δ is proportional to the natural birefringence $\Delta n = n_o - n_e$. The Jones matrix of the quarter waveplate with its fast axis parallel to the x-axis is given by

$$Q = \begin{bmatrix} i & 0 \\ 0 & 1 \end{bmatrix} \tag{4-21}$$

and that of the analyzer with its transmission axis at an azimuthal angle β to the x-axis, is given by

$$A = \begin{bmatrix} \cos^2(\beta) & \sin(\beta)\cos(\beta) \\ \sin(\beta)\cos(\beta) & \sin^2(\beta) \end{bmatrix} \tag{4-22}$$

The normalized optical field at the output of the PSCA polariscope is thus given by

$$\begin{bmatrix} E_x' \\ E_z' \end{bmatrix} = A \cdot Q \cdot R \cdot \begin{bmatrix} 0 \\ 1 \end{bmatrix} \tag{4-23}$$

where the last term on the right is the z-polarized input optical field with incident intensity normalized to 1. The output optical field given by (4-23) is of the form

$$\begin{bmatrix} E_x' \\ E_z' \end{bmatrix} = \begin{bmatrix} \cos^2(\beta)\cdot\Delta+\nabla \\ \sin(\beta)\cos(\beta)\cdot\Delta+\nabla \end{bmatrix} \tag{4-24}$$

where Δ and ∇ are given by

$$\begin{aligned} \Delta &= \sin\left(\delta/2\right)\sin\left(2(\theta+\alpha)\right) \\ \nabla &= \sin(\beta)\cos(\beta)\left[e^{-i\delta/2}\sin^2(\theta+\alpha)+e^{i\delta/2}\cos^2(\theta+\alpha)\right] \end{aligned} \tag{4-25}$$

The transmitted intensity is then given by

$$I = E_x' \cdot \left(E_x'\right)^* + E_z' \cdot \left(E_z'\right)^* \tag{4-26}$$

where $\left(E_i^{'}\right)^*$ is the complex conjugate of $E_i^{'}$. By using (4-24) thru (4-26) to determine the transmitted intensity with and without an applied E-field, the theoretical change in the transmitted intensity, ΔI, which is what is typically measured in ellipsometric EO measurements, is determined.

In the absence of an applied field the expression for the retardation due to the natural birefringence of a given domain variant is

$$\delta_o = \left(n_o - n_e\right)\frac{\ell 2\pi}{\lambda} \tag{4-27}$$

where ℓ is the interaction length which in the transmission geometry is simply the film thickness. For a free space wavelength of 633 nm and an assumed film thickness of 600 nm which is typical of the films examined, Γ_o is equal to ~0.31 radians. Under an applied E-field the retardation is determined from (4-27) after substituting $\left(n_1' - n_3'\right)$ from (4-17) for the natural birefringence $\left(n_o - n_e\right)$. Figure 4-15(a) shows the $\Delta I\left(\theta,\beta\right)$ of a single 600 nm thick domain for a <110> oriented 1 MV/m E-field. The same bulk $BaTiO_3$ material parameters assumed previously were used here. As mentioned above the input intensity is normalized to 1. The scale in Figure 4-15 is ±0.021 for all but (c) and (f). If the $\Delta I\left(\theta,\beta\right)$ in Figure 4-15(a) is that for domain variant 5 (T5) from Figure 4-2(b) then that for domain variant 6 (T6) is determined from the Jones calculus after switching the sign of the rotation angle α and substituting the correct retardation for T6 under a 1 MV/m E-field. As with T5, the retardation under field for T6 is determined using (4-27) after substituting $\left(n_1' - n_3'\right)$ from (4-17). Recall that $\delta\Delta n_{T6}\left(E,\theta\right) = \delta\Delta n_{T5}\left(-E,\theta\right)$ and due to the combined linear and quadratic dependencies on the E-field at θ = 45° $\delta\Delta n\left(E\right)$ is not symmetric about the origin $\left(\delta\Delta n\left(E\right) \neq \left(\delta\Delta n\left(-E\right), -\delta\Delta n\left(E\right)\right)\right)$. The $\Delta I\left(\theta,\beta\right)$ due to domain T6 is shown in Figure 4-15(b) while (c) shows the sum of the response due to T5 and T6. For clarity the scale in Figure 4-15(c) is just 5% of that from Figure 4-15(a) and (b). From Figure 4-15(a)-(c) one sees that while in general the ΔI due to T3 and T5 are opposite and largely cancel, the cancellation is incomplete for most $\left(\theta,\beta\right)$. In particular $\left(\Delta I_5 + \Delta I_6\right)$ is maximized at the points where ΔI_5 and ΔI_6 are smallest. This includes the region $\left(\theta = 0, \beta \approx 0\right)$ which is the typical operating

region used for transmission EO measurements with a <110> oriented E-field. At $(\theta = 0, \beta = 0)$ for example $(\Delta I_5 + \Delta I_6)/\Delta I_5$ and $(\Delta I_5 + \Delta I_6)/\Delta I_6$ equal 0.44 and -0.79 respectively.

In order to determine the $\Delta I(\theta, \beta)$ due to variant 3 (T3) from the Jones matrices of T5 given above the following changes are made. The sign of the rotation angle α is switched in the Jones matrix of the sample and the fast and slow axes of the samples Jones matrix are switched (θ subsequently represents the orientation of the fast axis with respect to the x-axis of the coordinate system in Figure 4-14). Figure 4-15(d) shows the $\Delta I(\theta, \beta)$ due toT3 while (e) shows the combined average ΔI due to both T5 and T3. It is apparent from Figure 4-15(d)-(e) that the EO responses of T3 and T5 are additive. The differences in the $\Delta I(\theta, \beta)$ patterns for T3 and T5 result from the different relative orientation of the domains to the quarter waveplate in the polariscope.

One last significant feature observed in Figure 4-15 is that for all domain variants shown, the optimal orientation of the sample in the polarimeter as given by the angle θ is at 0^o or $\pm 90^o$. In the absence of rotation of the eigenmodes the optimal orientation of the sample is always at $\theta = 45^o$ where the components of the incident light coupled to the "fast" and "slow" eigenmodes are equivalent. Figure 4-15(f) shows the $\Delta I(\theta, \beta)$ of T5 when α is artificially set to 0, and as seen the maximum $\Delta I(\theta, \beta)$ occurs at $\theta = \pm 45^o$. Furthermore the global maximum of $\Delta I(\theta, \beta)$ for $\alpha = 0$ is just 9% of that when the finite theoretical α is taken into consideration. The inset at upper right in Figure 4-15(f) shows the $\Delta I(\theta, \beta)$ for $\alpha = 0$ on the same scale as Figure 4-15(a).

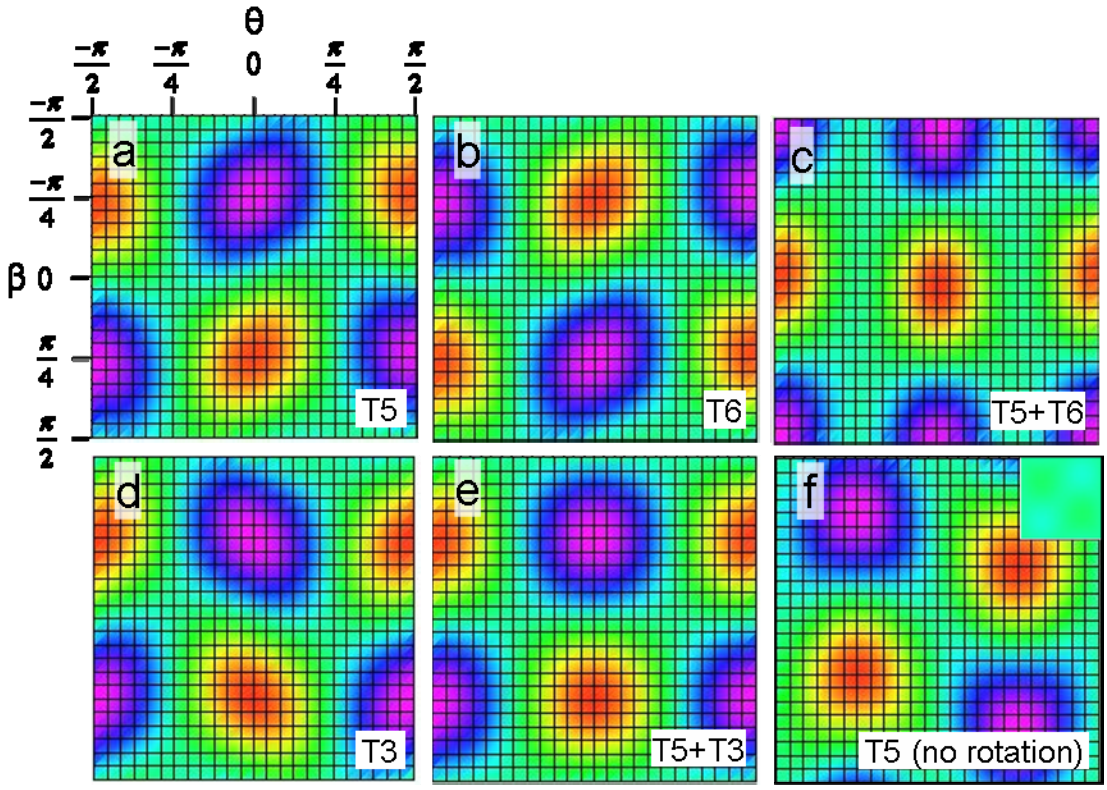

Figure 4-15. ΔI transmitted for a-domain variants from Figure 4-2(b): (a) domain variant 5, (b) domain variant 6 (c) average ΔI due to equal volume fractions of T5 and T6 (rendered on a scale of just 5% of that in (a) and (b)). (d) shows the ΔI due to variant 3 and (e) shows the average ΔI due to equal volume fractions of T5 and T3 on the same scale as (a) and (d). (f) shows the ΔI due to T5 when the rotation is artificially set to zero. The scale in (f) is just 10% of that in (a) and the inset in the upper right corner of (f) shows the result rendered on the same scale as (a).

In general when there is a rotation of the eigenmodes the optimal orientation of the sample in the polarimeter is dependent upon the interaction length. For $BaTiO_3$, when the interaction length is less than ~2 μm the general distribution of $\Delta I(\theta,\beta)$ of T5 is close to that from Figure 4-15(a). The change in retardation caused by the change in birefringence is dependent upon the interaction length while the rotation of the indicatrix is not. As such the effect of the rotation dominates for interaction lengths of less than 2 μm. For longer interaction lengths where the retardation becomes appreciable the optimal orientation of the sample is cyclical and goes as $\sin(\delta_o)$ where δ_o is the total retardation induced by the natural birefringence. To reiterate, in the absence of rotation of the eigenmodes, the optimal orientation of the sample is always at θ = 45°. In contrast when the eigenmodes rotate under the application of an

applied field the optimal orientation of the sample is at a θ of 0 or ±90° when the interaction length and therefore $\Delta\delta$ is small, and it is cyclically dependent upon $\sin(\delta_o)$ at longer interaction lengths where $\Delta\delta$ is appreciable.

E-field dependence of ΔI

It was previously demonstrated that for most field orientations in which $\left(\vec{k} \,||\, \left(\vec{E} \times \vec{P}\right)\right)$ the induced birefingence has both quadratic and linear dependencies upon the applied field while the rotation was strictly linearly dependent upon the applied field even for fields of several MV/m. The theoretical field dependence of the change in transmitted intensity for a <110> oriented E-field was modeled using the Jones calculus. For the simulation an analyzer angle of 3° and a sample orientation of 0° were assumed as these typify the polarimeter configuration used in transmission EO measurements with a <110> oriented E-field. The same bulk $BaTiO_3$ material parameters assumed in previous simulations were used here. Figure 4-16 shows the field dependence of ΔI for all four a-domain variants in the transmission geometry of Figure 4-2(b).

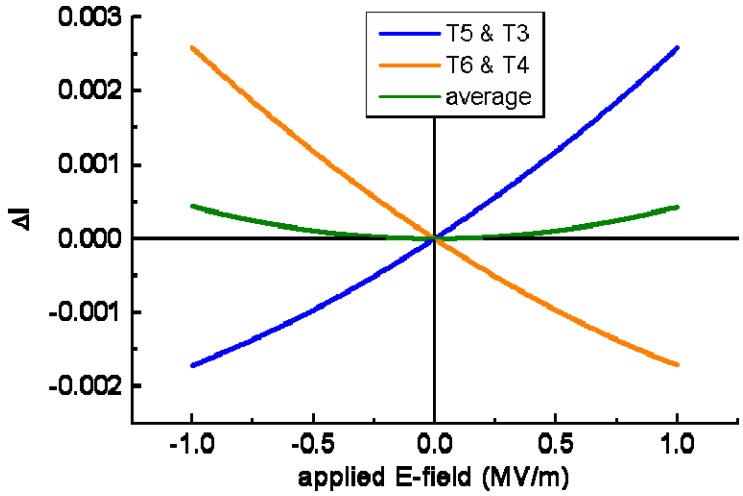

Figure 4-16. The theoretical field dependent change in the transmitted intensity for the domain variants from Figure 4-2(b) when $\vec{k} \,||\, \left(\vec{E} \times \vec{P}\right)$. The operating point used in the simulated theoretical $\Delta I(E)$ was $\theta = 0^\circ$ and $\beta = 3^\circ$ (see Figure 4-14) This typifies the operating points employed for transmission EO measurements with a <110>-oriented E-field. At the operating point the response due to domain variant 5 is the same as that due to variant 3. The incomplete cancelation of 180° domain variants is reflected in the finite average transmitted intensity with equal volume fractions of variants 5 and 6 or 3 and 4.

Equation (4-26) was used to generate the simulated result in Figure 4-16. However, equation (4-26) can be greatly simplified for the conditions assumed in the simulation. For an analyzer angle of $\beta = 3°$ the small angle approximations $\sin(\beta) = \beta$ and $\sin^2(\beta) = \beta^2$ can be made. Additionally because of the short interaction lengths in the transmission geometry, the small angle approximation can likewise be made for the terms involving the field induced retardation δ. After substituting equations (4-24) and (4-25) into equation (4-26) and simplifying, the resulting change in the transmitted intensity ΔI for variants T6 and T4 is given by

$$\Delta I_6\left(\delta(E),\beta,\theta,\alpha(E)\right) = \left[a\delta^3(E) + b\delta^2(E) + c\delta(E) + d\right] - I_\circ \tag{4-28}$$

where $\delta(E)$ is the E-field induced retardation given by substituting n_1' and n_3' from equation (4-14) into equation (4-27). The coefficients (a,b,c,d) are given by

$$\begin{aligned}
a &= \sin\left(2\left(\theta+\alpha(E)\right)\right)\left[\frac{-\beta\left(\beta^2-2\beta-2\right)\left(\beta^2-1\right)}{16}\right] \\
b &= \cos^2\left(\theta+\alpha(E)\right)\left[1-3\beta^2+2\beta^4+\cos^2\left(\theta+\alpha(E)\right)\left(3\beta^2-2\beta^4-1\right)\right] \\
c &= \sin\left(2\left(\theta+\alpha(E)\right)\right)\left[\frac{\beta\left(\beta^2-2\beta-2\right)\left(\beta^2-1\right)}{2}\right] \\
d &= -2\beta^2\left(\beta^2-1\right)
\end{aligned} \tag{4-29}$$

Figure 4-17 shows the theoretical field dependent transmitted intensity of domain variants T6 and T4 using the result of the full Jones calculus given by equation (4-26) as well as that using the small angle approximation given by equation (4-28). As seen in the figure the agreement is fairly good. Substituting the values of the analyzer angle β and the orientation angle of the sample θ used in the simulation from Figure 4-16 into equations (4-28) and (4-29) these equations are simplified further. After substitution the resulting equations for domain variants (T3,T5) and (T4,T6) are given by

$$\begin{aligned}
\Delta I_{(3,5)}\left(\delta(E),\alpha(E)\right) &= 0.2\delta^2\sin^2\left(2\alpha\right) - 0.05\delta\sin\left(2\alpha\right) \\
\Delta I_{(4,6)}\left(\delta(E),\alpha(E)\right) &= 0.2\delta^2\sin^2\left(2\alpha\right) + 0.05\delta\sin\left(2\alpha\right)
\end{aligned} \tag{4-30}$$

Figure 4-18 shows equation (4-30) plotted along with that given by the Jones calculus from equation (4-26) for variants T4 and T6. The agreement is reasonably good.

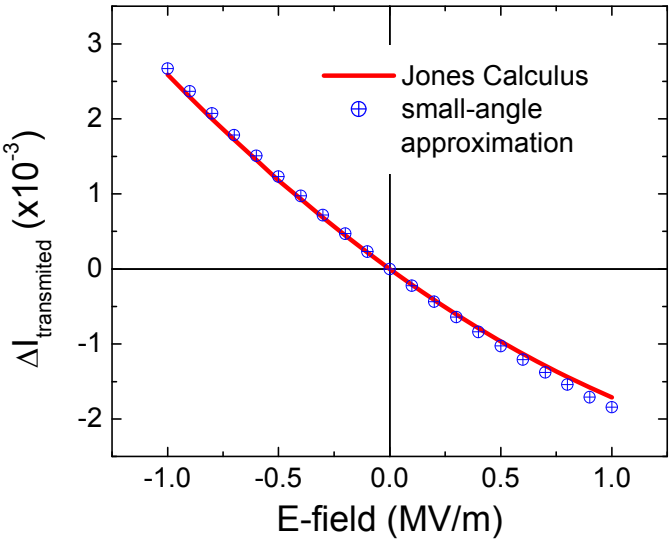

Figure 4-17. The theoretical change in the transmitted intensity of domain variants T6 and T4 from Figure 4-2b are shown. The solid red line was calculated using the Jones Calculus as given by equation (4-26). The blue circles show the change in transmitted intensity calculated using equations(4-28) and (4-29) in which the result of the Jones calculus is simplified using the small angle approximation.

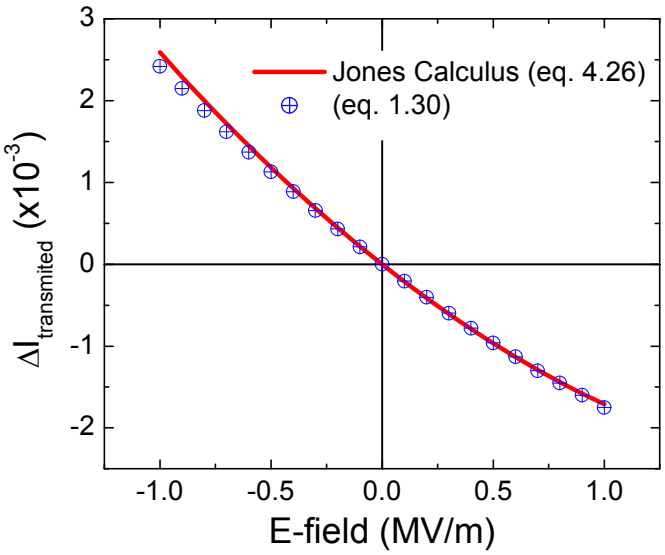

Figure 4-18. The theoretical transmitted intensity of domain variants T6 and T4 as given by equation (4-30) is plotted along with the result using the exact Jones calculus given by equation (4-26).

Lastly, because the field induced rotation of the principle axes given by α is less than 4° for applied fields of less than 1 MV/m, equation (4-30) can be further simplified without introducing any substantial error as

$$\begin{aligned}\Delta I_{(3,5)}\left(\delta(E),\alpha(E)\right) &= 0.8\left(\delta\alpha\right)^2 - 0.1\delta\alpha \\ \Delta I_{(4,6)}\left(\delta(E),\alpha(E)\right) &= 0.8\left(\delta\alpha\right)^2 + 0.1\delta\alpha\end{aligned} \tag{4-31}$$

Figure 4-19 shows the predicted change in the transmitted intensity from equation (4-31) plotted along with that using the result from the un-simplified Jones calculus given by equation (4-26)

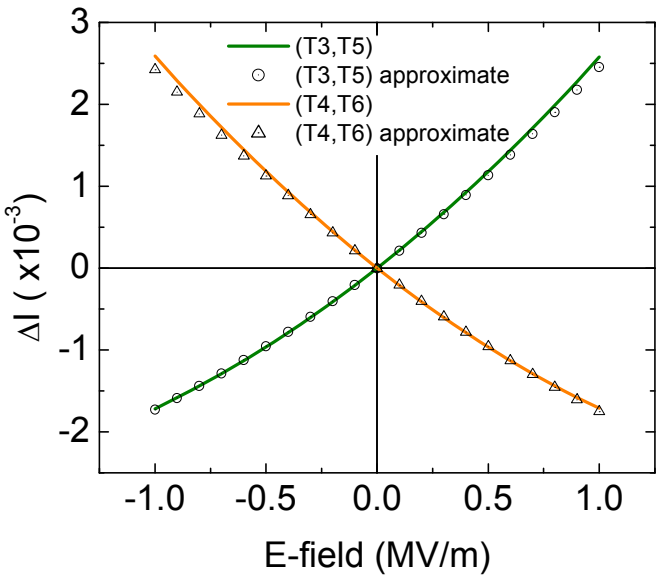

Figure 4-19. Theoretical change in the transmitted intensity for propagation perpendicular to the plane of rotation of the indicatrix when the applied field is along a crystallographic <110> direction. The results using the un-simplified Jones calculus expression given by equation (4-26) are shown (solid lines) along with the results in which small angle approximations were made for the parameters α, θ and β (see Figure 4-14) as given by equation (4-31).

Combined effect of c- and a-domains in <110> waveguide geometry

In the waveguide geometry with a <110> oriented E-field and orthogonal in-plane propagation direction all of the domain variants make individual r_{51} contributions to the EO response. In this geometry the rotation due to the r_{51} coefficient of the a-domains contributes to the change in the magnitude but not the orientation of the eigenvectors. In contrast the rotation due to the r_{51} coefficient of the c-domains causes the orientation of the eigenmodes to rotate under the applied field. The theoretical

change in the transmitted intensity for c- and a-domains in series is determined using the Jones calculus. For the a-domains the retardation with and without an applied field is determined from (4-27) after substituting the Δn values determined from (4-12) and (4-11) respectively and the rotation angle of the eigenmodes as just mentioned is zero. Additionally, the fast axis of the retarder representing the a-domains is in the plane of the film (along x in Figure 4-14). The ΔI of the c-domains is calculated as just shown in Section 4.2.2.2. Lastly because measurements in the waveguide geometry were made using the PSA polariscope described in chapter 3 the matrix for the quarter wave-plate compensator was omitted.

The results for a number of different assumed domain structures consisting of both c- and a-domains was examined. For any given analyzer angle the transmitted intensity remained finite for all sample orientations θ. In other words for a given analyzer angle β the EO response (ΔI) remains finite for all sample orientations θ. This reduced dependence of the EO response on the orientation of the input polarization is in contrast to that for a film consisting of only a-domains or only c-domains. In that case the theoretical response is such that for any analyzer angle β there are sample orientations θ for which the EO response (ΔI) goes to zero. Figure 4-20 shows the $\Delta I(\theta, \beta)$ for four different assumed domain structures. Figure 4-20(a) shows the $\Delta I(\theta, \beta)$ for a single 1.5 mm T5 and a single 1.5 mm T1 domain for the opto-geometry in Figure 4-2(d). Under this simple assumption ΔI shows no θ-dependence. Typical MOCVD grown films on MgO substrates are between 65% to 85% c-oriented. Figure 4-20(b) shows the $\Delta I(\theta, \beta)$ when the c-domain (T1) is modeled as 2.25mm while the a-domain is modeled as a 0.75 mm domain (75% c-oriented). In this case ΔI does show a θ dependence but for given analyzer angles the response remains finite and the θ dependence is far less than in the fully-c or fully-a oriented case. Figure 4-20(c) and (d) show for domains more on the order of the actual domain sizes observed in the thin

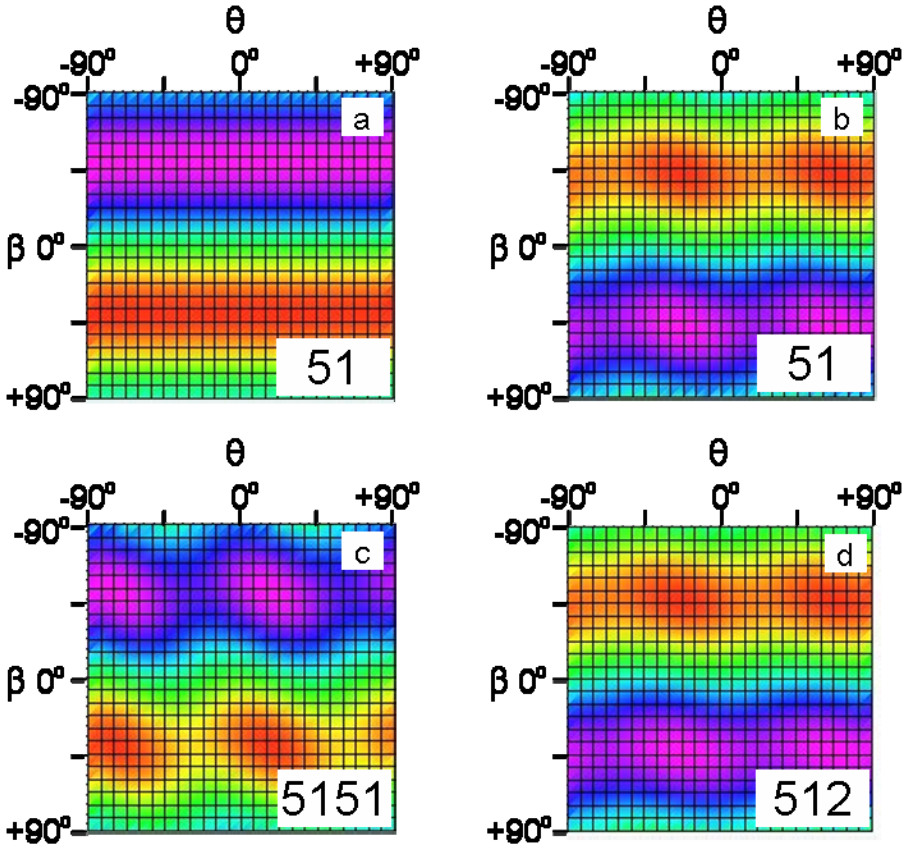

Figure 4-20. ΔI(θ,β) in the waveguide geometry with a <110> oriented E-field and orthogonal propagation direction for four different assumed domain structures. A reduced θ dependence is evident. The assumed domain variants are listed in the insets in the lower right of each image in the order transited by the propagating mode (refer to Figure 4-2(d)). In (a) both the a- and c-domain are assumed to be 1.5 mm thick. In (b) c-domain is 2.25 mm while the a-domain is 0.75 nm thick (75% c-domain). In (c) c-domain is 100 nm a-domain is 33 nm thick. In (d) c-domains are (100) nm thick and a-domain is 66 nm thick.

films (~100 nm)[36]. In (c) the c-domains were assumed to be 100 nm thick while the a-domains were assumed to be 33 nm across. Because the c-domains are not subject to poling by the applied E-field, in (d) the presence of both c-up (T1) and c-down (T2) domains were considered. To maintain the 75% c-domain assumption both c-domains were assumed to be 100nm thick while the a-domain was assumed to be 66 nm thick. Both Figure 4-20(c) and (d) appear quite similar to (b) with ΔI remaining finite for all θ at most analyzer angles.

The analysis here is admittedly highly simplified relative to the situation in a typical 3 mm device where as many as 30,000 100 nm domains are transited in series by the propagating beam. However it

demonstrates that a relative insensitivity of the EO response to the orientation of the input polarization can be achieved in the waveguide geometry when both c- and a- domains are present.

In this chapter a detailed analysis of the theoretical intrinsic electro-optic response of the different domain variants was provided for a variety of measurement geometries. Additionally the cumulative effect due to the polydomain structure was considered. $BaTiO_3$'s large off-diagonal EO coefficient is seen to give rise to a quadratic field dependence for the change in the birefringence. Furthermore it was demonstrated that for the short interaction lengths involved in the transmission geometry (~600 nm) the change in the transmitted intensity through the polariscope is dominated by the rotation of the propagation eigenmodes as opposed to the change in their value or $\delta\Delta n$.

5 FERROELECTRIC PROPERTIES OF $BATIO_3$ THIN FILMS

5.1 Electronic polarization of polydomain thin films

The primary objective of this study is to investigate the effect of domains and their dynamics on the electro-optic properties of polydomain $BaTiO_3$ thin films. Electronic polarization measurements are one of the principle methods of characterizing ferroelectric domain dynamics and in this section the results of electronic polarization measurements in our $BaTiO_3$ thin films are reported. These results will be used in Section 5.2.3 in the modeling of the hysteretic electro-optic response of the polydomain $BaTiO_3$ thin films. The electronic polarization hysteresis loops of thin films often differ greatly from those measured in single-domain bulk single crystals. A theoretical model of the domain structure dependent polarization of thin films is developed. Specifically it is proposed that the in-plane polarization is proportional to the a-domain volume fraction in the film. The results of in-plane polarization measurements are examined in the context of this model and the measured hysteresis loops are effectively reproduced using the model.

5.1.1 Model of domain structure dependence of in-plane polarization

A model is developed for the simulation of the in-plane electronic polarization of polydomain ferroelectric thin films. The model predicts that the in-plane remnant polarization is proportional to the a-domain volume fraction. In contrast the dielectric contributions to the polarization are predicted by the model to be inversely proportional to the a-domain volume fraction. The most common approach to measuring the change in the polarization is to measure the current flowing into the "plates" of a capacitor. Integrating the current with respect to time yields a change in the differential charge δQ on the plates of the capacitor. Dividing the change in charge δQ by the plate area A yields the change in polarization δP as given by[76,78]

$$\frac{1}{A}\int_0^t i(t)\delta t = \frac{\delta Q}{A} = \delta P \Leftrightarrow \frac{\delta P}{\delta t}(t) = \frac{i(t)}{A} \tag{5-1}$$

In measurements of the electronic polarization, the total differential charge in equation (5-1) come from a number of distinct sources as given in equation (5-2). These include contributions due to ferroelectric switching, dielectric contributions, finite leakage current, and the parasitic capacitance of the measurement system itself[69,76].

$$\delta Q_{total} = \delta Q_{ferro} + \delta Q_{diel} + \delta Q_{leak} + \delta Q_{para} \tag{5-2}$$

All of these sources of differential charge must be accounted for. Most ferroelectric testers including the Radiant RT6000 include automated routines for determining and removing the contributions due to leakage and parasitic capacitance. As such consideration is here limited to the contributions due to ferroelectric switching and dielectric contributions.

The dielectric contributions to the total polarization are given by[78]

$$\frac{\delta Q_{diel}}{A} = \delta P_{diel} = \varepsilon_{\circ}\chi E \tag{5-3}$$

where the electronic susceptibility χ is related to the relative permittivity by $\varepsilon = 1 + \chi$ [79]. In an anisotropic material such as $BaTiO_3$ equation (5-3) is written in Einstein notation as

$$P_{i_{diel}} = \varepsilon_{\circ}\chi_{ij}E_j \tag{5-4}$$

For the single domain variant of $BaTiO_3$ shown in Figure 5-1a, equation (5-4) takes the form

$$P_{1_{diel}} = \varepsilon_{\circ}\chi_a E_1 \quad P_{2_{diel}} = \varepsilon_{\circ}\chi_a E_2 \quad P_{3_{diel}} = \varepsilon_{\circ}\chi_c E_3 \tag{5-5}$$

where the values of the susceptibility are given by[56]

$$\chi_a = (\varepsilon_a - 1) \qquad \chi_c = (\varepsilon_c - 1) \tag{5-6}$$

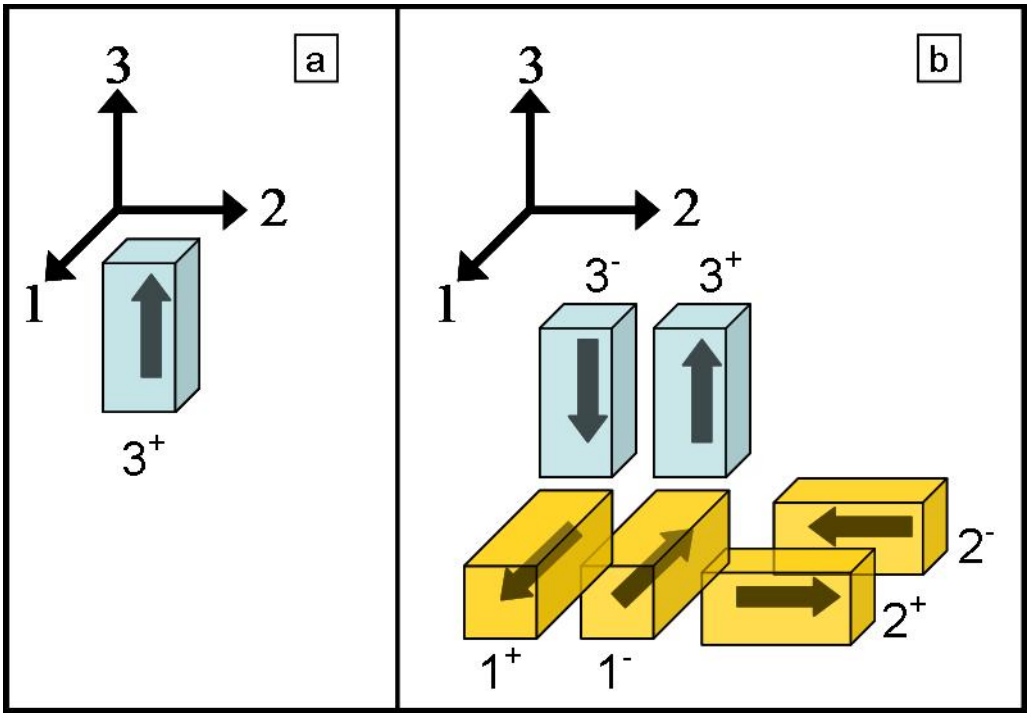

Figure 5-1. a) The c-up domain with is polar axis pointing out of the plane of the film is shown along with the associated coordinate system. The coordinate system of this domain variant serves as the reference coordinate system in which the polarization contributions from all six of the domain variants (shown in (b)) are reported. In (b) the c-domains are shown in blue and the a-domains are shown in gold.

However in a polydomain tetragonal $BaTiO_3$ thin film at room temperature there are six distinct domain variants in the film as seen in Figure 5-1b. The expression for the dielectric contributions to the electronic polarization is derived in Appendix **I** and is given by

$$\begin{aligned} P_{1_{diel}}(E) &= E_1\varepsilon_\circ\left\{\chi_c\left[A_{1+}(E)+A_{1-}(E)\right]+\chi_a\left[A_{2+}(E)+A_{2-}(E)+A_{3+}(E)+A_{3-}(E)\right]\right\} \\ P_{2_{diel}}(E) &= E_2\varepsilon_\circ\left\{\chi_c\left[A_{2+}(E)+A_{2-}(E)\right]+\chi_a\left[A_{1+}(E)+A_{1-}(E)+A_{3+}(E)+A_{3-}(E)\right]\right\} \\ P_{3_{diel}}(E) &= E_3\varepsilon_\circ\left\{\chi_c\left[A_{3+}(E)+A_{3-}(E)\right]+\chi_a\left[A_{1+}(E)+A_{1-}(E)+A_{2+}(E)+A_{2-}(E)\right]\right\} \end{aligned} \tag{5-7}$$

where $A_{i\pm}(E)$ are the field-dependent volume fractions of the different domain variants shown in Figure 5-1b and $\sum_1^3 A_{i\pm}=1$. From inspection of equation (5-5) it is apparent that the term in the brackets in equation (5-7) represents the effective electronic susceptibility of the polydomain film. Due to 90° domain flipping in the film, $\delta A_{i+}=\delta A_{i-}$ does not necessarily hold and a more general relation of the differential domain volume fractions is given by

$$\delta A_{i+}(\delta E) = -\delta A_{i-}(\delta E) - \sum \delta A_{(j\neq i\rightarrow i+)\pm}(\delta E) \tag{5-8}$$

where the summation represents the contribution to $\delta A^{i+}(\delta E)$ due to 90° domain flipping. From equation (5-7) the dielectric polarization along an in-plane <100> direction in terms of the a-domain volume fraction (A_a) is given by

$$P_{diel<100>}(E) = \varepsilon_\circ E\left[\frac{A_a}{2}(\chi_c - \chi_a) + \chi_a\right] \tag{5-9}$$

It is assumed in equation (5-9) that the volume fraction of 90° a-domain variants is equal due to the symmetry imposed by the cubic substrate[11]. The in-plane directional dependence due to the two 90° a-domain variants and the c-domain variants (a_1,a_2,c) is given by

$$\begin{aligned} P_{diel}(\theta,E) &= P_{diel(a1)} + P_{diel(a2)} + P_{diel(c)} \\ &= \frac{A_a}{2}\varepsilon_\circ\left\{\left(E\cos(\theta)\right)\left(\chi_c\cos(\theta)\right) + \left(E\sin(\theta)\right)\left(\chi_a\sin(\theta)\right)\right\} \\ &+ \frac{A_a}{2}\varepsilon_\circ\left\{\left(E\sin(\theta)\right)\left(\chi_c\sin(\theta)\right) + \left(E\cos(\theta)\right)\left(\chi_a\cos(\theta)\right)\right\} \\ &+ \varepsilon_\circ E(1-A_a)\chi_a \\ &= \varepsilon_\circ E\left[\frac{A_a}{2}(\chi_c - \chi_a) + \chi_a\right] \end{aligned} \tag{5-10}$$

where θ is the angle between the in-plane field direction and the x-axis (**1**-axis in Figure 5-1). After collecting terms and simplifying the last expression in (5-10) is equivalent to (5-9), indicating that the dielectric polarization is independent of the in-plane field direction.

The contribution to the total polarization due to domain switching in the polydomain $BaTiO_3$ thin films is by definition given by[64]

$$\begin{aligned} P_{1_{ferro}}(E) &= P_s\left[A_{1+}(E) - A_{1-}(E)\right] \\ P_{2_{ferro}}(E) &= P_s\left[A_{2+}(E) - A_{2-}(E)\right] \\ P_{3_{ferro}}(E) &= P_s\left[A_{3+}(E) - A_{3-}(E)\right] \end{aligned} \tag{5-11}$$

with reference to the coordinate system in Figure 5-1. In equation (5-11), P_s is the spontaneous polarization of the individual domains. In a strain-free film P_s is expected to equal the single domain bulk

[11] The results of phase field models of thin film ferroelectric domain structures on cubic substrates by Li et al. have shown this to be a reasonable assumption[189] Y. L. Li, S. Y. Hu, Z. K. Liu, and L. Q. Chen, "Effect of substrate constraint on the stability and evolution of ferroelectric domain structures in thin films," Acta Mater. **50** (2), 395-411 (2002).

value of the spontaneous polarization of $BaTiO_3$ of 26 μC/cm^2. Due to the strain state in the thin film, P_s is however likely to differ from the bulk value. Again assuming equal 90^o a-domain volume fractions, from equation (5-11) the ferroelectric polarization along an in-plane <100> direction can be expressed in terms of the a-domain fraction (A_a) as

$$P_{ferro<100>} = P_s \frac{A_a}{2} \Delta A_{ij}(E) \tag{5-12}$$

where $\Delta A_{ij}(E)$ is the relative volume fractions of the 180^o a-domain variants given by

$$\Delta A_{\pm i}(E) = \left[\left(A_{+i} - A_{-i} \right)(E) \right] \Big/ \left(A_{+i} + A_{-i} \right) \tag{5-13}$$

where A_i is the volume fraction of the ith domain variant. The form of $\Delta A_{ij}(E)$ is determined by the distribution of coercivities in the sample. The simplest probability density function (PDF) to describe the system is a Dirac delta function for which all of the domains are assumed to switch at a single value of the applied field. In this case the associated cumulative distribution function (CDF) is the Heaviside step function. A distribution of coercivities with a finite width is however more realistic. In a prior model due to Evans the distribution of coercivities was modeled as a Gaussian distribution[75]. No physical significance was ascribed to the use of a Gaussian distribution. Probability density functions employed here will be limited to those defined on the semi-infinite interval [0,∞] in order to preclude back switching in the model. As will be shown, this restriction yields a model that predicts the upper limit of the remnant polarization as a function of the a-domain volume fraction in the film. In order to model polarization loops with appreciable back switching the model could be extended by the use of coercivity PDFs supported on the whole set of Reals [-∞,∞]. Here a Weibull distribution will be employed initially. Figure 5-2 shows both a delta function and a Weibull PDF and their associated CDFs. The general expressions for the Weibull PDF and CDF are given by[141]

$$\begin{aligned} PDF_{Weibull} &= f(x;\alpha,\beta) = \frac{\alpha}{\beta^\alpha} x^{\alpha-1} \exp\left[-\left(x \big/ \beta \right)^\alpha \right] \\ CDF_{Weibull} &= F(x;\alpha,\beta) = 1 - \exp\left[-\left(x \big/ \beta \right)^\alpha \right] \end{aligned} \tag{5-14}$$

where β is a scale parameter and α is a shape parameter. In Figure 5-2 the assumed parameters of the Weibull distribution are $(\alpha,\beta)=(2.2,0.92)$.

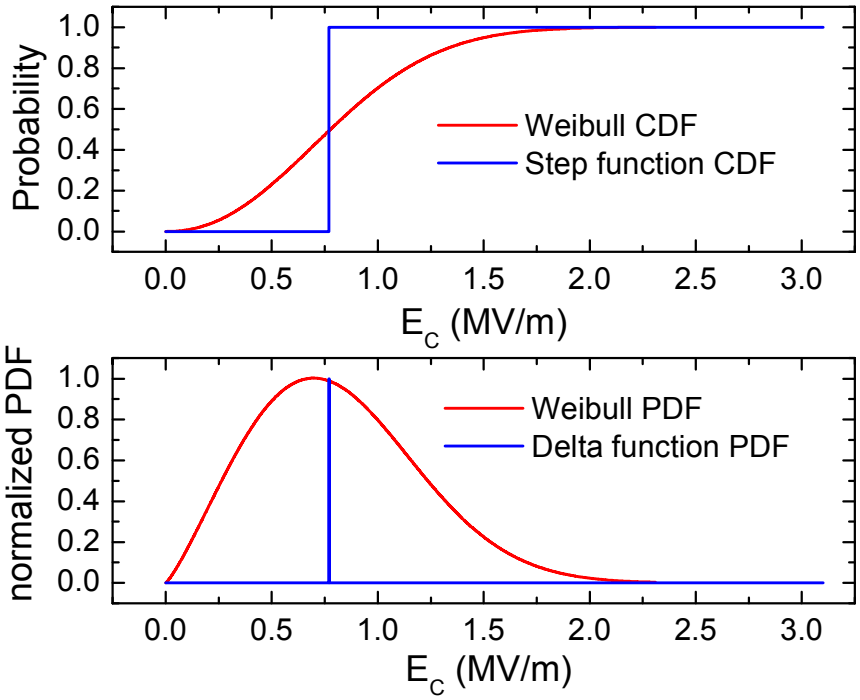

Figure 5-2. Two different theoretical coercivity distributions are shown. A Dirac delta function distribution and a Weibull distribution. Both CDFs and PDFs are shown.

For these two theoretical coercivity distributions, the resulting hysteretic contributions to the polarization due to domain switching determined from equation (5-12) are shown in Figure 5-3. The assumed a-domain fraction (A_a) and spontaneous polarization (P_s) were 0.17 and 26 μC/cm^2, respectively. Significant points on the theoretical hysteresis loops are labeled. The portion of the polarization loop due to domain switching between these labeled points is given by equation (5-12) after substituting the appropriate from of $\Delta A_{ij}(E)$. The resulting expressions used to generate the loop in Figure 5-3 are given by

$$
\begin{aligned}
1 \rightarrow 2 \; & P_{ferro}(E) = P_s \frac{A_a}{2}\left[F(E)\right] \\
2 \rightarrow 3 \; & P_{ferro}(E) = P_s \frac{A_a}{2}\left[F(E_{\max})\right] \\
3 \rightarrow 4 \; & P_{ferro}(E) = P_s \frac{A_a}{2}\left[F(E_{\max}) - 2F(-E)\right] \\
4 \rightarrow 5 \; & P_{ferro}(E) = P_s \frac{A_a}{2}\left[-F(E_{\max})\right] \\
5 \rightarrow 1 \; & P_{ferro}(E) = P_s \frac{A_a}{2}\left[2F(E) - F(E_{\max})\right]
\end{aligned}
\tag{5-15}
$$

where $F(E)$ is the cumulative distribution function of the assumed distribution of coercivities. Regardless of the form of the assumed distribution of coercivities, at saturation $F(E)$ is by definition equal to 1. A simplifying assumption of the model represented by equation (5-15) is that no back switching occurs upon reducing the applied field to zero.

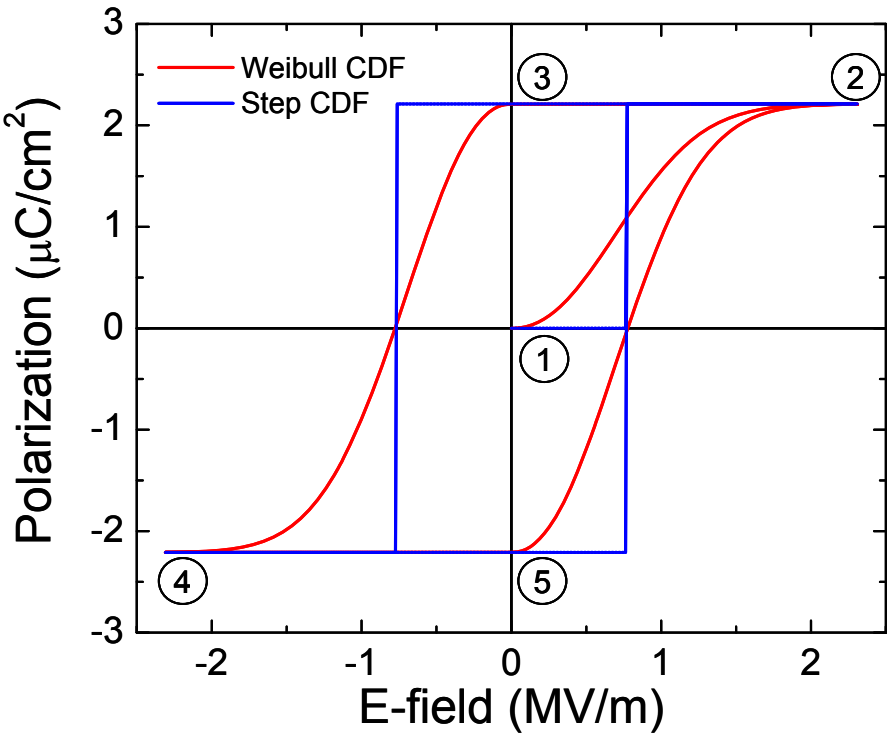

Figure 5-3. Theoretical polarization due to domain switching along an in-plane <100> direction. The polarization was determined using equation (5-15) after substituting a Weibull CDF (red) or a Heaviside CDF (blue).

The next step in the development of a general model of the in-plane polarization switching is the determination of the dependence of the polarization on the in-plane field direction. Equation (5-15) can be used when the applied field direction is along either of the in-plane <100> directions. For other field

directions, equation (5-15) can be used to determine the polarization along the particular in-plane <100> direction after substituting the component of the applied field in that direction. For an angle θ between the in-plane field direction and the x-axis (**1**-axis in Figure 5-1) the [100] and [010] components of the applied field are $E\cos(\theta)$ and $E\sin(\theta)$, respectively. Figure 5-4 shows the resulting [100] and [010] polarization from equation (5-15) for an angle θ of 30°. The Weibull CDF from Figure 5-2 was used in the evaluation of equation (5-15). The polarization in Figure 5-4 is plotted verses the component of the applied field along the corresponding <100> axis ($E_{[100]} = E\cos(\theta), E_{[010]} = E\sin(\theta)$). Figure 5-5 shows the resulting [100] and [010] polarization verses the applied field *E*. From Figure 5-5 it is apparent that the smaller component of the applied field along [010] results in a larger *apparent* coercive field for the [010] polarization.

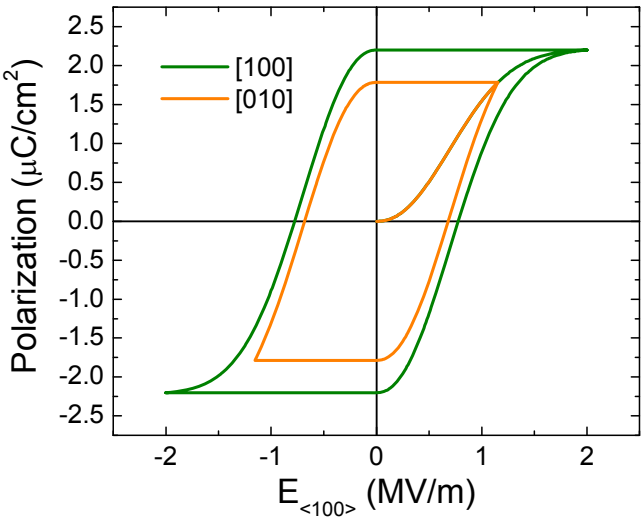

Figure 5-4. The theoretical [100] and [010] polarizations given by equation (5-15) for an in-plane field at 30° with respect to the [100] direction. The polarizations are plotted verses the components of the applied field along the corresponding axis.

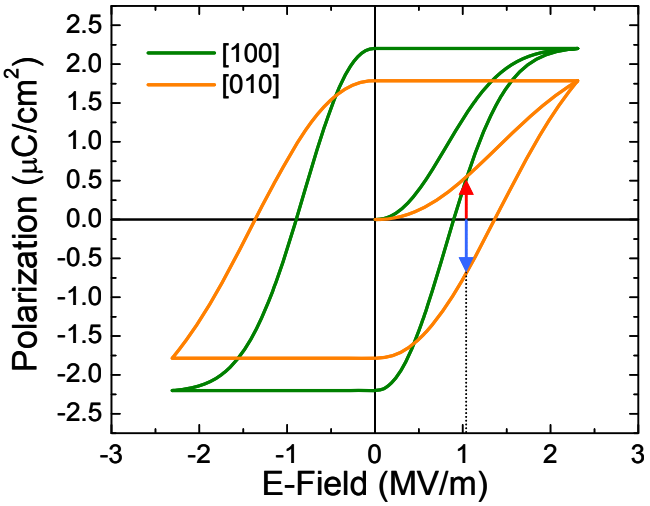

Figure 5-5. The theoretical [100] and [010] polarizations given by equation (5-15) for an in-plane field at 30° with respect to the [100] direction. The polarizations are plotted verses the applied field E.

Having determined the components of the polarization along the principle [100] and [010] axes the final step is the determination of the polarization parallel to the applied field direction. This is because the polarization is always *measured* along the direction of the applied field. From Figure 5-6 it is apparent that the polarization along the applied field direction is equal to the sum of the projections of the [100] and [010] polarizations onto a unit vector parallel to the applied $\bar{E}$. From inspection of Figure 5-6 the polarization parallel to the applied field is given by

$$P \,||\, E(\theta) = P_{[100]} \cos(\theta) + P_{[010]} \sin(\theta) \tag{5-16}$$

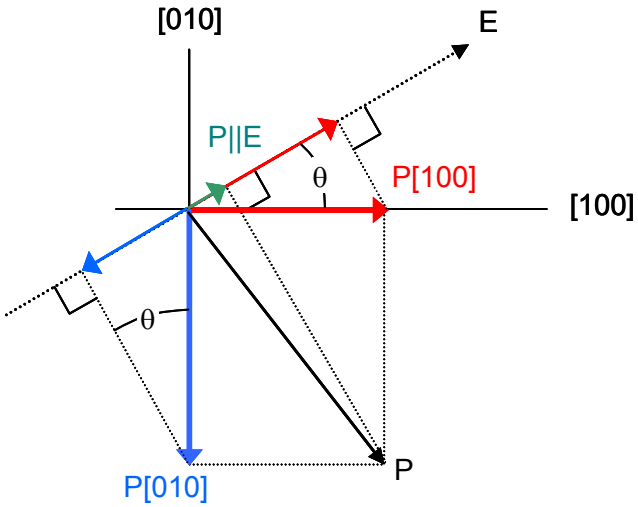

Figure 5-6. Schematic showing the relationship between the [100] and [010] polarization vectors and their components parallel to the applied field direction.

Figure 5-7a and b show the theoretical polarization for an angle θ of 30^o using the step and Weibull CDFs from Figure 5-2. The polarization hysteresis loops are generated by first evaluating equation (5-15) to find both $P_{[100]}$ and $P_{[010]}$. The results are then used in equation (5-16) to determine the theoretical polarization parallel to the applied field direction. In Figure 5-7a one sees the effect of the different apparent coercive fields on the resultant polarization loop. For θ equal to 0^o or 90^o the total polarization due to switching is determined solely by $P_{[100]}$ and $P_{[010]}$, respectively. For θ equal to 45^o the contributions from $P_{[100]}(E)$ and $P_{[010]}(E)$ are equivalent. However for all other θ angles $P_{[100]}(E)$ and $P_{[010]}(E)$ are distinct due to the different field magnitudes along the axes. For θ equal to 30^o, the smaller effective field along the [010] axis results in a larger apparent coercive field for the $P_{[010]}$ contribution.

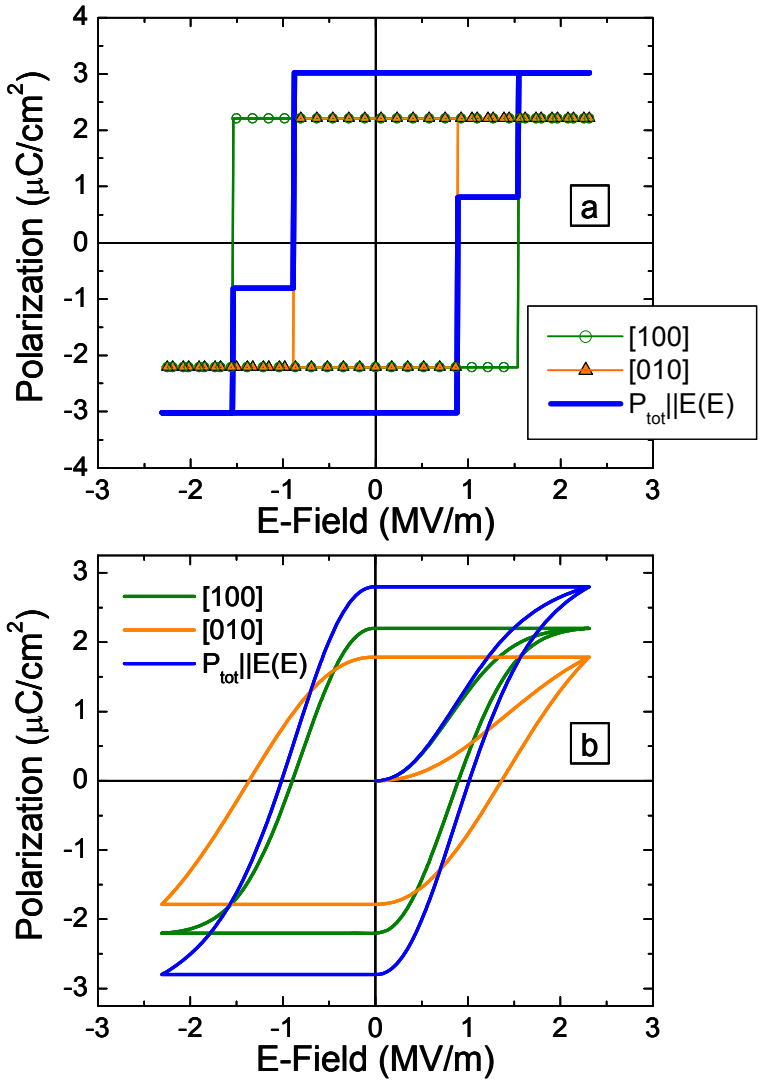

Figure 5-7. The theoretical polarizations for an applied in-plane field direction at 30° to the [100] axis. (a) show the result for a delta function distribution of coercivities from Figure 5-2 while (b) shows the result for the Weibull distribution of coercivities shown in Figure 5-2.

The directional dependence of the *magnitude* of the polarization due to domain switching depends upon the degree of saturation of $P_{[100]}$ and $P_{[010]}$. These in turn depend on the magnitude of the applied field and the width of the distribution of coercivities. Figure 5-8 show two Weibull distributions with parameters (α,β) equal to $(2.2,0.92)$ and $(8,0.92)$, respectively; the later corresponding to the narrower of the two distributions. Figure 5-9 and Figure 5-10 show the normalized in-plane directional

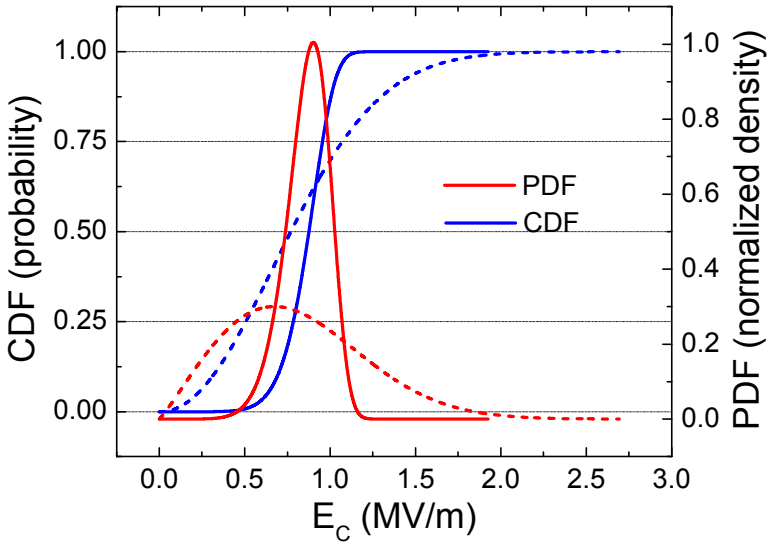

Figure 5-8. Two Weibull coercivity distributions are shown. The narrow distribution characterized by the solid lines corresponds to Weibull parameters of (8. 0.92). The wider distribution characterized by dashed lines corresponds to Weibull parameters of (2.2, 0.92)

dependence of the maximum polarization due to domain switching for the narrower and wider Weibull distributions from Figure 5-8, respectively. In each figure the maximum polarization is plotted for a range of maximum applied fields. General observations are as follows. When the maximum applied field is well below that required to saturate the polarization, polarization is maximized for applied fields along the <100> axes. As the magnitude of the maximum field increases the maximum polarization is realized for fields along in-plane <110> directions where appreciable contributions from both $P_{[100]}$ and $P_{[010]}$ are realized. For very large maximum applied fields the directional dependent polarization approaches a limit given by

$$P_{\max} \parallel E(\theta) = \frac{A_a}{2} P_s \left[\cos(\theta) + \sin(\theta)\right] \qquad (5\text{-}17).$$

Equation (5-17) is just equation (5-16) with $P_{[100]}$ and $P_{[010]}$ replaced by their saturation values of $P_s(A_a/2)$. Lastly it is apparent from Figure 5-9 and Figure 5-10 that a narrower distribution of coercivities accentuates the in-plane anisotropy of the polarization due to domain flipping.

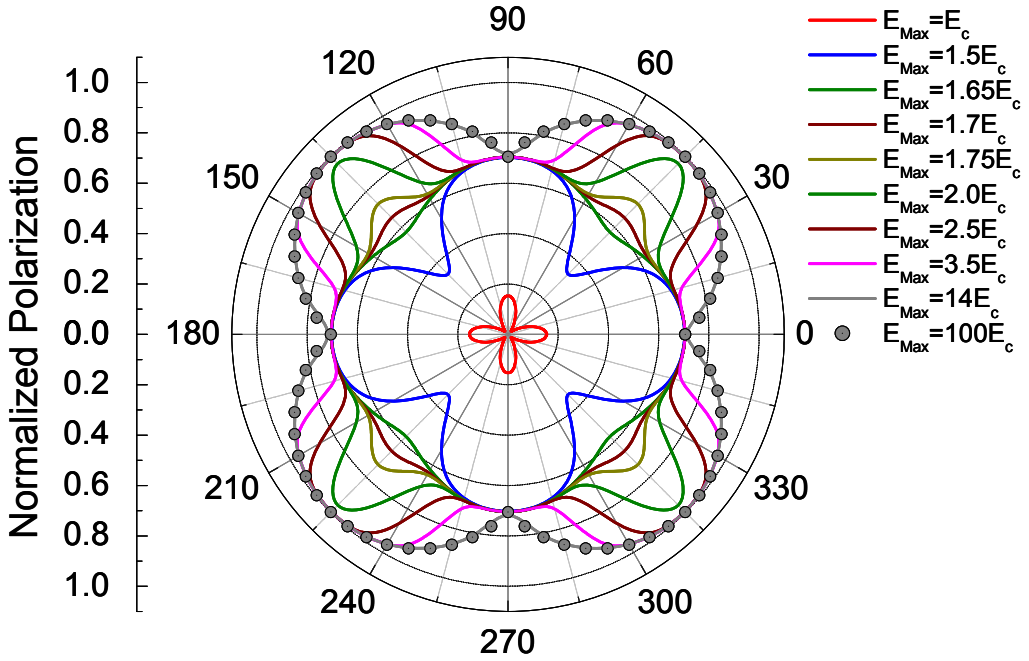

Figure 5-9. In-plane directional dependence of the maximum polarization due to domain flipping for a range of maximum applied fields. A Weibull distribution of coercivities with Weibull parameters (8, 0.92) is assumed (see Figure 5-8).

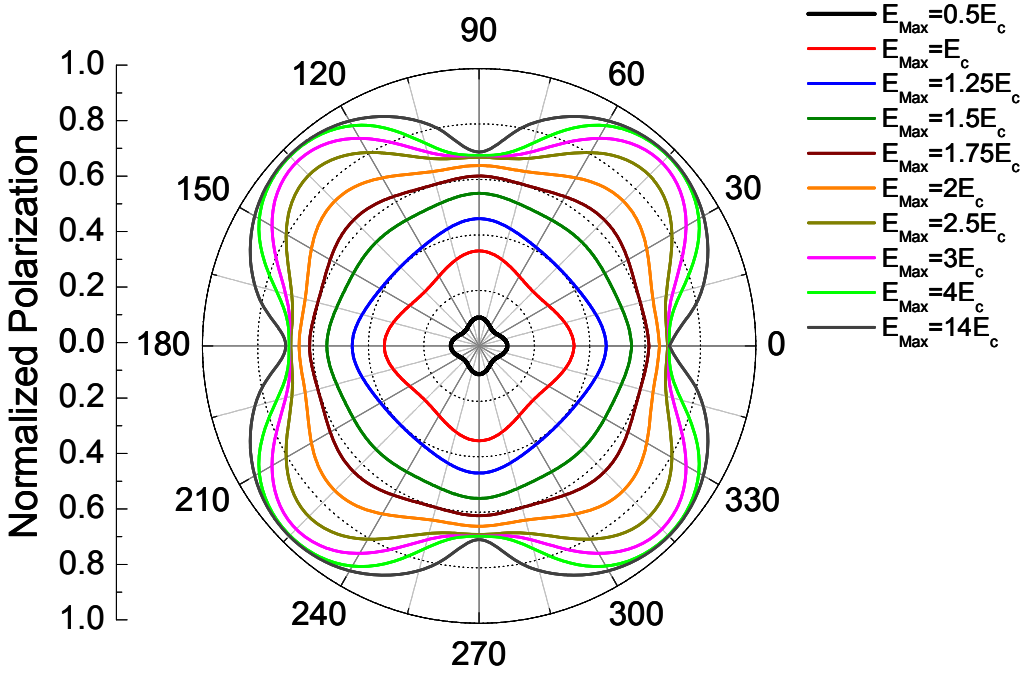

Figure 5-10. In-plane directional dependence of the maximum polarization due to domain flipping for a range of maximum applied fields. A Weibull distribution of coercivities with Weibull parameters (2.2, 0.92) is assumed (see Figure 5-8).

The total in-plane polarization is just the sum of the dielectric and ferroelectric contributions as given by

$$\begin{aligned} P1_{total}(E) &= P1_{diel}(E) + P1_{ferro}(E) \\ P2_{total}(E) &= P2_{diel}(E) + P2_{ferro}(E) \\ P3_{total}(E) &= P3_{diel}(E) + P3_{ferro}(E) \end{aligned} \tag{5-18}$$

where $P_{i_{diel}}(E)$ and $P_{i_{ferro}}(E)$ are given by equations (5-7) and (5-11) respectively. The total in-plane polarization expressed in terms of the a-domain volume fraction (A_a) is from equations (5-9) and (5-16) given by

$$\begin{aligned} P(E,\theta) = \varepsilon_o E\left[\frac{A_a}{2}\left(\chi_c - \chi_a\right) + \chi_a\right] \\ + P_{[100]}(E,\theta)\cos(\theta) \\ + P_{[010]}(E,\theta)\sin(\theta) \end{aligned} \tag{5-19}.$$

where $P_{[100]}(E,\theta) = P_{[100]}(E\cos(\theta))$ and $P_{[010]}(E,\theta) = P_{[010]}(E\sin(\theta))$. Both $P_{[100]}(E\cos(\theta))$ and $P_{[010]}(E\sin(\theta))$ are determined from equation (5-15). Recall from equation (5-15) that the in-plane polarization due to domain switching is proportional to the a-domain volume fraction A_a. In the following sections results of in-plane polarization measurements will be examined in the context of the model of the in-plane polarization in a polydomain thin film developed in this section.

As a demonstration of the efficacy of the model developed in the preceding paragraphs, the electronic polarization measured thin film $BaTiO_3$ sample DT443 is fit using equations (5-19), (5-16) and (5-15). Excellent fits to the measured polarization were realized using three different assumed coercivity distributions. The coercivity distributions employed included a Weibull distribution, a Gamma distribution and a distribution based on the measured normalized capacitance given by $(dP/dV)(E)$. Figure 5-11 shows the PDF and CDF for each of the three distributions. The rate of change of the polarization at any applied voltage (or field) is assumed to be proportional to the volume fraction of the film characterized by coercivities at that voltage or field. As such $(dP/dV)(E)$ represents a measured distribution of coercivities. The measured $(dP/dV)(E)$ was empirically fit as the sum of three Lorentzian distributions as given by

$$f = y_{\circ} + \sum_{i=1}^{3}\left[\frac{2A_i}{\pi}\frac{\omega_i}{4\left(E-E_{Ci}\right)^2+\omega_i^2}\right] \tag{5-20}$$

The form of the CDF was determined by taking the Riemann sum of this fit to $(dP/dV)(E)$. The trapezoid rule was employed whereby the average of the endpoints of each interval is used in the Riemann sum as given by[190]

$$\int_0^E dP/dV(E)dx \approx \sum_{i=1}^{n}(E_i - E_{i-1})\cdot\left(P(E_i)+P(E_{i-1})\right)/2 \tag{5-21}$$

The result from equation (5-21) normalized to 1 gives the final form of the CDF shown in the two graphs at right in Figure 5-11. The final form of the PDF shown in the upper right graph in Figure 5-11 is obtained by dividing $(dP/dV)(E)$ by the full integrated area of $(dP/dV)(E)$. The equations for the gamma distributions are given by[141]

$$\begin{aligned} PDF &= f(x;\alpha,\beta) = \frac{1}{\beta^{\alpha}\Gamma(\alpha)}x^{\alpha-1}\exp\left(-\tfrac{x}{\beta}\right) \\ CDF &= F(x;\alpha,\beta) = \frac{\gamma\left(\alpha, x/\beta\right)}{\Gamma(\alpha)} = \frac{\int_0^{x/\beta} t^{\alpha-1}\exp(-t)dt}{\int_0^{\infty} t^{\alpha-1}\exp(-t)dt} \end{aligned} \tag{5-22}$$

where $\Gamma(\alpha)$ is the complete gamma function given by the denominator on the right hand side of the lower expression and $\gamma(\alpha, x/\beta)$ is the lower incomplete gamma function given by the numerator on the right hand side of the lower expression.

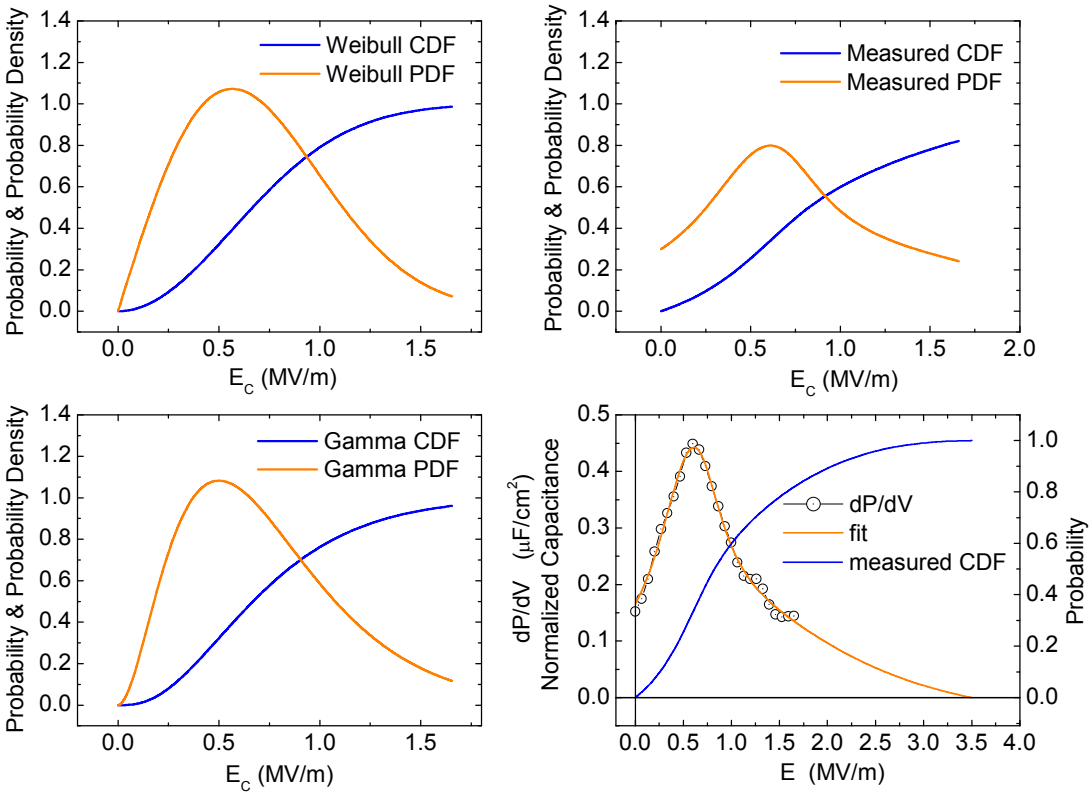

Figure 5-11. The three coercivity distributions used to model the electronic polarization of sample DT443 are shown. The distribution parameters for the Weibull and gamma distributions are given in Table 5-1 below. The lower right figure shows the measured dP/dV and the corresponding fit from which both PDF and CDF were calculated.

Figure 5-12 shows the resulting fits to the measured electronic polarization of sample DT443 using the coercivity distributions from Figure 5-11 in equation(5-15). The ferroelectric and dielectric contributions are both plotted as is their sum yielding the total polarization from equation (5-19). The fitting parameters including the assumed a-domain volume fraction, spontaneous polarization values and dielectric constants are given in Table 5-1. Based on the three fits the a-domain volume fraction is predicted to be between 0.16 to 0.21. That all three fits yield similar predictions for the a-domain fraction is an indication of the efficacy of the model. It should be noted that this range of predicted a-domain volume fractions is predicated on the assumption that the spontaneous polarization is equivalent to the bulk $BaTiO_3$ value of 26 $\mu C/cm^2$. For a lower spontaneous polarization a higher a-domain fraction would be predicted. From Table 5-1 one sees that the ε_a dielectric constant predicted from the model is between 2600 and 3000 with an effective dielectric constant of 2400.

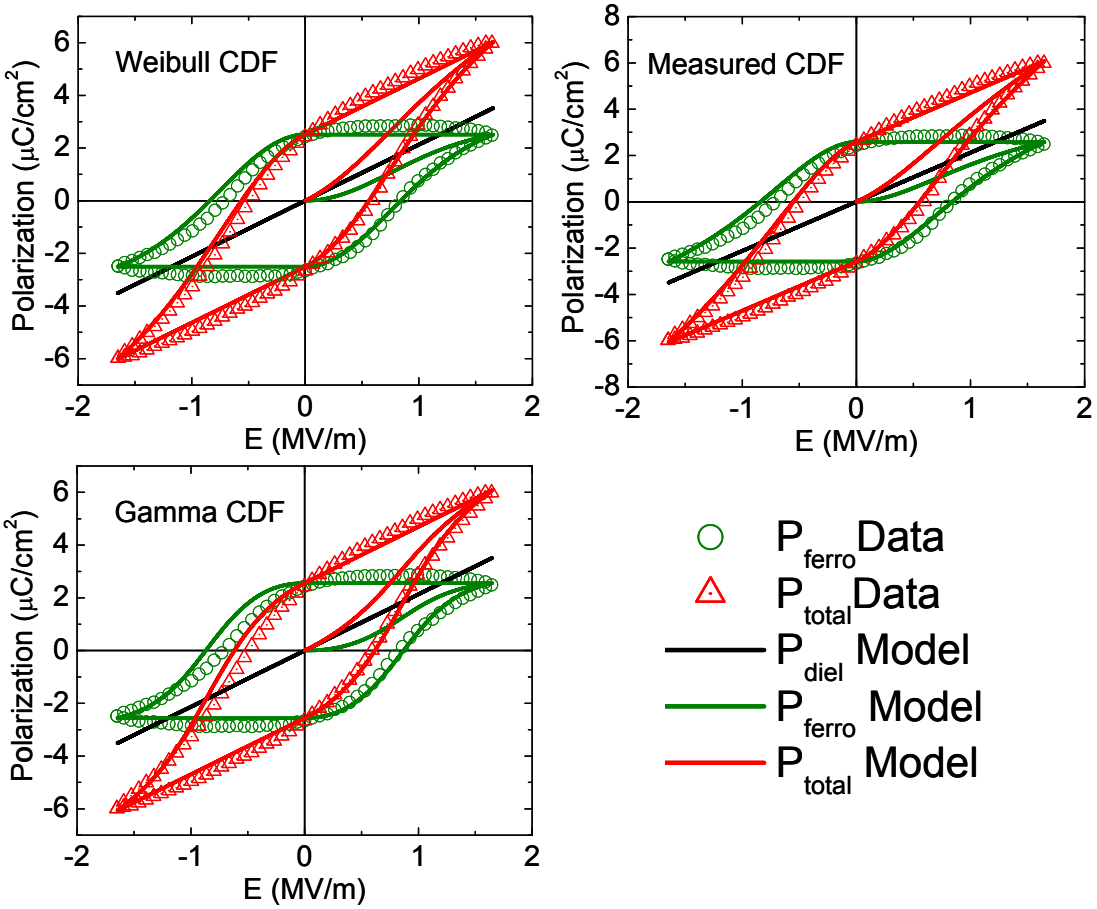

Figure 5-12. Fits to the measured polarization of sample DT443 were made using the thin-film polarization model given by equations (5-19), (5-16) and (5-15). Fits were made using the three different coercivity distributions from Figure 5-11.

Table 5-1. Fitting parameters for polydomain thin-film polarization fitting model

Dist.	ε_a	ε_c	ε_{eff}	P_s ($\mu C/cm^2$)	A_a	Distribution Parameters	
						α	β
Weibull	2600	130	2400	26	0.16	2	0.8
gamma	2800	130	2400	26	0.17	3	0.25
measured (dP/dV)	3000	130	2400	26	0.21	—	—

5.1.2 In-plane polarization along <100> and <110> directions

In order to characterize the domain switching characteristics in the polydomain $BaTiO_3$ thin films, in-plane electronic polarization measurements were made on over twenty samples with the in-plane electric field directed along either a <100> or a <110> direction. No directional dependence of the electronic polarization was observed. Figure 5-13 shows representative in-plane electronic polarization hysteresis loops measured on the polydomain $BaTiO_3$ thin films on MgO(100) substrates. Details of the device structure and electronic polarization measurement technique are given in Section 3.4 and 3.5 respectively. In Figure 5-13, three hysteresis loops are shown for samples with in-plane fields along a <110> direction and three loops are shown for samples with in-plane fields along a <100> direction. The larger applied fields for sample AM018 are due to the smaller 5 μm gap between the coplanar strip electrodes of sample AM018 as compared to gaps of 10 to 12 μm in the other samples. The maximum applied voltage of ±19.9 V was the same for all films measured and represents the limit of the RT6000S tester. Note that the polarization axis is rendered in the same scale for all of the hysteresis loops in Figure 5-13, and with the exception of AM018 the E-field axis is rendered in the same scale for all of the hysteresis loops.

The measured in-plane polarization at the maximum applied field (P_{max}) exhibited no dependence on the direction of the in-plane electric field. Figure 5-14 shows box and scatter plots of the maximum polarization (P_{max}) measured under a maximum applied voltage of ±19.9 V for both <110> and <100> directed in-plane electric fields. As seen in the summary statistics provided to the right of the plots, the median P_{max} for <110> and <100> oriented fields are effectively equivalent at ~10 $\mu C/cm^2$. In addition two-sample t-Tests find that with 95% confidence, the difference in the mean P_{max} for the <110> and <100> populations is less than 0.7 and 1 $\mu C/cm^2$ under the assumptions of equal and unequal population variance, respectively. Much of the variation in the P_{max} values is due to differences in the magnitude of the dielectric contributions due to variations in the electrode gaps in the various samples and therefore in the maximum applied fields. Typical a-domain fractions in the polydomain $BaTiO_3$ thin films are given

by Towner[36] as 0.28±0.08. From equation (5-9) it is apparent that the dielectric contribution to the polarization is inversely proportional to the a-domain volume fraction. As such, for the relatively low a-domain volume fractions in the films, a large field dependent dielectric contribution to the polarization is expected. Table 5-2 summarizes the electronic polarization parameters for all samples measured[12].

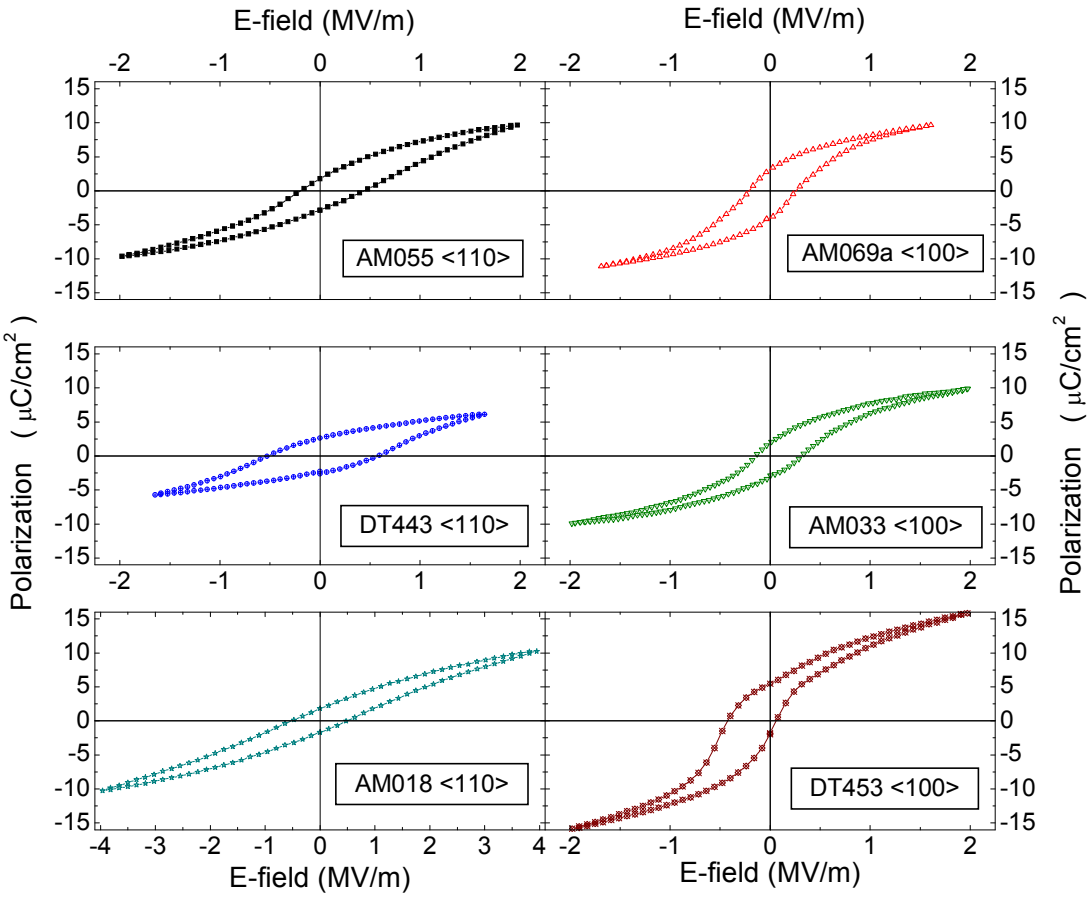

Figure 5-13. Electronic polarization hysteresis loops measured in the plane of the films using coplanar strip electrodes.

From both a qualitative graphic analysis as well as a statistical analysis of the polarization data in Table 5-2 no dependencies of any of the hysteresis loop parameters on the orientation of the in-plane field were observed. This includes the coercive fields, the remnant polarization and the polarization at maximum applied field. The observed asymmetry and horizontal shifts seen for some of the samples in

[12] In Table 5-2, the samples for which only P_{max} and the average coercive field are given were measured and tabulated by Pingsheng Tang and the remaining hysteresis loop parameters are unavailable.

Figure 5-13 and likewise reflected in differences in the positive and negative coercive fields and remnant polarizations reported in Table 5-2 have been widely attributed to internal fields within the samples.[191-194]

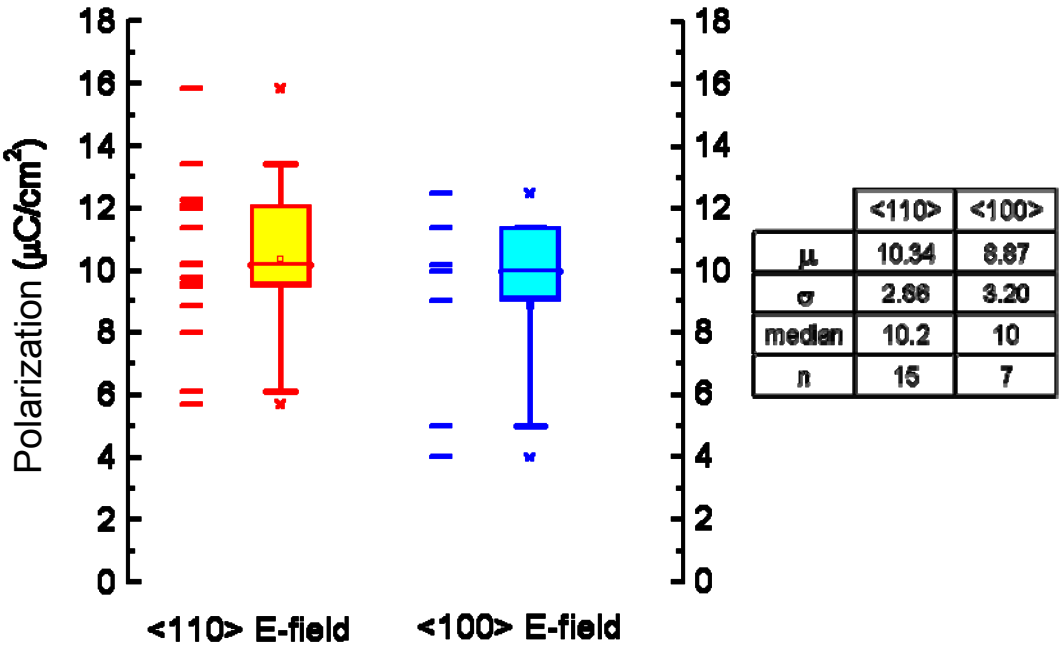

Figure 5-14. Box and scatter plots of the measured maximum polarization under a maximum applied voltage of 19.9 V. Summary statistics are provided to the right of the plots.

The average measured in-plane remnant polarization in the polydomain thin films was significantly less than that of a single-domain bulk $BaTiO_3$ sample but consistent with the theoretically predicted value from equation (5-15) based on the a-domain fractions observed in our films. The average remnant polarization in the polydomain $BaTiO_3$ thin films was 2.7 $\mu C/cm^2$ as compared to the bulk $BaTiO_3$ value of ~26 $\mu C/cm^2$. The reader should recall that in a single domain bulk ferroelectric sample in which complete switching occurs the remnant polarization and saturation polarization are approximately equivalent as seen in the hysteresis loop in Figure 5-15 taken from Wieder[195]. In the absence of non-remnant ferroelectric contributions to the polarization the non-remnant component consists solely of the dielectric contributions which define the slope of the hysteresis loop in the saturation region. Extrapolation back to the polarization axis along this line as shown in Figure 5-15

defines the saturation polarization[196]. As such the saturation polarization predicted by equation (5-15) and (5-17) represent a theoretical upper limit for the remnant polarization based on the a-domain fraction in the thin film. Equation (5-17) predicts a remnant polarization of $P_s(A_a/2)\left[\cos(\theta)+\sin(\theta)\right]$ where θ is the angle between the in-plane <100> x-axis and the in-plane field direction as shown in Figure 5-6. Assuming a bulk value for the spontaneous polarization of 26 μC/cm^2, for a-domain volume fractions of 0.28±0.08 equation (5-17) gives a range for the upper limit of the remnant polarizations of between 2.6 and 4.7 μC/cm^2 along a <100> axis. Again from equation (5-17) one sees that along an in-plane <110> direction ($\theta = 45^\circ$) this result is simply multiplied by ~1.4 giving an upper limit on the remnant polarization of between 3.7 and 6.6 μC/cm^2. It should be emphasized that these represents an *upper* limits on the remnant polarization under the assumption of complete saturation of the polarization with no back switching. When the maximum applied field does not completely saturate the polarization, the measured remnant polarization will be less than these theoretical upper limits. Back switching will likewise result in lower remnant polarizations. An additional observation from Figure 5-9 and Figure 5-10 is that when the polarization is less than the saturated value, the in-plane anisotropy of the polarization can be markedly reduced. This could explain the absence of in-plane anisotropy in the measured polarization of the polydomain $BaTiO_3$ thin films. The theoretical range for the upper limit on the remnant polarization is in excellent agreement with the both the range and average value of the remnant polarization measured in our films as seen from Table 5-2. The average remnant polarization of 2.7 μC/cm^2 measured in the films is slightly higher than the average value previously measured by Hoerman[12] of 1.4 μC/cm^2 and is fairly consistent with that predicted from electro-optic measurements by Nystrom[37] of 2 μC/cm^2 under a maximum applied field of 2.5 MV/m. Remnant polarization values for $BaTiO_3$ thin films in this range have likewise been reported by others (2.2 μC/cm^2 [197], 4 μC/cm^2 [198]).

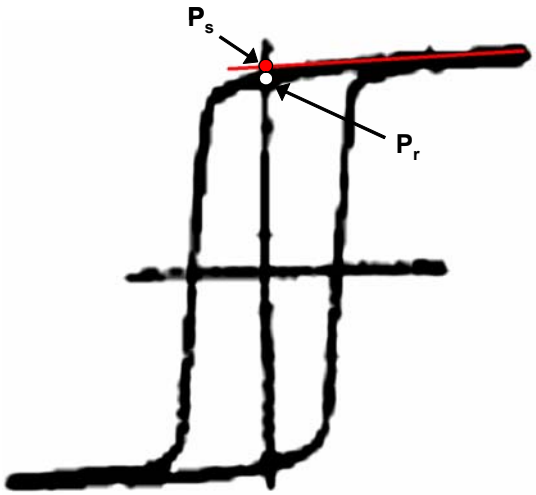

Figure 5-15. Electronic polarization hysteresis loop of bulk $BaTiO_3$ crystal taken from Wieder[195] shows that when full remnant switching occurs the remnant polarization is approximately the same as the saturation polarization of 26 $\mu C/cm^2$.

Table 5-2. Tabulated electronic polarization hysteresis parameters for all samples measured

	($\mu C/cm^2$)					(MV/m)					
Sample ID	P_{rem} -	P_{rem} +	P_{rem} avg	ΔP_{rem}	P_{max}	E_c-	E_c+	E_c avg	ΔE_c	orient.	n
AM003					10.2			0.69		100	1
AM033	3.2	2.1	2.7	-1.1	9.8	0.15	0.33	0.24	0.17	100	2
AM047					11.4					100	3
AM069a	4.0	3.2	3.6	-0.7	9.7	0.21	0.26	0.23	0.05	100	4
DT394					9.0			0.90		100	5
DT438					12.5			0.30		100	6
DT444					5.0					100	7
DT453	2.0	5.5	3.7	3.5	16.0	0.42	0.07	0.24	-0.35	100	8
DT454					4.0					100	9
AM008					12.3			0.73		110	10
AM009					12.1					110	11
AM016	3.0	3.2	3.1	0.2	8.9	0.47	0.73	0.60	0.26	110	12
AM018	1.7	2.0	1.9	0.3	10.3	0.59	0.48	0.53	-0.10	110	13
AM034					9.8					110	14
AM039	2.7	2.6	2.7	-0.1	5.8	0.66	0.73	0.69	0.07	110	15
AM055	2.8	1.8	2.3	-1.0	9.7	0.22	0.43	0.32	0.20	110	16
DT436					12.0			0.60		110	17
DT443	2.3	2.6	2.4	0.4	6.2	0.52	0.57	0.55	0.05	110	18
DT446					10.2			0.47		110	19
DT451					9.5			0.40		110	20
HR24a	3.0	2.9	3.0	-0.1	11.7	0.65	0.79	0.72	0.14	110	21
HR24b	1.7	1.6	1.6	-0.1	8.1	0.65	0.77	0.71	0.12	110	22
average	2.6	2.7	2.7	0.1	9.7	0.45	0.52	0.53	0.06		
bulk			**26.0**	0.0				**0.10**	0.00		

The coercive fields of the polydomain $BaTiO_3$ thin films effect the poling properties of the films and therefore the coercive fields in the polydomain $BaTiO_3$ thin films were likewise examined. The observed coercive fields in our $BaTiO_3$ thin films are significantly larger than those observed in bulk $BaTiO_3$ samples. This is consistent with previously reported results on ferroelectric thin films reported in the literature[197-200] as well as previous measurements on our films[12] The average and median coercive fields of the measured films are 0.53 and 0.55 MV/m, respectively. This is slightly less than the average coercive field previously measured by Hoerman[12] in polydomain $BaTiO_3$ thin films of 0.7 MV/m and slightly greater than the average coercive field from second harmonic generation hysteresis loops of 0.3 MV/m measured by Towner in polydomain $BaTiO_3$ thin films[36]. In general coercive fields measured in

thin films are higher than the bulk $BaTiO_3$ values of 0.1 to 0.24 MV/m [103,201]. In the case of coherent or only partially relaxed film that are highly strained, coercive fields ranging from 2.5 to 15 MV/m have been reported in $BaTiO_3$ thin films[197-200]. In our films, the in-plane strains are modest (~0.1 – 0.2%)[202] and as a result the increase in the coercive field is less dramatic than that for highly strained films.

5.1.3 Analysis of remnant and non-remnant contributions to the polarization

By measuring both the full hysteresis loop as well as the two non-switching half-loops one is able to distinguish and analyze the remnant and non remnant components of to the electronic polarization[69,74,80]. The drive profiles employed to measure the full hysteresis loop as well as the two non-switching half-loops are discussed in Section 3.5. An example along with the resulting polarization is shown in Figure 5-16. In Figure 5-16 the polarization associated with the full hysteresis loop as well as that of the two non-switching half-loops can be seen from the associated portions of the drive profile referred to in the legend of Figure 5-16. The non-switching half-loops reflect both the non-remnant ferroelectric contributions to the polarization as well as the dielectric contributions which are inherently non-remnant. The non-switching half-loops are measured immediately after a preset drive profile that is identical to that of the non-switching half-loop itself. As such the change in polarization during the non-switching half-loops reflects only non-remnant contributions to the polarization. Because the non-switching half-loops are measured immediately after a preset drive profile that is identical to that of the non-switching half-loop itself, the raw non-switching half-loops are biased by the remnant polarization as seen in Figure 5-17. The full-loop remnant polarization is subtracted from the raw non-switching half-loops to yield the true non-switching half-loops shown in Figure 5-18. Similar remnant and non-remnant hysteresis loops have been reported for PZT memory cell capacitors by Jung et al. as seen in Figure 5-19.

The remnant hysteresis loop is determined by subtracting the non-switching polarization half-loops from the full hysteresis loop as seen in Figure 5-17 and Figure 5-18. The resulting remnant loop therefore reflects only the remnant contributions to the measured polarization and as seen in Figure 5-16,

it is in fact fairly stable upon removal of the applied field, showing no discernable decay in the final 17ms with no applied field.

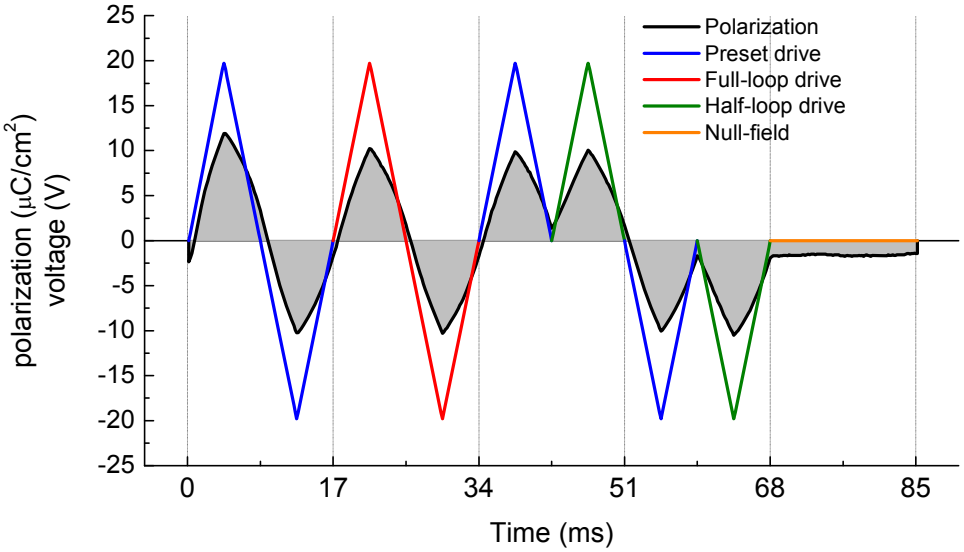

Figure 5-16. The drive profile used to determine the remnant and non-remnant components of the polarization is shown along with a typical example of the resulting polarization measured (sample HR24a).

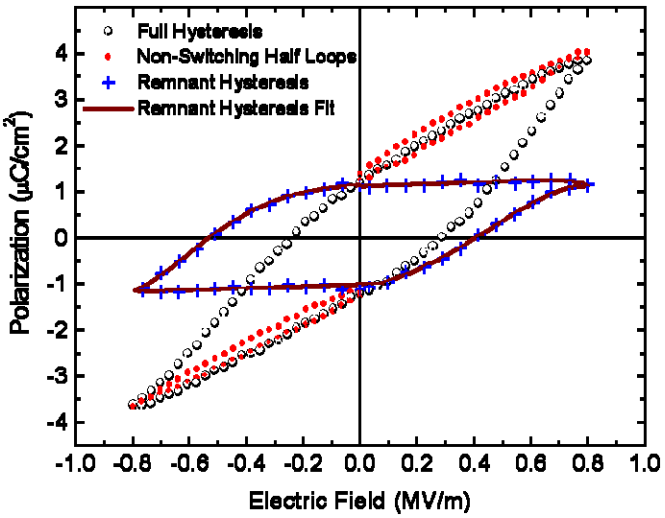

Figure 5-17. The measured full hysteresis loop and the two non-switching half-loops are used to determine the remnant polarization loop (sample DT443).

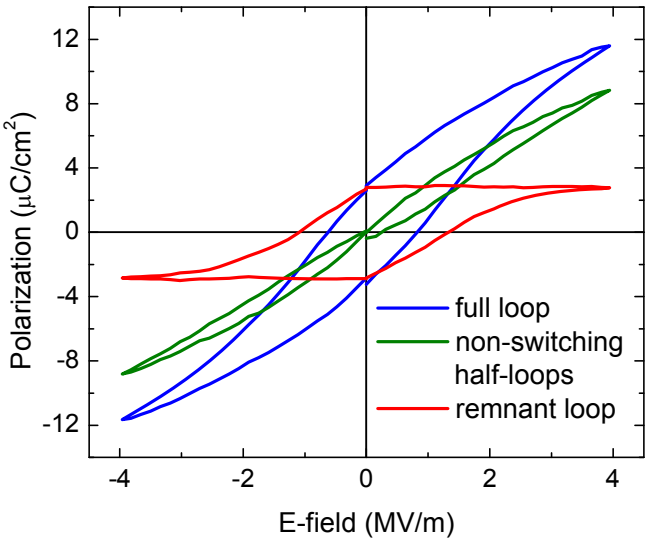

Figure 5-18. Remnant, non-remnant, and full electronic polarization hysteresis loops for sample HR24a.

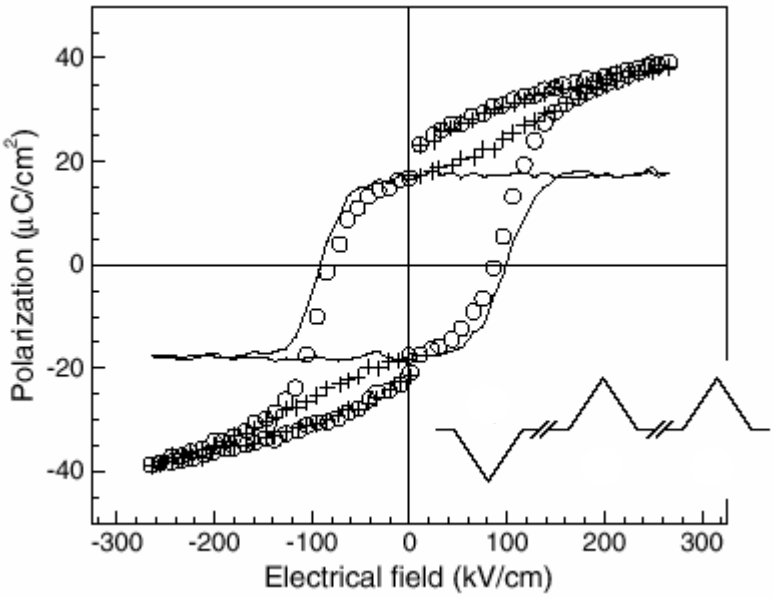

Figure 5-19. Full uncompensated (○) as well as remnant (solid line) and non-remnant (+) electronic polarization hysteresis loops of a 0.19 μm^2 PZT memory cell are shown [Jung et al.][80]

The differences between the full and remnant loops including the significantly larger coercive fields seen in the remnant polarization loops can be understood as follows. The polarity of the non-remnant contributions to the polarization is always the same as that of the applied field. This is in contrast to the remnant component. The polarity of the remnant component does not change until the applied field of opposite polarity exceeds the coercive field of the remnant domains. Because the total polarization is the scalar sum of the remnant and non-remnant contributions[77,203], the fact that the non-

remnant component switches sign at the moment the E-field switches sign results in a reduced apparent coercive field in the full loop[80]. When these non-remnant contributions are subtracted out, their reduction of the effective coercive field is removed as is their contribution to the net polarization measured in the film.

Due to the presence of significant non-remnant contributions to the polarization, the observed coercive fields in our electronic polarization measurements do not coincide with the fields at which dP/dE is maximized. Rather it is found that the fields at which dP/dE of the full hysteresis loops are maximized correspond to the coercive fields of the remnant hysteresis loops as seen in Figure 5-20. This is consistent with the results reported by Jung et al. for PZT memory cell capacitors[80]. Figure 5-18 shows the full hysteresis loops as well as the non-remnant half-loops and the remnant hysteresis loops for sample HR24a. In Figure 5-20 the full and remnant loops are show along with dP/dE for the full hysteresis loop. Theoretically, in the absence of significant non-remnant contributions to the polarization the value of the field where the capacitance or dP/dE reaches a maximum should correspond to the coercive field of the sample[78]. In our films however as seen in Figure 5-20 the field at which the maxima of the full-loop dP/dE occurs does not correspond to the coercive field of the full loop but rather the coercive field of the remnant polarization loop. This is observed consistently in our films for both saturated and unsaturated hysteresis loops. Furthermore it will be shown in Section 5.2.3.2 that the coercive fields determined from the hysteretic electro-optic response likewise correspond to those of the remnant hysteresis loop.

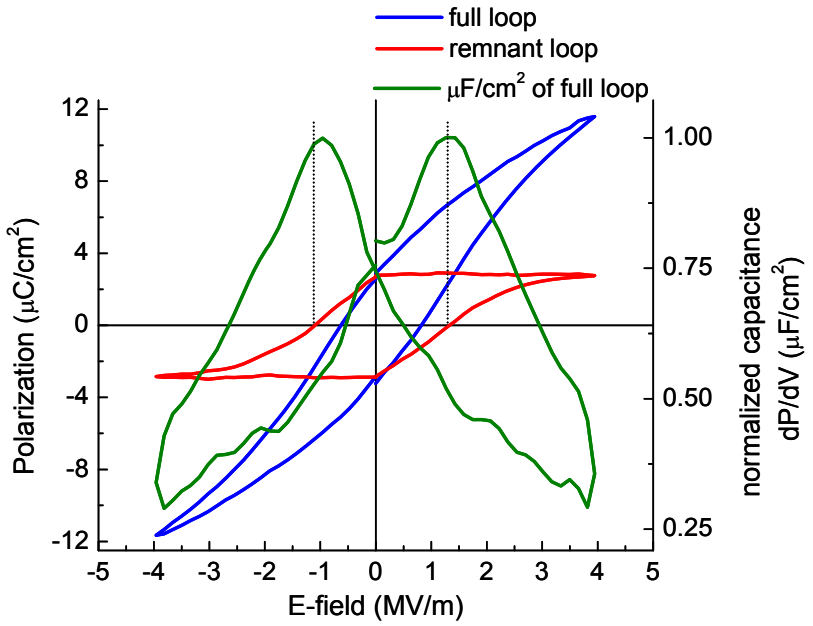

Figure 5-20. Full and remnant electronic polarization loops of sample HR24a are shown along with the field dependent capacitance (dP/dV) of the full loop. The maximum capacitance of the full loop occurs at fields that corresponds to the coercive fields of the remnant polarization loops

To better understand this observation it is instructive to examine both the polarization as a function of time and the switching current density verses time to see how the appreciable linear dielectric contribution to the polarization effects the measured full loop coercive field. Figure 5-21 shows the temporal evolution of the full uncompensated polarization, the non-remnant polarization and the remnant polarization of sample HR24b under the driving voltage shown in the upper plot. The total uncompensated polarization ($P_{Total}(t)$) is just the sum of the remnant ($P_{rem}(t)$) and non-remnant ($P_{n-rem}(t)$) components shown in Figure 5-21 as given by

$$P_{Total}(t) = P_{rem}(t) + P_{n-rem}(t) \tag{5-23}$$

Figure 5-22 shows the associated temporal evolution of the switching current densities of the different components of the electronic polarization. The total current density ($j_{Total}(t)$) is just the sum of the remnant ($j_{rem}(t)$) and non-remnant ($j_{n-rem}(t)$) current densities given by

$$j_{Total}(t) = j_{rem}(t) + j_{n-rem}(t) \tag{5-24}$$

The following observations are made from these figures. The maximum switching current densities observed in the total polarization are coincident with and determined by the maximum current

densities of the remnant polarization. In contrast to the remnant and total polarization current densities, that of the non-remnant polarization exhibits no clear peak, and is nearly uniform – though not constant – in time for a constant dV/dt. The near linear dependence of the non-remnant contributions indicate that it is dominated by the dielectric contributions to the polarization. Further evidence of this will be discussed in Section 5.1.4.

In contrast, the peak in the switching current density of the remnant contribution indicates a relatively narrow distribution of coercive fields centered on the measured value of the remnant loop's coercive field. The value of the applied field at the peak current densities of the full and remnant loops corresponds to the coercive field of the remnant loop. These observations are common to all samples examined and Figure 5-23 and Figure 5-24 are analogs of Figure 5-21 and Figure 5-22 for sample DT443, in which all the same patterns are observed. Similar results have reported in the literature[69,80,81,203] for other ferroelectric systems and are discussed in the following paragraphs.

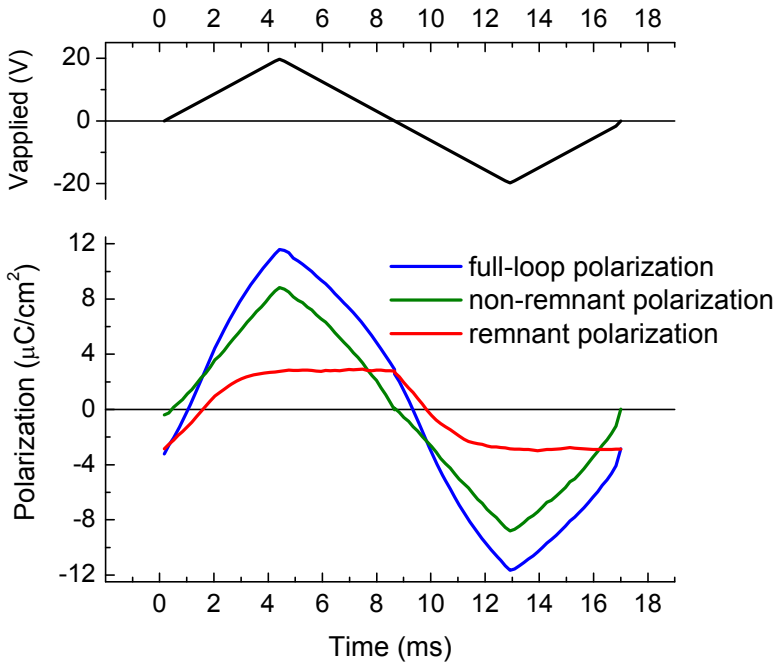

Figure 5-21. The temporal evolution of the full, remnant, and non-remnant electronic polarization of sample HR24a under the driving voltage shown in the upper plot are given

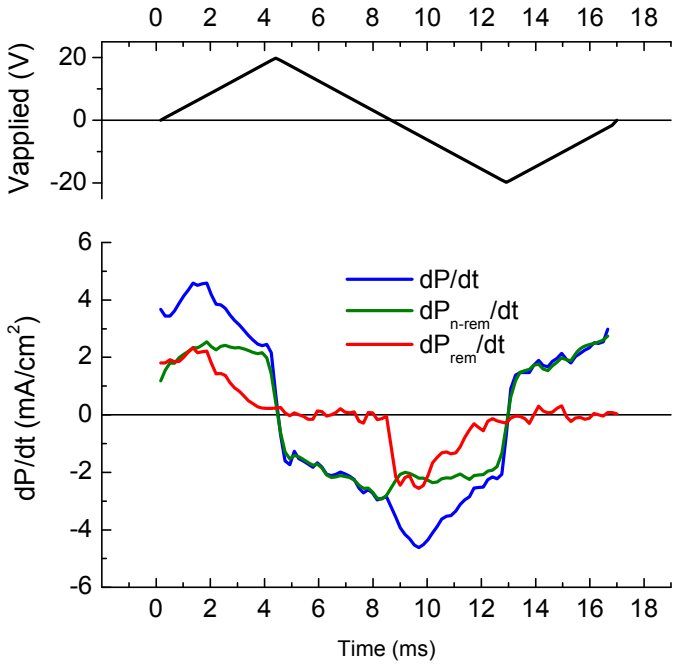

Figure 5-22. The temporal evolution of the switching current densities associated with the full, remnant and non-remnant electronic polarization of sample HR24a under the driving voltage shown in the upper plot are given.

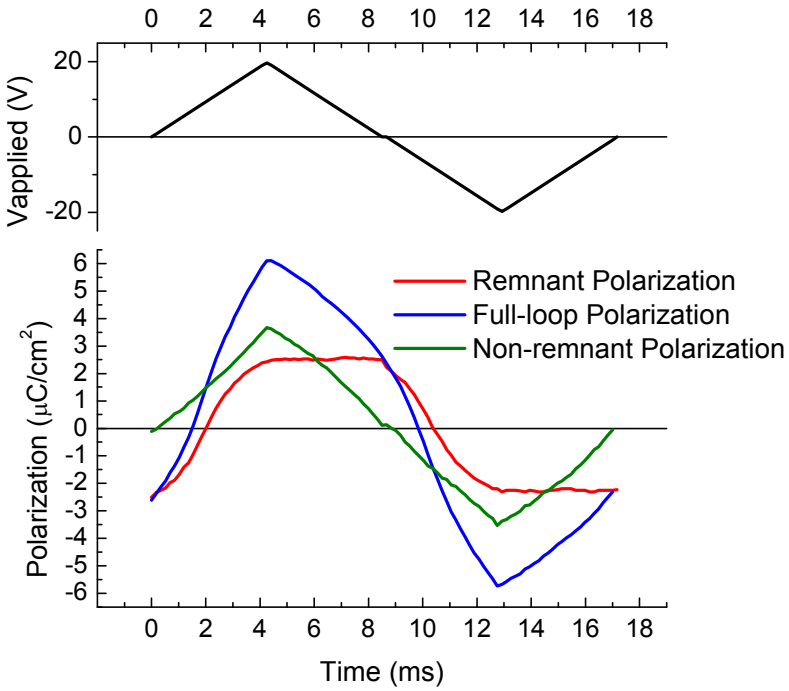

Figure 5-23. The temporal evolution of the full, remnant, and non-remnant electronic polarization of sample DT443 under the driving voltage shown in the upper plot are given

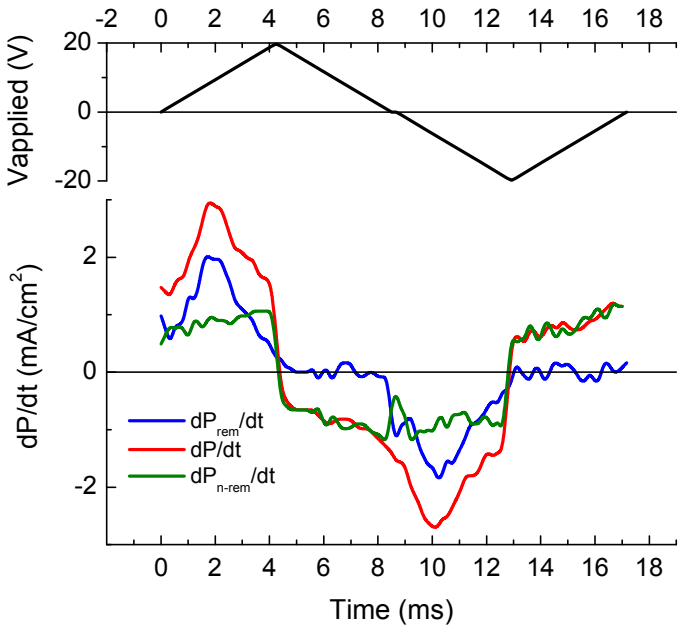

Figure 5-24 The temporal evolution of the switching current densities associated with the full, remnant and non-remnant electronic polarization of sample DT443 under the driving voltage shown in the upper plot are given.

Examination of the switching currents and the polarization loops reported by Wang and Chang[81] in PZT thin films it is apparent that the peak in the switching current occurs when the applied field is the same as that where dP/dE of the hysteresis loop is maximized. Their results are reproduced in Figure 5-25. As with the polydomain $BaTiO_3$ samples examined here, dP/dE reaches its maximum at fields in excess of the coercive field measured for the full uncompensated hysteresis loop.

Similarly, Dickens et al.[69] show that the peak in the switching current densities occur at applied fields that correspond to the coercive fields of the compensated remnant hysteresis loops in a polyvinylidene fluoride (PVDF) sample as shown in Figure 5-26. They likewise demonstrate that the total switching current density is the sum of that due to the remnant and non-remnant switching current densities, and that the peak of the total current density is coincident with and determined by that of the remnant current density as seen in Figure 5-27 reproduced from Dickens et al.[69].

Lastly Bhattacharyya et al.[203] demonstrate the larger coercive fields and lower maximum polarization of a remnant hysteresis loop after subtracting out the non-remnant dielectric contributions to

the total polarization as seen in their electronic polarization data for a $SrBi_2(Ta,Nb)_2O_9$ thin film reproduced in Figure 5-28.

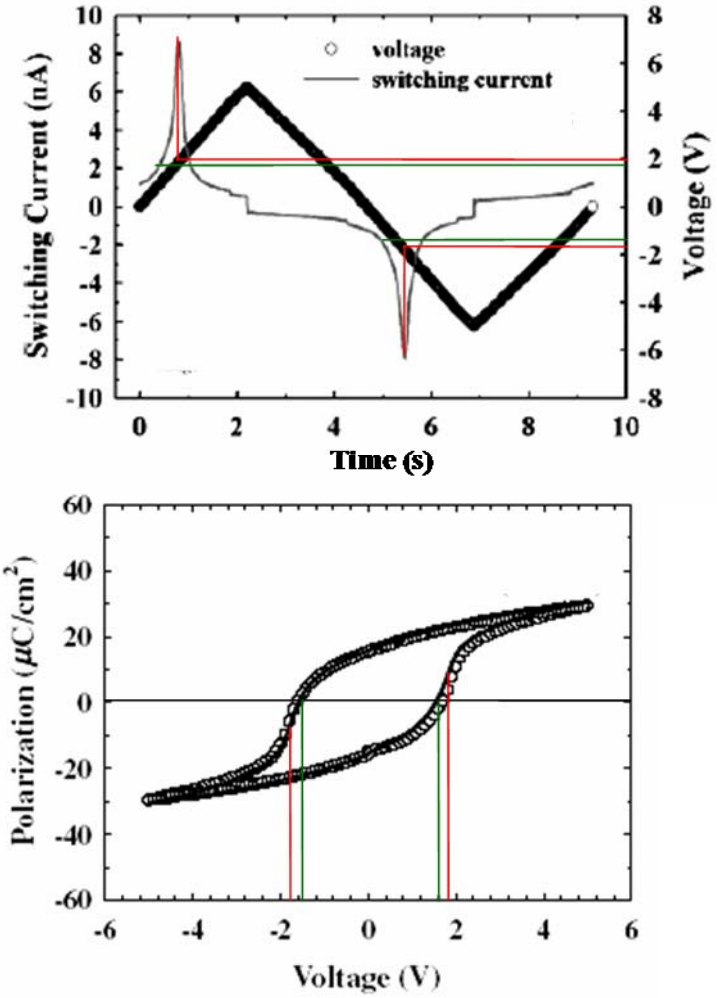

Figure 5-25. Electronic polarization measurements on PZT thin films reported by Wang and Chang[81]. The temporal evolution of the switching current is shown along with the triangle wave driving voltage in the upper figure. From the upper figure the applied voltages temporally coincident with the peaks in the switching current are just less than 2 and -2 V respectively (red lines). From the full uncompensated hysteresis loop shown in the lower figure it is evident that these voltages correspond to the points at which dP/dE of the full uncompensated loop are maximized. Additionally, the values of the fields at which dP/dE is maximized are larger than the coercive fields of the full uncompensated hysteresis loop consistent with the result measured on our polydomain $BaTiO_3$ thin films.

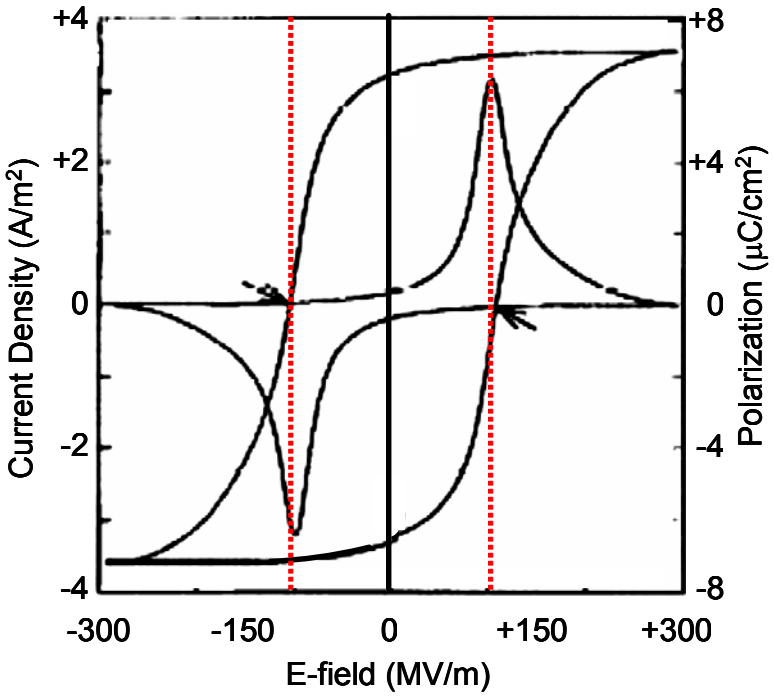

Figure 5-26. Compensated remnant hysteresis loop of a PVDF sample reproduced from Dickens et al.[69]. The peak in the total current density occurs at an applied field equal to the coercive field of the *compensated* remnant hysteresis loop, consistent with the observations in our polydomain $BaTiO_3$ thin films

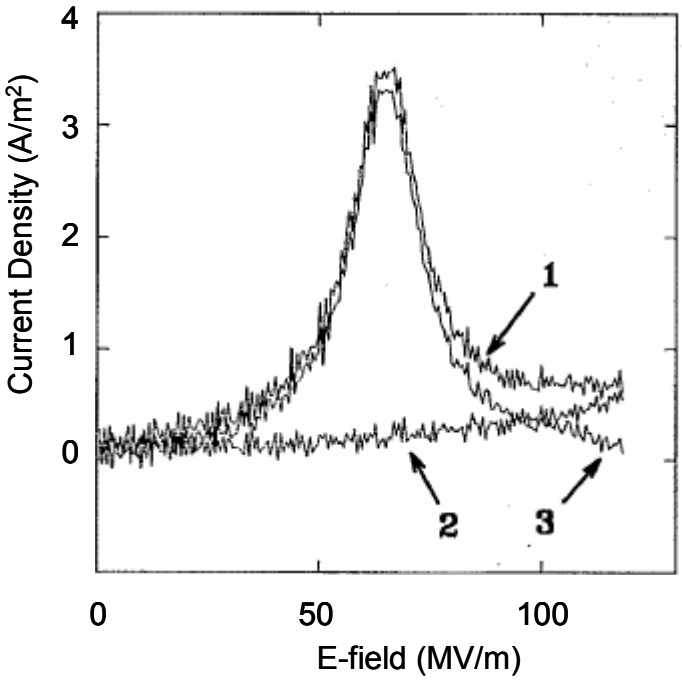

Figure 5-27. The field dependence of (1) the total current density, (2) the non-remnant current density and (3) the remnant current density of a PVDF sample are reproduced from Dickens et al.[69].

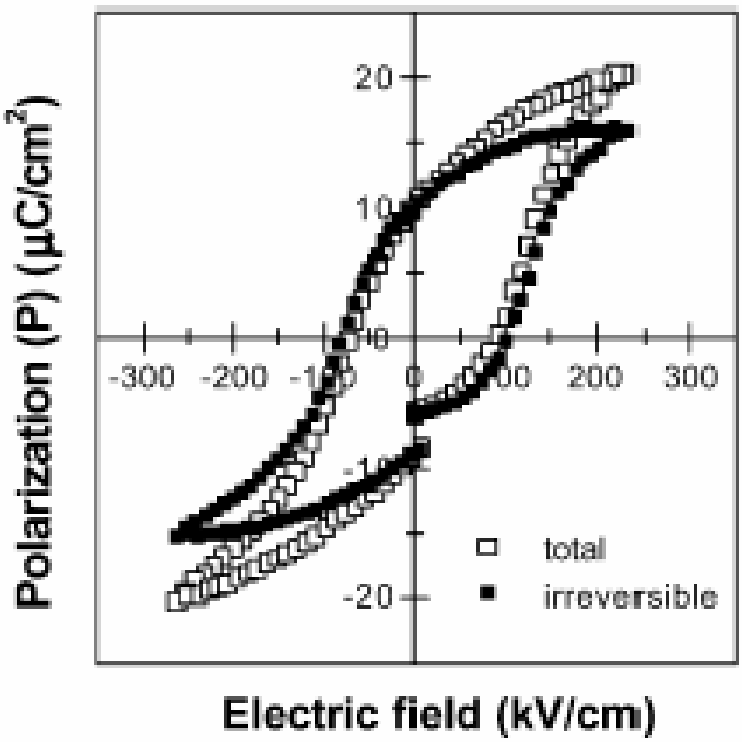

Figure 5-28. The full uncompensated hysteresis loop as well as the remnant hysteresis loop generated by subtracting the non-remnant dielectric component of the polarization from the full loop. The coercive fields of the resulting remnant polarization loop are observed to be larger than those of the full uncompensated hysteresis loop, consistent with the observed behavior in our polydomain $BaTiO_3$ thin films. Data shown is for a $SrBi_2(Ta,Nb)_2O_9$ thin film and is reproduced from Bhattacharyya et al.[203]

5.1.4 E-field dependent polarization (unsaturated hysteresis loops)

The evolution of the hysteresis loop parameters from series of unsaturated hysteresis loops can provide a qualitative insight into the degree of saturation of the polarization with increasing field[204]. With increasing maximum applied field (E_{max}), the onset of saturation of the polarization is indicated by the onset of saturation of the hysteresis loop parameters of the unsaturated loops. Parameters that are expected to show evidence of saturation include the remnant polarization, the coercive field and the polarization at maximum applied field[204].

In order to look for evidence of saturation of the polarization in the polydomain $BaTiO_3$ thin films, the evolution of the parameters of the electronic polarization hysteresis loops were analyzed as a function of the maximum applied electric field by measuring series of unsaturated hysteresis loops.

Figure 5-29a-c show series of full and remnant unsaturated hysteresis loops and dP/dV Vs E of the full hysteresis loops for sample DT443. For clarity, several of the measured loops in the series which are included in the subsequent analysis are omitted in the figure.

From Figure 5-29 one sees that the coercive fields of the *remnant* hysteresis loops correspond to the fields at which the maxima of dP/dV of both the full and remnant hysteresis loops occur. This is made clearer in Figure 5-30 where $(dP/dV)_{max}$ of the full loops as well as the coercive fields for the full and remnant series of unsaturated hysteresis loops of sample DT443 are plotted verses the maximum applied field. From Figure 5-30 it appears that the coercive field of the remnant hysteresis loops shows evidence of the *onset* of saturation for applied E_{max} in excess of 0.9 MV/m.

The dependence of the coercive field on E_{max} was likewise examined. Figure 5-31 shows the field dependent coercive field plotted together with the measured cumulative distribution of coercivities in sample DT443 previously seen in Figure 5-11. From the figure the field dependent coercivity seems reasonably well correlated to the measured CDF of coercivities and would tend to indicate that at the observed inflection of the field-dependent coercive field in sample DT443 approximately 65% of the domain volume fraction has undergone a 180^o domain switch. At the maximum applied field approximately 80% of the "switchable" volume fraction has undergone a 180^o domain reversal. The coercive fields of the full hysteresis loop exhibit an inflection at approximately the same field and it is assumed that the inflection reflects the more modest contributions from the remnant polarization at higher fields due to the onset of saturation.

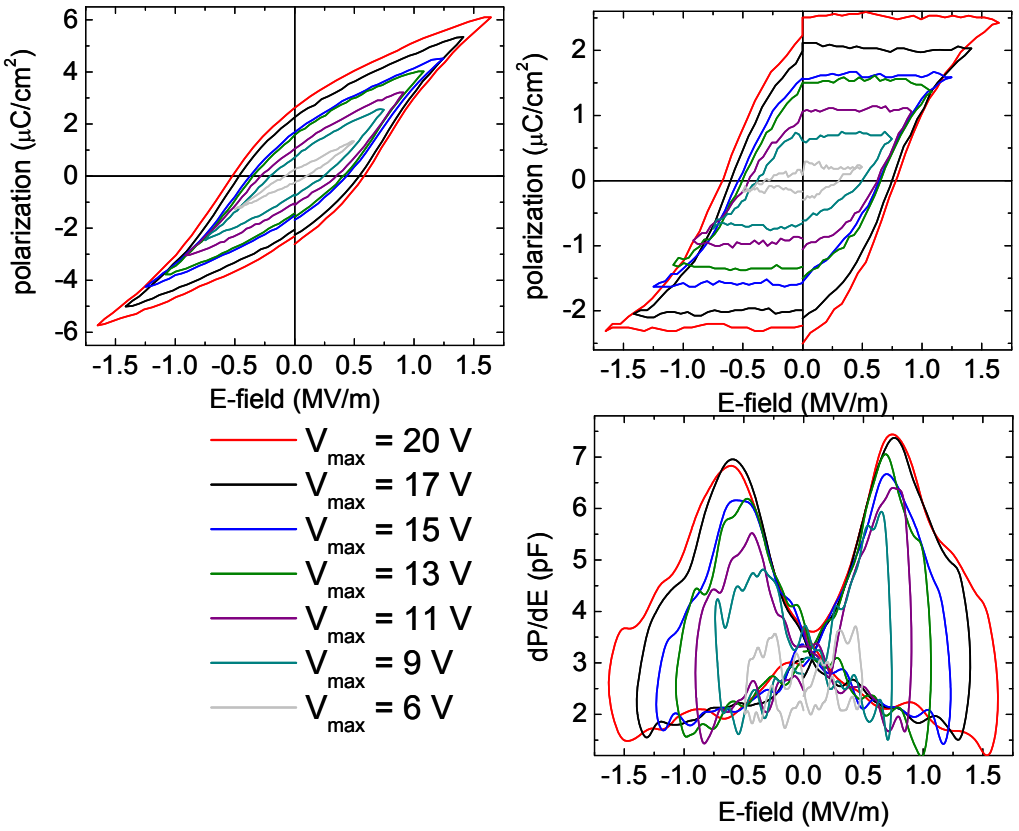

Figure 5-29. a. series of unsaturated full hysteresis loops; b. series of unsaturated remnant hysteresis loops generated by subtraction the measured non-switching half-loops from the full loops; c. the field dependent capacitance or dP/dV of the full loops [sample DT443].

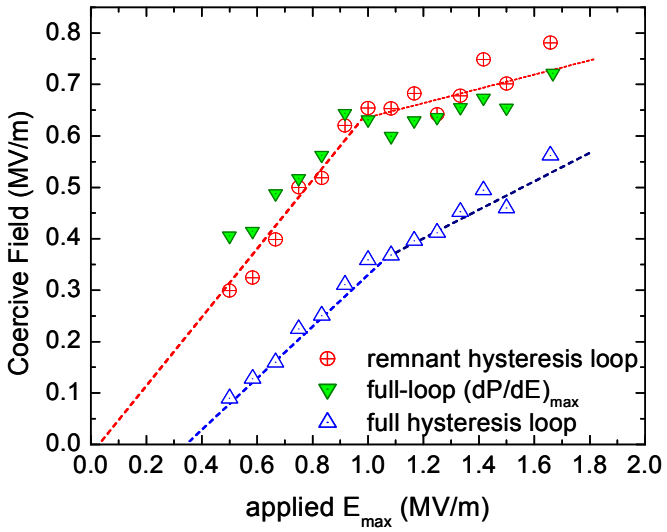

Figure 5-30. Coercive fields of the full and remnant hysteresis loops for a series of unsaturated hysteresis loops for sample DT443 are shown. Also shown is the value of the applied field at which $(dP/dE)_{max}$ of the full hysteresis loop occurs. As seen in the figure the coercive fields of the remnant hysteresis loops correspond to the fields at which the maxima of dP/dE of the full hysteresis loops occur for the entire series of unsaturated loops.

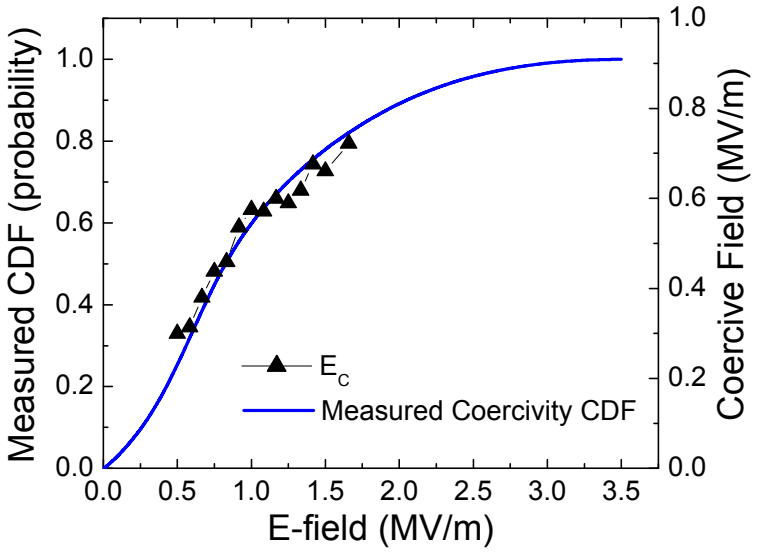

Figure 5-31. The field-dependent coercive field along with the measured cumulative distribution function of coercivities derived in Section are shown to be reasonably well correlated. At the inflection point of the field-dependent coercive fields at 0.9 MV the CDF would indicate that ~65% of the switchable volume fraction has undergone a 180° domain reversal [sample DT443].

The parameters for series of unsaturated full hysteresis loops for several additional samples were measured and are summarized in Figure 5-32 through Figure 5-34. Figure 5-32 shows the coercive fields for series of unsaturated full polarization loops for several samples, all of which exhibit an inflection with a reduced rate of increase in the coercive field at higher field. In all cases the inflections occur at maximum applied fields of between 0.7 and 1 MV/m. The second inflection point observed for sample AM016 is due to a clear increase in leakage at higher applied E_{max}. It is assumed that as was the case with sample DT443, these inflections in the measured coercive fields of the full loops reflect the onset of saturation of the remnant component of the polarization. This finding is consistent with the observation by Towner that the second harmonic generation hysteresis loops of the polydomain $BaTiO_3$ thin films begin to show signs of saturation for applied fields in excess of 0.75 MV/m[36].

The remnant polarization and polarization at maximum applied field were likewise examined. Figure 5-33 and Figure 5-34 , respectively, show the remnant polarizations and maximum polarizations for series of full unsaturated hysteresis loops on several samples. It should be noted that as inspection of Figure 5-18 makes clear, the *remnant* polarization of the full hysteresis loop is in general very nearly the

same as the maximum and remnant polarization of the remnant hysteresis loop. In Figure 5-33 one sees that samples AM016 and AM018 both exhibit evidence of saturation of the remnant polarization for maximum applied fields in excess of 0.9 MV/m. The subsequent increase at ~1.3 MV/m in sample AM016 is again due to the observed onset of increased leakage at fields in excess of 1.3 MV/m as noted previously with regard to the behavior of this samples coercive field. Sample AM039 likewise shows an inflection with a decreased dP_r/dE_{max} above ~0.9 MV/m though the degree of saturation is less complete. Neither sample DT443 nor AM069b exhibit any evidence of saturation of the remnant polarization.

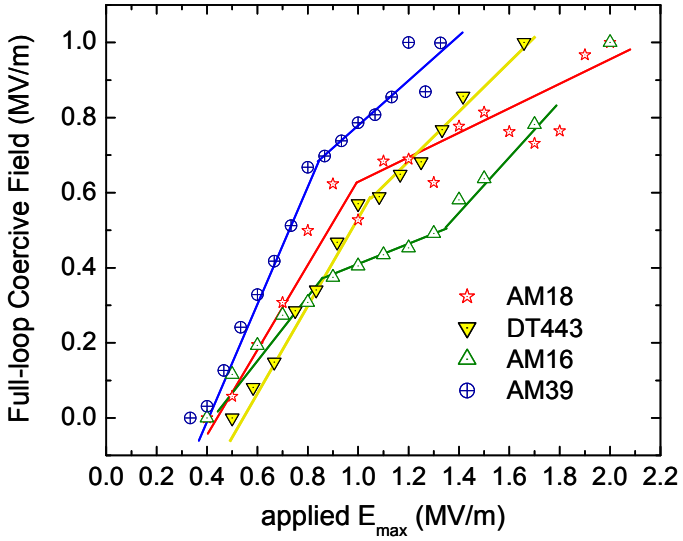

Figure 5-32. The evolution of the coercive field of full polarization hysteresis loops are shown for a number of samples. The measurements were made from series of unsaturated hysteresis loops measured for each sample.

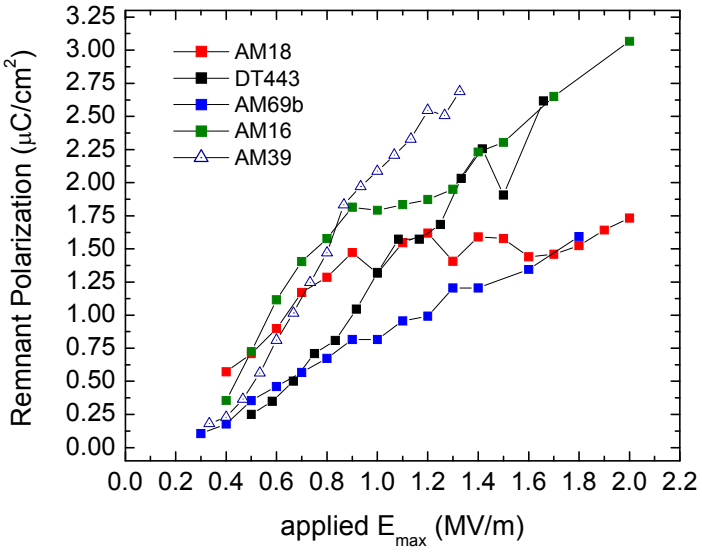

Figure 5-33. The evolution of the remnant polarization of full polarization hysteresis loops are shown for a number of samples. The measurements were made from series of unsaturated hysteresis loops measured for each sample.

P_{max} likewise showed evidence of saturation. From Figure 5-34 it is observed that while samples AM018, AM016, AM069 and to a lesser extent, sample AM039, all exhibit a decrease in dP_{max}/dE_{max} with increasing E_{max}. In fact, for all the samples examined the value of dP_{max}/dE_{max} at high E_{max} is constant with the rate in all the samples being similar. This is consistent with continuing dielectric contributions to the polarization (as given by equation (5-9)) after the onset of saturation of the ferroelectric contributions to the polarization. The average dP_{max}/dE_{max} at higher E_{max} was 330±50 pF/cm. This corresponds to a saturation value of the dielectric susceptibility of 3730 where the susceptibility is given by[203]

$$\chi(E) = \frac{1}{\varepsilon_o}\left(\frac{dP}{dE}\right) \tag{5-25}$$

in which $\varepsilon_\circ$ is the free-space permittivity. Given the bulk values of $\varepsilon_a = 4400$ and $\varepsilon_c = 129$ reported in the literature[56] the value of 3730 is not unreasonable (recall that $\chi = \varepsilon - 1$). However as will be seen shortly it is significantly larger than the dielectric constant determined from either the small signal capacitance measurement or the dP/dE of the linear non-remnant polarization half-loops. The larger dielectric constant determined from the constant dP_{max}/dE_{max} observed for fields in excess of 1 MV/m is possibly due to finite non-remnant ferroelectric contributions to P_{max}.

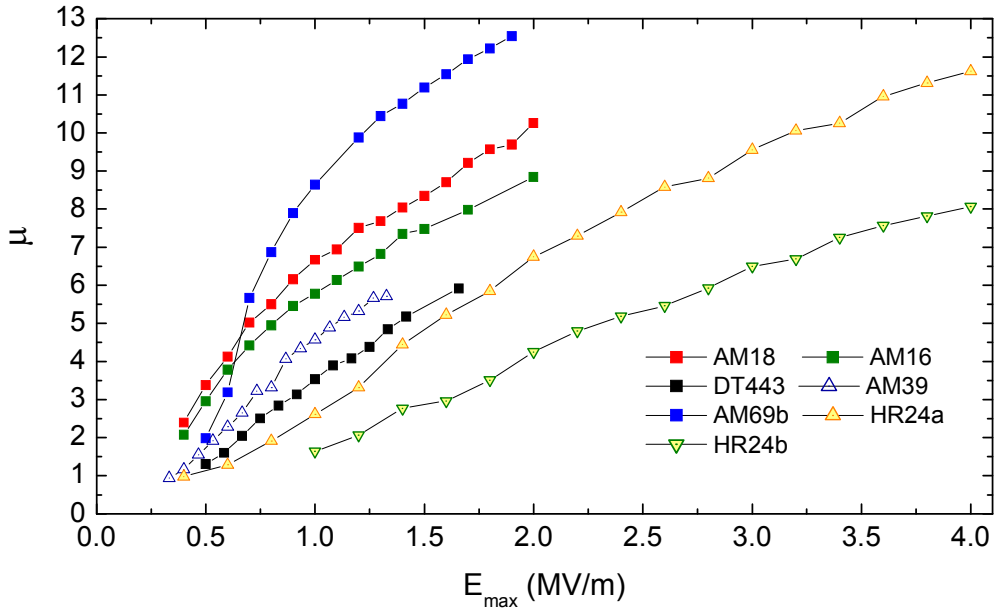

Figure 5-34. The evolution of the maximum polarization of full polarization hysteresis loops are shown for a number of samples. The measurements were made from series of unsaturated hysteresis loops measured for each sample.

The field dependent dielectric constant of sample DT443 was calculated from the non-remnant half loops. Consistent with other reports in the literature the maximum dielectric constant was found to occur at approximately the same field as the maximum capacitance measured for the full hysteresis loop[203]. The measured dielectric constants ranged from 2400 to 2900, in excellent agreement with earlier measurements of 2200 made 1 GHz on a similar film grown in the same reactor[186]. As seen in Figure 5-35, the nearly linear electric field dependence of the non-remnant polarization and very small non-remnant hysteresis would tend to suggest that the non remnant contributions are dominated by the dielectric contributions to the polarization. That this is the case is confirmed by the coincidence of the non-remnant polarization half-loops and the polarization determined from a small-signal capacitance measurement seen in Figure 5-38. The full hysteresis loop is included in Figure 5-35 for comparison. As noted by Bolten et al.[205] the fact that the slope of the full-loop hysteresis in the saturation region is approximately the same as that of the non-switching half-loops is consistent with the non-switching half-loops being dominated by dielectric contributions to the polarization.

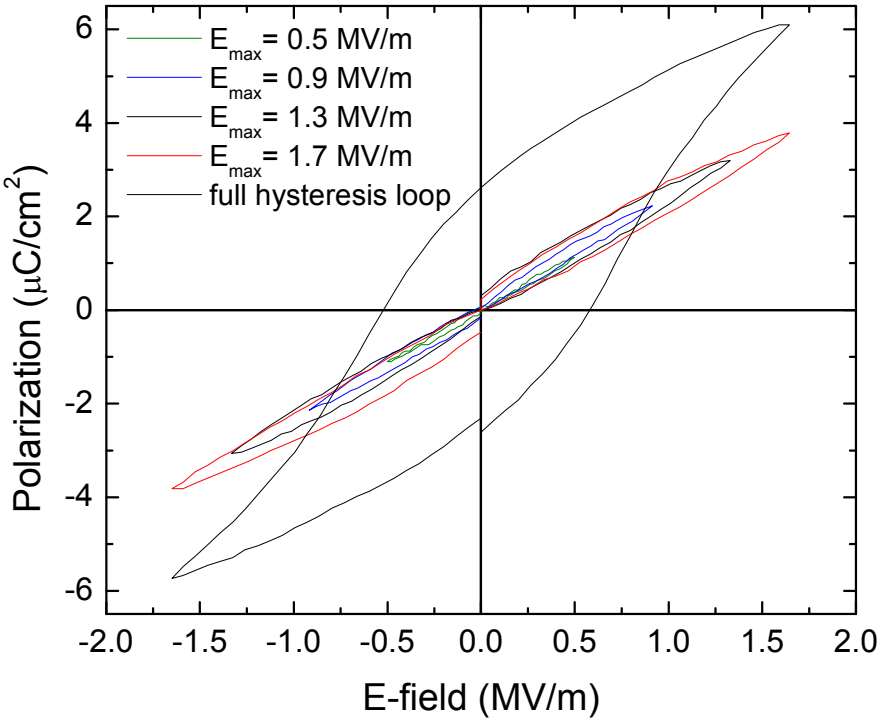

Figure 5-35. As seen in the figure, the non-remnant half-loop polarization exhibits an approximately linear dependence on the applied electric field with very little hysteresis observed relative to that in the full hysteresis loop included for comparison.

Assuming that non-remnant polarization is dominated by the linear dielectric contributions, the associated dielectric constants as well as the capacitance were calculated from the non-remnant half loops measured for all of the unsaturated hysteresis loops of sample DT443. The capacitance and dielectric constants were calculated from the approximately constant dP/dV and dP/dE of the non-remnant half-loops according to[77,203]

$$C(E) = A\frac{dP}{dV} \qquad \varepsilon(E) = (1+\chi) = \left(1+\frac{1}{\varepsilon_\circ}\left(\frac{dP}{dE}\right)\right) \tag{5-26}$$

where A is the effective capacitor plate area which for sample DT443 was $2.54\text{x}10^{-5}$ cm^2. $\varepsilon_\circ$ and χ are respectively the free-space permittivity and the dielectric susceptibility. As shown in Figure 5-36 the dielectric constant reaches it's maxima at approximately the same fields where the field dependent capacitance of the full hysteresis loop reaches it's maximum. This is consistent with the results of Battacharyya et al.[203] as shown in Figure 5-37 reproduced from [203]. The values of the dielectric constant of sample DT443 are consistent with the an earlier vector network analyzer measured value of

2200 at 1GHz on a similar film grown in the same reactor[186]. This would tend to suggest that the assumption that the non-remnant polarization of sample DT443 is dominated by the linear dielectric contributions for the range of applied fields employed is reasonable.

Further evidence comes from comparing the reversible polarization determined from a standard small signal capacitance measurement of sample DT443 with that of the non-remnant half-loops. Figure 5-38 shows both the reversible polarization from a standard small-signal capacitance measurement made on the Radiant RT6000 as well as the non-remnant half-loops of sample DT443 measured for a maximum applied voltage of 19.9 V. The full hysteresis loop is included for comparison. As seen from Figure 5-38 the slope or dP/dE from the small signal capacitance measurement is the same as that of the non-remnant half-loops. The permittivity determined from the small signal capacitance measurement was 2400 as compared to 2400 at E_{max}= -1.65 MV/m and 2500 at E_{max}= +1.65 MV/m determined from the non-remnant half-loops. The result is likewise consistent with those from the model results presented in Section 5.1.1.

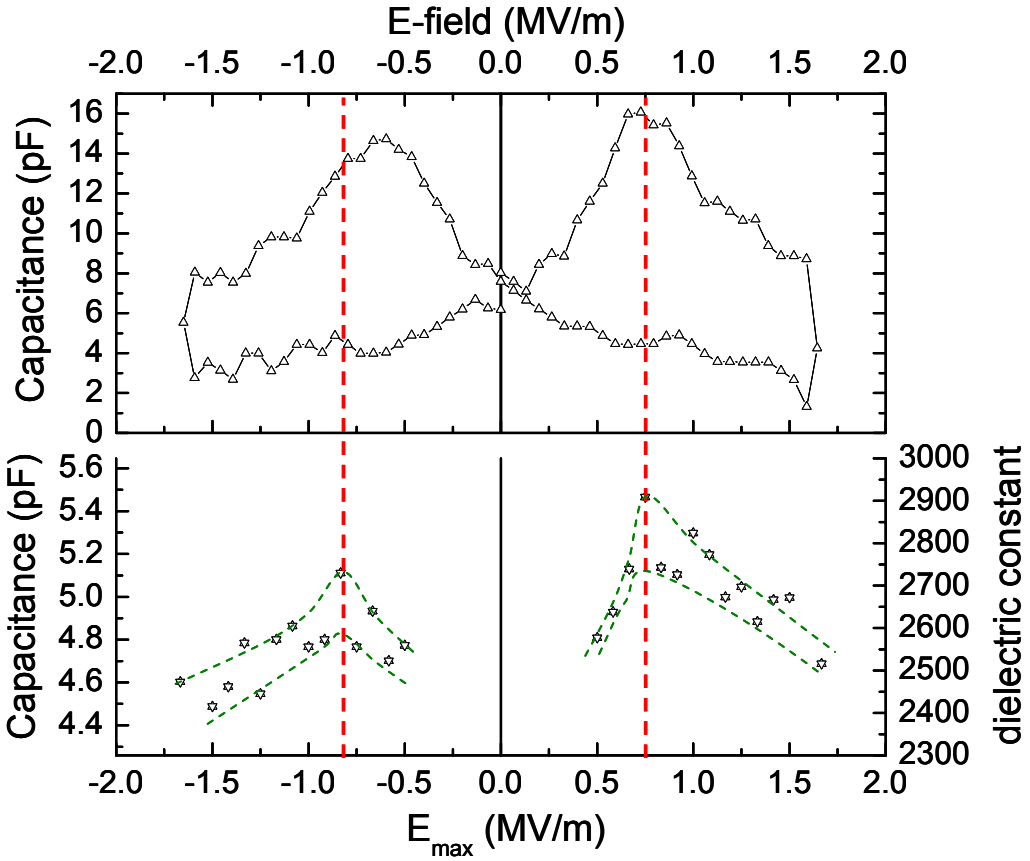

Figure 5-36. The small signal capacitance and dielectric constants calculated from the non-remnant polarization half-loops are plotted verses the maximum applied field of the non-remnant half-loop in the lower plot. The upper plot shows the full hysteresis loop capacitance measured under the maximum available test voltage (19.9V). As seen in the figure the small signal capacitance is maximized at approximately the same field value where the maximum capacitance of the full hysteresis loop is observed. The dashed green lines in the lower figure are included as a guide to the eye.

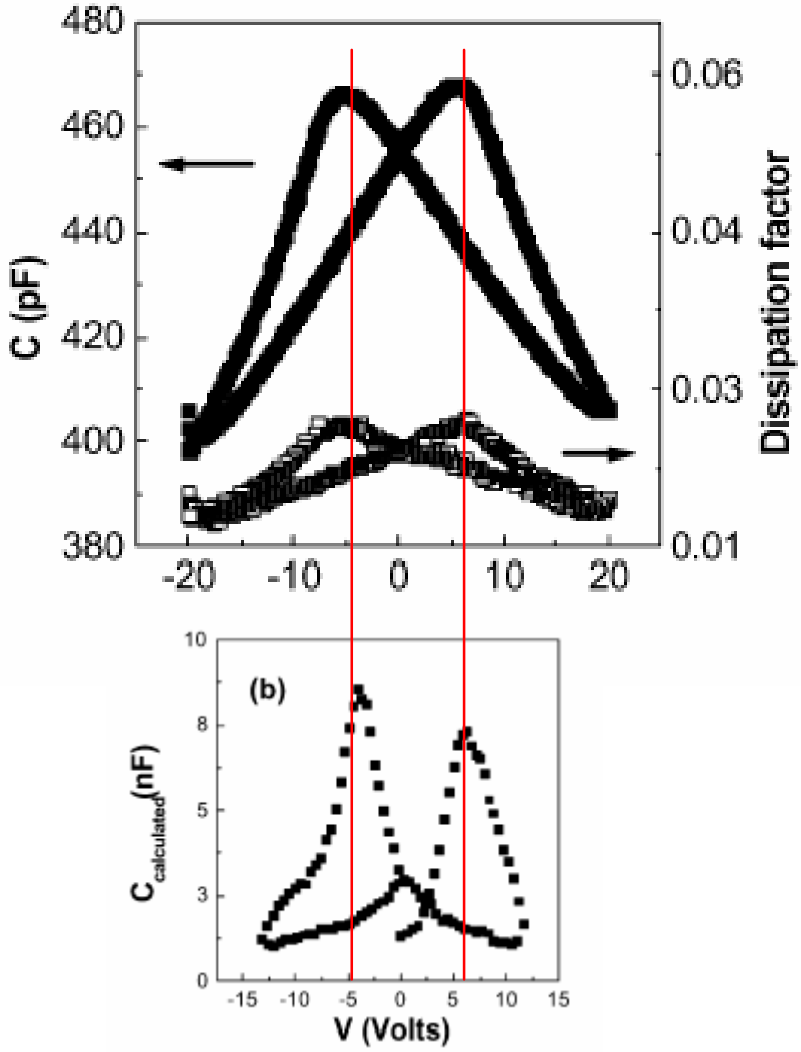

Figure 5-37. The upper plot shows the measured small signal capacitance of a $SrBi_2(Ta_{0.5},Nb_{0.5})_2O_9$ thin film[203]. The lower figure from the same reference shows the capacitance calculated from the full polarization hysteresis loop of the film. As seen the small signal capacitance is maximized at the same field for which the capacitance of the full hysteresis loop is maximized.

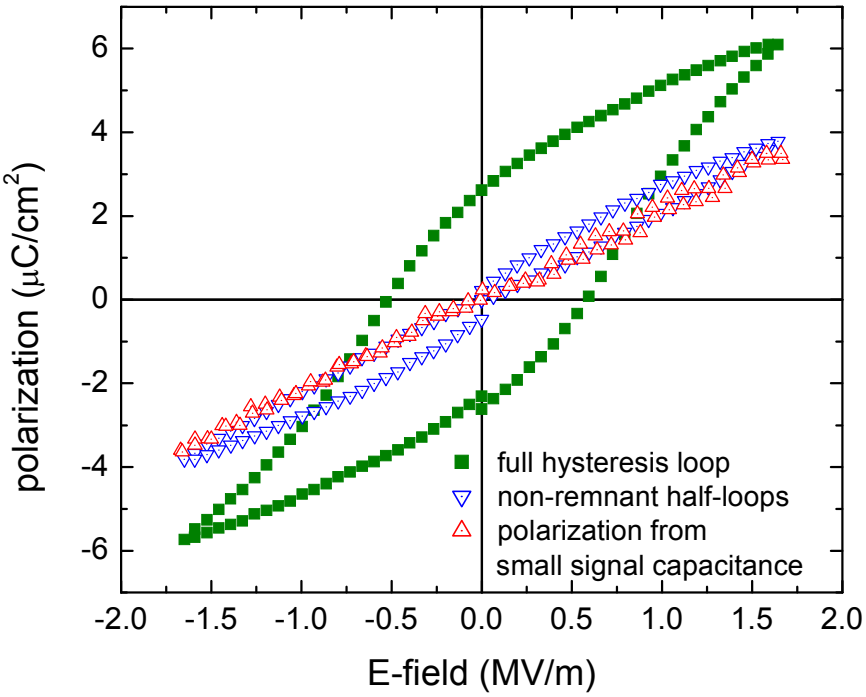

Figure 5-38. The reversible polarization of sample DT443 determined from a standard small signal capacitance measurement is nearly identical to that of the portion of the non-remnant half-loops that correspond to increasing magnitude of the applied field.

With both the reversible polarization measured from the small signal capacitance and the polarization due to the non-remnant half loops, it is possible to derive the polarization due solely to non-remnant domain flipping by simply subtracting the later from the former. This is because the polarization from the small-signal capacitance measurement includes *only* the dielectric contributions to the polarization with no contributions from domain flipping. In contrast, the non-remnant half-loops include both the dielectric contributions as well as any non-remnant ferroelectric contributions due to reversible domain flipping. The polarization due to non-remnant domain flipping is shown in Figure 5-39. Figure 5-39 likewise shows the full hysteresis loop as well as that after subtracting out the dielectric contributions determined from the small-signal capacitance measurement. Determination of a remnant loop by subtracting the dielectric contributions measured from a small-signal capacitance measurement is a common practice[70,203]. However, the resulting loop still reflects non-remnant ferroelectric contributions to the polarization. By subtracting the non-remnant half-loops from the full loop, all non-remnant

contributions including those due to 90° domain flipping are removed. This hysteresis loop with all non-remnant contributions subtracted out is likewise shown in Figure 5-39.

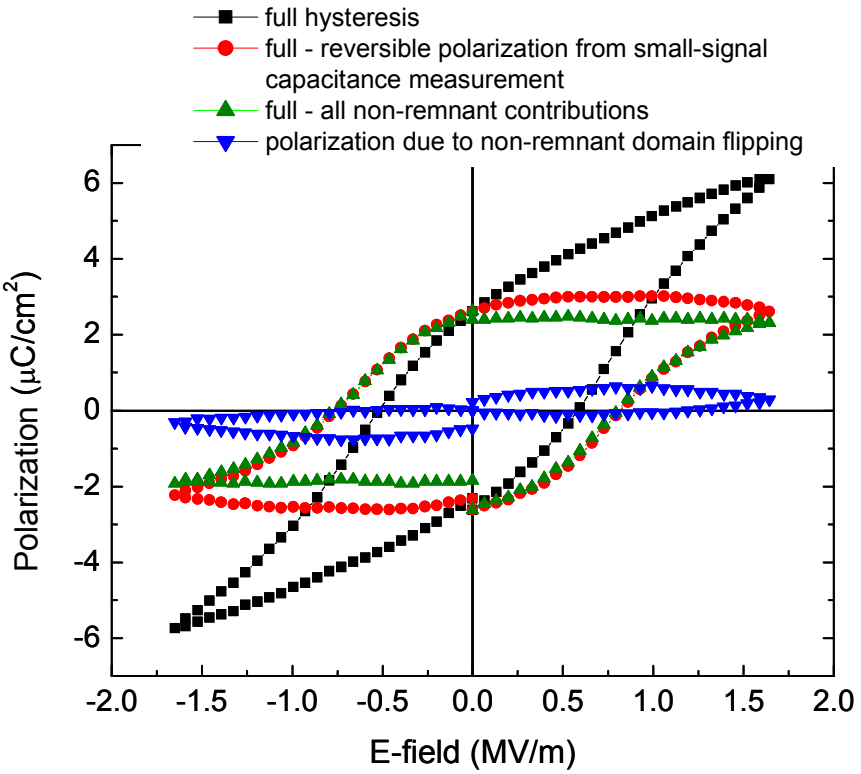

Figure 5-39. The full hysteresis loop of sample DT443 is shown (black squares) along with the remnant loop determined by subtracting out the reversible dielectric contributions determined from a small-signal capacitance measurement (red circles) and the remnant loop determined by subtracting the non-switching half-loops from the full loop (green upright triangles). Because the non-remnant half-loops include contributions from both the dielectric constant and non-remnant ferroelectric contributions, this represents the true remnant loop. The difference between these two remnant loops or equivalently the difference between the non-remnant half-loops and the dielectric contributions determined from the small signal capacitance measurement gives the non-remnant ferroelectric contributions to the polarization (blue inverted triangles).

While as previously mentioned the non-remnant switching currents are typically nearly constant in time, one exception to this was found in sample AM069b. Figure 5-40 shows the non-remnant current densities verses time for three samples as the applied voltage increases linearly from 0 to 19.9 V over the course of the 4 ms shown in the figure. Samples DT443 and HR24a exhibit the characteristic nearly time independent current densities normally observed, while AM069b's non-remnant current density is strongly peaked, more reminiscent of the remnant current densities for samples HR24a and DT443 shown

in Figure 5-22 and Figure 5-24. From the non-remnant polarization loops for these samples shown in Figure 5-41 it is apparent that the non-remnant loops of AM069b exhibit appreciable non-linear hysteresis as compared to the more characteristic behavior of the other two samples in which dP/dE of the non-remnant loops is nearly linear. A series of unsaturated full and non-remnant loops of sample AM069b are shown in Figure 5-41. The full hysteresis loops are "pinched off" as the field goes to zero. Just such "pinching" of the hysteresis loop due to 90° domain flipping has been predicted in phase field simulations of $PbTiO_3$ under combined electro-mechanical loading [206] as seen in Figure 5-98. Evidence from electro-optic measurements of AM069b to be presented in Section 5.2.4.1 support the theory that a relatively large domain volume fraction domains is undergoing 90°-domain reversal in this sample.

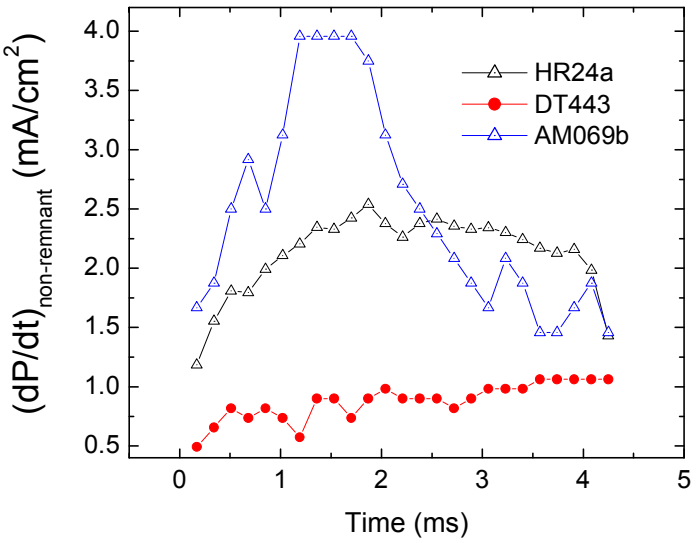

Figure 5-40. The temporal evolution of the current densities of the non-remnant components of the electronic polarization are shown for three samples. DT443 and HR24a exhibit the characteristically flat non-remnant current densities, while that of sample AM069b is highly peaked reminiscent of the remnant current densities normally observed in our films.

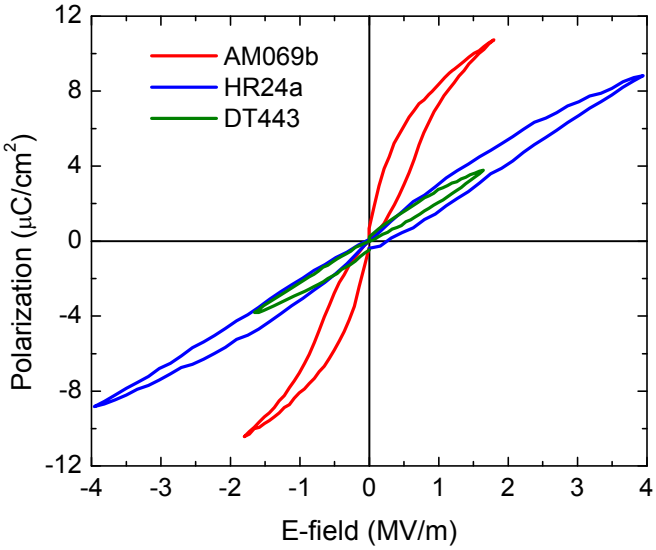

Figure 5-41. The non-remnant half-loops of samples DT443, HR24a and AM069b are shown. The nearly liner dP/dE with modest hysteresis observed in samples DT443 and HR24a is characteristic of our samples. In contrast a more clearly non-linear dP/dE and enhanced hysteresis is observed in the non-remnant half-loops of AM069b

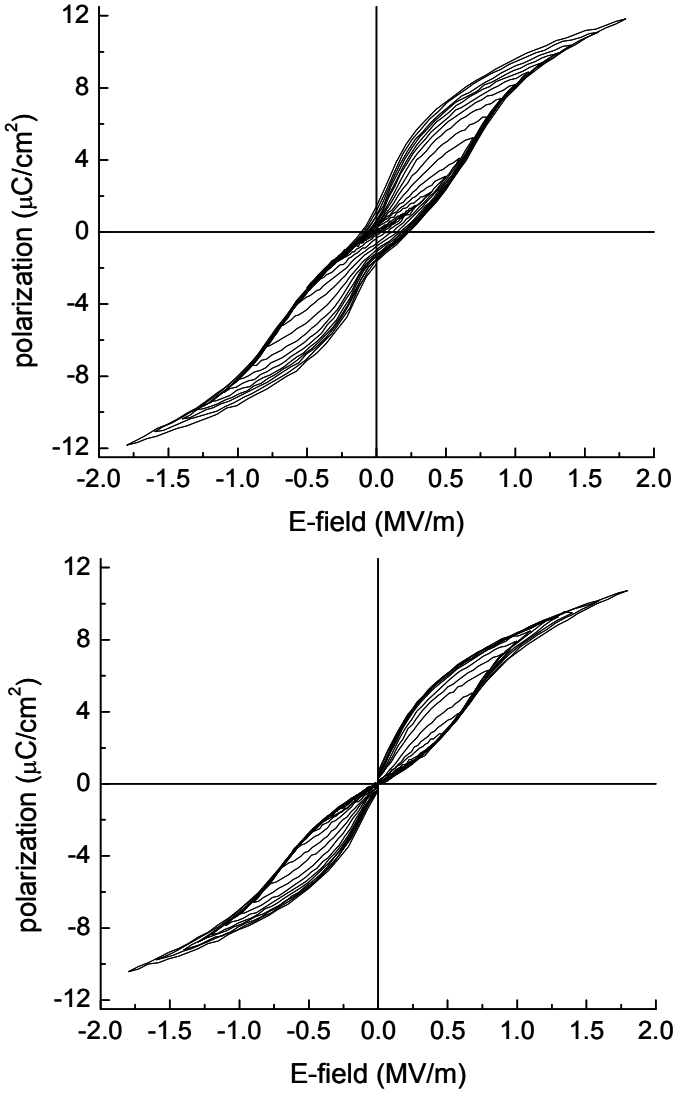

Figure 5-42. The series of unsaturated hysteresis loops of sample AM069b are shown. The upper figure shows the full hysteresis loops. The lower figure shows the non-remnant half loops. The pinching off of the full loop and the significant non-linear hysteresis of the non-remnant loops are believed to be due to 90°-degree domain flipping

5.1.5 Summary of in-plane electronic polarization measurements

In this section the hysteretic properties of the in-plane electronic polarization of polydomain $BaTiO_3$ thin films were examined. A model for the in-plane polarization of polydomain thin films was developed where the in-plane remnant polarization is proportional to the a-domain volume fraction. The model likewise predicts that the in-plane dielectric contributions to the polarization are inversely proportional to the a-domain volume fraction. Calculated polarization loops well described the

experimental data. Additional key findings include the following. No in-plane directional dependence of the electronic polarization was observed. From the in-plane polarization model developed in Section 5.1.1 it was shown that the in-plane anisotropy can be significantly diminished when the saturation of the polarization is incomplete. Furthermore, for relatively broad distributions of coercivities the in-plane polarization is relatively isotropic for a reasonable range of maximum applied fields. The average remnant in-plane polarization of 2.7 $\mu C/cm^2$ was shown to be consistent with the theoretically predicted range given by the model developed in Section 5.1.1 for the typical 28±8% a-domain volume fractions observed in the films[36].

The following conclusions are drawn from analysis of the remnant and non-remnant contributions to the electronic polarization. In examining the temporal response of the polarization, the maximum switching current density of the total electronic polarization is consistently found to be coincident with that of the remnant component of the polarization. In contrast to the well defined peak observed in the remnant switching current density, that of the non-remnant component is relatively flat. Given the linear increase in field with time this implies that the remnant component of the polarization is characterized by a distribution of coercivities centered at the coercive field of the remnant loop or equivalently the field at which the maxima of dP/dE of the total polarization loop occurs. In contrast, the nearly linear increase in the non-remnant component with field implies that the non-remnant component is dominated by the linear dielectric contributions to the polarization.

Series of unsaturated hysteresis loops indicate that on average, evidence for the *onset* of saturation of the remnant contributions to the polarization are observed for maximum applied fields in excess of 0.7 to 1 MV/m as determined from both the measured coercive fields and the remnant polarizations of the unsaturated hysteresis loops.

The maximum polarization values for the series of unsaturated loops of most samples examined exhibited a decrease in dP_{max}/dE_{max} over a similar range of E_{max} values of between 0.7 and 1 MV/m. For large E_{max}, dP_{max}/dE_{max} is nearly constant and of similar value for all films examined. The linear

dependence of P_{max} on E_{max} is attributed to the linear dielectric contributions to the measured polarization. However the dielectric constants determined from dP_{max}/dE_{max} are slightly higher than those determined from either standard small signal capacitance measurements or from the linear non-remnant polarization half-loops. It is likely that the larger dielectric constants determined from dP_{max}/dE_{max} are due to finite non-remnant ferroelectric contributions to the value of P_{max}.

The observed linearity of the non-remnant polarization half-loops is attributed to their dominance by linear dielectric contributions. Confirmation of this is found in the nearly identical dielectric constants determined from standard small-signal capacitance measurements and those determined from the linear dP/dE of the non-remnant polarization half-loops. Measurement of both allows for a determination of the non-remnant ferroelectric contributions to the electronic polarization.

5.2 Electro-optic measurements of polydomain $BaTiO_3$ thin films

5.2.1 Introduction

The electro-optic properties of polydomain $BaTiO_3$ thin films were measured in several different measurement geometries. The theoretical EO response of the domain variants in the various measurement geometries was likewise analyzed. Consideration of the theoretical response allows one to infer which domain variants are principally responsible for measured EO response in a given geometry. Previous work showed that the effective EO coefficients measured under in-plane electric fields along <110> directions were an order of magnitude larger than those measured along <100> directions[12]. This difference was previously attributed to anisotropic poling with an "easy" poling direction along the in-plane <110> direction. A similar anisotropic in-plane dependence of the EO coefficient is reported here. Furthermore measurements designed to probe the possible hysteresis of the EO response were made. From these measurements it is possible to determine for any given measurement geometry, which domain variants are contributing to the EO response. As a result of these measurements, it is shown in this section that the electro-optic response of polydomain $BaTiO_3$ thin films are *always* dominated by those

domains that contribute large off-diagonal r_{51} or r_{42} contributions to the measured response; importantly, this is true even when the applied field does not act to pole the r_{51} or r_{42} contributing domains.

In geometries where the applied field *does* act to pole the r_{51} or r_{42} contributing domains (<110> E-field), the effective electro-optic coefficients are on average an order of magnitude larger than those measured in geometries where the field does not pole the r_{51} or r_{42} contributing domains (<100> E-field). In Figure 5-43 a schematic representation of the a-domains along with representations of <100> and <110> oriented E-field vectors are shown. Only the component of the applied field perpendicular to the polar axis produces r_{51} and r_{42} contributions to the EO response. In Figure 5-43a it is apparent that among the a-domains, only the domain variants 5 and 6 can make r_{51} and r_{42} contributions. However because no component of the applied field is parallel to the polar axes of domain variants 5 and 6 they are not subject to 180^o poling. In contrast a-domain variants 3 and 4 *are* subject to poling by the <100> E-field. These domains make r_{13} and r_{33} contributions to the EO response, but no r_{51} or r_{42} contributions. Because these domains are subject to poling, a hysteresis of their collective EO response is expected upon cycling the magnitude of the applied voltage pulse train (see Figure 5-56). The fact that no hysteresis of the EO response is observed under the <100> fields indicates that the r_{13} and r_{33}-contributing domain variants (3 and 4) do not contribute appreciably to the total measured EO response under a <100> oriented E-field.

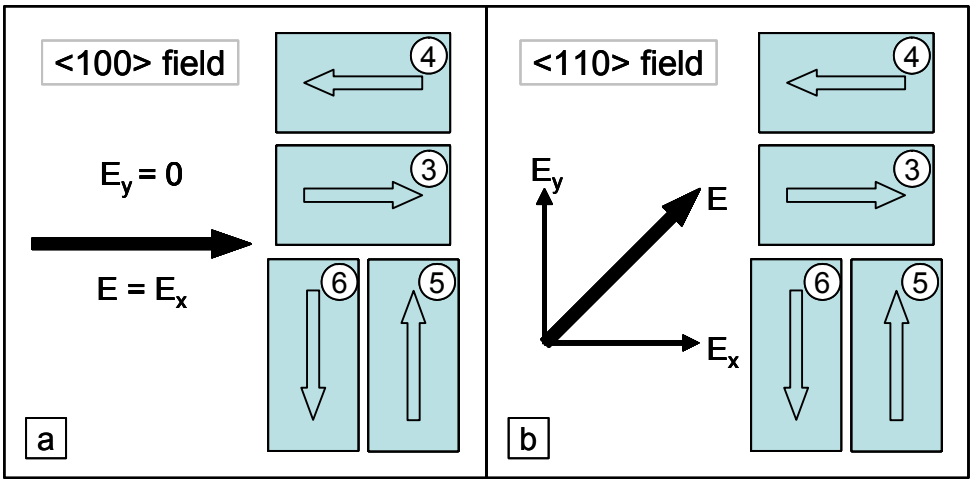

Figure 5-43. Schematic of the a-domains along with an applied (a) <100>, or (b) <110> E-field vector.

Additionally the hysteretic EO response measured under in-plane <110> fields is for the first time successfully modeled using measured electronic polarization in conjunction with the theoretical EO response of the different domain variants in the film. The elasto-optic effects that result from 90° domain switching are likewise considered. Finally, the dynamics of the extrinsic EO response due to both 90° and 180° domain switching were investigated as these have implications for the use of $BaTiO_3$ thin films in high frequency electro-optic devices[4,62] as well as potential applications for integrated MEMS devices[207].

5.2.2 EO coefficient measurements of epitaxial polydomain thin films

To determine the role of the domain structure on the EO response of the polydomain $BaTiO_3$ thin films, the bias dependence of the electro-optic coefficients was measured in both the waveguide and transmission geometries. In-plane electric fields were applied along either a <100> or <110> direction. As discussed in Chapter 4, the electro-optic response of $BaTiO_3$ thin films includes contributions effecting both the on-diagonal components of the impermeability tensor (r_{13} and r_{33}) as well as the off-diagonal components (r_{51}). While it will be shown from analysis of the hysteretic properties of the EO response discussed in Section 5.2.3 that the EO response is dominated by domains that contribute an off-diagonal r_{51} contribution to the EO response, it is not possible to quantify the individual components of the EO tensor using ellipsometric methods employed in this work. Additionally, the method used in determining the effective electro-optic coefficient assumes that the two allowed propagation eigenmodes do not rotate under an applied field. While it was shown in Chapter 4 that for most geometries, the orientation of the propagation eigenmodes does rotate under an applied field, by making the simplifying assumption that they do not, the derived effective electro-optic coefficients are directly comparable to those of $LiNbO_3$. In other words, the calculated *effective* electro-optic coefficient gives the magnitude of an on-diagonal electro-optic coefficient necessary to produce the measured modulation depth.

Transmission EO coefficient measurements

Measurements of the bias-dependence of the electro-optic coefficient were made in the transmission geometry using a phase retardation technique[175]. An in-plane electric field was applied

along either a <100> or a <110> direction with the propagation direction parallel to the surface normal as shown in Figure 5-44. Figure 5-45 shows the measured EO response at various analyzer angles of sample DT443 to a 1 kHz 10 V_{pp} sinusoidal driving voltage with a 20 V DC bias voltage.

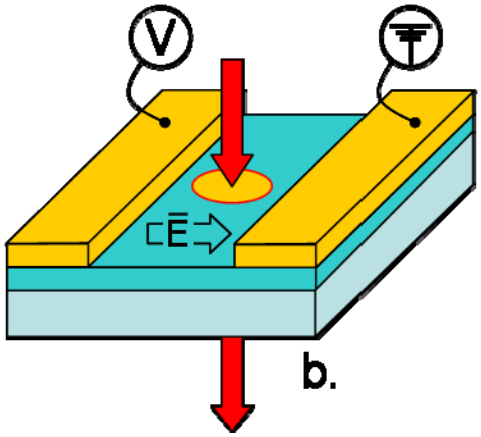

Figure 5-44. Schematic of typical transmission geometry EO measurement

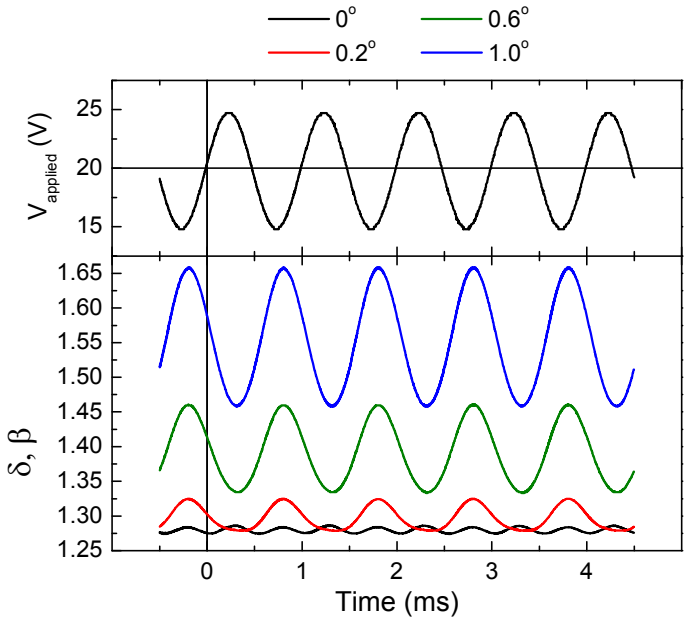

Figure 5-45. Sample DT443 measured response voltage due to the EO effect for a range of analyzer angles. As shown in the upper plot, the sample was driven with a 1kHz 10 V_{pp} sinusoidal driving voltage with a 20 V DC bias voltage. The legend refers to the response in the lower figure at the given analyzer angle. Note the characteristic frequency doubling at the null transmission point.

The transmitted intensity $I(\delta,\beta)$ of a Senarmont polariscope as a function of the analyzer angle β and the phase retardation due to the sample δ is given by[175,181]

$$I(\delta,\beta) = I_{\min} + I_{amp}\sin^2\left[\frac{\delta}{2} - \beta\right] = I_{\min} + I_{amp}\sin^2\left[\left(\frac{\delta_{amp}}{2}\sin(t\omega)\right) - \beta\right] \tag{5-27}$$

where as noted in Section 3.7, the zero of the analyzer angle is defined as that of the null transmission point under the applied bias voltage. I_{amp} is the peak-to-peak amplitude of the Senarmont transmission curve and $I_{\min}$ is just the noise level of the light entering the PMT due to stray light in the room and the imperfection of the optical elements employed in the polariscope. As discussed in Chapter 3, at points where the amplitude of the AC component of the applied voltage goes to zero, the field induced phase shift δ_{amp} likewise goes to zero such that equation (3.5) reduces to

$$I(\beta) = I_{\min} + I_{amp}\sin^2[-\beta] \approx I_{\min} + I_{amp}\beta^2 \tag{5-28}$$

where the approximation at right holds for the small analyzer angles typically employed. By measuring the response voltage at these points for a range of analyzer angles (with the input polarizaer and quarter wave-plate orientations fixed) and subsequently fitting the measured response with equation (5-28), the value of the response voltage corresponding to I_{amp} can be determined. I_{amp} corresponds to the response measured upon application of an applied voltage equal to the half-wave or V_π voltage. Due to the short interaction length in the transmission geometry I_{amp} can not be directly measured.

Figure 5-46 shows a plot of the measured response voltage when the field induced phase retardation angle δ_{amp} equals zero for a range of analyzer angles. From the fit to the measured data using equation (5-28) the response voltage corresponding to I_{amp} is ~390 V. As noted above, for small β, $\sin^2(-\beta) \approx \beta^2$, thus the observed parabolic dependence. Fits to the measured data using equation (5-28) or $I(\beta) = I_{\min} + I_{amp}\beta^2$ are equivalent for the small β angles employed.

As discussed in Chapter 3, for an ideal polariscope I_{min} is zero. Dropping I_{min} and dividing (3.5) by I_{amp} yields an expression for the transmitted intensity T of an ideal Senarmont polariscope normalized to unity as given by equation (3.6)

$$T = I/I_{amp} = \sin^2\left[\left(\frac{\delta_{amp}}{2}\sin(t\omega)\right) - \beta\right] \tag{5-29}$$

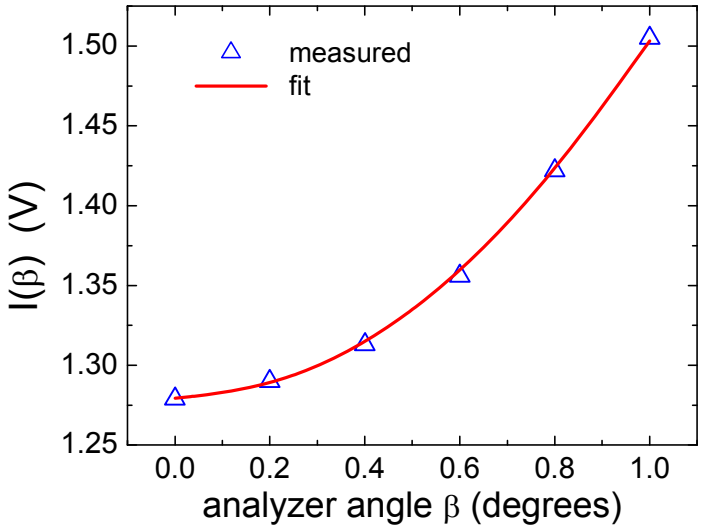

Figure 5-46. Sample DT443 response voltage measured at points where the AC amplitude of the applied voltage goes to zero plotted for a range of analyzer angles. From a fit to the data using equation (5-28) the response voltage corresponding to I_{amp} was found to be ~390V

Once the measured data shown in Figure 5-45 is normalized with respect to the value of I_{amp} determined from the fit to equation (5-28) or $I(\beta) = I_{\min} + I_{amp}\beta^2$, the now normalized data is described by equation (5-29).

All that is needed to determine the effective electro-optic coefficient is the magnitude of the field induced retardation angle δ_{amp}. It is not necessary to fit the normalized measured data in order to determine the magnitude of the field induced retardation angle δ_{amp}. It is sufficient to plot the peak-to-peak amplitude of the normalized EO response as a function of the analyzer angle. Then using δ_{amp} as the sole fitting parameter, this data is fit to the theoretical peak-to-peak amplitude given by equation (5-29) for a range of analyzer angles. Only the amplitude of the field induced retardation is required, the functional form being irrelevant to the determination of $T_{\max} - T_{\min}$ at a given analyzer angle β. As such the relevant fitting equation is

$$\left[T_{\max} - T_{\min}\right](\delta,\beta) = \sin^2\left(\frac{\delta_{amp}}{2} + \beta\right) - \sin^2\left(\frac{\delta_{amp}}{2} - \beta\right) \tag{5-30}$$

with the sole unknown fitting parameter being δ_{amp}. Using the small-angle approximation ($\sin^2 a \approx a^2$) equation (5-30) can be further simplified as

$$\left[T_{\max} - T_{\min}\right](\delta,\beta) = 2\delta_{amp}\beta \tag{5-31}$$

Figure 5-47 shows the normalized amplitude of the measured data at six different analyzer angles as well as the fit to equation (5-30). In this case the optimal fit was found for $\delta_{amp} = 7.2$ mRadians. From this data the change in the birefringence and r_{eff}

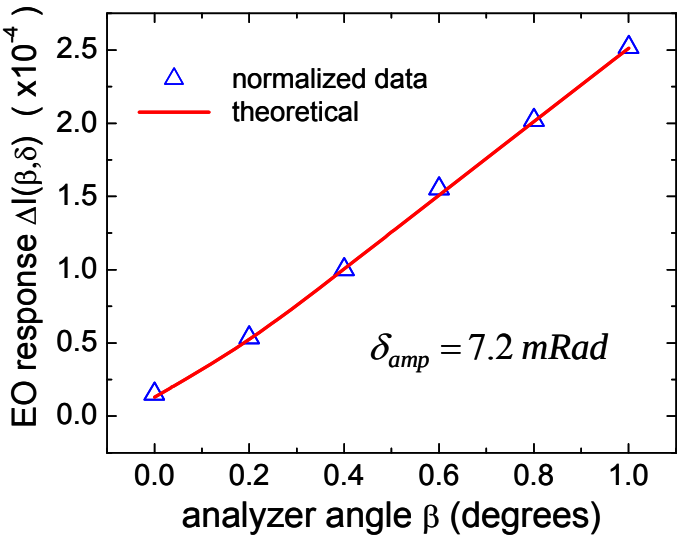

Figure 5-47. (DT443 20V bias 10Vpp 1kHz). Normalized measured modulation depth and theoretical modulation depth for a retardation amplitude of 7.2 mRad.

can be calculated. The phase retardation angle due to birefringence is given by[175,179]

$$\delta = \frac{2\pi\ell}{\lambda_o}\delta\Delta n \tag{5-32}$$

where ℓ is the interaction length which in the transmission geometry corresponds to the film thickness. The field induced change in the birefringence is here assumed to be given by[179]

$$\delta\Delta n(E) = \frac{1}{2}n^3 r_{eff} E \tag{5-33}$$

Substituting (5-33) into (5-32) yields

$$\delta(E) = \frac{\pi\ell}{\lambda_o}n^3 r_{eff} E \tag{5-34}$$

Solving for r_{eff} yields

$$r_{eff} = \frac{\delta(E)\lambda_o}{\pi\ell n^3}\left(\frac{1}{E}\right) = \frac{(2\delta_{amp})\lambda_o}{\pi\ell n^3}\left(\frac{g}{V_{PP}}\right) \tag{5-35}$$

where λ_o is the free space wavelength, n is the average refractive index in the film at λ_o, g is the electrode gap and ℓ is the film thickness. For sample DT443, the film thickness and index of refraction ($\lambda_o = 633$ nm) were 636 nm and 2.365, respectively. The electrode gap was 12 μm. Taking $\delta(E) = 2\delta_{amp}$ the

effective electro-optic coefficient for λ_o of 633 nm as determined from equation (5-35) is 414 pm/V. This is comparable to values previously measured on similar epitaxial $BaTiO_3$ thin films[12,47].

The electro-optic coefficients measured in the transmission geometry were routinely determined and in general the measured data was well described using equations (5-28) and (5-30). Figure 5-48 shows results for sample DT443 when the bias voltage is set to zero as well as for two additional samples. HR26 consists of a 550 nm $BaTiO_3$ thin film integrated on a Si(001) substrate using a 155 nm MgO buffer layer on top of a $SrTiO_3$ integration layer that is approximately 5 nm thick. The index of refraction of HR26 at 1550 nm is 2.309. The in-plane electric field was applied along a <110> direction. For an electrode gap of 5 μm and a V_{pp} of 30V, the effective electro-optic coefficient is calculated from equation (5-35) to be 8 pm/V. The quality of the fit demonstrates that the method is not limited by the relatively low electro-optic coefficient observed in this case.

EO measurement results are shown for a sample in which the in-plane field was applied along a <100> direction in Figure 5-48c. Sample AM069a is a 404 nm $BaTiO_3$ thin film with a refractive index of 2.389 at λ_o = 633 nm. The sample in question was annealed post growth for 10 hours in air at 1100 ^oC. For an electrode gap of 10 μm and a V_{pp} of 10V, the effective electro-optic coefficient is found from equation (5-35) to be 377 pm/V. From the top two plots in Figure 5-48, the electro-optic coefficient of sample DT443 with no bias field and the same 10V Vpp is 322 pm/V. The relevant parameters used in the determination of the effective electro-optic coefficients for samples DT443, HR26 and AM069a are given in Table 5-3.

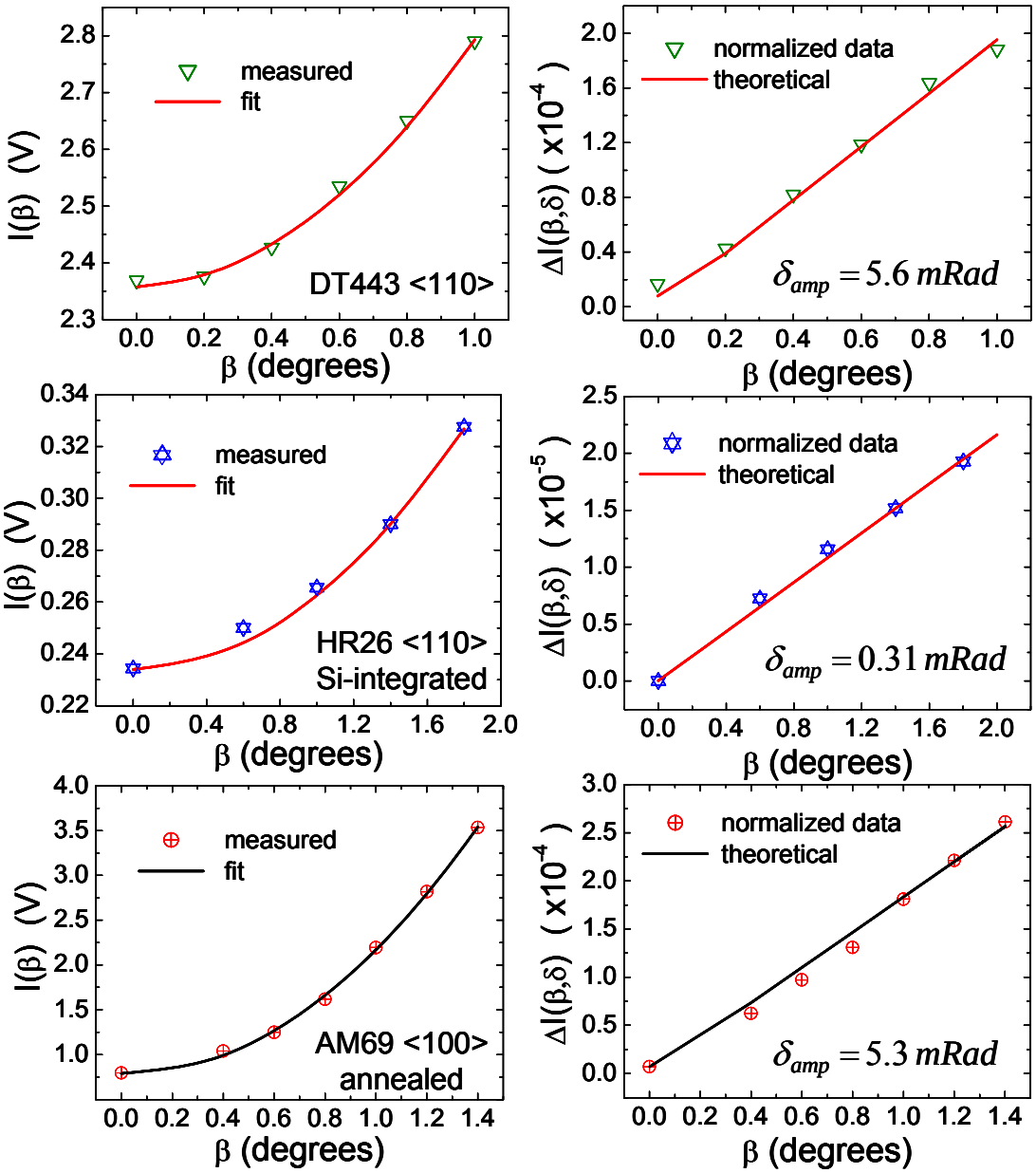

Figure 5-48 Data for three additional EO coefficient analyses are presented. As in Figure 5-46, the fit to the measured data in the figures at left is used to determine the value of I_{amp} that is subsequently used to normalize the measured modulation depth. The figures at right show the resulting normalized modulation depth (unitless) as a function of the analyzer angle as well as the fit using equation (5-30). The values of δ_{amp} corresponding to the fits to the data are given in the figures at right.

Table 5-3. Relevant parameters for the samples examined in demonstration of the efficacy of the method of determination of the effective electro-optic coefficient

Sample ID	ℓ (nm)	g (μm)	λ_o (nm)	n @ λ_o	V_{bias} (V)	Vpp (V)	δ_{amp} (mRad)	r_{eff} (pm/V)
DT443	636	12	633	2.365	20	10	7.2	414
DT443	636	12	633	2.365	0	10	5.6	322
AM069a	404	10	633	2.389	12.5	10	5.2	377
HR26	550	5	1550	2.309	15	30	0.31	8

The error in the calculated r_{eff} value due to inaccuracies in the estimate of I_{amp} was analyzed. Because the magnitude of the response voltage I_{amp} is determined by fitting equation (5-28) over a small range of analyzer angles very close to the null transmission point, this constitutes a possible source of error. By determining the deviation in the calculated effective electro-optic coefficient due to error in the estimate of I_{amp} it was found that the error is proportional to the magnitude of the electro-optic coefficient. Figure 5-49 shows the percent error in the calculated r_{eff} value due to error in the determination of I_{amp} for two samples HR26 (r_{eff} = ~8 pm/V) and AM069a (r_{eff} = 377 pm/V). As seen from the figure, the percent error introduced is similar in both cases despite the large difference in the magnitude of the r_{eff} values. The plots at left in Figure 5-49 show the optimal fits to equation (5-28) for both films as well as those for ±10% error in the estimate of I_{amp}. From these it is apparent that ±10% error in the estimate of I_{amp} should represent a very conservative estimate of the rage of possible error in the estimate of I_{amp}. This corresponds to a conservative range for the error in the estimate of r_{eff} of +10 to12% to -7.5%.

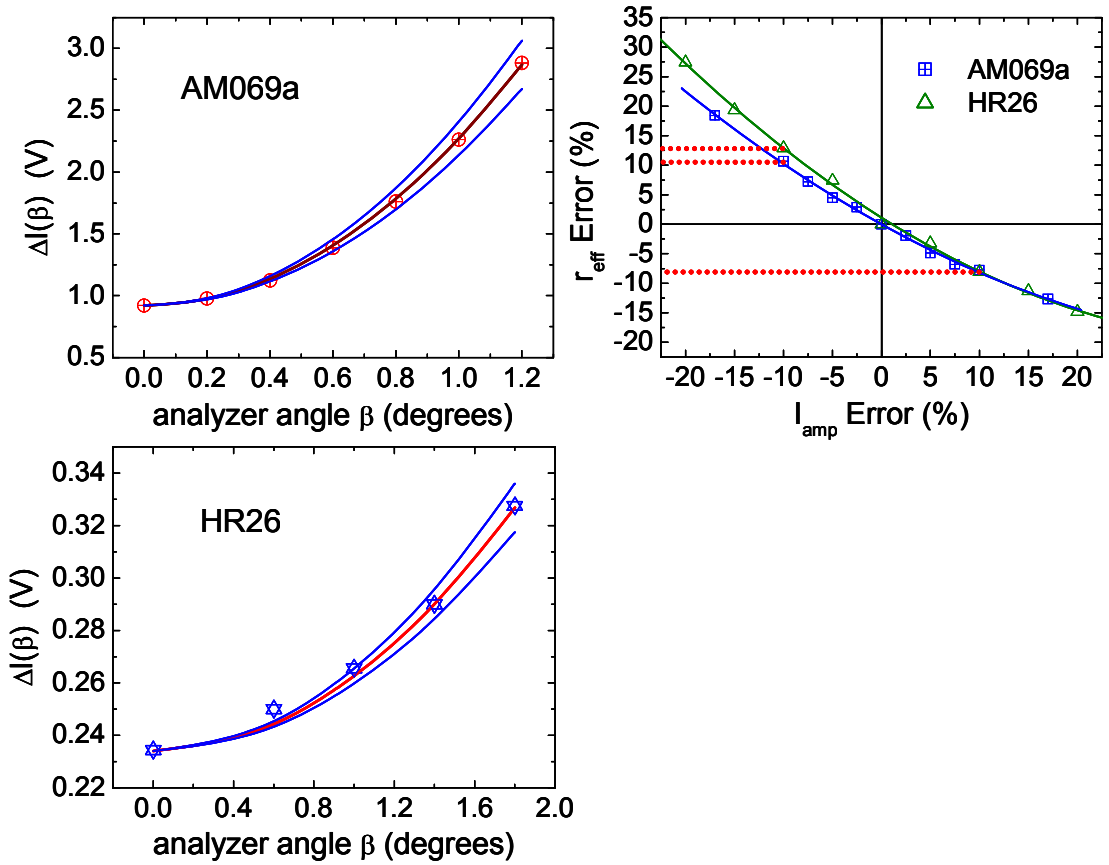

Figure 5-49. Figures at left show optimal fit to equation (5-28) as well as those for ±10% error in the estimate of I_{amp}. The figure at right shows the resulting percentage error in the calculated r_{eff} value due to error in the estimate of I_{amp}

Waveguide EO coefficient measurements

The electro-optic coefficients of the $BaTiO_3$ thin films were also measured in the waveguide geometry. The long interaction lengths realized in the waveguide geometry make determination of the electro-optic coefficient far simpler than in the transmission geometry. In the waveguide geometry, V_π is measured directly from the scope and the effective electro-optic coefficient is then given by.

$$r_{eff} = \frac{\lambda_o g}{n^3 \ell V_\pi \Gamma \phi} \tag{5-36}$$

where λ_o is the free space wavelength, n is the average refractive index in the film at λ_o, g is the electrode gap and ℓ is the interaction length which in this case is device length. Γ is the overlap integral of the optical and microwave modes and ϕ is an attenuation factor due to the presence of the SiO_2 buffer layer.

Figure 5-50 shows the electro-optic response of sample DT446 captured from the oscilloscope. From the driving voltages corresponding to the peak and trough of the electro-optic response of the overdriven sample, the V_π voltage is found to be 3.3 V. The device length and electrode gap for this sample were 3.2 mm and 8μm, respectively. For the 570 nm thick film the overlap factor Γ calculated using conformal mapping techniques was 0.59. As the sample in question has no SiO_2 buffer layer, the attenuation factor ϕ is just 1. Using the given film parameters in equation (5-36), the corresponding electro-optic coefficient for a V_π of 3.3 V is 162 pm/V at the measurement λ_o of 1561 nm.

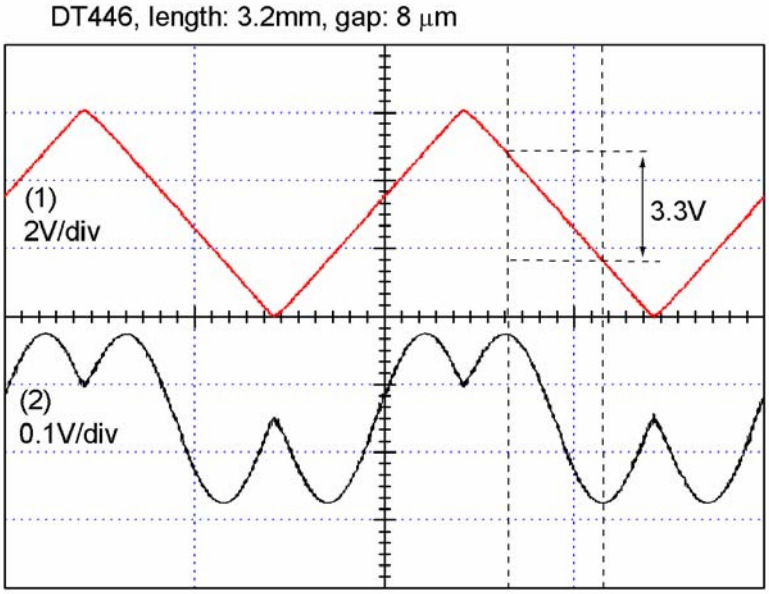

Figure 5-50. Electro-optic response and a I kHz driving voltage of sample DT446 measured in the waveguide geometry. Measurement was made at a bias voltage of 10 V. From the measured V_π of 3.3 V and the geometry of the modulator, the effective electro-optic coefficient under the 10 V bias was 162 pm/V at λ_o of 1561 nm.

Summary of EO coefficient measurements

Electro-optic coefficient measurements were made on twenty $BaTiO_3$ thin films. For fifteen of these samples the bias dependence of the EO coefficient is likewise reported. General observations are as follows. The observed bias dependence of the EO coefficient under <100> and <110> oriented in-plane E-fields is consistent with the hypothesis that the ability of the field to pole the domain variant that make r_{51} or r_{42} contribution to the EO response under the applied field is a necessary condition to realize large

effective electro-optic coefficients. The domains making r_{51} and r_{42} contributions under a <100> oriented field are not subject to 180° poling which would improve the measured r_{eff}, but rather to 90° poling which diminishes the measured r_{eff}, hence the flat to declining r_{eff} values observed with increasing bias field.

As shown in the box and scatter plots in Figure 5-51, the median and average effective electro-optic coefficient for measurements under an in-plane <100> oriented field of as-grown films was just 12 pm/V with values ranging from 2 to 25 pm/V. In contrast the median and average effective electro-optic coefficients for measurements under an in-plane <110> oriented field were 153 and 181 pm/V respectively with values ranging from 8 to 424 pm/V. The results of all of the EO coefficient measurements including their bias dependence are summarized Table 5-4 and Table

5-5 which respectively give the results for measurements under in-plane E-fields along <100> and <110> directions.

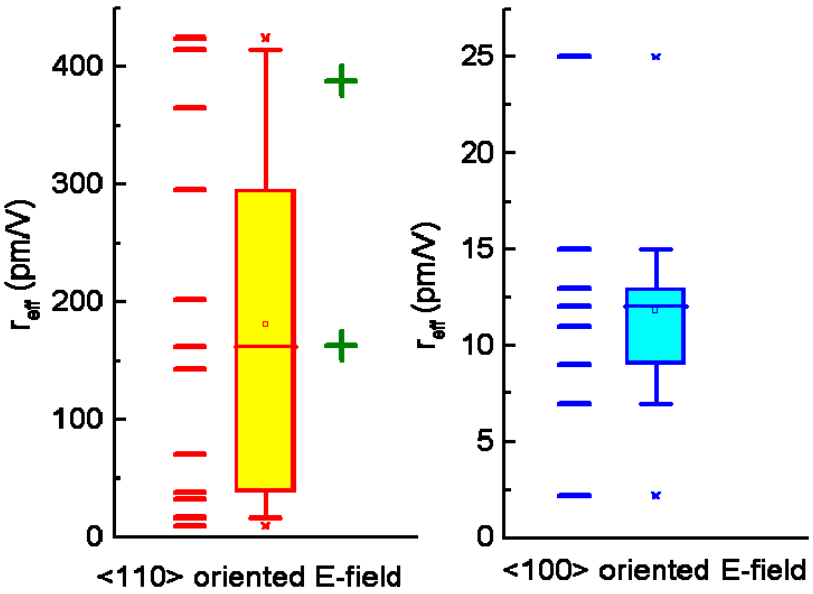

Figure 5-51. Scatter and box plots of the effective electro-optic coefficients measured with in-plane electric field oriented along <110> and <100> directions respectively. The two samples marked by green crosses in the left figure are the two <100> samples that were annealed in air at 1100 °C prior to measurement. The median r_{eff} values for measurement under <110> and <100> fields were 153 pm/V and 12.5 pm/V respectively.

Distinct trends in the bias dependence of the EO coefficient were observed for in-plane <100> and <110> oriented fields. In Figure 5-52 and Figure 5-53 the bias dependence of the effective EO coefficients are given for representative films from Table 5-4 and

5-5. Figure 5-52 and Figure 5-53 show the bias dependent r_{eff} values for films measurements under <110> and <100> in-plane electric fields, respectively. As seen from Figure 5-52, under <110> oriented fields the EO coefficient is in all cases optimal at a finite bias. From Figure 5-53 it is observed that under <100> oriented fields, the effective EO coefficient decreases with increasing bias.

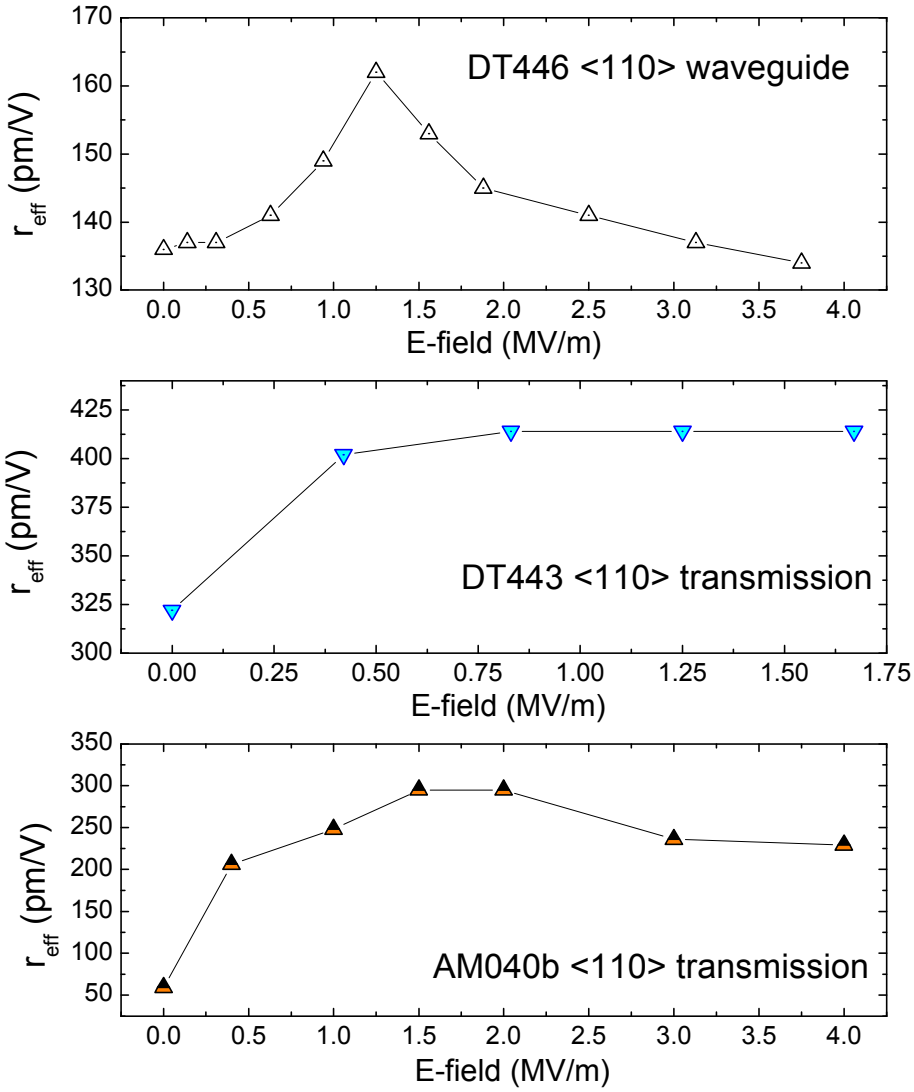

Figure 5-52. Bias dependence of r_{eff} under in-plane <110> oriented E-fields are shown for samples DT446, DT443 and AM040b. Foe each sample, the measurement geometry is indicated.

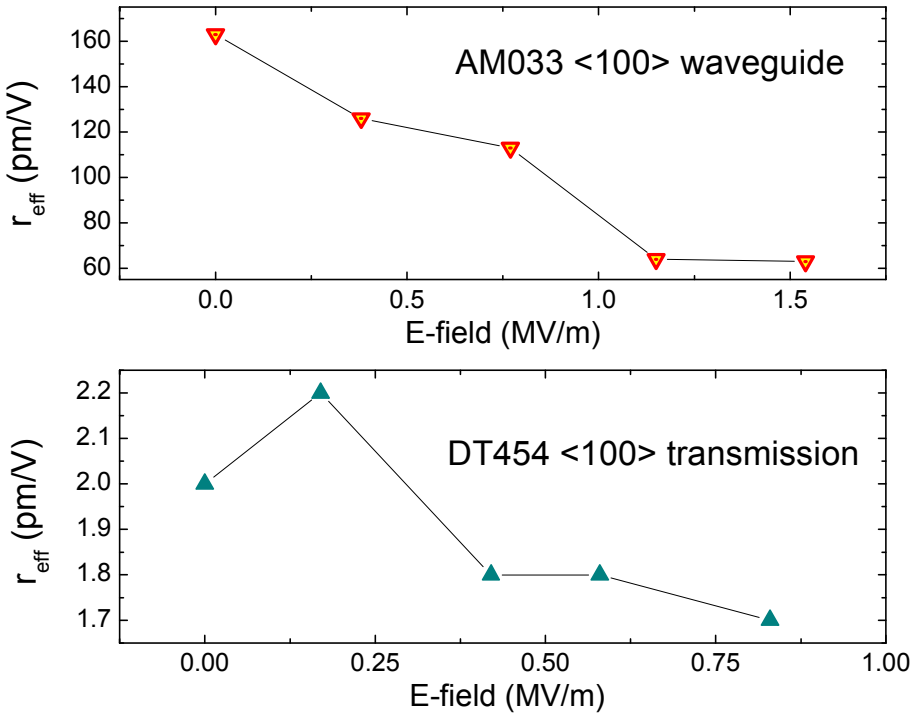

Figure 5-53. Bias dependence of r_{eff} under in-plane <100> oriented E-fields are shown for samples AM033 and DT454, measured in the waveguide and transmission geometries respectively.

The decrease in the measured r_{eff} values with increasing bias under a <100> oriented field is consistent with increased 90° flipping of the r_{51} and r_{42} contributing domains with increasing bias. When the r_{51} and r_{42} contributing domains undergo a 90° domain flip they no longer make r_{51} and r_{42} contributions to the response as no component of the applied E-field is perpendicular to their polar axis subsequent to the flip.

The effective electro-optic coefficients measured under <110> oriented E-field were generally observed to increase with increasing bias field in contrast to measurements under <100> oriented E-fields. Under an in-plane <110> oriented field all of the a-domain variants in the film are subject to 180° poling by the bias field while none are subject to 90° poling. A component of the applied field of $E_{app}/\sqrt{2}$ is likewise maintained perpendicular to the polar axis of every a-domain variant. Hence the increasing r_{eff} values with increasing bias under in-plane <110> oriented E-fields.

Table 5-4. Effective electro-optic coefficient measurement results under an in-plane <100> oriented electric field

Film ID	Orient.	Meas. Geo.	λ_o (nm)	Effective EO Coefficient (pm/V) under Bias E-Field of (MV/m)				
				R_{eff}	R_{eff}	R_{eff}	R_{eff}	R_{eff}
				E_{bias}	E_{bias}	E_{bias}	E_{bias}	E_{bias}
AM069b	100	Tran	633	5	9			
				0	+0.33			
AM069a	100	Tran	633	388	512	373	377	439
				0	+0.42	+0.83	+1.25	+1.67
DT454	100	Tran	633	2	2.2	1.8	1.8	1.7
				0	+0.17	+0.42	+0.58	+0.83
AM003*	100	WG	1550	12				
				0				
AM033	100	WG	1555	163	126	113	64	63
				0	+0.38	+0.77	+1.15	+1.54
AM047*	100	WG	1550	18	19	22	24	25
				0	+0.67	+1.33	+2.00	+2.67
DT394*	100	WG	1550	7				
				+0.67				
DT438*	100	WG	1550	11				
				+0.5				
DT444*	100	WG	1550	13				
				+0.5				
DT454*	100	WG	1550	15				
				+0.5				

* measured by Pingsheng Tang

Table 5-2. Effective electro-optic coefficient measurement results under an in-plane <110> oriented electric field

Film ID	Meas. Geo.	λ_o (nm)	Effective EO Coefficient (pm/V) under Bias E-Field of (MV/m)										
			R_{eff}	R_{eff}	R_{eff}	R_{eff}	R_{eff}	R_{eff}	R_{eff}	R_{eff}	R_{eff}	R_{eff}	R_{eff}
			E_{bias}	E_{bias}	E_{bias}	E_{bias}	E_{bias}	E_{bias}	E_{bias}	E_{bias}	E_{bias}	E_{bias}	E_{bias}
HR26	Tran	1561	8										
			-3										
AM016	Tran	633	23	32	22	20							
			+3.0	-3.0	-2.6	-2.4							
AM040b	Tran	633	59	206	248	295	295	236	229				
			0	+0.4	+1.0	+1.5	+2	+3.0	+4.0				
DT443	Tran	633	322	402	336	414	379	414	344	414	344		
			0	+0.42	-0.42	+0.83	-0.83	+1.25	-1.25	+1.67	-1.67		
AM009*	WG	1550	24	33	45	47	54	63	70				
			0	+0.33	+0.67	+1.00	+1.33	+1.67	+2.00				
AM034*	WG	1550	12.5	12.9	13.7	14.9	16.3	16.5	17				
			0	+0.33	+0.67	+1.00	+1.33	+1.67	+2.00				
AM039*	WG	973	303	353	424	424	424	424					
			0	+1.0	+2.0	+3.0	+4.0	+5.0					
AM039*	WG	1561	225	300	360	364	364	360					
			0	+1.0	+2.0	+3.0	+4.0	+5.0					
AM055	WG	1550	152	170	202	198	202						
			0	+0.31	+0.63	+0.94	+1.25						
DT436*	WG	1550	38										
			+2.5										
DT443*	WG	1561	125	127	129	135	143	139	131	125			
			+0.63	+1.25	+1.88	+2.50	+3.13	+3.75	+4.38	+5.00			
DT446*	WG	1550	136	137	137	141	149	162	153	145	141	137	134
			0	+0.14	+0.31	+0.63	+0.94	+1.25	+1.56	+1.88	+2.50	+3.13	+3.75

* measured by Pingsheng Tang

Since annealing effects the domain structure as well as the defect structure of the film, the EO coefficient was measured on annealed films as well. Two films (AM033 and AM069a) that were annealed in air at 1100 ^{o}C for 4 and 10 hours, respectively prior to measurement under an in-plane <100> oriented field. They exhibited effective electro-optic coefficients when driven at 1 kHz, of 163 and 388 pm/V, respectively when measured at zero bias. They correspond to the two data points marked by green crosses in Figure 5-51. In contrast, the effective electro-optic coefficients of the as grown sample AM069b from the same film was just 5 pm/V when driven at 5kHz under zero bias. No as grown EO measurement was made on sample AM033.

The c-domain volume fraction increased significantly in both films upon annealing as seen from the surface normal {200} Bragg reflections in Figure 5-54. The post annealed c-domain fractions for AM033 and AM069a were 84% and 85% respectively, representing increases of the c-domain volume fraction of 21% and 15% respectively[13]. In spite of the large increase in the c-domain volume fractions, this is not believed to be the source of the large increase in the effective electro-optic coefficient. The reasons for this are as follows. No correlation was observed between the c-domain fractions and the EO coefficients measured in our films. From the x-ray data shown in Figure 5-54 it is evident that none of the as-grown films have c-domain fractions as large as those observed in the two annealed samples. The c-domain fraction is still appreciable in several of the films. The c-domain fraction in samples DT454 and DT394 are 0.75 and 0.69, respectively. Nevertheless the EO coefficients are characteristically small in all the as-grown films measured with an in-plane <100> oriented E-field. Additionally, sample AM069a was measured in the transmission geometry and as noted in Chapter 4, the c-domains do not contribute to the EO response in the transmission geometry[187].

As such an increase in the c-domain fraction can not possibly explain the improved EO response of AM069a after annealing. While the mechanism responsible for the improved EO response observed in

[13] The volume fractions were determined from the integrated intensities of the (200) and (002) surface normal Bragg reflections determined from a fit of the sum of two Gaussian peaks to the surface normal {200} peak with consideration given to the relative intensities of the $BaTiO_3$ (200) and (002) peaks. A more detailed explanation of the method is given by Towner[36] D. J. Towner, Ph.D. Thesis, Northwestern University, 2005.

the annealed films is not known one possibility is modification of the point defect structure. Both first principles[208,209] and experimental studies[210-214] have indicated that the defect dipoles associated with oxygen vacancies can act to pin domain walls. Consequently, domain wall pinning by defects could prevent poling of the domains or possibly effect their intrinsic EO response. Quantitative analysis of defect structures in conjunction with electro-optic characterization would be required to unambiguously determine the role of oxygen vacancies on the electro-optic properties of the $BaTiO_3$ thin films.

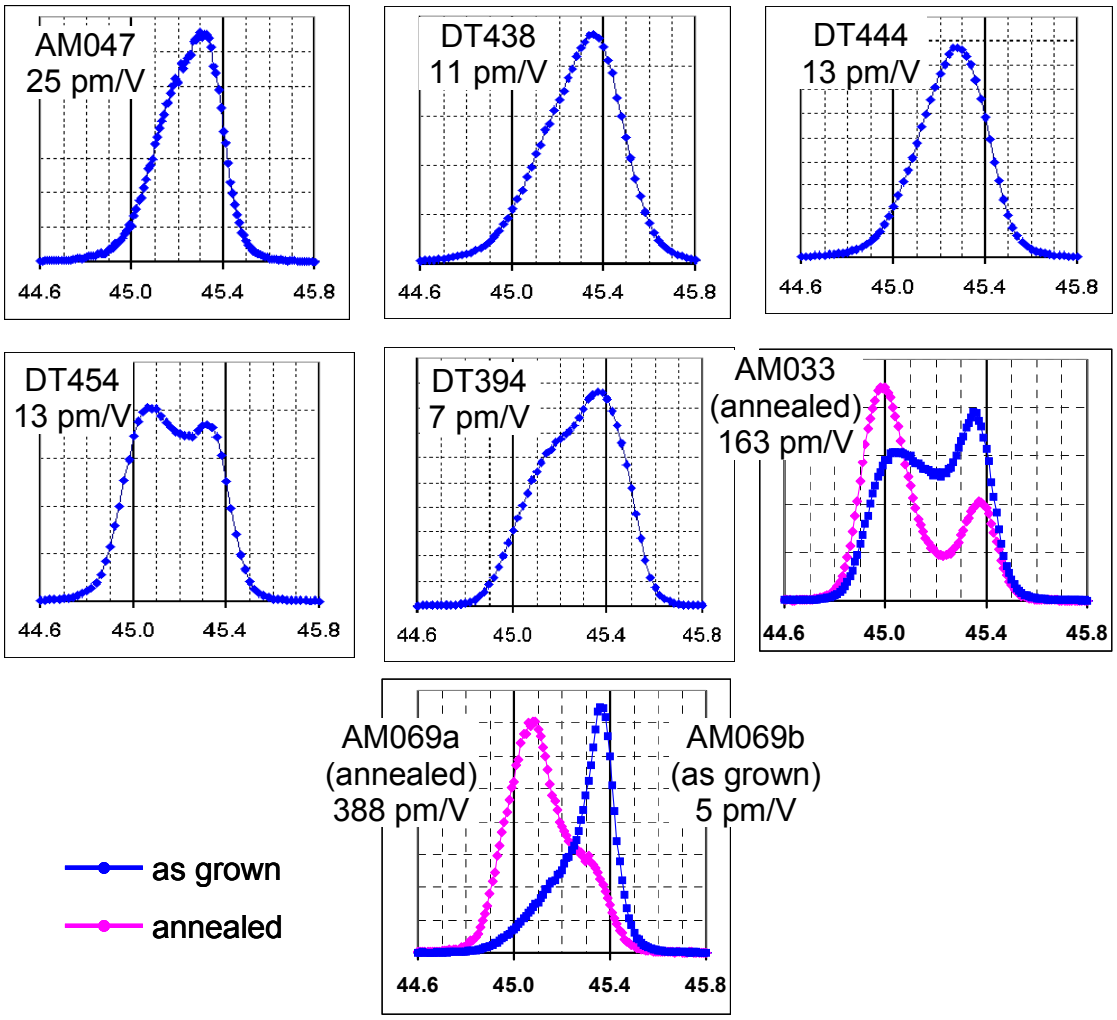

Figure 5-54. X-ray diffraction analysis of domain structure. Surface normal Bragg reflections for a number of samples are shown along with the corresponding EO coefficients measured under an in-plane <100> oriented electric field. Significant increases in the c-domain fractions were observed for the two annealed films in which relatively large EO coefficients were measured. However several of the as-grown samples such as DT454 and DT394 have fairly large c-domain fractions and yet their EO coefficients are rather modest.

5.2.3 Effect of field on the EO response

The effect of field on the EO response was investigated to gain insight into the relationship between the EO response to the domain structure in the thin films. From analysis of the EO response to monopolar voltage pulse trains it is concluded that under both in-plane <100> and <110> oriented E-fields, the EO response is dominated by the domains that make off-diagonal (r_{51} or r_{42}) contributions to the measured EO response; this is true regardless of whether the applied field direction acts to pole the r_{51} and r_{42} contributing domains. In order to pole a domain an appreciable component of the applied field must be parallel to the polar axis of the domain. Hysteresis of the EO response is a direct result of the poling of the domains contributing to the response. When hysteresis is not observed in the EO response this is because the contributing domains are not subject to 180^o poling under the applied field. The particular domain variants that contribute appreciably to the EO response can therefore be inferred from the presence or absence of hysteresis in the EO response.

Under in-plane <100> oriented fields EO hysteresis is not observed; this is attributed to the inability of a <100> field to pole the r_{51} and r_{42} contributing domains. In Figure 5-55a the four a-domain variants are shown along with a <100> field vector[14]. Only the component of the applied field perpendicular to the polar axis produces r_{51} and r_{42} contributions to the EO response. In Figure 5-55a it is apparent that among the a-domains, only the domain variants 5 and 6 can make r_{51} and r_{42} contributions. However because no component of the applied field is parallel to the polar axes of domain variants 5 and 6 they are not subject to 180^o poling. In contrast a-domain variants 3 and 4 *are* subject to poling by the <100> E-field. These domains make r_{13} and r_{33} contributions to the EO response, but no r_{51} or r_{42} contributions. Because these domains are subject to poling, a hysteresis of their collective EO response is expected upon cycling the magnitude of the applied voltage pulse train (see Figure 5-56). The fact that no hysteresis of the EO response is observed under the <100> fields indicates that the r_{13} and r_{33}-contributing

[14] The c-domains are not shown as the c-domains are never subject to 180^o poling by an in-plane field.

domain variants (3 and 4) do not contribute appreciably to the total measured EO response under a <100> oriented E-field.

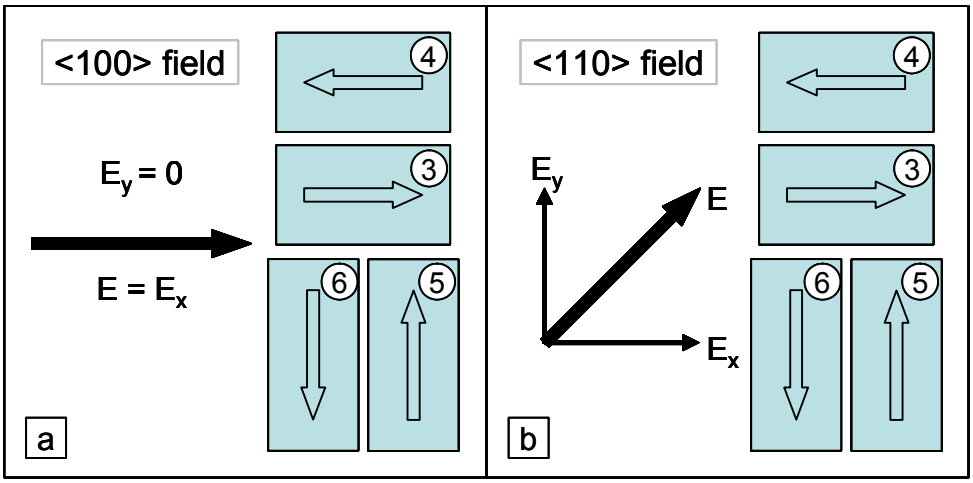

Figure 5-55. Schematic of the a-domains along with an applied (a) <100>, or (b) <110> E-field vector.

Under in-plane <110> oriented fields EO hysteresis is observed; this is attributed to the ability of the <110> field to pole the r_{51} or r_{42} contributing domains. In Figure 5-55b the four a-domain variants are shown along with a <110> field vector. In Figure 5-55b it is apparent that E_x gives rise to r_{51} and r_{42} contributions for domain variants 5 and 6 while E_y acts to pole these domain variants. Similarly, E_y gives rise to r_{51} and r_{42} contributions for domain variants 3 and 4 while E_x acts to pole these domain variants. Therefore, under an in-plane <110> field all of the a-domains contribute r_{51} or r_{42} contributions to the EO response and all of the a-domains are likewise subject to 180^o poling by the applied field. As a result hysteresis of the EO response is observed as seen in Figure 5-56. It is proposed that the large effective electro-optic coefficients under in-plane fields along the <110> direction result from the ability of the field to pole the domains making r_{51} and r_{42} contributions to the EO response while maintaining a large component of the applied field perpendicular to the polar axis so that appreciable r_{51} and r_{42} EO contributions are realized.

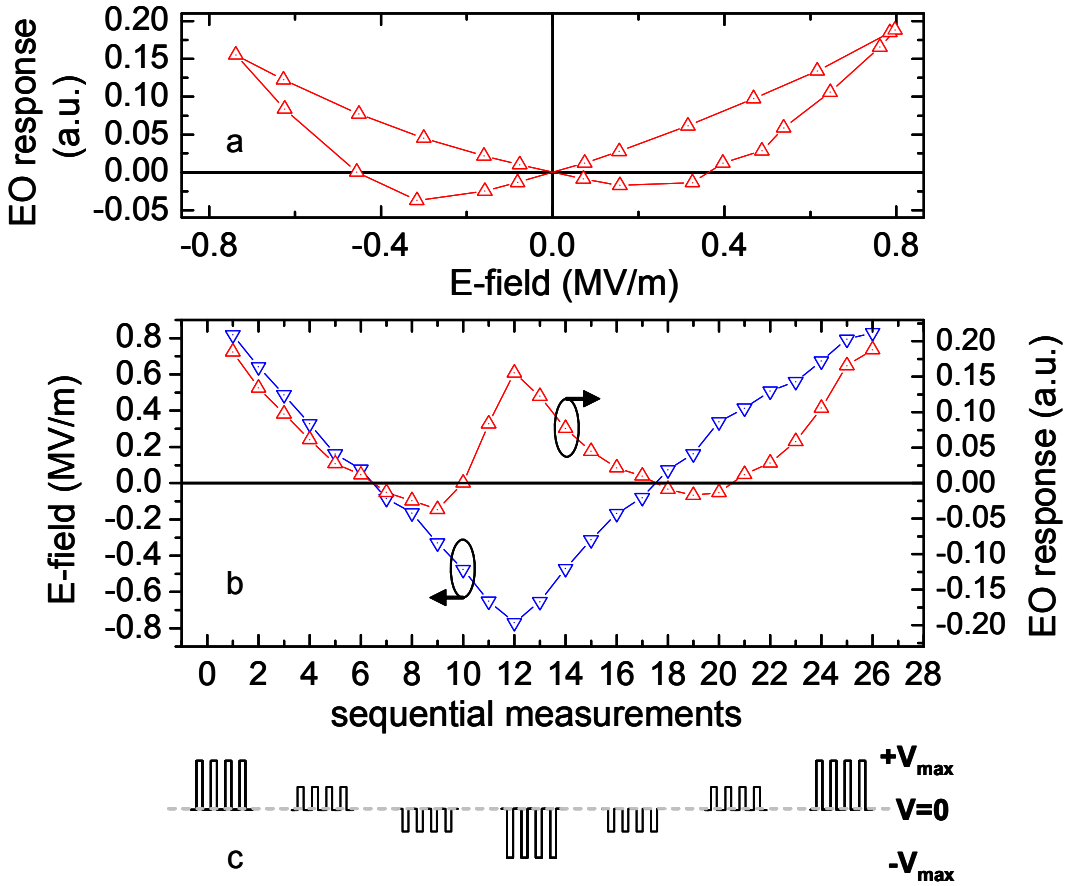

Figure 5-56.**a**. shows the resulting hysteretic EO response observed when the response is due to domain variants subject to poling by the applied field. **b**. shows the cycling of the voltage pulse train amplitude and polarity along with the resulting EO response. In **c**. a stylistic representation of the monopolar voltage pulse trains of varying amplitude and polarity is shown. The result shown here are from sample DT443 measured with an in-plane E-field along a <110> direction.

Prior to discussing the experimental results of the voltage pulse measurements a brief description of the measurement technique is given. During the voltage pulse measurements, the samples were driven with a continuous monopolar pulse train by the HP214B pulse generator as outlined in Chapter 3 and shown schematically in Figure 5-56c. Pulse trains consisting of typically 10 ms pulse widths were employed at a frequency of 1 to 10 Hz yielding low duty cycles of 0.01 to 0.1. The applied voltage was cycled as shown in Figure 5-56b and c in order to observe evidence of hysteresis in the EO response. Figure 5-57(a) and (b) show typical results for samples measured in the transmission geometry with in-plane electric fields in a <100> and a <110> direction respectively. As stated previously, under a <110> field hysteresis is observed while under a <100> field no hysteresis is observed. Figure 5-57(c) shows the

result for a sample measured in the waveguide geometry with an in-plane E-field applied along a <100> direction with an orthogonal in-plane propagation direction. No hysteresis is observed in the waveguide geometry under a <100> field. A more detailed analysis of the voltage pulse measurement results under <100> and <110> fields is provided in the following sections.

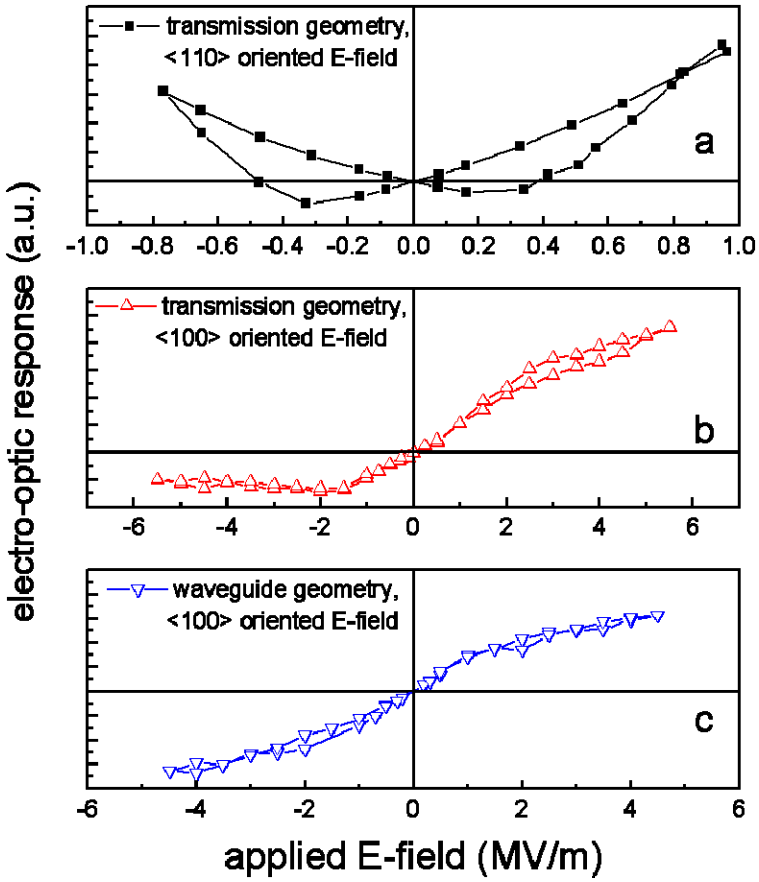

Figure 5-57. EO response verses the E-field associated with the application of a monopolar continuous voltage pulse train. Hysteresis is observed in (a) (DT443) where an in-plane <110> oriented E-field is applied, while no hysteresis is observed for an in-plane <100> oriented field for either propagation in transmission (b) (AM069a) or in a waveguide (c) (DT454).

5.2.3.1 EO pulse response under in-plane <100> oriented E-field

The lack of any observed hysteresis in the electro-optic response under <100> oriented in-plane E-fields is consistent with that response being due to the domain variants that make finite r_{51} and r_{42} contributions to the EO response as shown in Figure 5-55a. Since the r_{51} and r_{42} contributing domain variants under a <100> field are not subject to 180° poling by these fields, no hysteresis in their EO

response is expected. In contrast, those domain variants that do not make r_{51} and r_{42} contributions to the EO response *are* subject to 180° poling by the <100> oriented E-fields. As such, if these contributions were appreciable, then hysteresis should be observed in the EO response as shown in the following analysis.

An analysis is given of how poling of domains contributing to the EO response gives rise to the typical "butterfly" EO hysteresis loops often[37,41,165,167,169] reported in the literature and observed in our films. While the analysis is developed in terms of domain variants 3 and 4 in Figure 5-55a it is completely general in nature. Consider the expected change in the EO response for domain variants 3 and 4 from Figure 5-55a with changing applied E-field as shown schematically in Figure 5-58a. It is assumed in Figure 5-58 that non-remnant back switching of the domains is negligible. Let ΔA_{ij} represent the difference in *relative* volume fractions of domain variants i and j as given by

$$\Delta A_{ij} = \left(A_i - A_j\right) \Big/ \left(A_i + A_j\right) \tag{5-37}$$

where A_i is the volume fraction of the ith domain variant. For two anti-parallel domain variants such as 3 and 4, ΔA_{ij} should be proportional to the contributions to the electronic polarization hysteresis loop due strictly to the ferroelectric switching. In the absence of appreciable back switching this is the same as the remnant hysteresis loop defined in Section 5.1. For a film initially poled to a maximum value of ΔA_{43} (point 0 in Figure 5-58), the amplitude of the EO response decreases as the applied E-field decreases due strictly to the intrinsic field dependence of $\delta\Delta n$ as seen in quadrants I of Figure 5-58a with ΔA_{43} (Figure 5-58b) remaining fairly constant. With the change in polarity of the applied E-field, the sign of $\delta\Delta n$ changes as seen in quadrant III of Figure 5-58a. As the magnitude of the E-field of reverse polarity increases, the coercive field of an increasing number of type 4 domains is exceeded, resulting in 180° domain reversal (4⇒ 3) and the magnitude of ΔA_{43} decreases as seen in quadrant III of Figure 5-58b. At point (1) equal volume fractions of variants 3 and 4 ($\Delta A_{43} = 0$) result in an r_{eff} of zero[15]. These points

[15] Because we are here considering the EO effects involving changes in the on-diagonal components of the impermeability tensor equal volume fractions of 180° domain variants cancel completely. As already pointed out in Chapter 4 this is not strictly the case when the EO effect includes off-diagonal components of the impermeability tensor (i.e. due to r_{51} and r_{42} contributions)

where $\Delta A_{43} = 0$, labeled 1 and 3 in Figure 5-58, correspond to the coercive field of the remnant hysteresis loop of the film as defined in Section 5.1. With further increase in the magnitude of the E-field of negative polarity, the volume fraction of domain variant 3 exceeds that of type 4 ($\Delta A_{43} < 0$) and the sign of δΔn again becomes positive as seen in quadrant II of Figure 5-58a and b.

Analogous arguments hold for the change in the EO response in going from point (2) back to point (0) in Figure 5-58a and b. The predominant domain type (3 or 4) based on volume fraction in each quadrant of Figure 5-58a and b is indicated in the figure. In other words, when $\Delta A_{43} > 0$ type 4 is the predominant variant, while when $\Delta A_{43} < 0$ type 3 is the predominant variant.

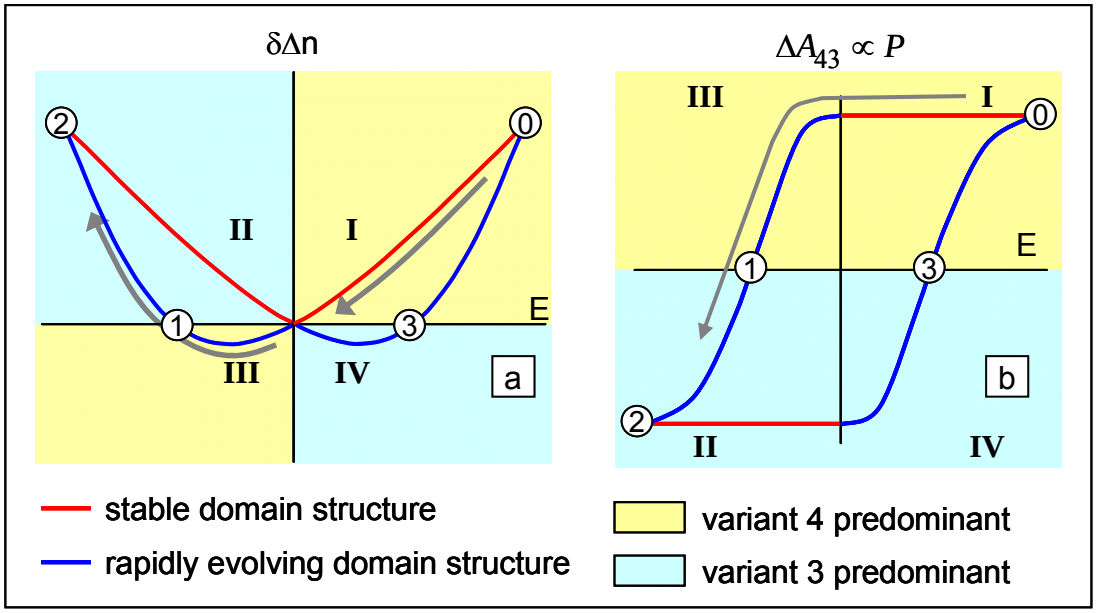

Figure 5-58.(a) Theoretical E-field dependence of the film average δΔn due to domain variants 3 and 4 from Figure 5-55a.(b) theoretical relative volume fractions ΔA_{43} of anti-parallel domain variants 3 and 4 from Figure 5-55a. ΔA_{43} is expected to be proportional to the remnant polarization hysteresis loop defined in Section5.1.

The observation that the measured EO response as a function of the applied <100> oriented E-field shown in Figure 5-57(b) and (c) bears no resemblance to that in Figure 5-58 indicates that domain variants 3 and 4 do not contribute appreciably to the measured EO response seen in Figure 5-57(b) and (c). In contrast if the observed EO response was due to domain variants 5 and 6 in Figure 5-55a then

consistent with the observed response, no hysteresis is expected as these variants are not subject to 180^o poling.

The non-hysteretic EO response under a <100> field shown in Figure 5-57b and c are consistent with the theoretical EO response due to domain variant 5 from Figure 5-55a, with attenuation due to the onset of 90^o-domain flipping at higher fields. Figure 5-59 shows a schematic representation of the theoretical EO response due to domain variant 5 from Figure 5-55a. adapted from the calculated theoretical response shown in Figure 4-16. Domain variants 5 and 6 *are* subject to 90^o domain flipping under the <100> oriented E-fields. Subsequent to such a 90^o flip the domain in question no longer makes any r_{51} or r_{42} contributions to the EO response because subsequent to the flip the polar axis is parallel to the applied E-field. If an increasing fraction of the domains undergo 90^o domain flipping as the E-field increases then the domain volume fraction contributing to the response decreases. The EO response or $\Delta I(E)$ (since what is measured is the change in transmitted intensity upon application

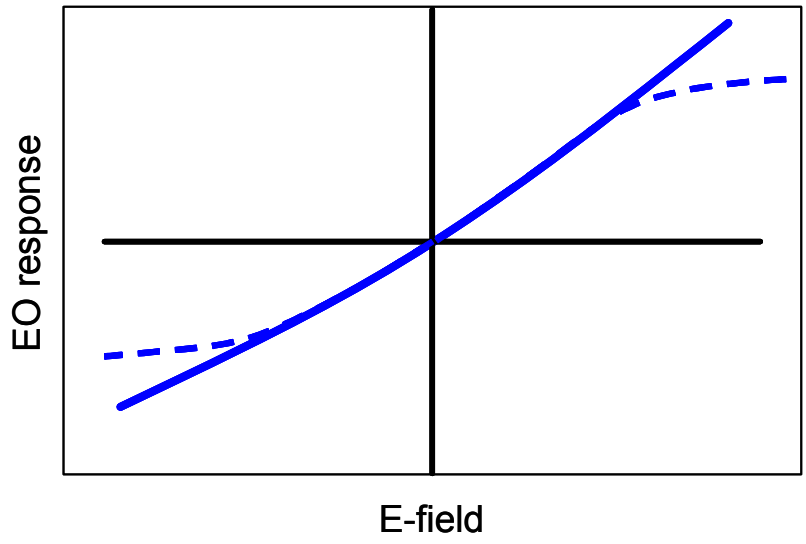

Figure 5-59. Schematic showing the theoretical field dependent EO response(solid line) and a hypothetical attenuated response due to 90^o-domain flipping of the r_{51} and r_{42} contributing domain variants.

of an E-field) in this case would be of the functional form $\Delta I(E) = \Delta I_{th}(E)\left(1 - F(E)\right)$ where $\Delta I_{th}(E)$ is just the theoretical field dependent EO response given by the solid blue line in Figure 5-59, and $F(E)$ is the relative volume fraction of r_{51} or r_{42} contributing domains that have undergone a 90^o flip and therefore no

longer contribute to the measured response. While the form of $F(E)$ is unknown, the general trend will be an attenuation of the EO response with increasing field as shown schematically by the dashed blue lines in Figure 5-59 which is consistent with the observed EO response under <100> field shown in Figure 5-57b and c. This attenuation in the EO response with increasing <100> oriented E-field is consistent with the observed decrease in the measured r_{eff} value with increasing bias under <100> oriented E-fields seen in Figure 5-52.

5.2.3.2 Modeling the hysteretic EO pulse response under an in-plane <110> oriented E-field

The hysteretic EO response can be modeled in terms of the theoretical E-field dependent EO response of the individual domain variants ($\Delta I_i(E)$) and the field-dependent relative volume fractions[16] of those variants ($\Delta A_{ij}(E)$)[12,37,38]. The hysteretic EO response of sample DT443 is shown in Figure 5-56a. In this section the hysteretic EO response of sample DT443 from voltage pulse measurements under an in-plane <110> oriented field will be modeled. The model demonstrates the relationship between the measured hysteretic electro-optic response and the measured electronic polarization of a given sample.

While "butterfly" EO hysteresis loops are widely reported in the literature[12,37,41,157,159-162,164-173,216], this represents the first time that a measured EO hysteresis loop has been modeled using measured electronic polarization data to determine the effect of the field dependence of the domain structure on the EO response.

In order to model the hysteretic EO response appropriate forms for both $\Delta I_i(E)$ and $\Delta A_{ij}(E)$ must be found. All four of the a-domain variants in a thin film are subject to 180° poling under

[16] The measured polarization is proportional to the relative *volume* fractions of the contributing domains. However in modeling the EO response it is assumed that any given section of the wavefront passes through just a single a-domain in transiting the film and therefore in the EO analysis an areal domain fraction is used. By the Principle of Delesse the volume fraction is equal to the sum of the weighted areal fractions observed for regularly spaced sections through the thickness of a sample [215 Lawrence R Lawson and John E. Hilliard, *Physics: Measurement Techniques/ Instruments: Stereology and Stochastic Geometry*. (Springer, Boston, 2004).

an in-plane <110> oriented E-field; as a result, hysteresis of the EO response is observed due to the EO contributions of the a-domains. Because the remnant hysteresis loop (Section 5.1) gives the remnant contributions to the polarization *due* to 180° domain switching, it can be used to model the field dependence of the relative domain areal fractions (ΔA_{ij}) of the a-domains. The remnant hysteresis loop given by the ferroelectric contributions to the polarization was given in Section 5.1 by equation (5-15) as

$$P_{ferro}^{+\to-} = A_a P_s \left\{ \left[1 - \exp\left(-\left(E_{\max} \middle/ \beta \right)^{\alpha} \right) \right] - 2 \left[1 - \exp\left(-\left((-E) \middle/ \beta \right)^{\alpha} \right] \right] \right\}$$
$$P_{ferro}^{-\to+} = A_a P_s \left\{ \left[\exp\left(-\left(E_{\max} \middle/ \beta \right)^{\alpha} \right) - 1 \right] + 2 \left[1 - \exp\left(-\left((E) \middle/ \beta \right)^{\alpha} \right] \right] \right\} \tag{5-38}$$

where A_a and P_s are the volume fraction of a-domains and the assumed spontaneous polarization, respectively. As noted in Section 5.1 the terms in square brackets correspond to the cumulative distribution function (CDF) for an assumed Weibull distribution of coercivities of the domains. α and β are, respectively, shape and scale parameters for the Weibull distribution. The first bracketed term evaluated at the maximum applied field ($E_{\max}$) gives the maximum polarization. Normalizing equation (5-38) with respect to the maximum polarization gives the correct form for $\Delta A_{ij}(E)$ which is given by

$$\Delta A_{ij}^{\left(\begin{smallmatrix}+\to- \\ -\to+\end{smallmatrix}\right)}(E) = \pm S \left\{ 1 - 2 \frac{\left[1 - \exp\left(-\left((\mp E) \middle/ \beta \right)^{\alpha} \right] \right]}{\left[1 - \exp\left(-\left(E_{\max} \middle/ \beta \right)^{\alpha} \right) \right]} \right\} \tag{5-39}$$

where S is a constant giving the maximum assumed amplitude of $\Delta A_{ij}(E)$. Figure 5-60 shows the fit of equation (5-38) to a remnant hysteresis loop of sample DT443. Also shown is the corresponding $\Delta A_{ij}(E)$ from equation (5-39) where S is set to unity. The values of the parameters used in the fit are given in Table 5-6.

Table 5-6. Equation (5-38) fitting parameters assumed in the fit to the remnant hysteresis loop of Sample DT443 shown in Figure 3-4

A_a	P_s ($\mu C/cm^2$)	α	β	E_{max} (MV/m)
0.1	26	1.5	1.4	0.83

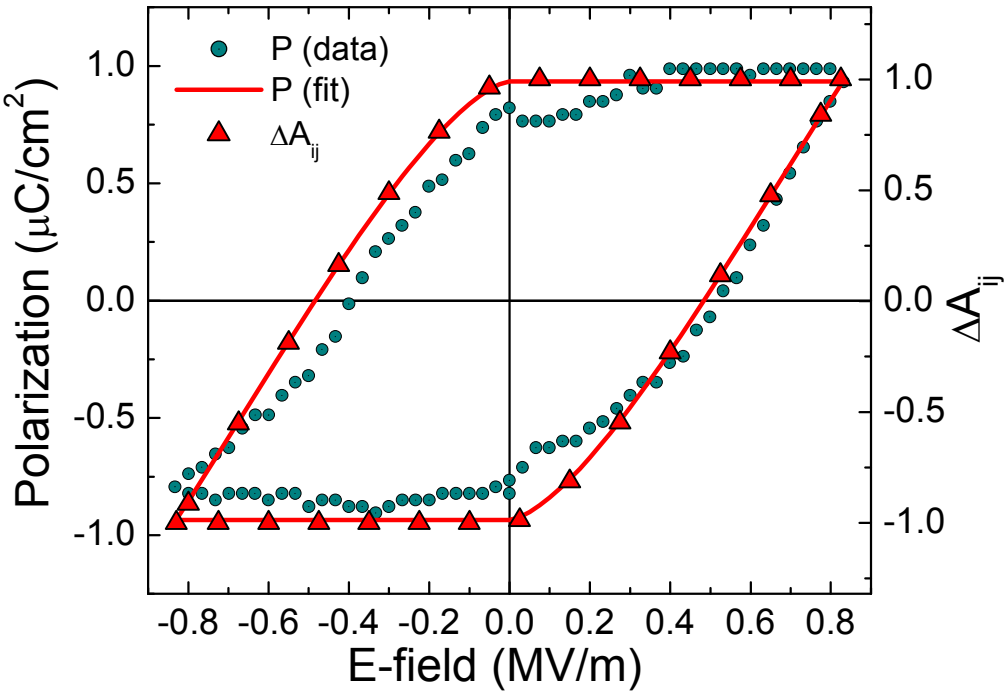

Figure 5-60. Remnant hysteresis loop of sample DT443 and the corresponding fit to equation (5-38). The corresponding $\Delta A_{ij}(E)$ determined from equation (5-39) with *S* set to 1 is likewise shown.

Appropriate forms for the E-field dependent EO response of the individual domain variants ($\Delta I_i(E)$) are likewise required to model the hysteretic EO response. The theoretical E-field dependent EO response of the different domain variants ($\Delta I_i(E)$) was derived in Chapter 4 using the Jones calculus. Figure 5-61c shows the theoretical $\Delta I_i(E)$ for all four of the a-domain variants simulated using the same configuration of the measurement system polarimeter used to measure the EO response of sample DT443 (see Section 4.2.2 for details). The interaction length assumed in calculating the $\Delta I_i(E)$ in Figure 5-61c was 600 nm, reasonably close to the 636 nm film thickness of sample DT443. As such the theoretical $\Delta I_i(E)$ shown in Figure 5-61c will be used in modeling the hysteretic EO response of sample DT443. Expressed simply as a function of the applied field the theoretical change in transmitted intensity of the distinct a-domain variants seen in Figure 5-61c is given by

$$\Delta I_{(i,j)}(E) = 4.4\times10^{-4}E^2 \pm 2.2\times10^{-3}E \qquad (5\text{-}40)$$

where for domain variants (3,5) the linear term is positive and for variants (4,6) it is negative. Note that equation (5-40) is only valid for the specific measurement geometry simulated and employed in the

measurement of sample DT443. The more general expressions for the transmitted intensity are given in Chapter 4.

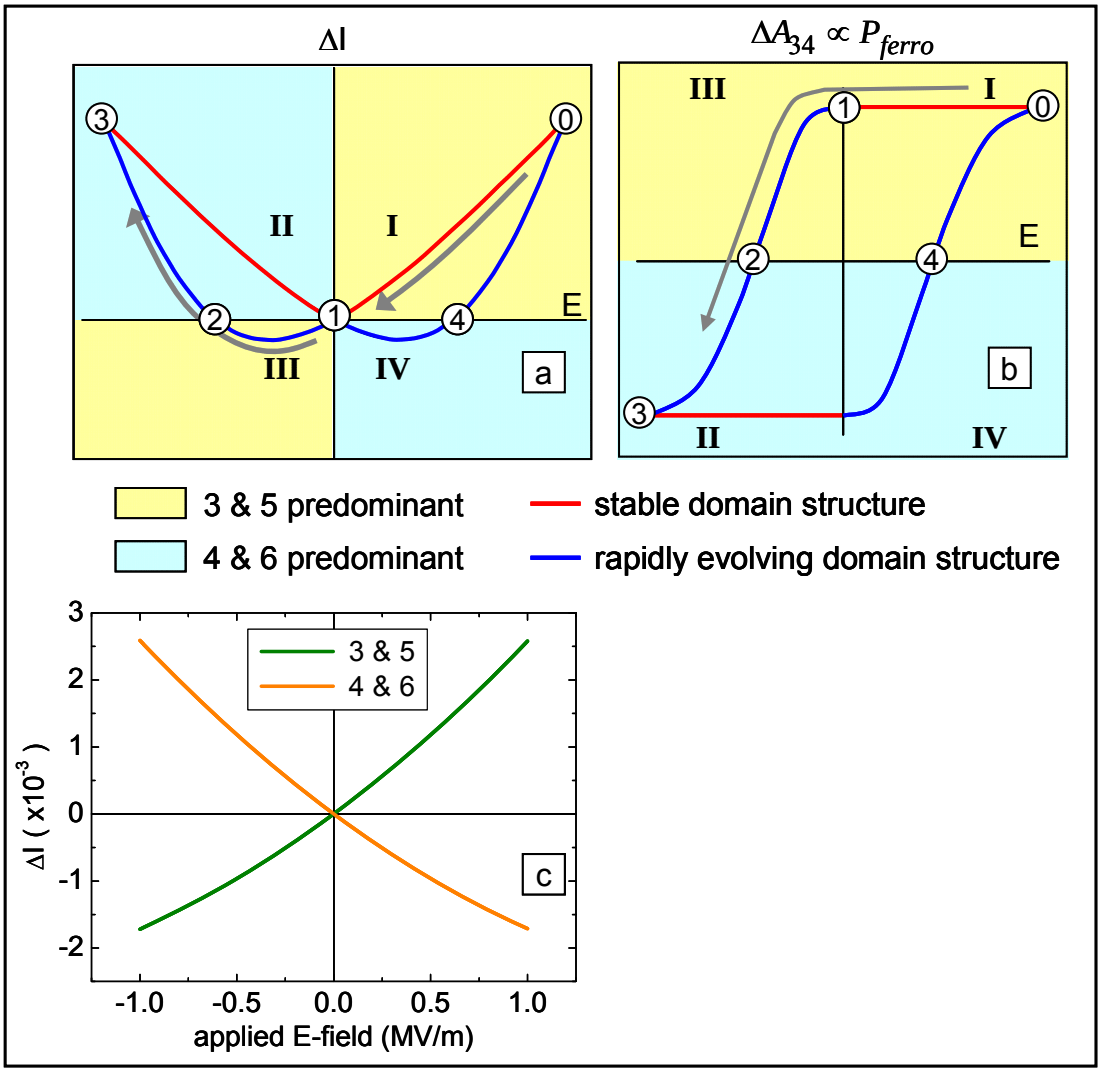

Figure 5-61(a) a schematic representation of a typical "butterfly" EO hysteresis loop. (b) a schematic representation of the field-dependent relative domain volume fraction $\Delta A_{ij}(E)$ of the same form as the remnant polarization hysteresis loop. The $\Delta A_{ij}(E)$ values in a given quadrant in (b) correspond to the EO response in the like-numbered quadrant in (a). (c) Theoretical EO response of the four a-domain variants under a <110> field as shown in Figure 5-55b. Note the similarity of the intrinsic response in (c) to that of the in (a) in the regions where the domain structure is relatively stable (in red).

Before proceeding, a brief discussion is given of the relationship between the hysteretic field-dependent domain structure $\Delta A_{ij}(E)$ in Figure 5-61b and the hysteretic EO response in Figure 5-61a. The form of the relative domain volume fraction ($\Delta A_{ij}(E)$) shown in Figure 5-61b assumes that no

appreciable back switching of domains occurs while reducing the field towards zero. This is not strictly the case. However from both the electronic polarization measurements presented in Section 5.1 and the 90° domain relaxation measurements that are presented in Section 5.2.4.2, it is found that for applied fields of less than 1 MV/m only a modest degree of back switching is observed. At point **0** in Figure 5-61 where the maximum positive field is applied, $\Delta A_{ij}(E)$ is at its maximum positive value. If the a-domains are fully poled by the applied field then $\Delta A_{ij}(E) = 1$ at point **0**. However if the maximum applied field is insufficient to completely pole the a-domains then $0 < \Delta A_{ij}(E) < 1$. In this poled state domain variants 3 and 5 are the predominant a-domain variants present in the sample. The domain structure is assumed to be unchanged in moving from point **0** to point **1**. Therefore, as the field is reduced to zero at point **1** from a maximum at point **0**, the EO response is the net intrinsic response due to the unchanging poled domain structure. For $\Delta A_{ij}(E)$ values close to 1 (nearly full poling) the EO response between points **0** and **1** are expected to resemble the intrinsic response of the predominant domain variants shown in Figure 5-61c.

The change in the sign of the EO response in passing through point **1** results from the change in the polarity of the applied field while the predominant a-domain variants in the film remain unchanged[17]. Between points **1** and **2** in Figure 5-61, variants 3 and 5 are still the predominant a-domain variants present. However, the polarity of the applied field changed at point **1**. Because variants 3 and 5 are still predominant, the change in polarity of the applied filed results in a change in the sign of the EO response. As the magnitude of the negative field increases the domain structure evolves rapidly such that at point **2** equal volume fractions of the 180° variants (3 and 4) and (5 and 6) exist in the film. As seen in Figure 5-61c, $\Delta I_3(E) \neq -\Delta I_4(E)$ for $E \neq 0$. Therefore the point at which equal volume fractions of oppositely oriented domains exist should not correspond to the point at which the net EO response equals zero.

[17] All three points where there is a change in the sign of the EO response correspond to points at which there is a change in *either* the predominant domain variant *or* the polarity of the applied field but not both. For both passages through point 1 the polarity of the field changes while the predominant domain variants are the same. In passing through points 2 and 4 the polarity of the applied field remains constant while the predominant domain variants change.

However $\Delta A_{ij}(E)$ is quite steep in the vicinity of the coercive field of the remnant hysteresis loop (point **2**). As a result the field at which equal volume fractions of 180° variants exist is very close to that at which the net EO response goes to zero as seen in Figure 5-62 where the remnant polarization loop and the measured EO response of sample DT443 are plotted together. For sample DT443 the net EO response goes to zero for applied fields of ~|0.5| MV/m. From the intrinsic EO responses shown in Figure 5-61c the relative domain fraction necessary to produce a null EO response at ±0.5 MV/m are (0.45,0.55). In moving beyond point **2** towards point **3** domain variants 4 and 6 replace 3 and 5 as the predominant a-domain variants present in the sample and the sign of the EO response again becomes positive. Finally at point **3** $\Delta A_{ij}(E)$ reaches its maximum negative value. The remainder of the loop from point **3** back to point **0** is completely analogous to the passage from **0** to **3** just described.

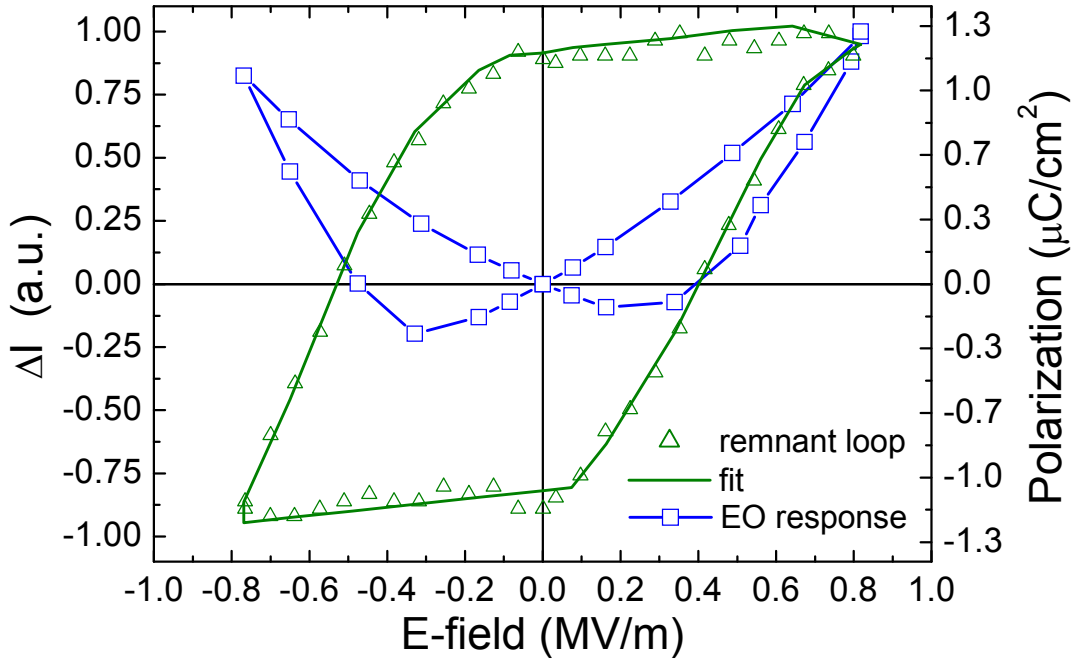

Figure 5-62. Remnant polarization loop and EO hysteresis loop of sample DT443. Coercive fields from both measurements are in good agreement. Theoretically the "coercive field" from the EO measurement should be somewhat smaller than that from the remnant polarization measurement due to the finite ΔI predicted for equal volume fractions of 180° a-domain variants.

Consideration will now be given to the correct form for the final expression of the hysteretic field-dependent transmitted intensity $\Delta I_{net}(E)$ under a <110> field. If the intrinsic EO response of the

different 180° domain variants were either even or odd functions *and* the condition $\Delta I_i(E) = -\Delta I_j(E)$ was satisfied for any applied field where (i, j) represent 180° domain variants (such as $(3,4),(5,6)$ in Figure 5-55) then the transmitted intensity could be written simply as

$$\Delta I_{net}(E) = \Delta I_i(E)\Delta A_{ij}(E) \tag{5-41}$$

These conditions hold for domain variants 3 and 4 from Figure 5-55a where only r_{13} and r_{33} EO coefficients are responsible for the EO response. Figure 5-63b shows a "butterfly" EO hysteresis loop generated using equation (5-41) for the very simple form of $\Delta A_{ij}(E)$ shown in the figure. Figure 5-63a shows the assumed linear form of the intrinsic response, satisfying the condition $\Delta I_i(E) = -\Delta I_j(E)$. The intrinsic EO response of domain variants 3 and 4 from Figure 5-55a should be linearly dependent on the applied field so although Figure 5-63 is just a schematic representation it does give the qualitative behavior expected for variants 3 and 4 under the <100> field shown in Figure 5-55a.

However, it is evident from Figure 5-61c that the EO contributions due to equal volume fractions of 180° a-domain variants under a <110> field do not completely

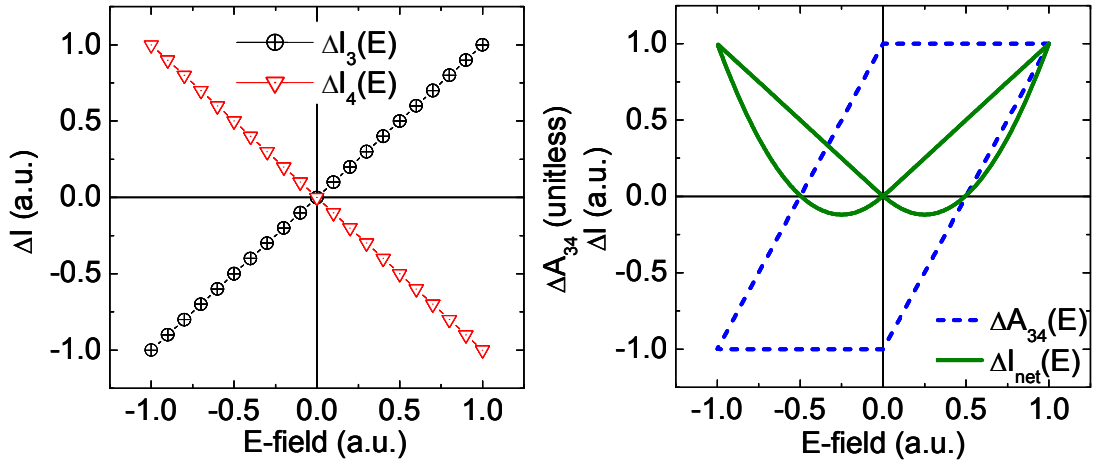

Figure 5-63(a) schematic representation of intrinsic EO response satisfying the condition $\Delta I_i(E) = -\Delta I_j(E)$. The intrinsic response of domain variants 3 and 4 from Figure 5-55a under a <100> field will be of this form.(b) "butterfly" EO hysteresis loop generated using equation (5-41) with $\Delta I_3(E)$ from (a) and the simple $\Delta A_{34}(E)$ from (b).

cancel; as such the condition $\Delta I_i(E) = -\Delta I_j(E)$ is not satisfied and equation (5-41) can not be used to model the hysteretic EO response of the a-domains shown in Figure 5-55b[18]. Instead the final expression for the hysteretic transmitted intensity must include separate terms for the intrinsic EO contributions due to domain variants (3 and 5) and (4 and 6). Because the EO response due to variants 3 and 5 are identical a single term $\Delta I_{(3+5)}(E)$ can be used to represent the intrinsic response due to these domain variants. The same is true for variants 4 and 6 from Figure 5-55b. Additionally, because the magnitude of the applied field parallel to the polar axes of variants (3 and 4) and (5 and 6) are the same under a <110> field as seen in Figure 5-55b, a single expression for the relative domain fractions can be used to characterize all four a-domain variants. The expression for the relative volume fractions of the 180° a-domain variants is given by

$$\Delta A_{ij}(E) = \left[(A_3 - A_4)(E)\right] / (A_3 + A_4) = \left[(A_5 - A_6)(E)\right] / (A_6 + A_5) \tag{5-42}$$

where A_i is the volume fraction of the ith domain variant. The final expression of the hysteretic field-dependent transmitted intensity $\Delta I_{net}(E)$ under a <110> field is given by

$$\Delta I_{net}(E) = \Delta I_{(3+5)}(E) \cdot A^{norm}_{(3+5)}(E) + \Delta I_{(4+6)}(E) \cdot A^{norm}_{(4+6)}(E) \tag{5-43}$$

where $\Delta I_{(3+5)}$ and $\Delta I_{(4+6)}$ are the theoretical $\Delta I_i(E)$ from Figure 5-61c. $A^{norm}_{(i)}$ is the normalized volume fraction of the i-th domain variant defined by

$$A^{norm}_i(E) = \frac{A_i(E)}{A_i + A_j} \tag{5-44}$$

where A_i represents the volume fraction of variants that give rise to equivalent $\Delta I(E)$ and A_j are the corresponding 180° variants (i.e. $i = (3,5) \Rightarrow j = (4,6)$). When the total volume fraction of a-domains is normalized to 1, one has

$$\begin{aligned} 1 &= A^{norm}_{(3+5)}(E) + A^{norm}_{(4+6)}(E) \\ \Delta A_{ij}(E) &= A^{norm}_{(3+5)}(E) - A^{norm}_{(4+6)}(E) \end{aligned} \tag{5-45}$$

[18] Additionally, the intrinsic EO responses of the individual domains in Figure 5-61c are neither even nor odd functions and so neither of the two conditions necessary for the use of equation (5-41) are met.

From (5-45), $A_{(3+5)}^{norm}(E)$ and $A_{(4+6)}^{norm}(E)$ are given by

$$A_{(3+5)}^{norm}(E) = \frac{\Delta A_{ij} + 1}{2}$$
$$A_{(4+6)}^{norm}(E) = \frac{1 - \Delta A_{ij}}{2} \tag{5-46}$$

Therefore equation (5-43) can be expressed in terms of $\Delta A_{ij}(E)$ as

$$\Delta I_{net}(E) = \tfrac{1}{2}\left\{\left[\Delta I_{(3+5)}(E) - \Delta I_{(4+6)}(E)\right]\Delta A_{ij}(E) + \Delta I_{(3+5)}(E) + \Delta I_{(4+6)}(E)\right\} \tag{5-47}$$

The field dependence of $\Delta A_{ij}(E)$ is expected to be proportional to the remnant polarization hysteresis loop in the film as defined in Sections 3.5 and 5.1. Therefore, in order to characterize $\Delta A_{ij}(E)$, in-plane polarization measurements were made on sample DT443 using the same range of applied voltages employed in the EO pulse response measurement shown in Figure 5-56a (±0.8 MV/m). In addition to measuring the full hysteresis loop, the positive and negative non-switching half-loops were measured. As outlined in sections 3.5 and 5.1[19], the remnant polarization hysteresis loop is derived by subtracting the non-switching half loops from the full hysteresis loop. The measured hysteresis is shown in Figure 5-64. Also shown in Figure 5-64 is a fit to the remnant hysteresis loop. Each of the four "sides" of the loop was fit to a polynomial, in order to generate analytic expressions with wich to represent the remnant hysterisis. For clarity, every other point of the remnant loop is shown.

When the a-domains are fully poled such that there are no type 4 or 6 domains, $\Delta A_{ij}(E)$ is equal to 1. However for the 0.8 MV/m fields applied in the EO measurement, the a-domains may not be fully poled. A second polarization measurement was made employing driving voltage near the V_{max} of the Radiant Technologies RT6000S (±19V). It is assumed that under the ±1.6 MV/m fields employed, $\Delta A_{ij}(E)$ approaches unity. As seen in Figure 5-65, the maximum remnant polarization under a 1.6 MV/m field was ~2.4 μC/cm^2. The analytic fit to the remnant hysterisis measured under a ±0.8 MV/m driving field was normalized with respect to the remnant P_{max} of 2.4 μC/cm^2 measured with ±1.6 MV/m

[19] A detailed description of the remnant polarization hysteresis loop and its relation to the full uncompensated polarization hysteresis loop is given in Section 5.1. The interested reader should refer to Section 5.1 for more information on the remnant polarization hysteresis loop.

fields. The result, shown in Figure 5-66, gives the hysteretic $\Delta A_{ij}(E)$ for the range of driving fields employed in the EO pulse response measurement from Figure 5-56a.

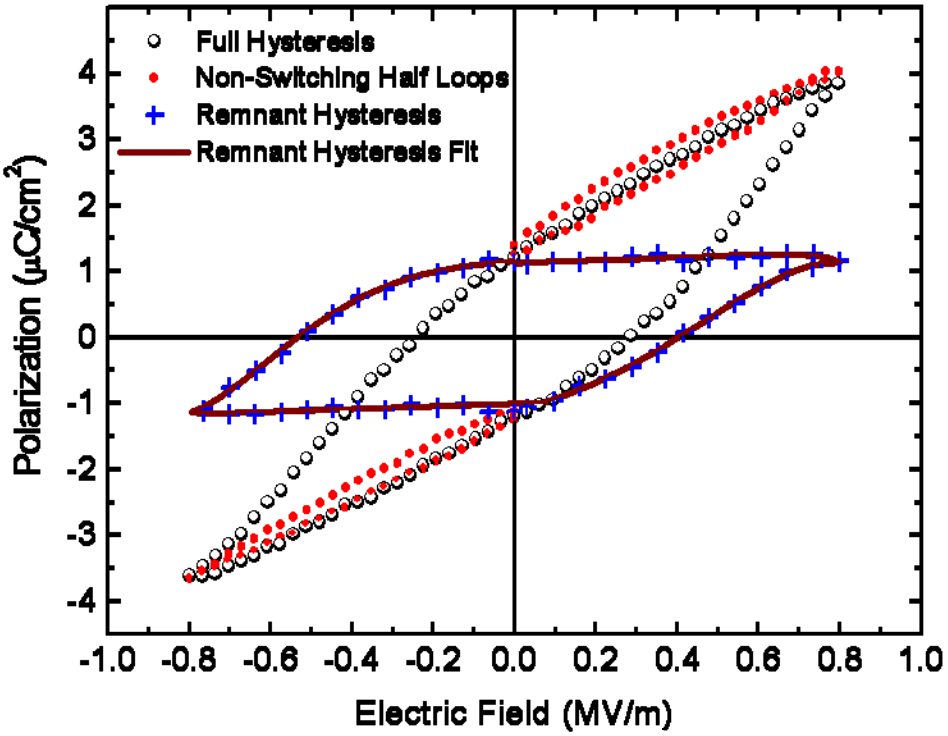

Figure 5-64. In-plane electronic polarization measurement of DT443. The maximum applied fields employed were the same as those in the EO pulse response measurements from Figure 5-56a. As outlined in sections 3.5 and 5.1, the remnant polarization hysteresis loop is derived by subtracting the non-switching half loops from the full hysteresis loop. The four "sides" of the remnant hysterisis loop were fit to separate polynomial functions so as to generate analytic expressions with wich to represent the remnant hysterisis. For clarity, every other point of the remnant loop is shown.

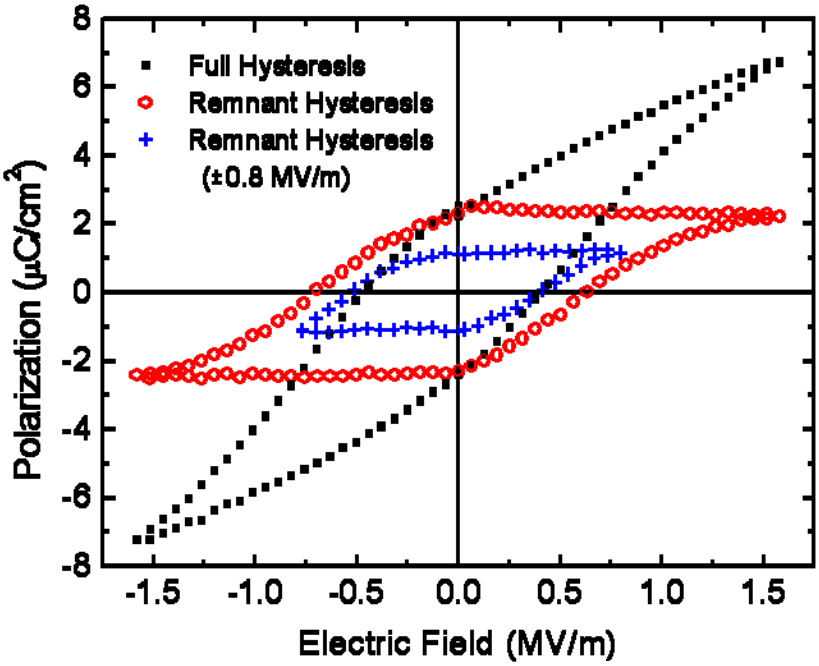

Figure 5-65.Polarization Hysteresis measurement on sample DT443 under ±19V driving voltages. The remnant hysteresis loop derived from the full loop and the non-switching half loops is likewise shown. Also shown for comparison is the remnant hysteresis loop measured with maximum applied fields of ±0.8 MV/m.

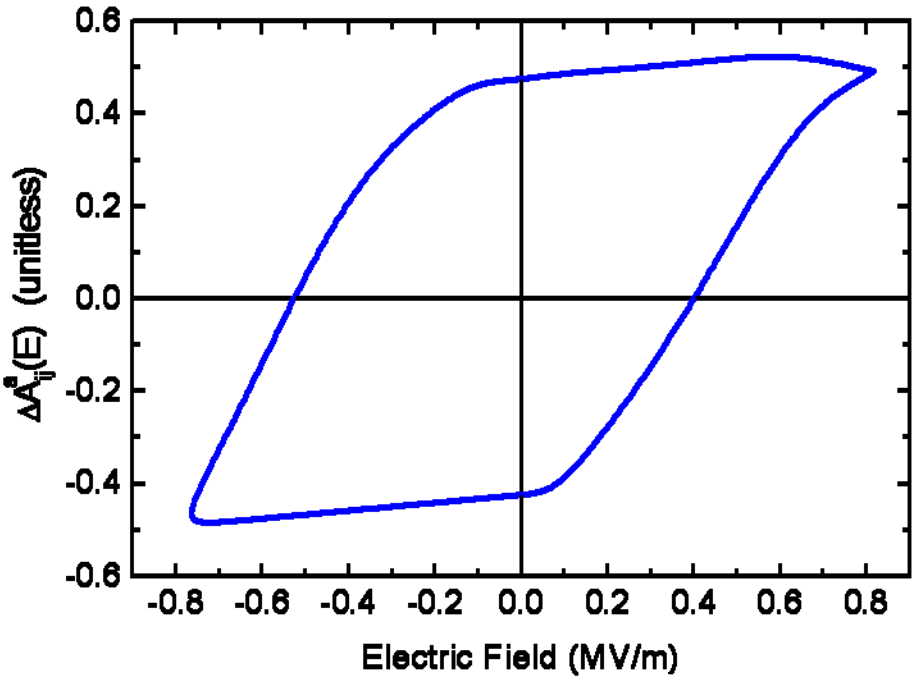

Figure 5-66. Plot of the field-dependent hysteretic relative domain fraction ΔA_{ij} under the driving conditions employed in the pulse response EO measurements in Figure 5-56a. Where $\Delta A_{ij}(E) > 0$, variants 3 and 5 are the predominant a-domain variants in the film. Where $\Delta A_{ij}(E) < 0$, variants 4 and 6 are the predominant a-domain variants in the film.

The hysteretic EO response of sample DT443 can now be modeled using equation (5-47). Figure 5-67 shows the fit after plugging equations (5-39) and (5-40) into equation (5-47). The fit using equations (5-39) is reasonably good, however the form of $\Delta A_{ij}(E)$ shown in Figure 5-66 was determined by polynomial fits to the remnant hysteresis loop. Because the resulting form of $\Delta A_{ij}(E)$ shown in Figure 5-66 was a purly emperical fit to the remnant polarization hysteresis loop, its use improves the resulting fits to the hysteretic EO response. The form of form of $\Delta A_{ij}(E)$ shown in Figure 5-66 is therfore used throughout the remainder of this section. Using $\Delta A_{ij}(E)$ plotted in Figure 5-66 and the theoretical $\Delta I(E)$ given by equation (5-40), Figure 5-68 shows the resulting fit of the theoretical $\Delta I_{net}(E)$ from equation (5-47) to the measured data after multiplication by a constant arbitrary multiplier of 61[20]. Figure 5-69 shows the theoretical fit after normalizing both the theoretical and measured response with respect to the magnitude of the applied field. The finite linear slope observed in Figure 5-69 as the applied field is reduced towards zero in both the measured and theoretical response, is due to the quadratic dependence of $\Delta I(E)$ associated with the quadratic dependence of $\Delta\delta n(E)$ discussed in Section 4.2.2.1. The slope of the theoretical $\Delta I_{net}(E)$ is particularly well matched to that of the measured EO response in these regions. As noted previously, each point in Figure 5-68 and Figure 5-69 was measured at a frequency of 1Hz. As seen from Figure 5-39 the degree of non remnant ferroelectric switching is relatively modest for the fields applied in the pulse measurements shown in Figure 5-68 and Figure 5-69. Therefore the use of a monopolar voltage pulse train should result in an EO response at any given field magnitude that is relatively insensitive to the measurement frequency as long as the non-remnant ferroelectric contributions are negligible.

[20] As discussed in Section 3.7, the $\Delta I(E)$ through the polariscope is converted to a change in current by the PMT and due to the impedance of the measurement system is measured as a change in voltage at the oscilloscope. As such the units (mV) of the measured $\Delta I(E)$ are arbitrary and in order to fit the theoretical $\Delta I_{net}(E)$ to the measured data, the theoretical $\Delta I_{net}(E)$ must be scaled by a constant multiplier.

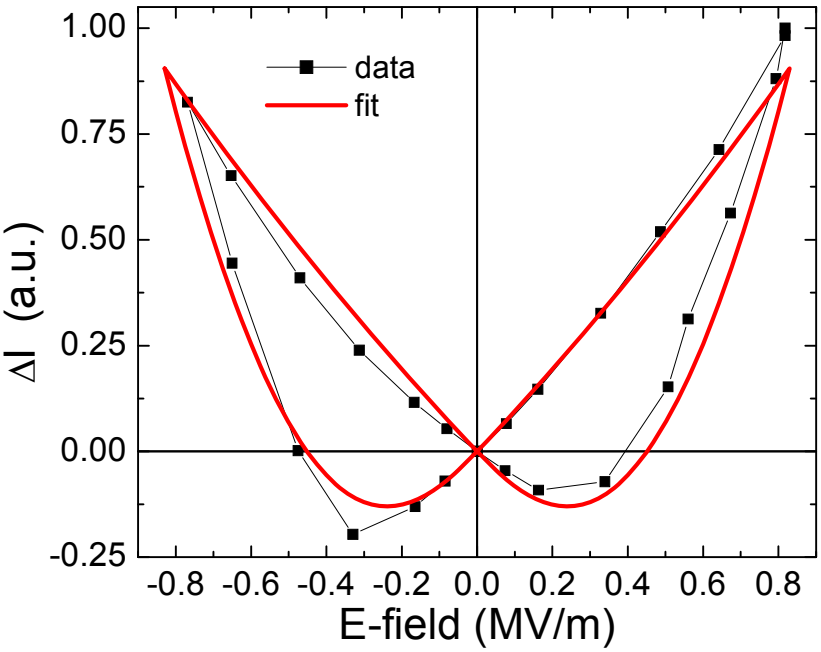

Figure 5-67. Hysteretic EO response of sample DT443 and the corresponding fit using equation (5-47) after plugging in equations (5-39) and (5-40)

From both Figure 5-68 and Figure 5-69 one sees that the fit is poorest in regions where the sign of the applied field has changed but the predominant domain variants have not (the troughs of the "butterfly" loops). The fit of equation (5-47) to the measured EO response is improved when one assumes that the domain structure is in fact fully poled ($\left|\Delta A_{ij}\left(\left|E_{MAX}\right|\right)\right|$ = 1). Figure 5-70 and Figure 5-71 show the fit of the theoretical $C\cdot\Delta I_{net}\left(E\right)$ to the measured EO response assuming that the a-domains are fully poled by the applied electric field. As in Figure 5-68, C is a constant scaling factor which for Figure 5-70 and Figure 5-71 is equal to 37.5. The assumption of a nearly fully poled remnant component of the polarization is consistent with the measured remnant loop coercive fields of this sample for a series of hysteresis loops under increasing E_{max} as seen in Figure 5-30.

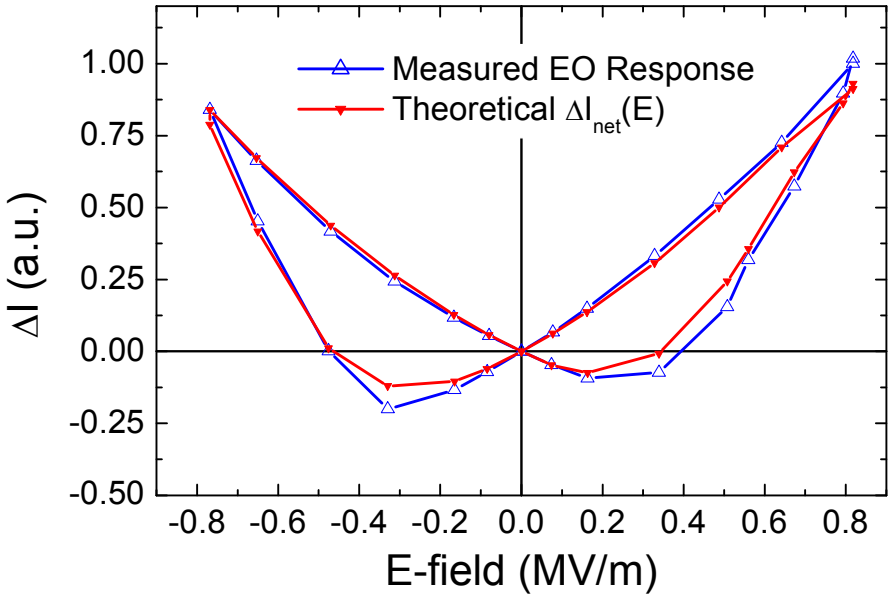

Figure 5-68. Comparison of theoretical ΔI_{net} based on measured remnant polarization to the measured field-dependent EO response of DT443.

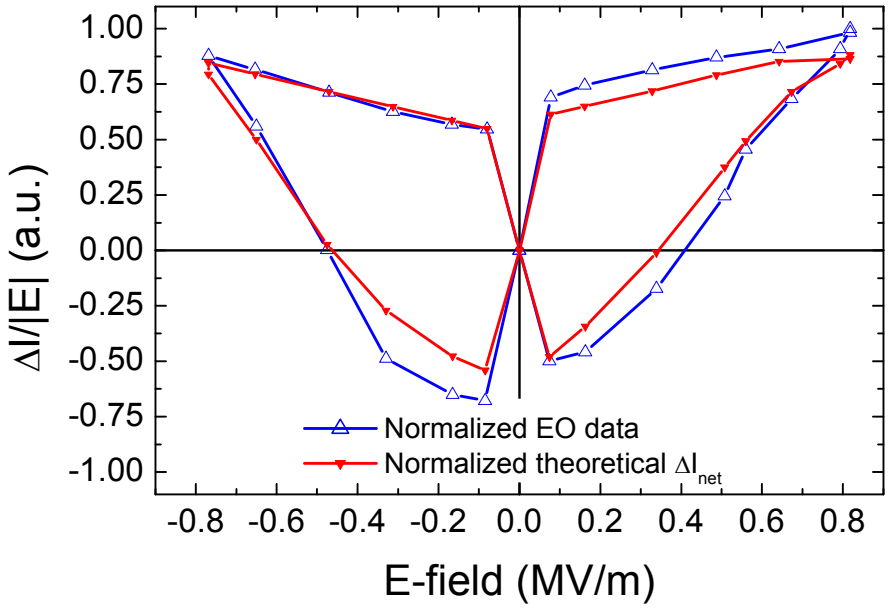

Figure 5-69. E-field normalized theoretical ΔI_{net} and measured EO response of DT443. The finite linear slope upon reducing the field towards zero is due to the quadratic E-field dependence of $\delta\Delta n$ and therefore ΔI.

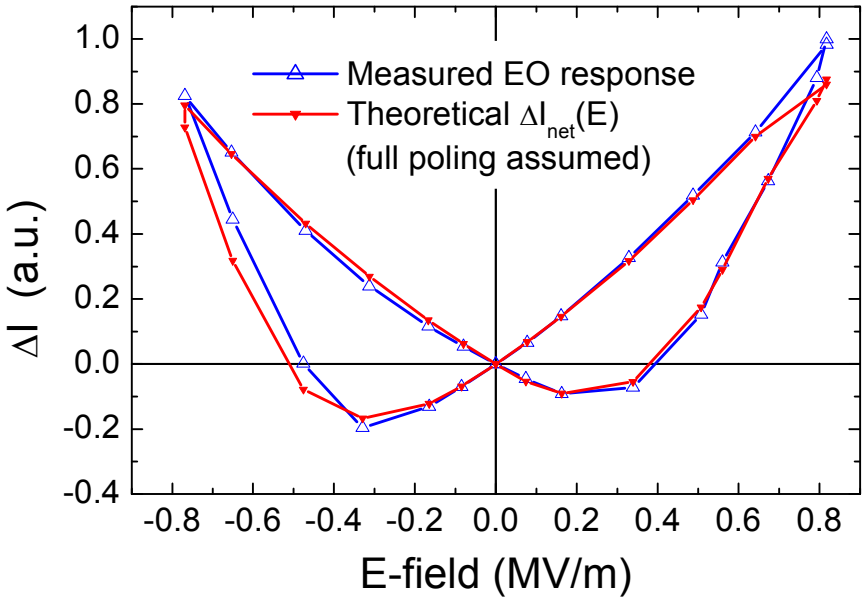

Figure 5-70. Fit of theoretical ΔI_{net} to the measured EO response of DT443 assuming that the domain structure is fully poled by the ±0.8 MV/m $|E_{MAX}|$

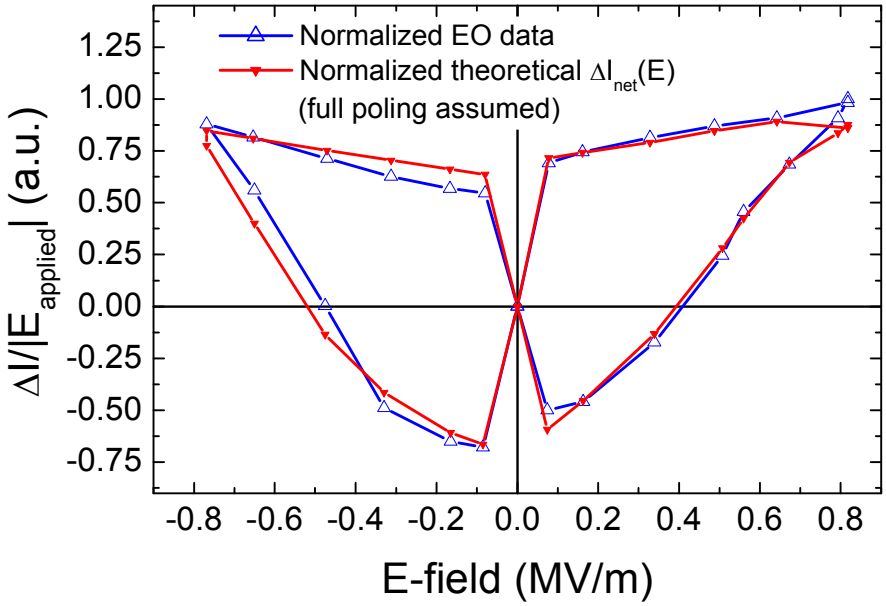

Figure 5-71. Fit of field-normalized theoretical ΔI_{net} to field-normalized EO response data of DT443 assuming the domain structure is fully poled by the ±0.8 MV/m $|E_{MAX}|$

In this section a typical "butterfly" EO hysteresis loop was effectively modeled using equation (5-47) in which the hysteretic EO response is given by product of the theoretical EO response of contributing domains and their field-dependent relative volume fraction. The form of the field dependent relative volume fraction $\Delta A_{ij}(E)$ was assumed to be proportional to the remnant polarization hysteresis

loop. The quality of the fits based on this assumption indicates the efficacy of modeling $\Delta A_{ij}(E)$ from the measured remnant polarization hysteresis loop.

High-field hysteretic EO measurements

It is proposed that under applied fields in excess of 1 MV/m strain induced by 90°-domain flipping contributes appreciably to the optical response through the elasto-optic effect[217,218]. In several of the films studied it was observed that for applied field magnitudes in excess of 1 MV/m, the effective electro-optic coefficient determined from the voltage pulse measurements was inversely proportional to the applied field. Some reports of hysteretic EO response from the literature for PZT, PLZT and BST thin films exhibit a similar inverse relationship between the applied field and the effective EO coefficient. Neither the intrinsic EO response nor 180° poling or back switching can account for the observed inverse field dependence of the effective EO coefficient. The intrinsic EO response increases with increased field and both 180° poling of the domain structure and 180° back switching should give rise to an r_{eff} that is positively correlated to the magnitude of the applied field. Figure 5-72 and Figure 5-73 show the butterfly EO hysteresis loops of samples DT443 and AM040b, respectively along with the loop normalized with respect to the applied field. The field-normalized EO response is proportional to the effective EO coefficient of the sample. In samples DT443 and AM040b r_{eff} is inversely proportional to the applied field magnitude for applied fields in excess of ~|0.9| and |2| MV/m, respectively. Figure 5-74 shows similar EO hysteresis loops for a polycrystalline PZT thin film due to Potter et al.[165]. Figure 5-75 and Figure 5-76 show EO hysteresis loops for epitaxial PLZT and BST thin films due respectively to Reitze et al.[161] and Li et al.[168] In all cases upon reducing the magnitude of the applied field the effective EO coefficient increases contrary to expectation if only the intrinsic EO response and 180° back switching are considered.

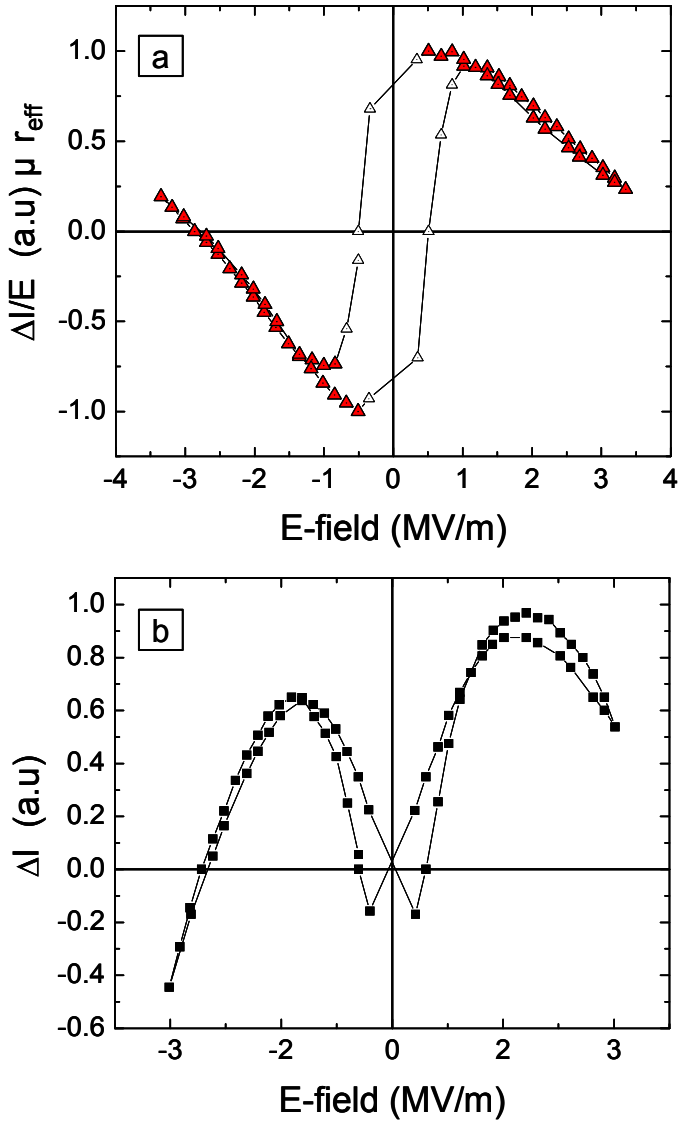

Figure 5-72. EO hysteresis loops of sample DT443. (a) shows the EO response normalized with respect to the applied field which is proportional to the $r_{eff}(E)$ in the sample. The regions in red show where r_{eff} is inversely proportional to the applied field. (b) shows the "butterfly" EO hysteresis loop of the field dependent transmitted intensity.

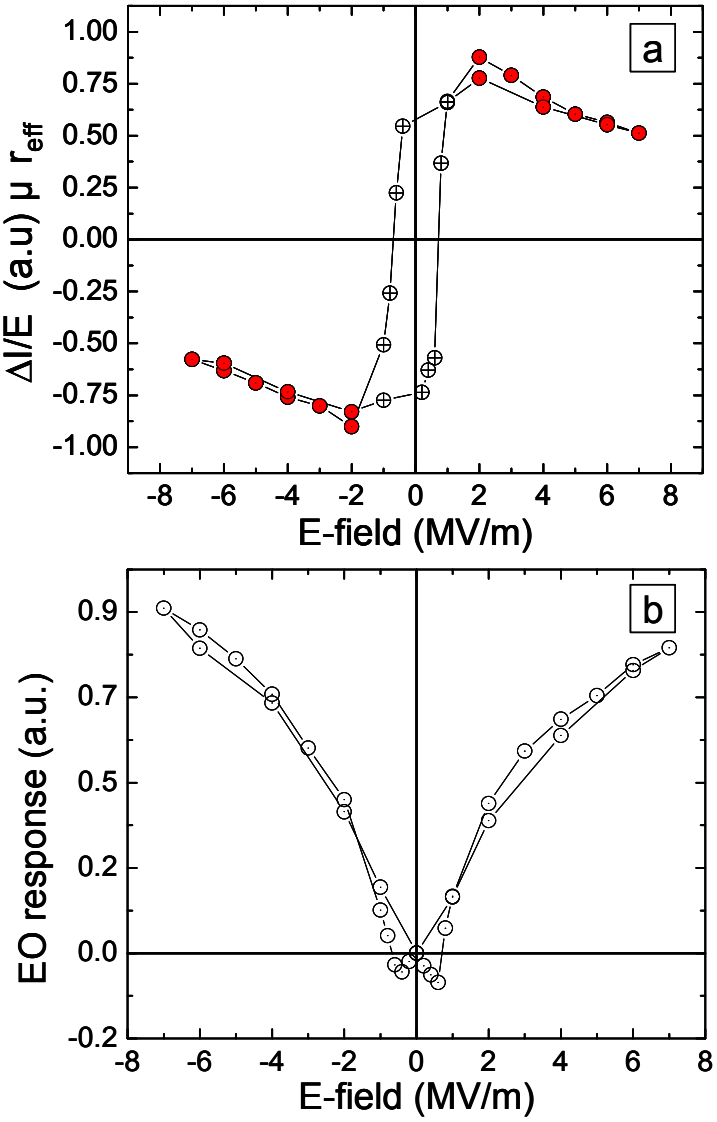

Figure 5-73. EO hysteresis loops of sample AM040b. (a) shows the EO response normalized with respect to the applied field which is proportional to the $r_{eff}(E)$ in the sample. The regions in red show where r_{eff} is inversely proportional to the applied field. (b) shows the "butterfly" EO hysteresis loop of the field dependent transmitted intensity.

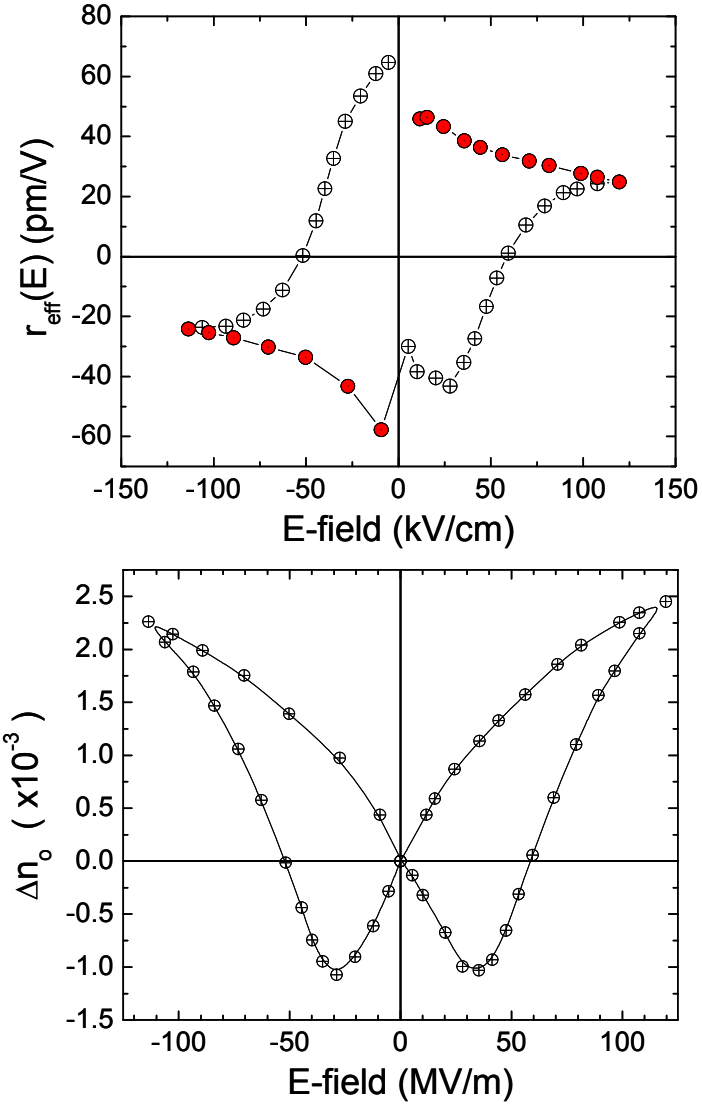

Figure 5-74. EO hysteresis loops of a polycrystalline PZT thin film. (a) shows $r_{eff}(E)$ in the sample. The regions in red show where r_{eff} is inversely proportional to the applied field(b) shows the "butterfly" EO hysteresis loop of the field dependent transmitted intensity.[Potter et al. 1993][165]

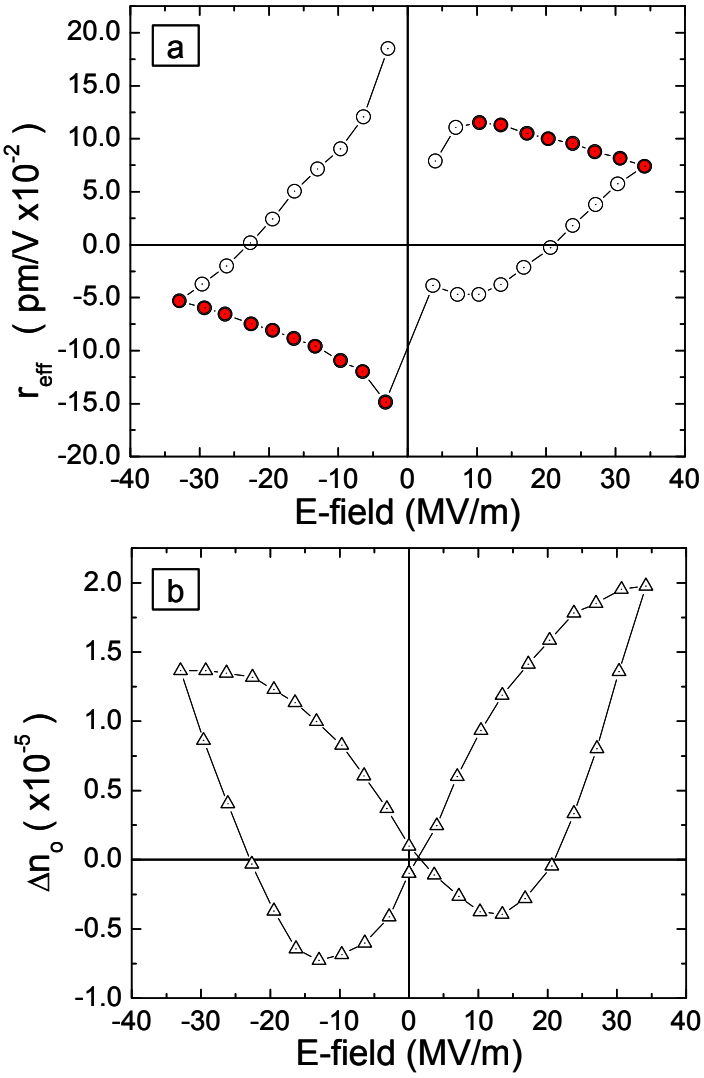

Figure 5-75. EO hysteresis loops of an epitaxial PLZT thin film. (a) shows $r_{eff}(E)$ in the sample. The regions in red show where r_{eff} is inversely proportional to the applied field (b) shows the "butterfly" EO hysteresis loop of the field dependent transmitted intensity.[Reitze et al. 1993][161]

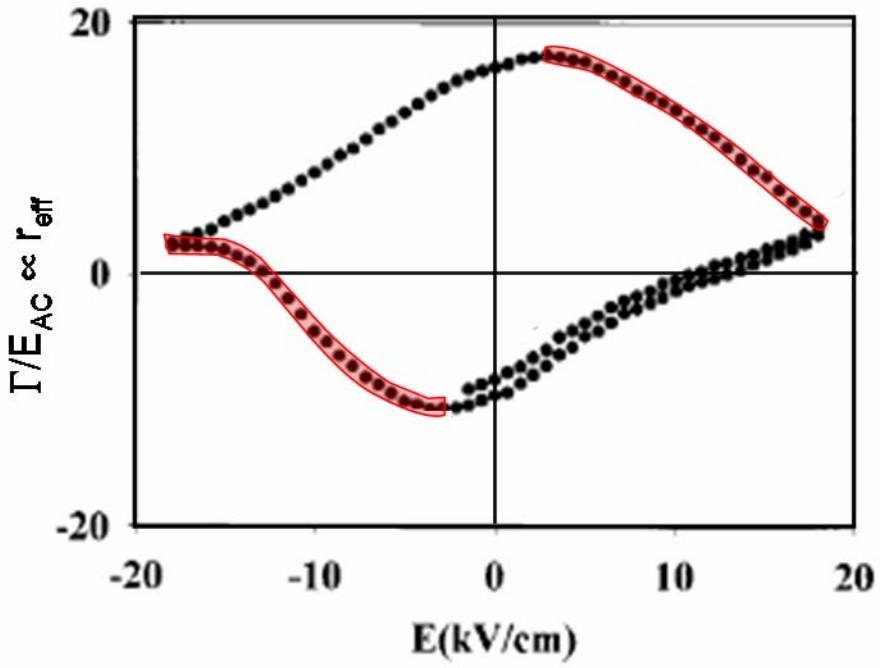

Figure 5-76. EO hysteresis loop of an epitaxial BST thin film. The regions in red show where r_{eff} is inversely proportional to the applied field.[Li et al. 2000][168]

In this section it will be shown that the attenuation of r_{eff} at high field can be successfully modeled by including the elasto-optic contributions to the total optical response. The elasto-optic contributions arise due to the strains associated with E-field driven 90° domain switching in the thin film. As the magnitude of the in-plane E-field increases, c-domains begin to undergo 90° switching into the plane of the film. Appreciable stresses and strains are associated with the accommodation of these 90°-switched c-domains[153,156]. As discussed in Section 2.3.3, in studies of strain actuation in bulk $BaTiO_3$ induced by 90° domain flipping, strains as large as 0.8% have been realized at for applied fields of just 1 MV/m[153,156]. In this case the change in the impermeability tensor must include the additional contributions due to the strain associated with the 90° c-domain flipping using the elasto-optic coefficients[56,217] This change to the impermeability tensor at optical frequencies is given by

$$\Delta\eta_{ij} = r_{ijk}E_k + \rho_{ijrs}\varepsilon_{rs} \tag{5-48}$$

where the ρ_{ijrs} are the components of the elasto-optic tensor[21] and ε_{rs} are the components of the strain tensor. The first term on the right gives the contribution due to the linear electro-optic effect. Equation (5-48) is then substituted for equation (4.18). The analysis of the EO response is otherwise the same as that given in Section 4.2.2. A detailed description of the analysis when elasto-optic contributions are included is given in Appendix II.

To determine if c-oriented domains were switching, x-ray diffraction analysis was performed under applied in-plane electric fields. Figure 5-77 shows the surface normal Bragg reflections of the $BaTiO_3\{200\}$ peaks for different applied E-fields in sample DT443. The $BaTiO_3(002)$ peak of the c-domains diminishes in intensity as the magnitude of the E-field increases. Simultaneously the intensity of the $BaTiO_3(200)$ peak of the a-domains increases, while its position shifts to a lower 2θ angle indicating that the out-of-plane strain of the a-domains is tensile. Analysis of the peaks indicates that the diminished $BaTiO_3(002)$ peak of the c-domains is likewise shifted to a slightly lower 2θ angle. As the magnitude of the electric field increases the c-domain peak diminishes slightly while the a-domain peak becomes stronger as c-domains are flipped into the plane of the film (becoming a-domains). The resulting in-plane compressive strain results in a tensile strain in the surface normal direction consistent with the shift of the $BaTiO_3$ Bragg reflections to lower 2θ angles.

It should be noted that in measuring the field-dependent surface normal lattice parameter, the smallest available slit size was 50 μm. Given an electrode gap of just 12 μm and the incidence angle of ~22.5° for examination of the $BaTiO_3\{200\}$ peaks, the total area illuminated by x-rays was ~11x larger than that between the electrodes where the applied field is strongest as seen in Figure 5-78. As such the measured surface normal strain represents the modal average of the entire illuminated area which will be substantially less than that between the electrodes where the in-plane field is maximized. The x-ray absorption due to the 300 nm Au electrode is approximately 23% as given by[219]

$$I_x = I_o \exp\left[-\left(\mu/\rho\right)\rho x\right] = I_o \exp\left[-\left(82.33\,\frac{cm^2}{g}\right)19.28\,\frac{g}{cm^2}\cdot 1650nm\right] \tag{5-49}$$

[21] A brief discussion of the elasto-optic tensor of $BaTiO_3$ is given in Appendix II

where $\left(\mu/\rho\right)$ is the appropriate mass absorption coefficient of Au (Cu-$k_{\alpha 1}$) and ρ is the density of Au. As the x-rays pass through the electrode twice the interaction length is given by $x = 1650nm = 2 \cdot 315nm / \sin\left(22.5°\right)$. Even taking the absorption into consideration the ratio of the signal from the material under the electrode to that in the

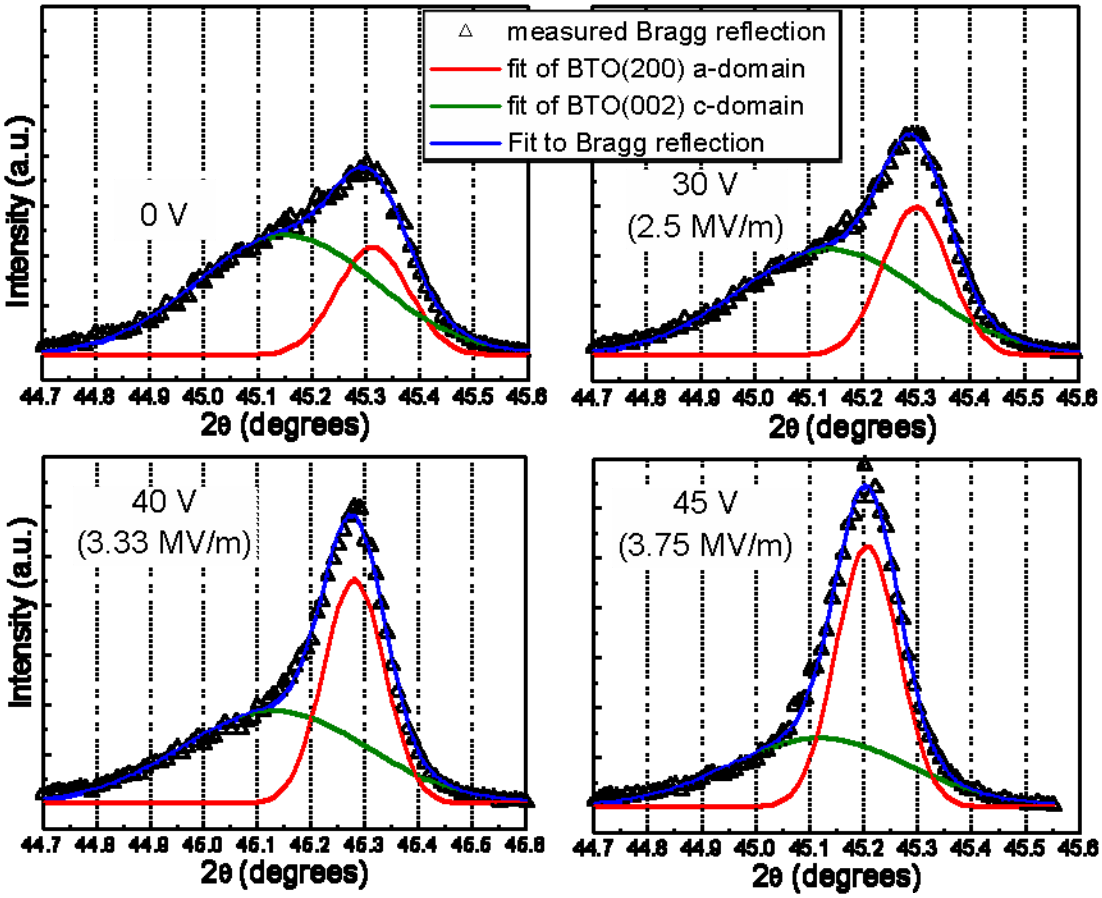

Figure 5-77. $BaTiO_3$ {200} Bragg reflections of sample DT443 at different applied electric fields

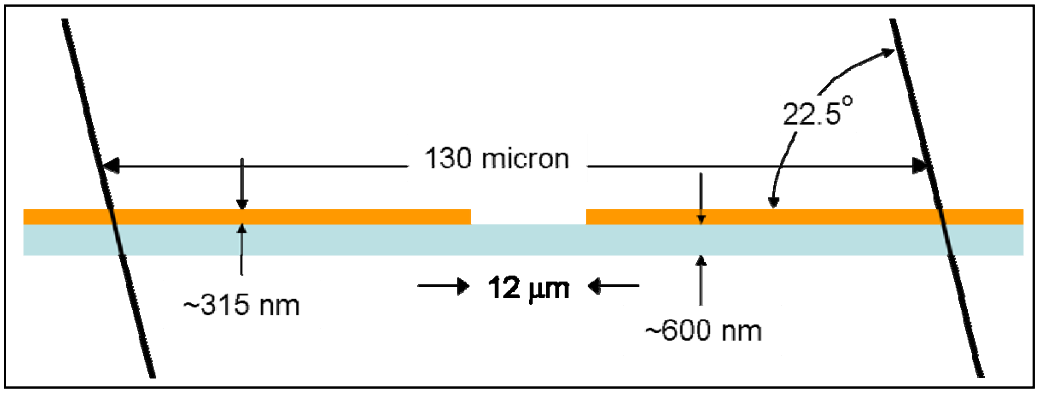

Figure 5-78. Schematic of geometry during field dependent lattice parameter measurements by x-ray diffraction. Given the theta angle of 22.5° and the slit width of 50 μm, the x-ray illuminated area is ~11x larger than that in the 12 μm electrode gap where the in-plane E-field is maximized. The measured lattice parameter represents the modal average of the entire illuminated area.

electrode gap is given by $0.77(130-12)/12 = 7.6$ as seen in Figure 5-78.

The field-dependent surface normal strain in the a-domains was determined from the field dependence of the surface normal lattice parameter. The strain is given by

$$\varepsilon_{22}(E) = \frac{a_n(E) - a_{no}}{a_{no}} \tag{5-50}$$

where a_{no} is the surface normal lattice parameter in the absence of an applied field and $a_n(E)$ is the field dependent surface normal lattice parameter. Figure 5-79 shows both the field dependent surface normal lattice parameters as well as the surface normal strain of the a-domains. In order to model the field dependent strain the surface-normal strain of the a-domains was fit empirically to the function

$$\varepsilon_{22}(E) = 8.96\times10^{-6}\exp\left(\frac{E-3.15}{0.121}\right) + 5.5\times10^{-4}\exp\left(\frac{E-3.15}{1.00}\right) \tag{5-51}$$

This fit to the surface normal strain is likewise shown in Figure 5-79.

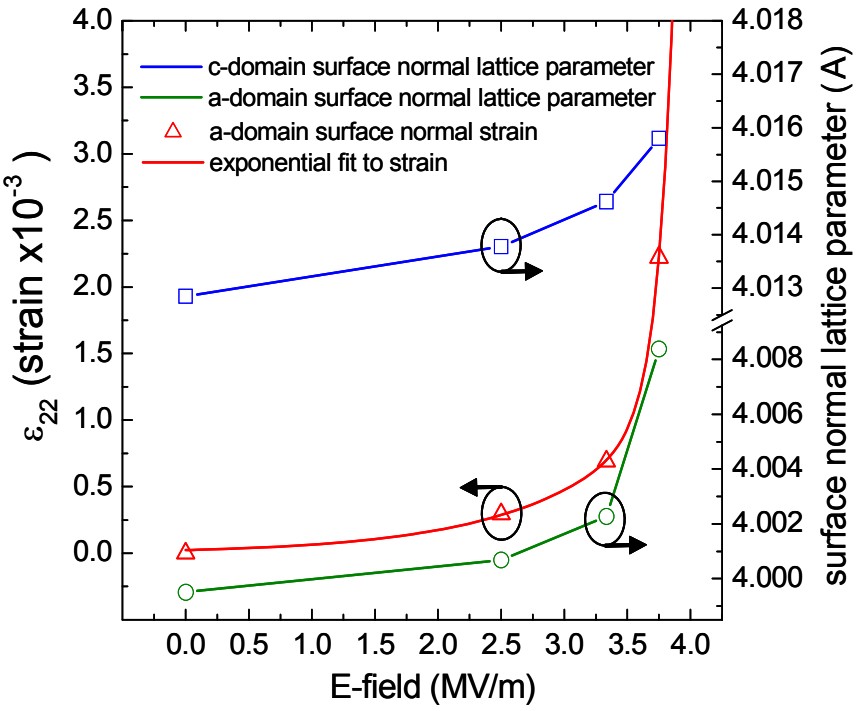

Figure 5-79. Surface normal lattice parameters and strain in sample DT443 are plotted verses the applied field.

In order to model the optical response with the elasto-optic contributions included, the E-field dependent in-plane strains must first be determined from the measured field-dependent out-of-plane strain. Figure 5-80 shows schematics of the in plane stresses that result from the 90° flipping of c-domains. Because the electric field is along an in-plane <110> direction, equal volume fractions of c-domains should be flipped into the two orthogonal in plane <100> directions. Given that there should be equal volume fractions of orthogonal a-domains, the resulting in-plane stresses are expected to be equivalent as shown in the schematic. The bulk elastic compliance values of $BaTiO_3$ are given by[56]

$$\begin{aligned} s_{1111} &= 7.4 \\ s_{3333} &= 13.1 \\ s_{1122} &= -1.4 \\ s_{1133} &= -1.7 \end{aligned} \quad \left(\times 10^{-12} m^2 N^{-1}\right) \tag{5-52}$$

Using these bulk compliance values, the following stress strain relationships are derived for a given a-domain in the film assuming that no shear strains arise due to the 90° flipping of the c-domains.

$$\sigma_{11} = \sigma_{33} = \frac{\varepsilon_{22}}{s_{1122} + s_{1133}}$$
$$\varepsilon_{11} = \sigma_{11}\left(s_{1111} + s_{1133}\right) \tag{5-53}$$
$$\varepsilon_{33} = \sigma_{11}\left(s_{1133} + s_{3333}\right)$$

As such, using equation (5-51) for the field induced surface normal strain of the a-domains, one can derive the associated in-plane strains using equation (5-53). The resulting field dependent strains are shown in Figure 5-81. From Figure 5-81 it is apparent that the anisotropic elastic properties of $BaTiO_3$ result in an in-plane strain along the polar axis that is appreciably greater than the in-plane strain perpendicular to the polar axis resulting in a reduction of the tetragonality of the domain. These field dependent strain values are used in equation (5-48) which in its expanded form, assuming no sheer strains, is given by

$$\begin{aligned}
\Delta\eta_{11} &= r_{113}E_3 + \rho_{1111}\left(\varepsilon_{22} + \varepsilon_{11}\right) + \rho_{1133}\varepsilon_{33} \\
\Delta\eta_{22} &= r_{113}E_3 + \rho_{1111}\left(\varepsilon_{22} + \varepsilon_{11}\right) + \rho_{1133}\varepsilon_{33} \\
\Delta\eta_{33} &= r_{333}E_3 + \rho_{3311}\left(\varepsilon_{22} + \varepsilon_{11}\right) + \rho_{3333}\varepsilon_{33} \\
\Delta\eta_{23} &= r_{133}E_2 \\
\Delta\eta_{13} &= r_{133}E_1 \\
\Delta\eta_{12} &= 0
\end{aligned} \tag{5-54}$$

The bulk values of the unitless $BaTiO_3$ elasto-optic tensor components (ρ_{ijmn}) employed[56] were

$$\rho_{1111} = 0.50 \quad \rho_{1133} = 0.20$$
$$\rho_{3333} = 0.77 \quad \rho_{3311} = 0.07 \tag{5-55}$$

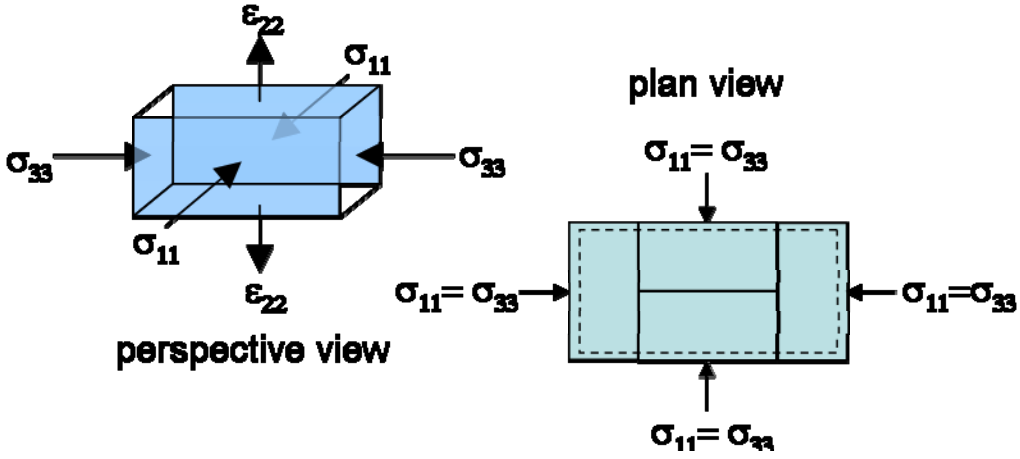

Figure 5-80. Schematics showing stress and strain that results from 90° c-domain flipping. Left figure shows a single a-domain unit cell. Right figure shows plan view with equal number of 90° a-domain unit cells. Equal volume fractions of 90° a-domain variants are expected in the thin films.

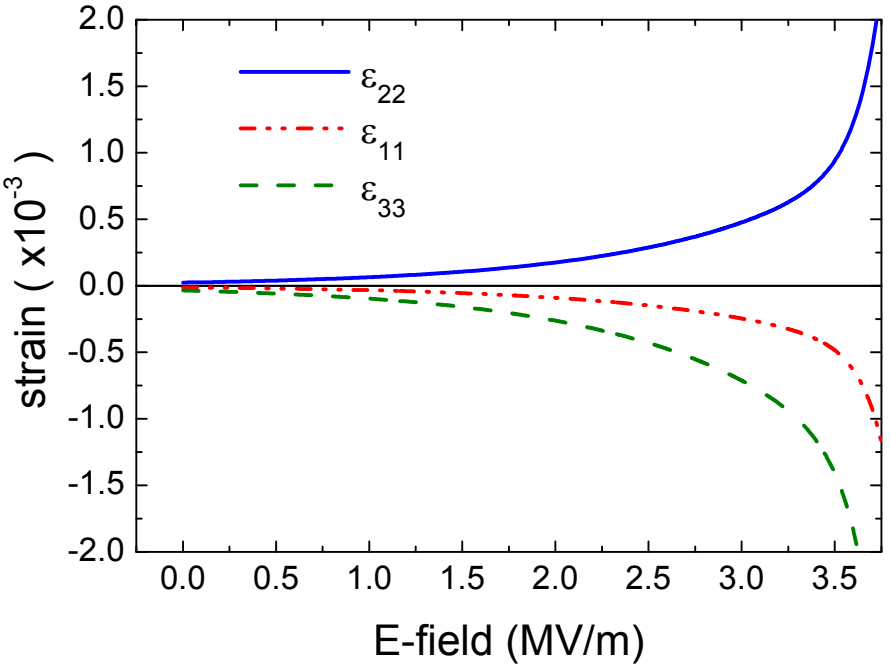

Figure 5-81. Theoretical E-field dependent strains in the a-domains of sample DT443 due to 90° c-domain flipping. ε_{22} is gven by the emperical equation (5-51), while ε_{11} and ε_{33} are given by equation (5-53).

The theoretical EO response of the different a-domain variants is determined using the procedure outlined in Section 4.2.2 and Appendix II, after determining the change to the impermeability tensor given by equation (5-54). The resulting theoretical electro-optic response for a 650 nm thick film is shown in Figure 5-82. Comparison of the theoretical EO response in Figure 5-82 with that at low fields where c-domain flipping can be neglected (as shown in Figure 4-16) shows that while in both cases ΔI has a quadratic dependence on the applied field, the sign of the quadratic component is different in the two cases. At low fields where c-domain flipping is absent or negligible, the birefringence of the T5 a-domain (see Figure 4-2) increases quadratically with increasing positive E-field magnitude giving rise to the positive curvature of the EO response due to domain variant 5. In contrast, the anisotropic field induced in-plane strain results in a negative curvature of the EO response seen in Figure 5-82.

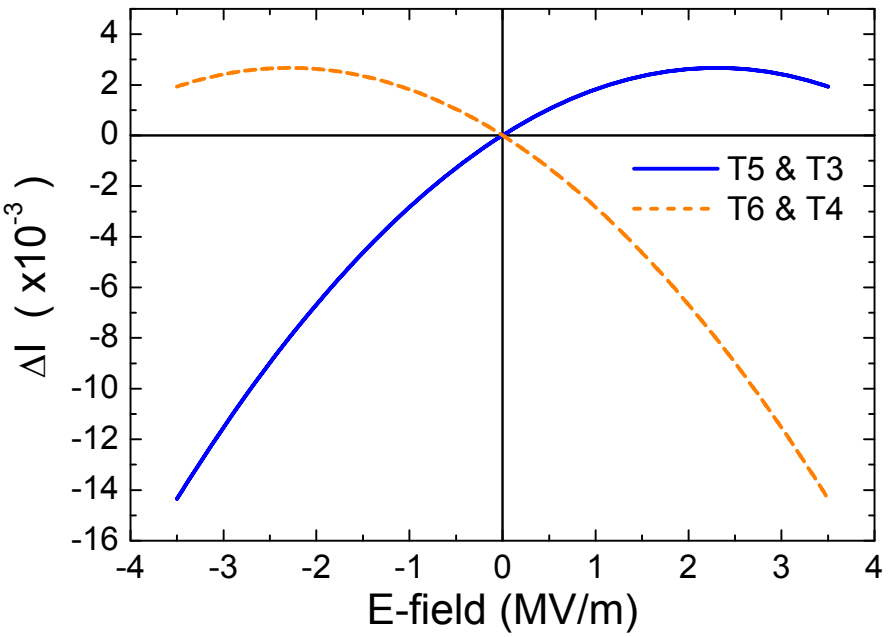

Figure 5-82. Theoretical EO response of a 650 nm thick $BaTiO_3$ thin film when the effect from strain due to 90° c-domain flipping is included.

As with the measurement at low fields discussed previously in this section, one needs a means to predict the relative volume fraction of 180° a-domain variants. Inspection of Figure 5-83 shows that even upon measuring the EO response with an applied field of 3.5 MV/m (more than 4x that used in the low field measurement) the film average coercive field is only marginally larger than that measured under an applied field magnitude of 0.8 MV/m. This is consistent with the saturation of the remnant electronic polarization hysteresis loop coercive fields above 0.8 MV/m measured in this sample (see Figure 5-30). Therefore it was assumed that the remnant polarization loop measured at 0.8 MV/m corresponds to nearly full poling of the a-domains. As such the hysteretic $\Delta A_{ij}(E)$ used in fitting the high-field EO response was derived from the remnant hysteresis loop measured at 0.8 MV/m. Figure 5-84 shows a plot of the $\Delta A_{ij}(E)$ assumed in modeling the EO response in Figure 5-85 as well as the remnant polarization loop from Figure 5-66 measured with field magnitudes of 0.8 MV/m renormalized to 1 to reflect the assumption of full poling of the a-domains. The resulting theoretical EO response is shown in Figure 5-85 along with the measured EO response.

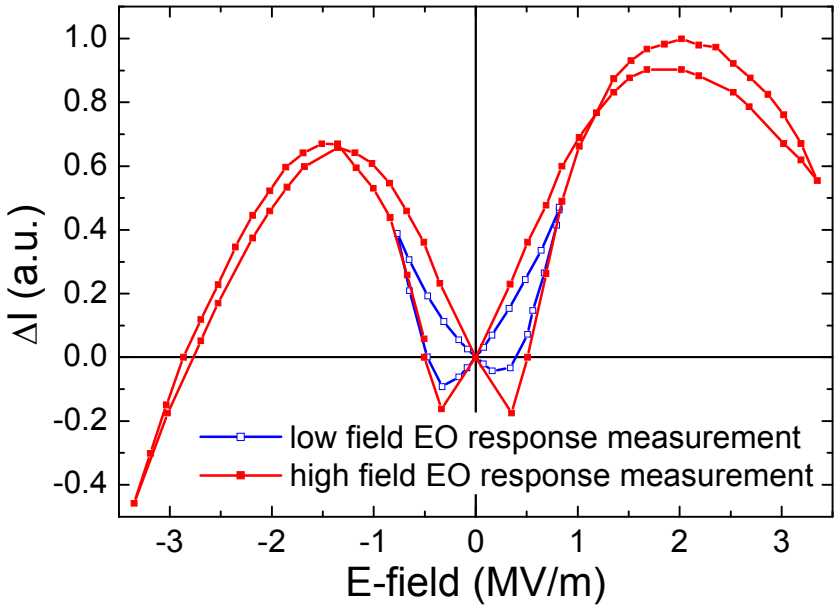

Figure 5-83. Hysteretic EO response of sample DT443 under applied electric field of magnitudes as high as 3.5 MV/m. The "bending over" of the response as field magnitudes exceed ~1.5 MV/m is attributed to strain induced by 90° flipping of c-domains. The EO response under a maximum field amplitude of 0.8 MV/m is included for comparison.

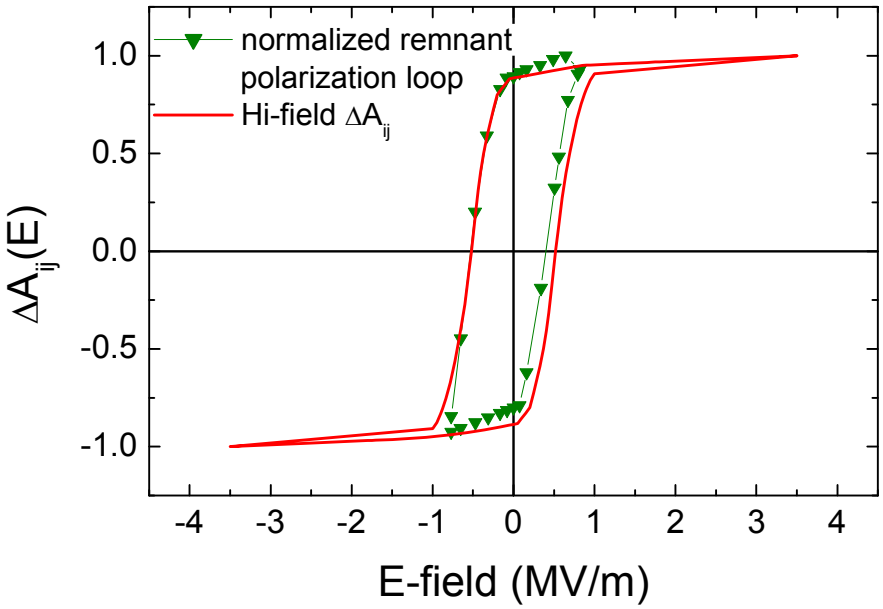

Figure 5-84. Remnant hysteresis loop measured with a field magnitude of 0.8 MV/m. The remnant loop is normalized to 1 to reflect the assumption of full poling of the a-domains. The fit in red was used to model the difference in relative domain fractions of 180° a-domains, $\Delta A_{ij}(E)$, for the purpose of modeling the EO response shown in Figure 5-85. (DT443).

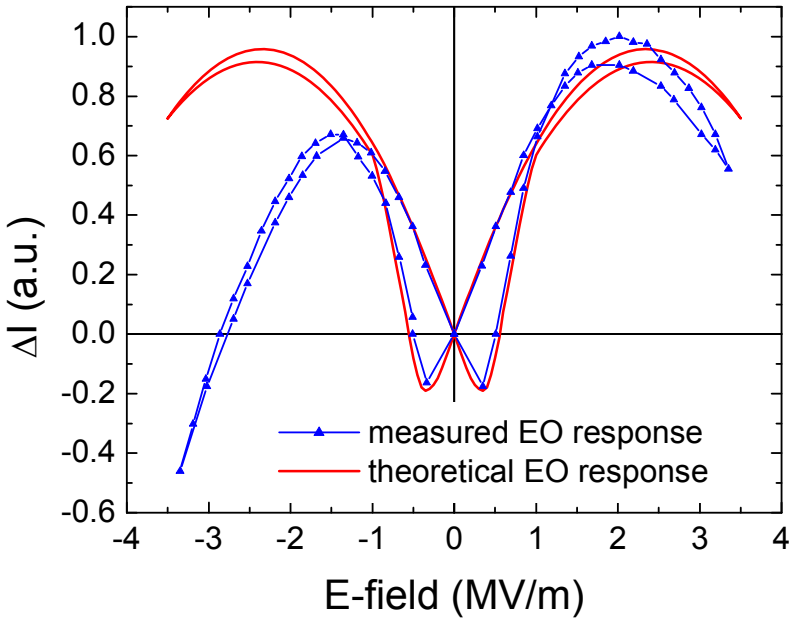

Figure 5-85. Theoretical EO response when the difference in relative volume fraction of 180° a-domains, $\Delta A_{ij}(E)$, is modeled using the remnant polarization loop measured at a maximum field amplitude of 0.8 MV/m. (DT443).

The asymmetry observed in the measured high-field EO data could be accounted for by the presence on a built in potential in the film due either to the defect structure or compositional variations. As mentioned in Section 5.1, compositional variations can give rise to a field dependent offsets of the measured electronic polarization hysteresis loops due to internal fields and associated "nonreversible" components of the polarization[220]. It was shown in Section 5.1 that like most samples measured, sample DT443 exhibits a field dependent offset of the electronic polarization. From the remnant polarization values from Table 5-2 sample DT443 is determined to have a +8% polarization offset as given by

$$\frac{\left|{}^{+}P_r\right|-\left|{}^{-}P_r\right|}{\left|{}^{+}P_r\right|+\left|{}^{-}P_r\right|}=+0.08 \tag{5-56}$$

By incorporating a modest polarization offset that is then reflected in a similar offset of $\Delta A_{ij}(E)$, a theoretical EO response reflecting the asymmetry of the measured EO response is reproduced. Figure 5-86 shows the original symmetric $\Delta A_{ij}(E)$ function as well as that after positively biasing the relative volume fraction by 0.0575 or just less than 6%. Note from the figure that the shifted $\Delta A_{ij}(E)$ function is

not allowed to exceed unity. The resulting theoretical EO response is plotted along with the measured response in Figure 5-87.

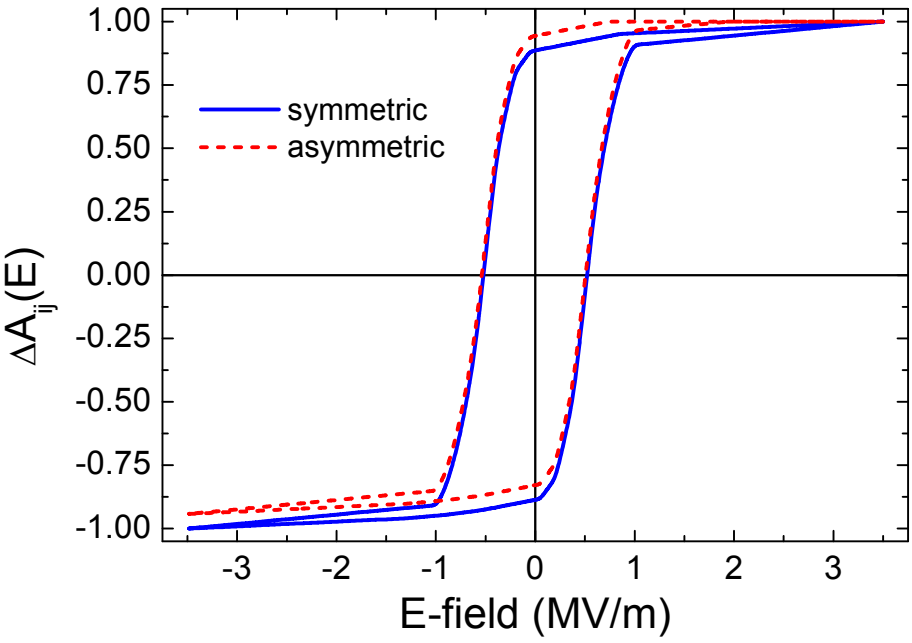

Figure 5-86. The original symmetric ΔA_{ij} function and the shifted function due to internal fields are shown. Both assume that poling is nearly complete at an applied field magnitude of 0.8 MV/m.

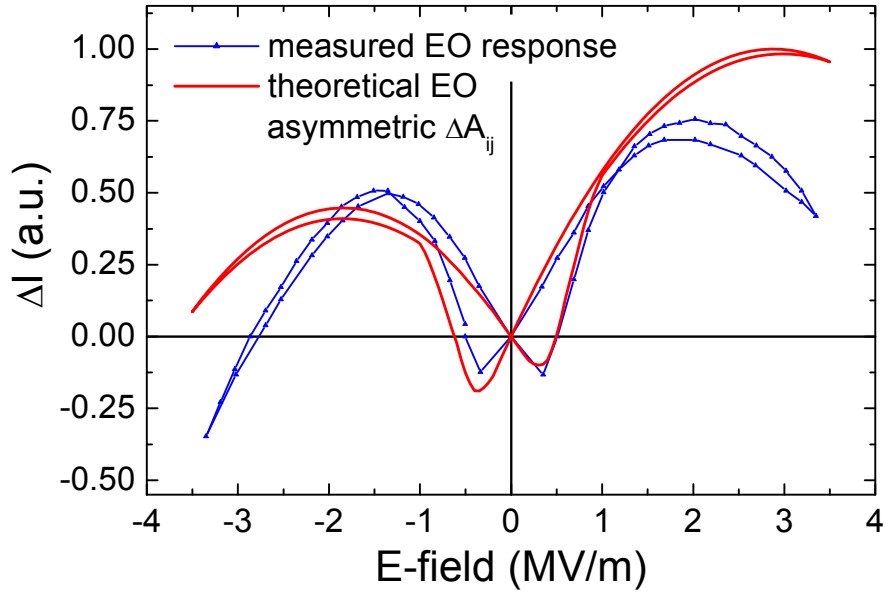

Figure 5-87. The asymmetry of the measured EO response is qualitatively reflected in the theoretical response under the assumption of a finite internal field (DT443)

The strain measured from the field dependent x-ray experiments is likely considerably smaller than the actual strain in the 12 μm electrode gap where the optical mode propagates and the resulting fit is markedly improved by assuming a 10x larger in-plane strain. As mentioned previously due to the illumination by the x-rays of a 130 μm wide area of the sample In measuring the field-dependent surface normal lattice parameter, the smallest available slit size was 50 μm. Given an electrode gap of just 12 μm and the incidence angle of ~22.5^{o} for examination of the $BaTiO_3${200} peaks, the total area illuminated by x-rays was ~11x larger than that between the electrodes where the applied field is strongest as seen in Figure 5-78. As such the measured surface normal strain represents the modal average of the entire illuminated area which will be substantially less than that between the electrodes where the in-plane field is maximized. Figure 5-88 shows the resulting theoretical EO response under the assumption of a 1% strain at ±3.5 MV/m. In other words 10x the measured surface normal strain from Figure 5-77 and Figure 5-79. While the assumption of a 1% strain yields an excellent fit it is not a reasonable assumption as the strain can not exceed the self-strain of $BaTiO_3$ which in the bulk is approximately 1%. Therefore to realize a 1% strain would require a fully c-oriented film of bulk tetragonality undergoing full 90^{o}-domain switching. The fit from Figure 5-87 using the *measured* strain is reasonably good. As such it is more likely that the measured EO response can be explained by strains *moderately* higher than those determined from the x-ray diffraction analysis, in conjunction with some deviation of the various parameters (r_{ij}, ρ_{ijmn}, n_o, n_e) from their bulk values.

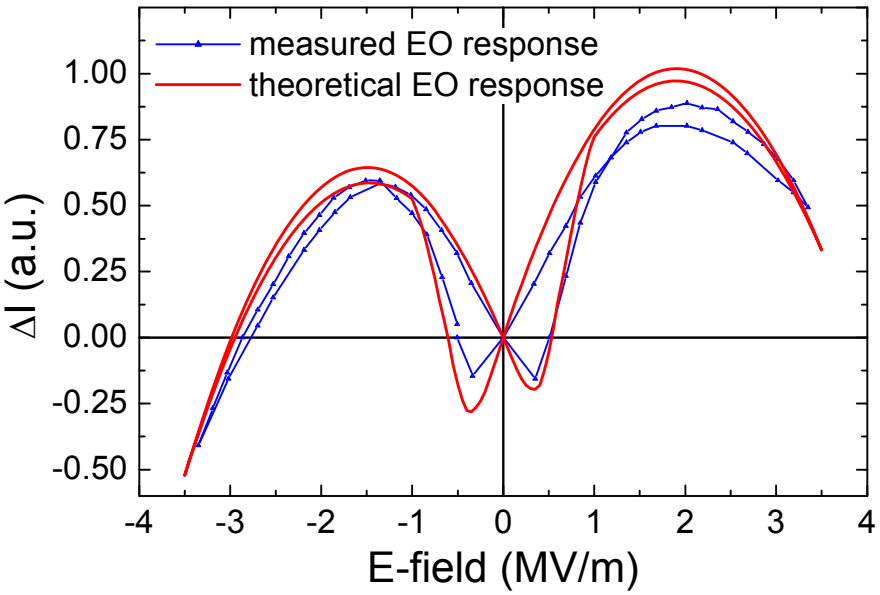

Figure 5-88. The theoretical EO response assuming the same finite internal field as in Figure 5-87 but assuming the strain within the 12 μm gap between the electrodes is 10x that determined from the surface normal x-ray diffraction measurements (DT443).

One final aspect of the measured hysteretic EO response that has yet to be considered is the ascending and descending branches crossing at finite field magnitudes for both positive and negative polarities of the applied voltage. It is proposed that this could be explained by the presence of slow-relaxing quasi-stable 90°-switched domains. It will be shown in Section 5.2.4.2 that the strain-driven relaxation of a 90°-flipped domains back to the unflipped state is significantly slower than the initial E-field-driven 90° domain flipping process. If some fraction of the flipped c-domains relaxes back to the unflipped state sufficiently slowly or are quasi-stable in the flipped state, then some transient hysteresis would be observed in the transmitted intensity due to these slow-relaxing c-domains as shown in Figure 5-89. Such hysteresis in the optical response would give rise to the "cross over" observed in the measured EO response as shown in Figure 5-90. It should be noted that the hysteresis in Figure 5-89 is strictly hypothetical and only intended to show that such transient hysteresis would give rise to the observed "cross over " of the ascending and descending branches of the measured hysteretic EO response.

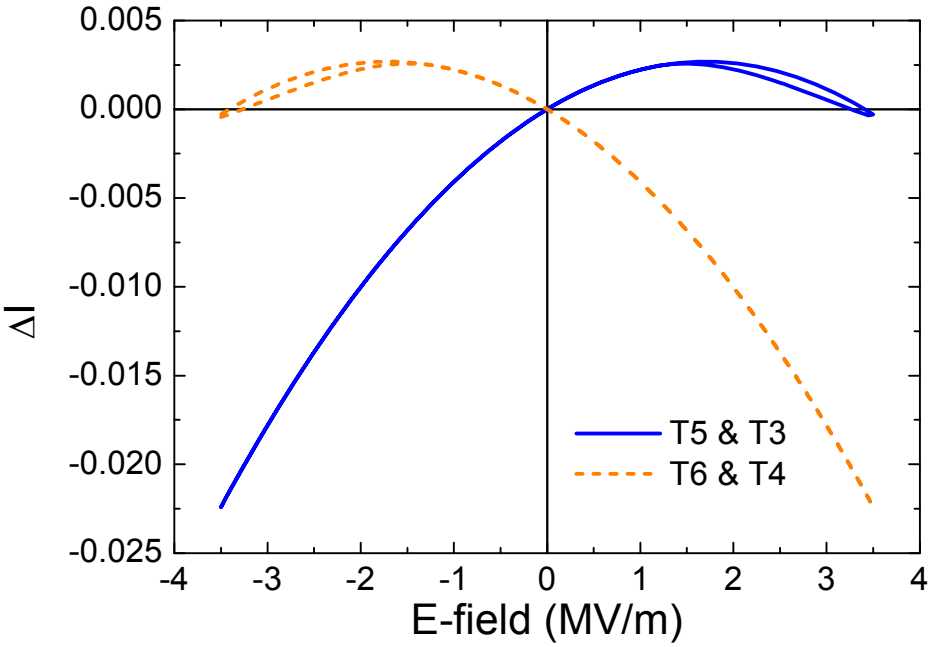

Figure 5-89. Figure shows a hypothetical hysteretic dependence of the transmitted intensity of the various a-domain variants due to slow relaxation dynamics of some fraction of the flipped c-domains.

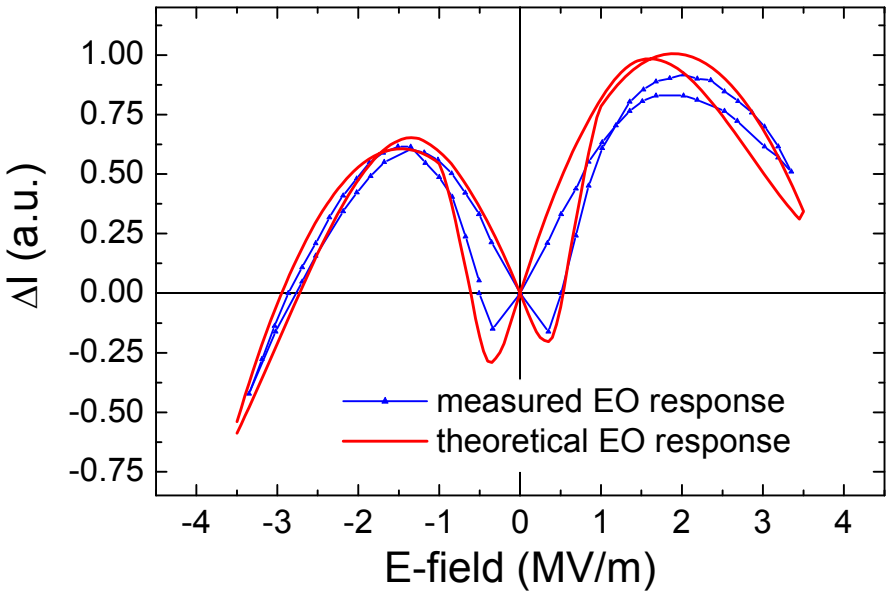

Figure 5-90. The resulting theoretical EO response under the assumption of a hysteretic dependence of the transmitted intensity due to the various a-domain variants, exhibits "cross over" at finite field of the ascending and descending branches of the response curve which is qualitatively similar to that observed in the measured EO response (DT443).

5.2.4 *Extrinsic EO effect and its frequency dependence*

5.2.4.1 *Slow f-response /large extrinsic EO effect due to significant 90° domain flipping*

Large electro-optic coefficients have been measured that are consistent with the large change in birefringence that occurs as a result of 90°-domain switching. When a ferroelectric domain undergoes a 90° domain switch the associated change in the birefringence is trivially twice the natural birefringence of the ferroelectric as seen in Figure 5-91c. For $BaTiO_3$ with a natural birefringence in bulk single domain samples of $\Delta n = 0.052$ at $\lambda_o = 633$ nm this corresponds to a change in birefringence of $\delta\Delta n = 0.104$. In contrast the intrinsic change in the birefringence due to the intrinsic linear electro-optic effect in $BaTiO_3$ is given by[175]

$$\delta\Delta n = -\tfrac{1}{2}\left\{ n_e^3 \left[r_{33} - \left(\frac{n_o}{n_e}\right)^3 r_{13} \right] E_3 + \tilde{n}^3 \left[r_{51} E_1 \right]^2 \right\} \qquad (5\text{-}57)$$

$$\tilde{n}^3 = \left(n_o^3 - n_e^3\right)\left(n_o^2 n_e^2\right) \Big/ \left(n_o^2 - n_e^2\right)$$

where n_o and n_e are the ordinary and extraordinary refractive indices (2.412 and 2.36 respectively for λ_o=633 nm)[22]. For an applied <110> field of ~1.4 MV/m (E_1=E_3= 1 MV/m) the change in birefringence in $BaTiO_3$ from equation (5-57) is just less than 1×10^{-3} or two orders of magnitude smaller than the extrinsic effect of a 90° domain reversal.

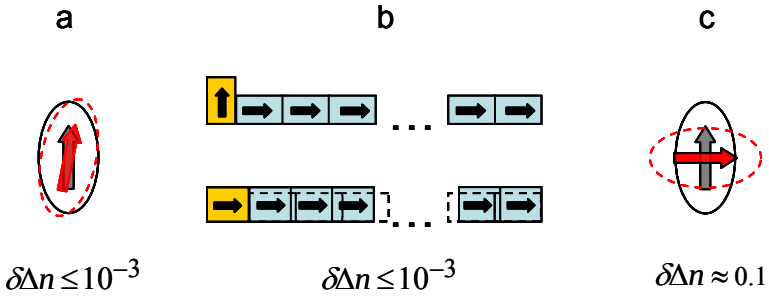

Figure 5-91. For 1 MV/m E-fields the change in birefringence due to both a.) the intrinsic EO effect and b.) the elasto-optic effect due to 90°-domain flipping a small domain volume fraction are on the order of 10^{-3}. That due directly to a 90°-domain flip c.) in which the ordinary and extraordinary axes effectively trade places is ~0.1

[22] Equation (5-57) must be used to find the change in birefringence in $BaTiO_3$. For an applied field of 1 MV/m using the large off diagonal coefficient in the often used expression $\delta\Delta n = \tfrac{1}{2} n^3 r_{51} E$ overestimates $\delta\Delta n$ by approximately 5x.

Changes in birefringence due to intrinsic and extrinsic effects are expected to have very different frequency dependencies as well. The intrinsic linear electro-optic coefficient is generally dominated by ionic contributions and the frequency dispersion is generally expected to be similar to that of the dielectric constant[221-223]. In contrast the frequency response of extrinsic effects due to 90° domain switching is determined by the kinetics of domain nucleation and growth. The switching time is limited in this case by either the nucleation rate or the domain wall velocity. It is generally accepted that the later is limited to the speed of sound as no supersonic domain wall velocities have been reported[4]. This upper limit on the domain wall velocity still allows for switching times on the order of 10s to 100s of picoseconds depending on the device geometry[62]. However as reported by Zhang and Ren the presence of defects can result in significantly longer switching times[224]. In Mn-doped $BaTiO_3$ single crystals, Zhang and Ren observed close to a 3dB attenuation of both the maximum electronic polarization and the electro-strictive strain due to 90° domain switching over the very narrow frequency range from 0.05 to 10 Hz which they attribute to the effects of defect dipoles created ny the Mn-doping[224].

An exceptionally large low frequency EO coefficient that attenuates rapidly with increasing frequency has been observed in our $BaTiO_3$ thin films. The magnitude of the EO coefficient and its marked attenuation with increasing frequency suggest that the response is due to the direct effect of 90° domain switching of a significant c-domain volume fraction in the thin film. The temporal response and its bias dependence are likewise shown to be consistent with that expected due to 90° domain switching. Figure 5-92 shows the effective electro-optic coefficient as a function of frequency for sample AM069b. Sample AM069b is an as-grown (unannealed) 404 nm thick $BaTiO_3$ thin film with a refractive index of 2.389 at λ_o = 633 nm. The effective electro-optic coefficient at 1Hz is 7600 pm/V, a factor of 10 greater than the intrinsic EO coefficient. As seen in the figure the frequency dispersion of the electro-optic coefficient is dramatic, dropping to just 9 pm/V at 5kHz.

The EO coefficient measured at 1 Hz is of the same order of magnitude as the expected amplitude when the response is due primarily to 90°-domain flipping. The theoretical value can be determined using

the bulk indices of refraction of $BaTiO_3$ of n_o=2.412 and n_e= 2.360[56]. The theoretical amplitude of the induced retardation from equation (5-32) for a 404 nm interaction length at a 633 nm wavelength is 0.417 radians[175,179].

$$\Delta\delta = \delta\Delta n\left[\frac{2\pi\ell}{\lambda_o}\right] = 2\Delta n\left[\frac{2\pi\ell}{\lambda_o}\right] = (0.104)\left[\frac{2\pi\ell}{\lambda_o}\right] = 0.417\ Rad \tag{5-58}$$

From equation (5-35) for a 5 V_{PP} driving field with a 10 μm electrode gap, this corresponds to a theoretical effective electro-optic coefficient r_{eff} due to 90° domain flipping of ~30,000 pm/V, approximately four times the magnitude as the measured effective electro-optic coefficient.

$$r_{eff} = \frac{\delta(E)\lambda_o}{\pi\ell n^3}\left(\frac{1}{E}\right) \tag{5-59}$$

That the measured r_{eff} is approximately one fourth of the theoretical value is not surprising given that the c/a ratio or tetragonality of the MOCVD grown $BaTiO_3$ films on MgO(100) substrates is generally reduced relative to that of bulk $BaTiO_3$. Additionally the volume fraction involved in the 90° flipping is certainly less than unity; the c-domain fraction in the film is 70%.

The dramatic frequency dispersion of the extrinsic EO response ($r_{eff}(\omega)$) is in contrast to that when the intrinsic EO response dominates as seen in comparing Figure 5-92 and Figure 5-93. The frequency dependent r_{eff} data of sample AM069b was fit to a KWW stretched exponential function shown in red in Figure 5-92. The frequency dependent effective EO coefficient determined from the fit is given by

$$r_{eff}(\nu) = 10^4 \exp\left[-\left(\frac{\nu}{30}\right)^{0.4}\right] \equiv r_{eff}(\omega) = 10^4 \exp\left[-\left(\frac{\omega}{60\pi}\right)^{0.4}\right] \tag{5-60}$$

In Figure 5-93 the sample AM069a shown in red is from the same sample as AM069b but was annealed in air at 1100 °C for 10 hours prior to measurement. Annealing results in a clear change in the domain structure as previously shown in Figure 5-54 and is likewise presumed to change the defect structure. The EO response in the annealed sample decreases by less than 0.1 dB from 1 kHz through 3 MHz. In contrast the EO response of sample AM040b is attenuated by 0.75 dB over the same frequency range.

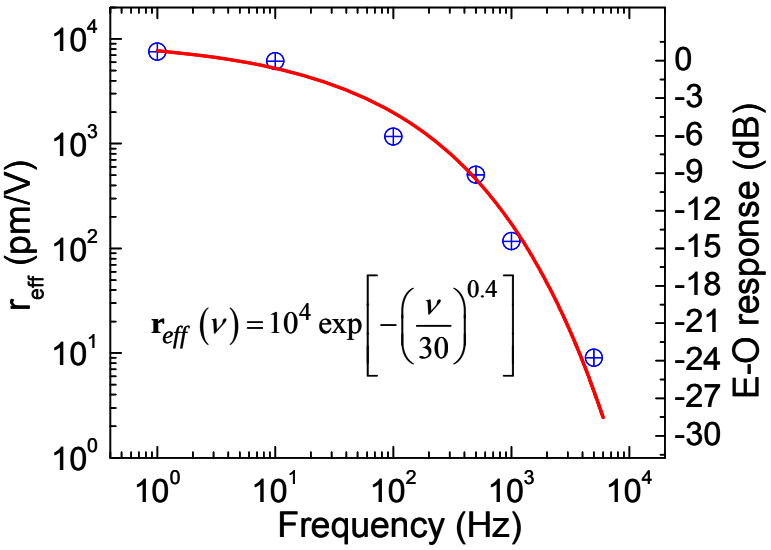

Figure 5-92. Frequency dispersion of the extrinsic electro-optic response of sample AM069b due to 90° domain flipping.

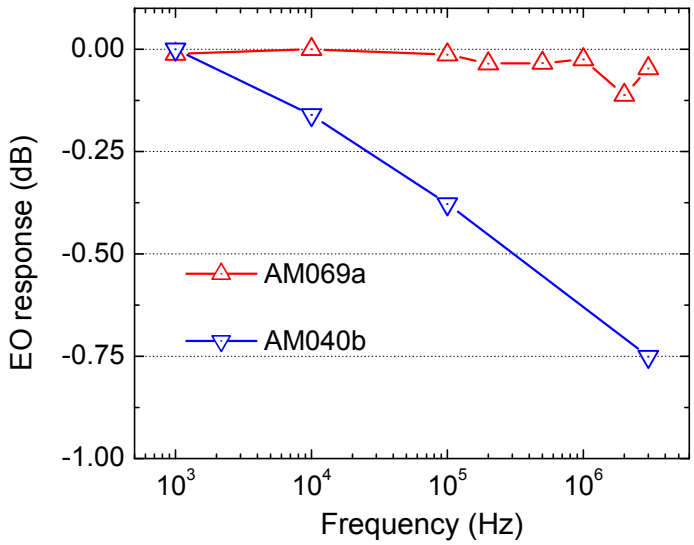

Figure 5-93. Frequency dependence of EO response from 1 kHz to 3 MHz

The most compelling evidence that the observed electro-optic response is due to 90° domain flipping comes from examination of the temporal electro-optic response. When operated at zero bias away from the polariscope's null transmission point, the observed EO response of sample AM069b is at 2x the frequency of the driving voltage. As noted previously, a frequency doubling of the EO response is normally observed for operation at the null transmission point, however the EO response in sample AM069b is at 4x the driving frequency at the null transmission point. Operation under a bias such that

the polarity of the applied voltage does not change sign, the EO response frequency is that for the driving voltage away from the null transmission point, and 2x the driving voltage at the null transmission point. The observed behavior is perfectly consistent with 90^{o}-domain flipping as will be shown in the following discussion.

In chapter 3 it was pointed out that at the null transmission point a characteristic frequency doubling of the observed EO response normally occurs where the observed response frequency is twice that of the driving frequency as seen for sample DT443 in Figure 5-45. The normally observed frequency doubling of the transmitted intensity at the null transmission point is simply a characteristic of the Senarmont polariscope and it is important to emphasize that the actual (or material) EO response frequency of the sample is still that of the driving voltage. A similar frequency doubling occurs at the maximum transmission point while at all other operating points (analyzer angles) the observed intrinsic EO response frequency is the same as the driving frequency.

In contrast to the intrinsic EO response observed in most samples, in sample AM069b the material EO response frequency at zero bias is twice that of the driving voltage. As a result at the null transmission point where an observed doubling of the EO response frequency is normally observed, that of sample AM069b is 4x the frequency of the driving voltage, while at all other points it is at 2x the frequency of the driving voltage. Figure 5-94 shows the electro-optic response of sample AM069b as well as the driving voltage when the analyzer angle is approximately at the null transmission point. At top in the figure is a schematic showing how the operating point on the transmission curve evolves near the null transmission point for one cycle of the driving voltage with zero bias voltage applied. The schematic is meant to represent a very small section near the null transmission point of the full transmission curve shown in Figure 3-7. At the bottom of the figure another schematic shows the evolution of the orientation the domains

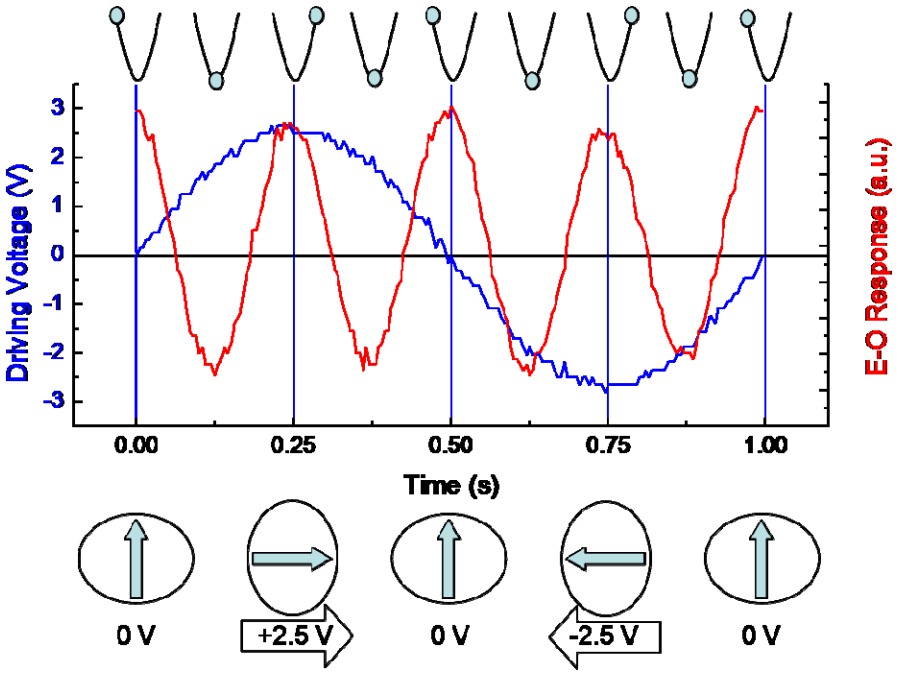

Figure 5-94. Extrinsic EO response of sample AM069b due to 90° domain flipping when operated near the null transmission point with zero bias voltage. Upper schematic shows section of the Senarmont transmission curve near the null transmission point. Lower schematic shows the elliptic cross-section of the negative uniaxial indicatrix of a $BaTiO_3$ domain and the associated orientation of the polar axis under different applied E-fields.

susceptible to 90° domain flipping during the course of one cycle of the driving voltage. The lower schematic shows the orientation of the polar axis as well as the associated indicatrix cross-section. For the device in question the electric field was along a <100> direction such that the c-domains as well as two of the four a-domain variants are susceptible to 90° domain flipping (see Figure 4-2).

The response in Figure 5-94 is explained as follows. Application of a finite field in excess of the coercive field of a domain susceptible to 90° flipping causes the domain to flip such that its polar axis is parallel to the applied E-field. The associated E-field induced retardation results in a shift in position on the transmission curve. As seen in the upper schematic, the shift moves the instantaneous operating point through the null transmission point to a point which relative to the original operating point is equidistant from the null transmission point. This corresponds to one-full cycle of the transmitted intensity in a quarter cycle of the driving voltage. As the applied E-field returns to zero the 90°-flipped domain relaxes back to its original orientation and the instantaneous operating point returns to the original operation point

as the field-induced retardation returns to zero. This corresponds to two full cycles of the response in one half cycle of the driving voltage. Because the associated $\delta\Delta n$ for a 90° domain flip is the same regardless of the polarity of the applied voltage, so too is the induced retardation. As such, when the sign of the applied field changes during the second half of the driving voltage cycle, the process is simply repeated resulting in a total of four cycles of the observed response in a single cycle of the driving voltage.

Figure 5-95 shows the electro-optic response for the same driving voltage when the analyzer angle is adjusted approximately 4° away from the null transmission point. The results from Figure 5-94 and Figure 5-95 can be summarized as follows. Application of a finite field results in a 90° domain flip.

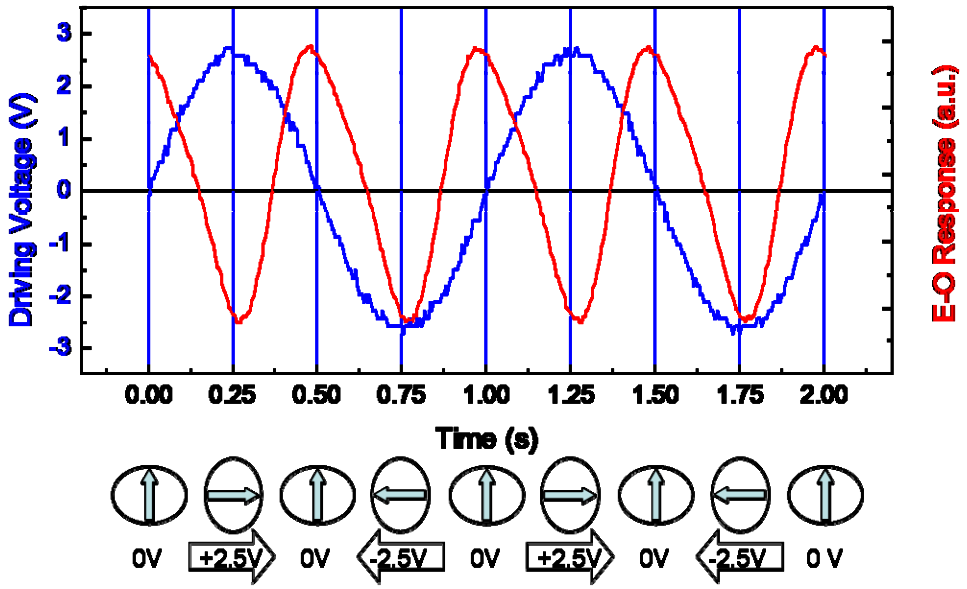

Figure 5-95. Extrinsic EO response of sample AM069b due to 90° domain flipping when operated approximately 4° away from the null transmission point with zero bias voltage

There is a strain associated with accommodating the 90°-flipped domain, and upon removal of the electric field this strain provides a driving force for the reverse 90° flipping process returning the domain to its original state. As just mentioned, because the cross-sectional ellipse of the indicatrix of a flipped domain is the same for either polarity of the applied electric field (as shown in the schematics in Figure 5-94 and

Figure 5-95), the electro-optic response goes through two full cycles in one cycle of the applied voltage as seen in Figure 5-95.

When sample AM069b is driven with a finite DC bias applied, the observed EO response reverts to the normally observed 2x the driving frequency at the null transmission point and 1x the driving voltage frequency at all other operating points. This is consistent with a 90°-degree domain flipping mechanism. In the proposed model of 90°-domain flipping, operation under a small bias voltage such that the polarity of the total applied field does not change sign should result in an EO response with the same frequency as the driving voltage since in this case the c-domains experience a finite switching voltage just once per cycle as opposed to twice per cycle at zero bias. Figure 5-96 shows that as predicted, the EO response under bias is at the same frequency as the driving voltage.

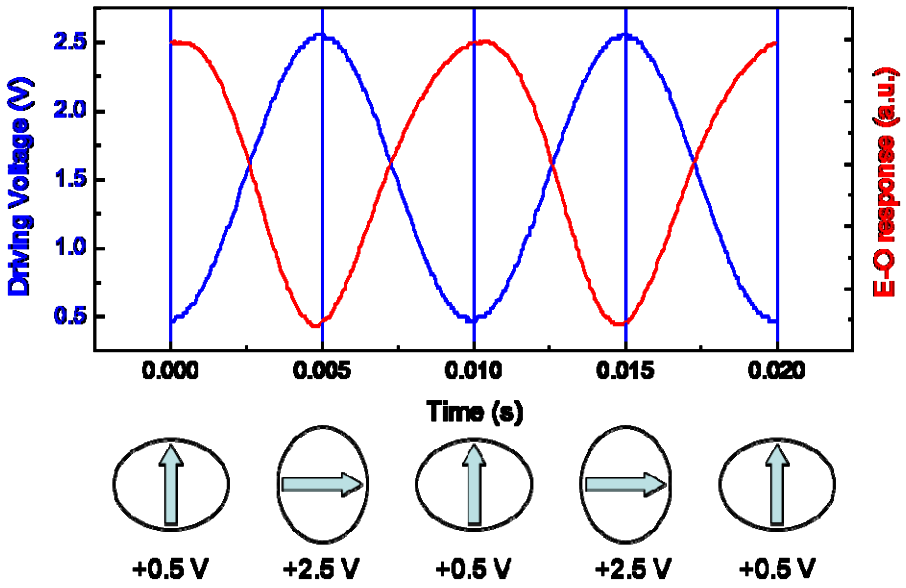

Figure 5-96. Extrinsic EO response of sample AM069b due to 90° domain flipping when operated approximately 1° away from the null transmission point with a +1.5V bias voltage.

Additional support for a 90°-domain flipping mechanism is found by examining the "pinched" electronic polarization hysteresis loops of sample AM069b. Figure 5-97 shows the electronic polarization hysteresis loop of the as-grown sample AM069b. From the figure one sees that the polarization loop is "pinched" for applied fields close to zero. At finite applied field, the polar axes of the 90°-flipped

domains are aligned with that of the applied field and the flipped domains contribute to the measured polarization. As the field returns to zero, the 90°-flipped domains relax back to their original orientation where they do not contribute to the measured polarization. This gives rise to the effective "pinching" of the hysteresis loop in the vicinity of zero applied field. In their study of the switching characteristics of Mn-doped $BaTiO_3$, Zhang and Ren observed a similar pinched hysteresis loop attributed to non-remnant 90° domain switching in which the 90° back switching was mediated by the presence of defect dipoles due to the Mn-doping[224,225]. Similarly "pinched" hysteresis loops due to 90° domain flipping have been predicted in phase field simulations of $PbTiO_3$ under combined electro-mechanical loading as seen in Figure 5-98[206].

Figure 5-97 shows the two non-switching half-loops for the as-grown sample AM069b. As shown in Section 5.1, non-switching half loops typically exhibit a linear dependence on the applied field with modest hysteresis relative to that of the corresponding full-loop. In contrast, those of sample AM069b show significantly more hysteresis than is typical observed and the non-remnant polarization is highly nonlinear. The enhanced non-linear hysteresis of the non-switching half-loops is consistent with the proposed 90° domain switching model.

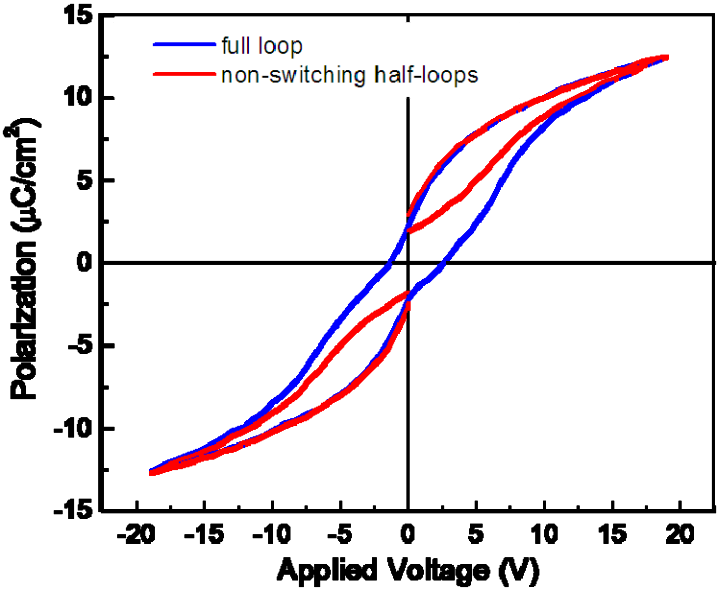

Figure 5-97. "Pinched" hysteresis loop of sample AM069b is consistent with the proposed 90° domain switching model.

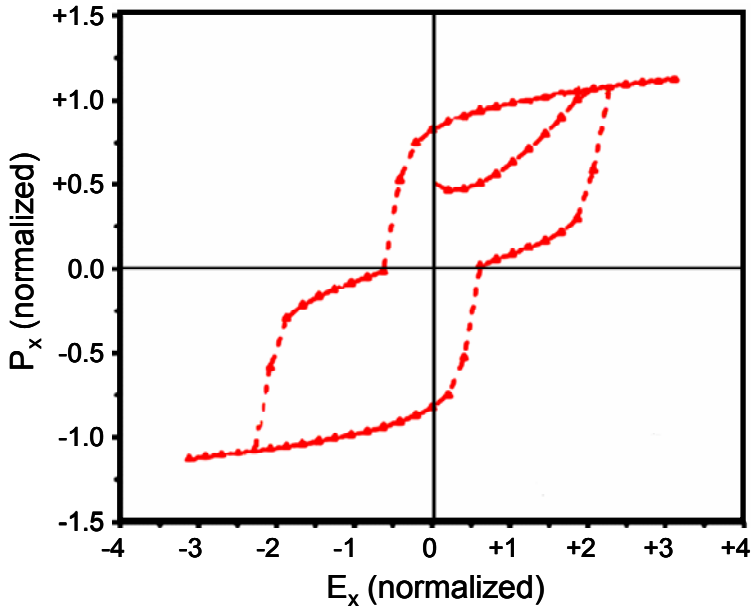

Figure 5-98. The theoretical "pinched" hysteresis loop of a compressively loaded $BaTiO_3$ sample due to 90° domain flipping. Adapted from figure 4a of Soh, Song and Ni (2006)[206].

From the forgoing discussion it is clear that the extrinsic EO effect due to 90° domain switching is easily distinguishable from the intrinsic EO response of the ferroelectric domains. The clearest indication of the extrinsic EO effect due to 90° domain flipping is the doubling of the EO response frequency when operating at zero bias. A rapid attenuation of the EO response with increasing frequency is another indication that domain dynamics are contributing directly to the measured EO response.

5.2.4.2 Transient analysis of the extrinsic EO effect due to 90^o domain switching

The relaxation of the extrinsic EO response due to 90^o domain switching was investigated as a function of the applied field. The observed transient extrinsic EO response under a monopolar voltage pulse is attributed to 90^o-domain switching based upon the accepted theoretical EO response of the given domain variants[178]. In this case the 90^o-switching is driven by the applied E-field while the reverse process upon removal of the applied field is strain driven. The effective relaxation time of the transient EO response upon removal of the applied field increased with the magnitude of the applied E-field. Not surprisingly the magnitude of the transient EO relaxation upon removal of the applied E-field likewise increased with increasing magnitude of the applied field. This simply indicates that larger applied fields resulted in a larger volume fraction of 90^o switched domains in the film at the end of the 12 ms voltage pulse.

A brief discussion of the theoretical support for the attribution of the transient response upon removal of the applied monopolar E-field to the strain-driven back-switching of 90^o-flipped domains rather than 180^o domain reversal is given. Figure 5-99 shows schematics of the indicatrix cross-sections of two 180^o domain variants both under field and in the absence of an applied field. The vertical transitions in Figure 5-99 correspond to intrinsic contributions to the EO response while the horizontal transitions represent domain switching (extrinsic) contributions. The upper horizontal transition associated with ΔI_3 corresponds to the extrinsic contribution from a 180^o domain reversal with a finite field both before and after switching. The lower horizontal switch represents a thermally activated 180^o domain flip in the absence of an applied field. Because the indicatrix cross-section in the absence of a field is identical before and after the flip there is no change in the transmitted intensity associated with this transition. While some 180^o back switching is likely occurring upon removal of the applied field, this back switching in the absence of an applied field does not give rise to a change in the transmitted intensity and therefore does not affect the observed EO response.

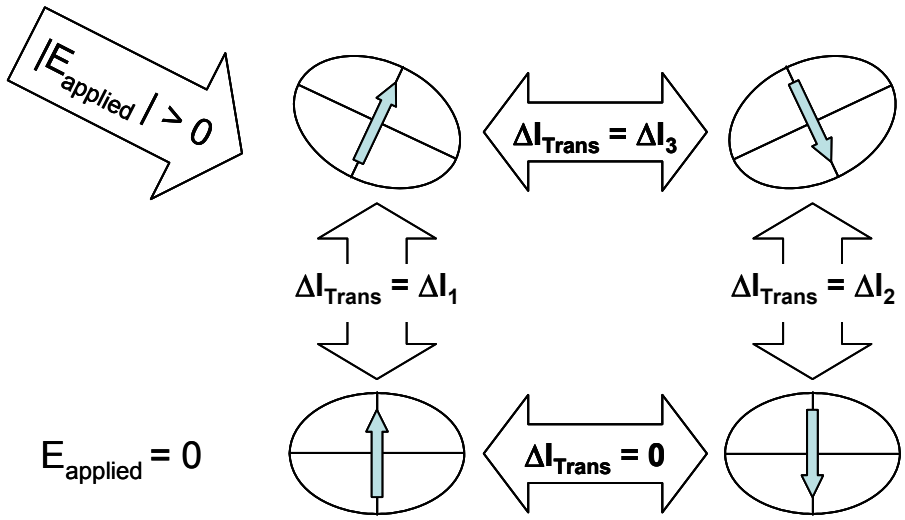

Figure 5-99. Schematic showing the indicatrix cross-section of two anti-parallel domain variants both under field and in the absence of a field. The vertical transitions represent the intrinsic EO contributions of the domain variants while the horizontal transitions represent 180° domain flipping. While a finite extrinsic EO contribution results from a 180° reversal under a finite field (ΔI_3), a 180° reversal in the absents of a field makes no contribution to the EO response as the indicatrix cross-section is unchanged as a result of the flip.

The field dependence of the dynamic EO relaxation was analyzed for sample DT443. The remnant hysteresis loop coercive field for this sample was 0.77 MV/m. Figure 5-100 shows the electro-optic response of sample DT443 for a series of monopolar voltage pulse trains corresponding to field amplitudes ranging from 0.4 to 3.8 MV/m. Fast rise-times are observed in contrast to the much slower strain-driven relaxation times. In order to realize reasonable signal to noise ratios, all of the EO response curves in Figure 5-100, were measured using 3.27 kΩ load resistor. The system rise time with the 3.27 kΩ load resistor was 1.5 μs. A rise time measurement for an applied voltage pulse of 11 V (0.92 MV/m) using a 500 Ω load resistor yielded a 10% to 90% rise times of 28 ns as seen in Figure 5-101a. As seen in Figure 5-101b, the transients follows a simple exponential with a time constant of 11 ns which is attributed to the RC time constant of the system.

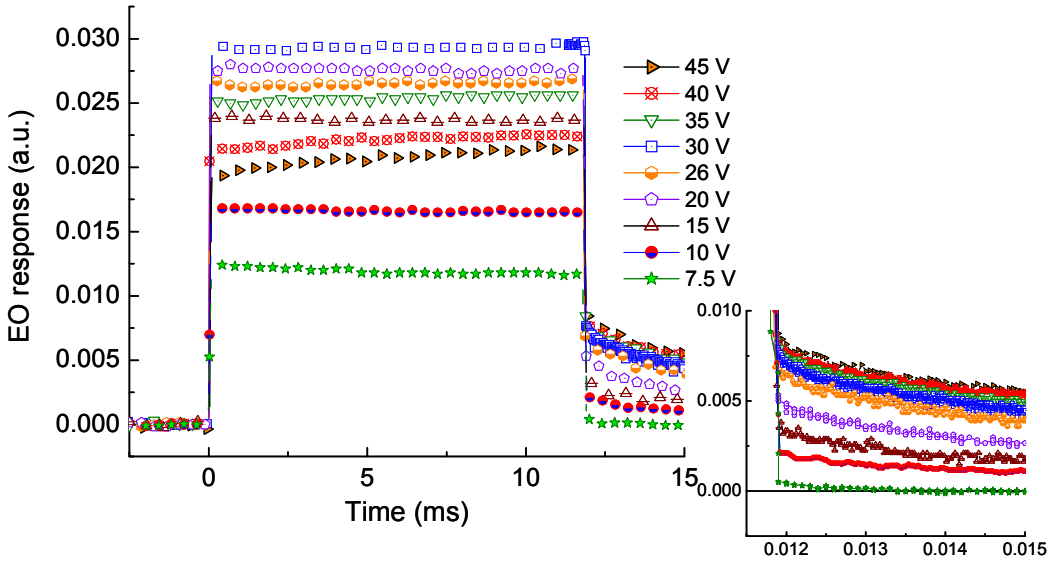

Figure 5-100. Shown are a series of EO response curves of sample DT443 under the application of monopolar voltage pulse trains of different amplitude.

As further evidence that the transient rise time is due to the system RC time constant and not the domain response time of the $BaTiO_3$ thin film, the frequency dependence of the electro-optic response was measured for range of load resistors on the same sample (DT443). The 3dB cutoff frequency (f_c) is related to the RC time constant by $\tau_{RC} = (2\pi f_c)^{-1}$ In Figure 5-102 the inverse of the 3dB bandwidth is given as a function of the load resistor on a log-log plot. As seen in the figure, a 100 Ω load resistor should correspond to an RC time constant of ~10 ns in excellent agreement with the measured time constant of 11 ns. Thus the rise time for the E-field driven 90° domain flipping is faster than the 11 ns RC time constant of the measurement system.

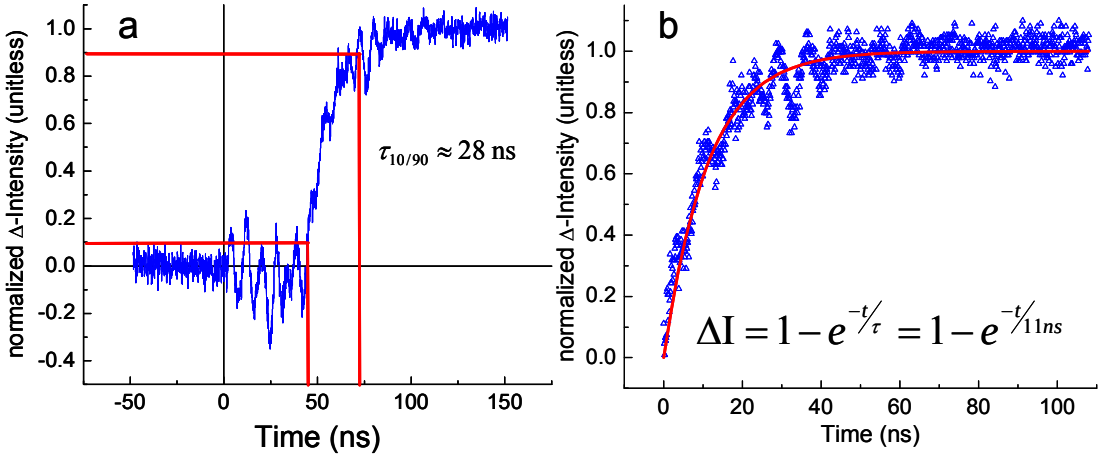

Figure 5-101.a. transient EO rise time when driven by an 11 V pulse (0.92 MV/m). The "ringing" in the response beginning at t=0 is due to channel crosstalk at the oscilloscope. The 10%-90% rise time is 28 ns. b. The transient response is well fit to a simple exponential with a time constant of 11 ns (DT443).

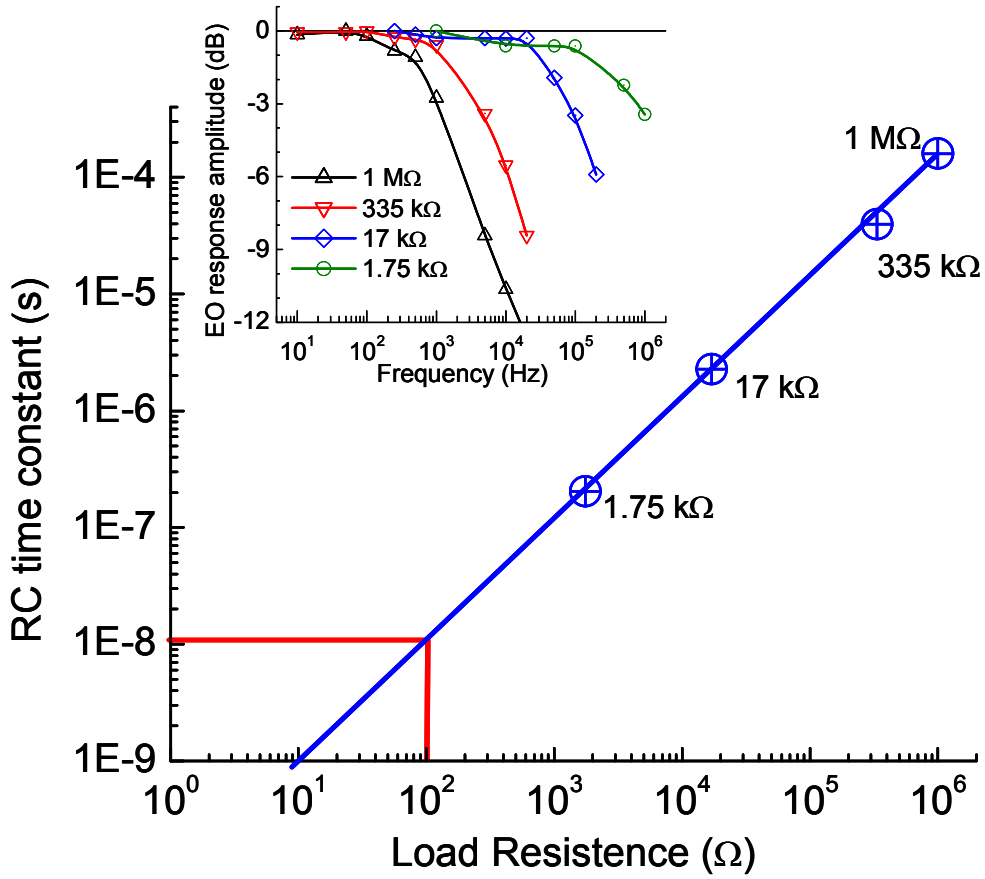

Figure 5-102, τ_{RC} as a function of load resistor determined from the measured 3dB cutoff frequency. Inset shows the frequency dependence of the EO response measured with different load resistors from which the relationship was derived. A 100 Ω load resistor corresponds to a τ_{RC} of ~10 ns in excellent agreement with the measured 11 ns τ_{RC} determined from the fit in Figure 5-101b.

The relaxation dynamics for the polydomain sample was was subsequently measured and analyzed. In contrast to the fast rise times, the decay of the EO response upon removal of the applied field was significantly slower, as seen in Figure 5-100. A simple Debye-like exponential decay is not observed. The dynamic response can however be described by the collective relaxation due to a distribution of Debye-like (exponential) relaxation processes all characterized by different relaxation times[140,143]. Given that these polydomain films consist of domains with a distribution of volumes the assumption of a distribution of relaxation times is a reasonable one[126,149,150]. The distribution of relaxation times however in the polydomain samples is unknown. As such, two different approaches are used to describe the non-exponential relaxation due to a distribution of relaxation times. The first assumes a Pareto power-law distribution of domain volumes over some finite size range[12,66,140]. The justification for this assumption is the previous observation of power-law relaxation in our $BaTiO_3$ thin films over 11 orders of magnitude[12,66]. It is assumed that the origin of the power-law relaxation response results from a Pareto distribution of domain sizes in the polydomain thin films. A second approach is based on the well established fact that a relaxation process that is properly characterized by the well known Kohlrausch-Williams-Watts (KWW) stretched exponential function, must have a distribution of relaxation times that correspond to a Levy α-stable distribution[140,142,143,145-147].

The electro-optic relaxation was first analyzed under the assumption of a Pareto distribution of domain volumes. Previously, a power-law electro-optic relaxation response was observed in our polydomain $BaTiO_3$ thin films[12,66]. The power-law relaxation observed by Hoerman was attributed to a fractal ferroelectric domain structure in the films. It was assumed that the relaxation time was proportional to the domain volume ($\tau_i\left(V_i\right)=\tau_P V_i$) where τ_P is a constant scaling factor. In the earlier work by Hoerman, a limit on the range of domain volumes of 1 nm^3 to 1 μm^3 was assumed. It was likewise assumed that the distribution of domain volumes was given by a "percolative" distribution according to[66]

$$N\left(V\right)=N_{\circ}V^{-\gamma} \tag{5-61}$$

where $N_\circ$ is a constant scaling factor. Because equation (2-8) gives the number density of domains by volume, (2-8) is multiplied by the volume V to get the distribution of relaxation times (DRT) $\Pi(\tau)$ given by

$$\Pi(V) = N_\circ V^{2-\gamma} \Leftrightarrow \Pi(\tau) = N_\circ \left(\frac{\tau}{\tau_P}\right)^{2-\gamma} = N_\circ \left(\frac{\tau}{\tau_P}\right)^{-m} \tag{5-62}$$

For which the response is given by [66,140]

$$\Phi(t) \propto \left(\frac{t}{\tau_P}\right)^{(2-\gamma)} = \left(\frac{t}{\tau_P}\right)^{-m} \tag{5-63}.$$

The right side of equation (2-9) is equivalent to a Pareto distribution[140,141]. It is known that a Pareto DRT gives rise to a power-law transient response of the form given in equation (2-10)[140]. The Pareto probability distribution given on the right in equation (2-9) is equal to zero for $\tau < \tau_P$ as shown in Figure 2-7 where, for illustration purposes, equation (2-9) is plotted for $\tau_P = 5$ ms and *m* ranges from 0.9 to 0.1.

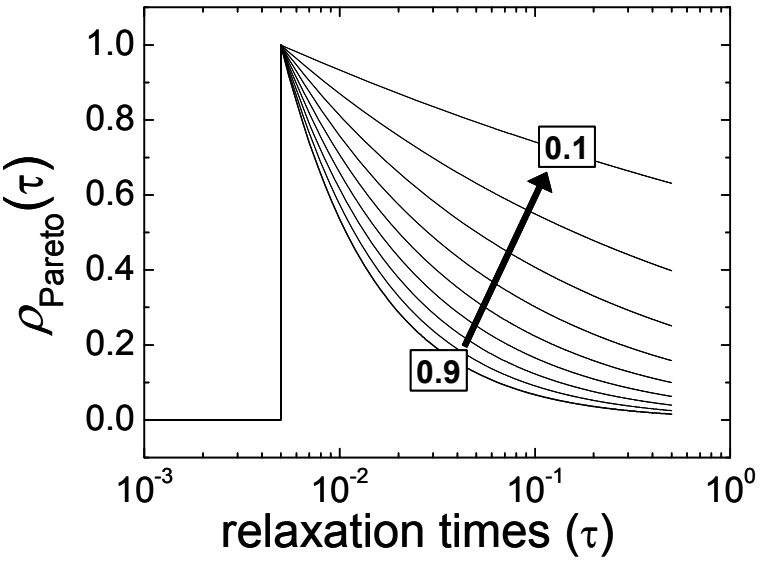

Figure 5-103. Pareto probability distributions of relaxation times given by equation (2-9) are shown for a τ_P value of 5 ms and *m* values ranging from 0.9 to 0.1. For $\tau < \tau_P$ the probability equals zero.

In the long time limit, the relaxation was found to be better characterized by a modified stretched exponential given by

$$\Phi(t) = At^{-m} \exp\left[-\left(\frac{t}{\tau}\right)^{\beta}\right] \tag{5-64}.$$

A is a constant and the exponential in equation (2-11) is of the form of the Kohlraush-Williams-Watts (KWW) stretched exponential[140,142,143]. As the electro-optic relaxation data reported here does not follow a simple power law relaxation we can assume that times longer than 10 μs belong to the long-time-limit regime. The EO relaxation data of sample DT443 were reasonably well fit using equation (2-11) as seen in Figure 5-104. For clarity only every 10th data point is shown. The associated fitting parameters are plotted in Figure 5-105 verses the maximum applied electric field. They are tabulated in Table 5-7.

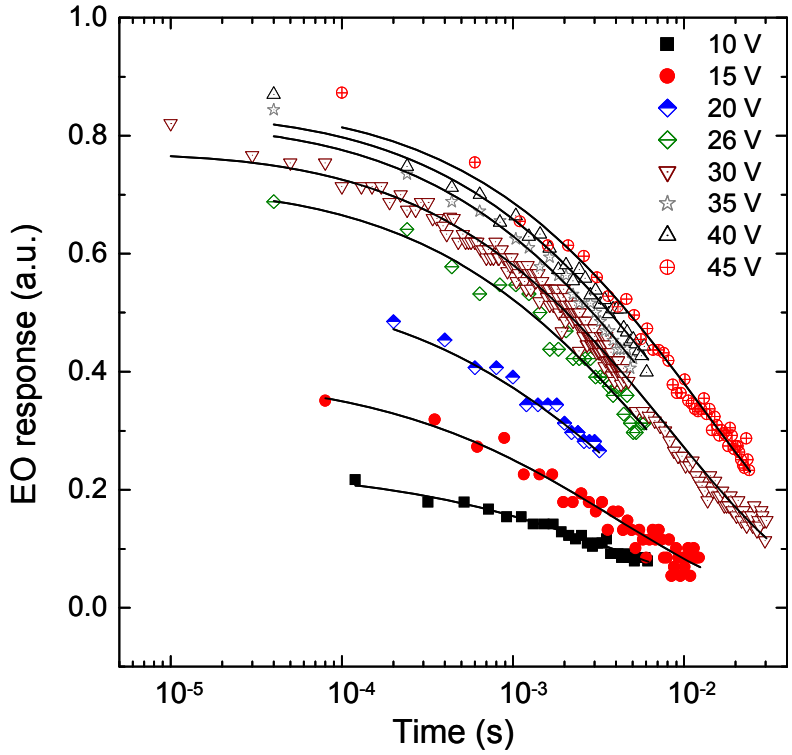

Figure 5-104. The transient electro-optic decay observed in sample DT443 subsequent to removal of the applied 12 ms voltage pulse are shown on a semi-log plot along with the fits to the data using equation (2-11).

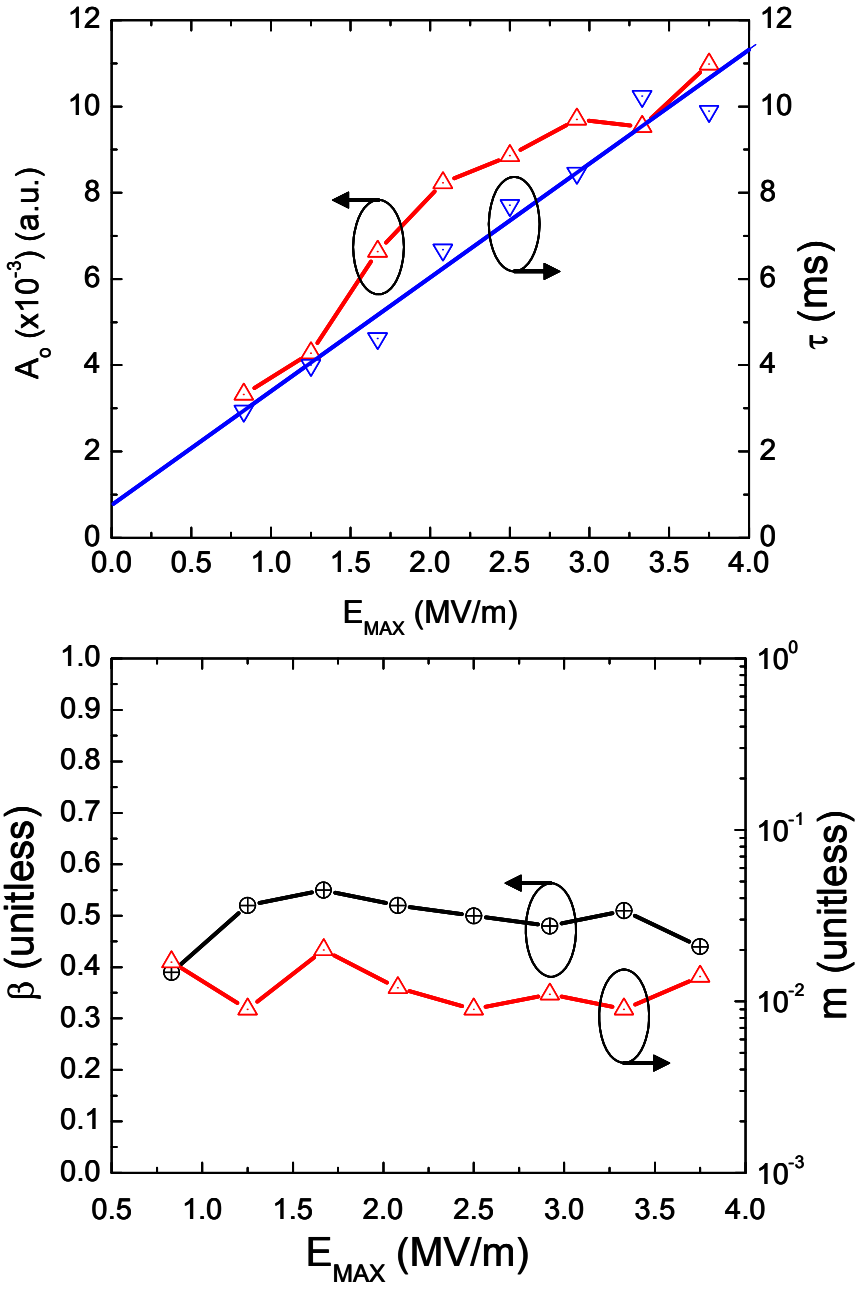

Figure 5-105. The dependence of the fitting parameters in equation (2-11) on the maximum applied field are shown for the transient EO measurements on sample DT443.

Table 5-7. Tabulated fitting parameters of equation (2-11) for the range of applied voltages in sample DT443

V_{max} (V)	E_{max} (MV/m)	A_o (a.u.)	τ (ms)	β	m		$A_{o\ (\beta=0.5)}$ (a.u.)	$\tau_{(\beta=0.5)}$ (ms)
10	0.83	0.332	2.94	0.39	0.017		0.270	4.40
15	1.25	0.428	4.00	0.52	0.009		0.457	3.66
20	1.67	0.664	4.62	0.55	0.200		0.636	4.76
26	2.17	0.823	6.68	0.52	0.012		0.833	6.57
30	2.50	0.886	7.71	0.50	0.009		0.901	7.60
35	2.92	0.970	8.46	0.48	0.011		0.957	8.50
40	3.33	0.953	10.2	0.51	0.009		0.975	10.0
45	3.75	1.10	9.89	0.44	0.014		0.986	12.3

From Figure 5-105 the characteristic relaxation time of the exponential in equation (2-11) τ increases linearly with the maximum applied field with the dependence given by

$$\tau\left(E_{\max}\right) = 2.9E_{\max} + 0.32 \quad (ms) \tag{5-65}$$

The amplitude of the slow transient EO response likewise increases with increasing E_{max}, showing signs of saturation at the higher fields as evidenced by the decrease in dA_o/dE_{max}.

To explain the observed field dependence of the dynamic response, the domain structure that results from the application of the poling voltage needs to be considered. A model due to Molotskii and Shvebelman predicts that the domain "lifetime" upon removal of a poling field increases monotonically with the radius of the domain[149]. Domain switching occurs through a process of nucleation and growth and that the switching times under an applied electric field are generally inversely related to the applied field[226]. For fields in excess of 1 MV/m the domain wall velocity has been reported to be proportional to $E^{3/2}$ [149,227]. Consequently under a larger E_{max} the resultant newly formed a-domains grow to a larger final size during the application of the 12 ms voltage pulse. As a result longer relaxation times are observed for larger E_{max}. In support of this assumption, Agronin et al. have observed a linear dependence of the final domain size on the applied voltage in atomic force microscopy (AFM) studies of domain switching in $LiNbO_3$. Nucleation during domain switching is widely accepted to be homogeneous,

occurring preferably at defect sites and at domain walls[2]. As the average domain size increases the domain wall area per unit volume within the film decreases. If the switching kinetics are nucleation limited as has been suggested[4] then the a larger final domain size results in fewer nucleation sited per unit volume within the thin film. This would explain the longer relaxation times subsequent to larger poling voltages. Interestingly Koval et al. have observed strikingly similar results for 90° domain relaxation in PZT thin films[124].

The parameters τ and A_o just examined are both "scale" parameters. A_o is proportional to the volume fraction of relaxing domains, while τ gives the characteristic time constant for the distribution of relaxation times effecting the scale of the distribution of relaxation times but not the shape of that distribution. In contrast to these "scale" parameters the "shape" parameters consisting of the power-law exponent m and the exponential stretching exponent β exhibit no appreciable dependence on the maximum applied field. These are referred to as shape parameters as they effect the shape of the distribution of relaxation times. Comparing the results reported here with the previous work by Hoerman it is found that the values of the exponent m observed here (~0.011) are an order of magnitude smaller than those previously measured by Hoerman for electro-optic relaxation in the $BaTiO_3$ thin films (0.2 to 0.3)[66]. However the *largest* applied fields by Hoerman (1MV/m) are comparable to the *smallest* applied fields in this study. Furthermore the transient response in Hoerman's work was measured subsequent to the application of a 1 μs pulse while the pulse widths in the present study were 12 ms (five orders of magnitude longer). As observed by Hoerman[66] "for very large applied E and long t_E (duration of applied E pulse), a smaller m is measured, corresponding to the removal of the fractal domain features." Given that E_{max} is as much as 4x greater that that employed by Hoerman and t_E is five orders of magnitude longer, the smaller values of m observed here are expected.

Since the m and β parameters were independent of field, a subsequent set of fits to equation (2-11) were made with the values of m and β held constant in hopes of reducing the noise in the E_{max} dependence of the parameters A_o and τ. The relaxation data of sample DT443 was refit with m and

β held constant at values of 0.011 and 0.5 respectively (their average values excluding apparent outliers). Figure 5-106 shows the resulting fits to equation (2-11) along with the original fits where m and β where allowed to vary. The field dependent amplitude A_o is improved somewhat by holding m and β fixed. The solid blue line in Figure 5-106a is a fit to A_o using a Weibull cumulative distribution function given by

$$A_o(E) = A\left(1-\exp\left[-\left(E/\psi\right)^{\alpha}\right]\right) = \left(1-\exp\left[-\left(E/1.6\right)^{1.9}\right]\right) \tag{5-66}$$

The inset shows the corresponding Weibull probability density function that is expected to approximate the distribution of coercivities for 90° c-domain switching. Since the relaxation amplitude should be proportional the domain volume fraction switched by the poling field, $A_o(E)$ is effectively the distributi of coercive fields for 90° domain switching. Upon holding m and β fixed the linear fit to τ excluding the first and last data points is found to go through the origin and is given by

$$\tau(E) = 3E + 0.1 \quad (ms) \tag{5-67}$$

where the field is in MV/m.

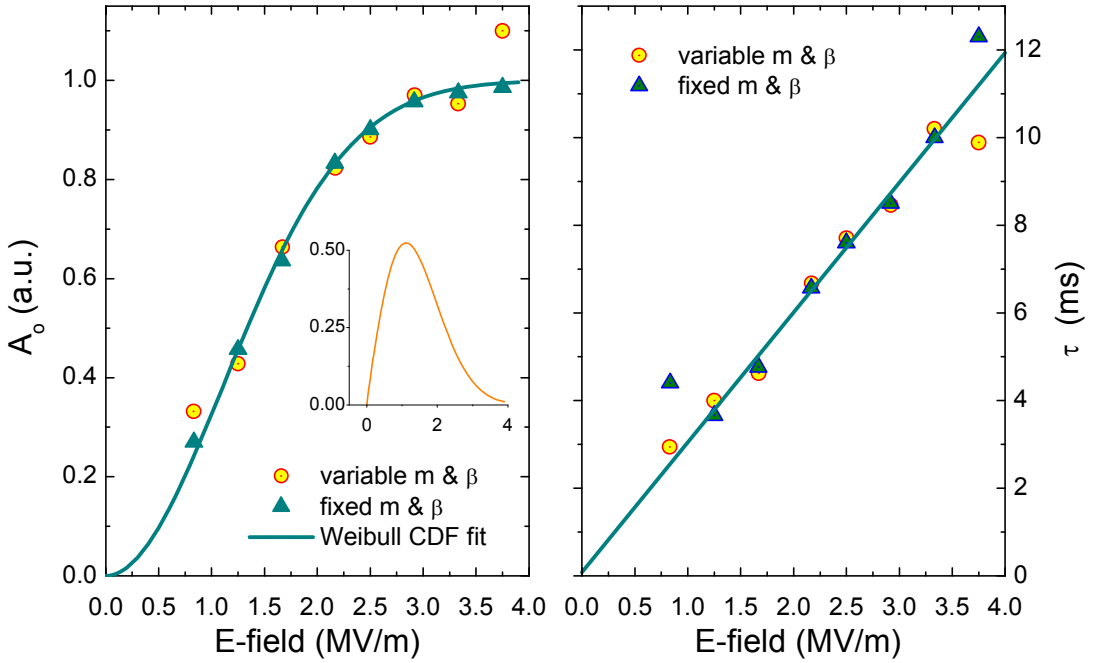

Figure 5-106. Comparison of the resulting scale parameters A_o and τ of equation (2-11) when the shape parameters given by the power exponent m and the stretching exponent β are left variable or fixed.

The dynamic electro-optic response upon removal of the applied field was also analyzed using the well known Kohlrausch-Williams-Watts (KWW) stretched exponential function. The KWW stretched exponential has been used extensively to model the relaxation of ferroelectric domains[117-135]. The KWW stretched exponential is given by

$$\Phi(t) = 1 - \exp\left[-\left(\frac{t}{\tau}\right)^{\beta}\right] \tag{5-68}$$

where τ is a characteristic relaxation time of the system and β is referred to as the stretching exponent. When β equals 1, equation (2-12) reduces to a simple exponential and for small β of approximately 0.1 or less equation (2-12) predicts a logarithmic time dependence[144]. It has been well established that a relaxation process that is properly characterized by the Kohlrausch-Williams-Watts stretched exponential function, is characterized by a distribution of relaxation times that correspond to a Levy α-stable distribution[140,142,143,145-147]. The general form of the Levy α−stable distribution is given by[140,142,145]

$$\rho_{KWW}(\tau) = \frac{-\tau_{KWW}^{\,2}}{\pi\tau}\sum_{k=0}^{\infty}\left[\frac{(-1)^k}{k!}\sin(\pi\beta k)\Gamma(\beta k+1)\left(\frac{\tau}{\tau_{KWW}}\right)^{(\beta k+1)}\right] \tag{5-69}$$

where $\Gamma(n)$ is the Gamma function. For $\beta = ½$, equation (2-13) takes the closed analytic form[142,145]

$$\rho_{KWW}(\tau) = \frac{1}{2}\sqrt{\frac{\tau}{\pi\tau_{KWW}}}\exp\left[\frac{-\tau}{4\tau_{KWW}}\right] \tag{5-70}.$$

In Figure 2-9 equation (5-70) is plotted for τ_{KWW} equal to 4 ms. The similarity between the Levy α-stable distribution in Figure 2-9 and the Pareto distribution of relaxation times in Figure 2-7 is rooted in the fact pointed out by Mcdonald[140] that a Pareto distribution of relaxation times given by

$$G(\tau) = \left(\tau/\tau_p\right)^{-\beta} \tag{5-71}$$

is the asymptotic limit of the Levy α-stable distribution as τ_{kww} goes to zero.

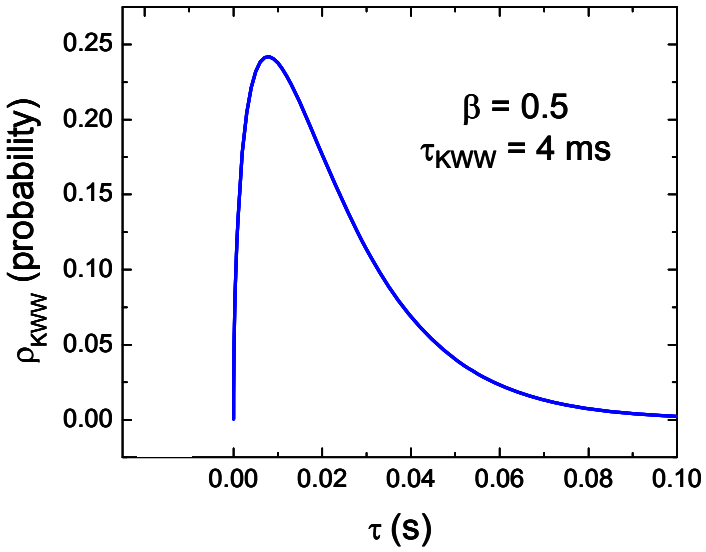

Figure 5-107. A typical Levy α-stable distribution of relaxation times corresponding to the KWW parameters $\beta = \frac{1}{2}$ and $\tau_{KWW} = 4$ ms is shown.

The field dependence of both the relaxation time τ_{KWW} and the magnitude of the response A_o determined from the KWW-fitting were qualitatively similar to that determined from the fitting based on the assumption of a fractal domain structure characterized by a Pareto distribution of both domains volumes and relaxation times. Additionally, the stretching exponent β determined from the KWW-fitting was independent of the applied field, similar to the result based on the assumption of a fractal domain structure. Figure 5-108 shows the decay of the EO response as well as the KWW-fit on a semi-log plot for fields ranging from 0.8 to 3.75 MV/m (E=V/12 μm). For clarity only every 10th data point is shown. Figure 5-109 shows the corresponding fitting parameters A_o, τ and β as a function of the maximum applied field. The field dependent fitting parameters are likewise tabulated in Table 5-8. τ_{KWW} increases linearly with the applied field and the solid red line in Figure 5-109 gives the field dependence of τ as

$$\tau_{KWW}(E) = 3.0E + 0.8 \quad (ms) \tag{5-72}$$

where the field is in MV/m. The amplitude of the decay likewise increases with field but shows signs of saturation at high fields. The solid black line is a fit to the field dependent amplitude to a Weibull cumulative distribution function given by

$$A_o(E) = 0.98\left(1 - \exp\left[-\left(E/1.84\right)^{1.6}\right]\right) \tag{5-73}.$$

β is relatively independent of the maximum applied field with an average value of 0.52. In order to take advantage of the closed form expression for the distribution of relaxation times given in equation (5-70), the relaxation data was refit using equation (2-12) under the assumption of β = ½. In Figure 5-110, the original fit along with that assuming β = ½ are shown for just two of the data series for reasons of clarity. For all of the data series, the fits assuming β = ½ were essentially qualitatively equivalent to the original fits where β was allowed to vary. The field dependent values of A_o and τ for β = ½ are shown in Figure 5-111 and Figure 5-112, respectively with the tabulated parameter values given in the last two columns of Table 5-8. Under the assumption of β = ½ the field-dependent amplitude was again fit to a Weibull cumulative distribution function shown by the solid blue line in Figure 5-111 and given by[141]

$$A_o(E) = A\left(1-\exp\left[-\left(E/\psi\right)^{\alpha}\right]\right) = 0.89\left(1-\exp\left[-\left(E/1.6\right)^{1.9}\right]\right) \quad (5\text{-}74).$$

The dashed orange line in Figure 5-111shows the associated Weibull probability density function given by[141]

$$\rho_{A_o}(E) = \frac{\alpha}{\psi^{\alpha}}E^{\alpha-1}\exp\left[-\left(E/\psi\right)^{\alpha}\right] = \frac{1.9}{1.6^{1.9}}E^{1.9-1}\exp\left[-\left(E/1.6\right)^{1.9}\right] \quad (5\text{-}75)$$

Given that the amplitude of the relaxation response is expected to be proportional to the volume fraction of 90^o switched domains, the plot of equation (5-75) in Figure 5-111 is assumed to give the approximate distribution of coercivities for 90^o switching of c-domains in sample DT443. The relaxation time constant τ shown in Figure 5-112 is linearly dependent on the magnitude of the applied field with a field dependence given by

$$\tau_{KWW} = 3.7\mathrm{E}_{\max} - 0.8 \quad (ms) \quad (5\text{-}76)$$

The dependence of A_o and τ on $\mathrm{E}_{\max}$ is both qualitatively and qualitatively nearly identical to that based on the assumption of a fractal domain structure. Namely A_o increases linearly with the maximum applied field (E_{MAX}) up to just over 2 MV/m, beyond which it begins to saturate. τ increases linearly

from ~1 MV/m through the maximum E_{MAX} employed (3.75 MV/m) as given by equation (5-76) which is nearly identical to equation (5-65).

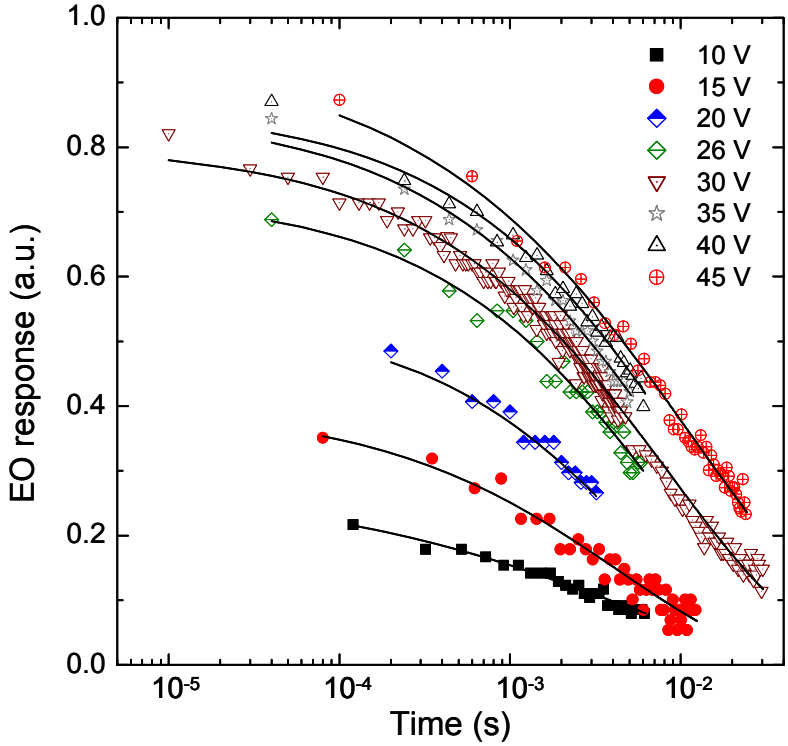

Figure 5-108. Stress-driven EO relaxation after removal of the applied 12 ms voltage pulse. For clarity only every 10th data point is shown. Solid lines show the KWW stretched exponential fit of equation (2-12) to the data (DT443)

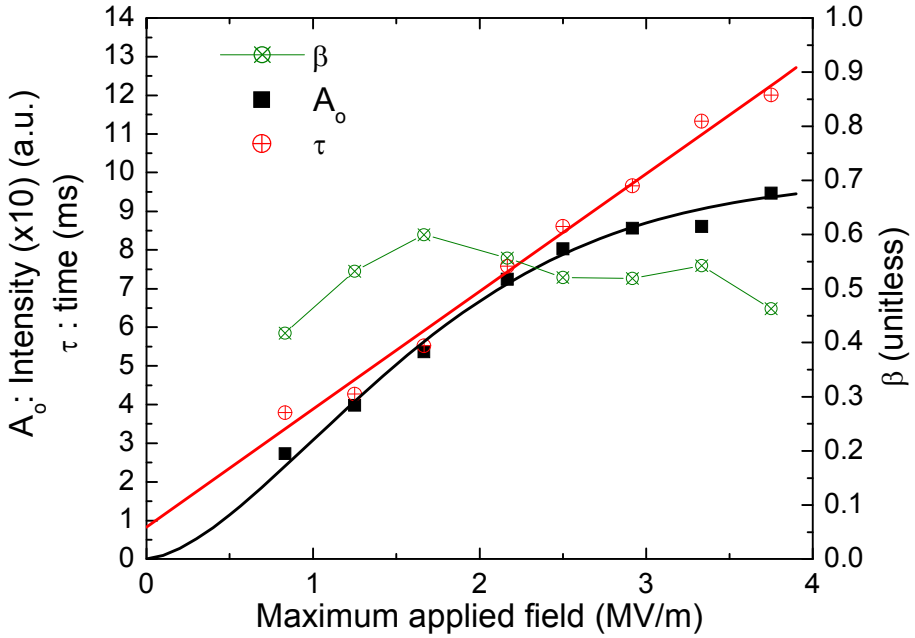

Figure 5-109. The KWW fitting parameters for the stress-driven EO decay as given in equation (2-12) are plotted verses the maximum applied electric field (DT443).

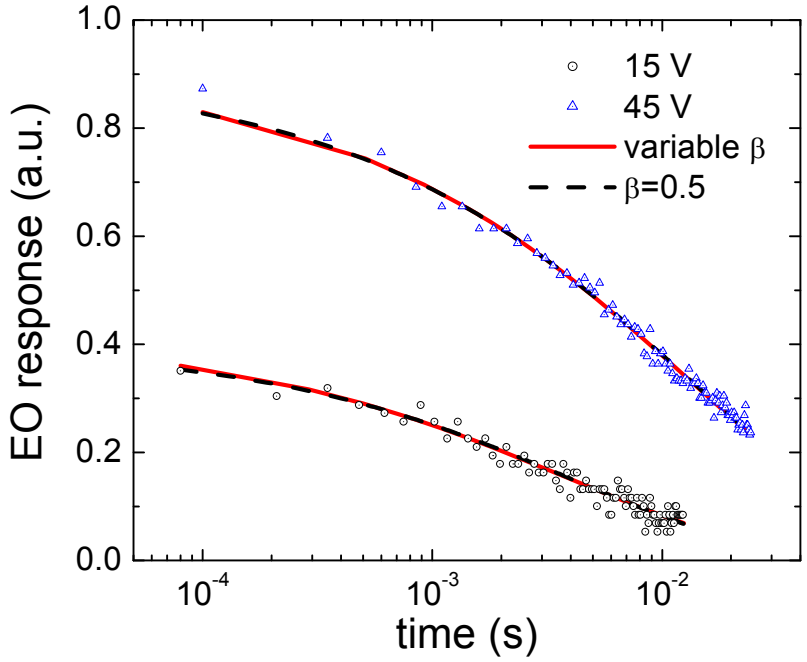

Figure 5-110. The stress-driven EO decay upon removal of the applied voltage pulse is shown along with fits to equation (2-12) with β as a fitting variable and β fixed at 0.5.

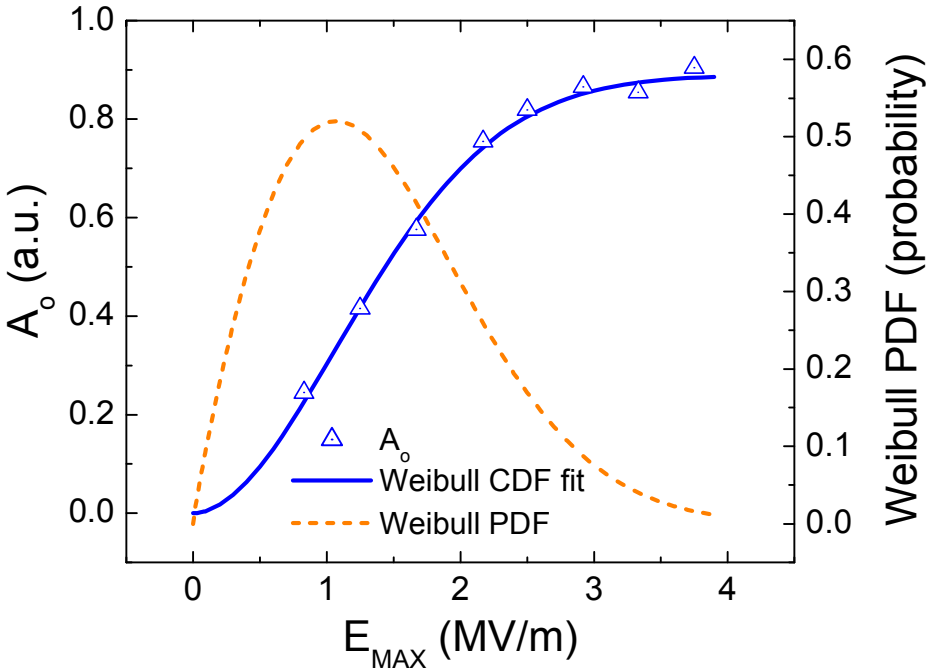

Figure 5-111. The KWW fitting parameter A_o of equation (2-12) with $\beta = 0.5$ is plotted verses the maximum applied field (DT443). The solid blue line gives the fit to the data using a Weibull CDF function. The dashed orange line gives the associated Weibull probability density function.

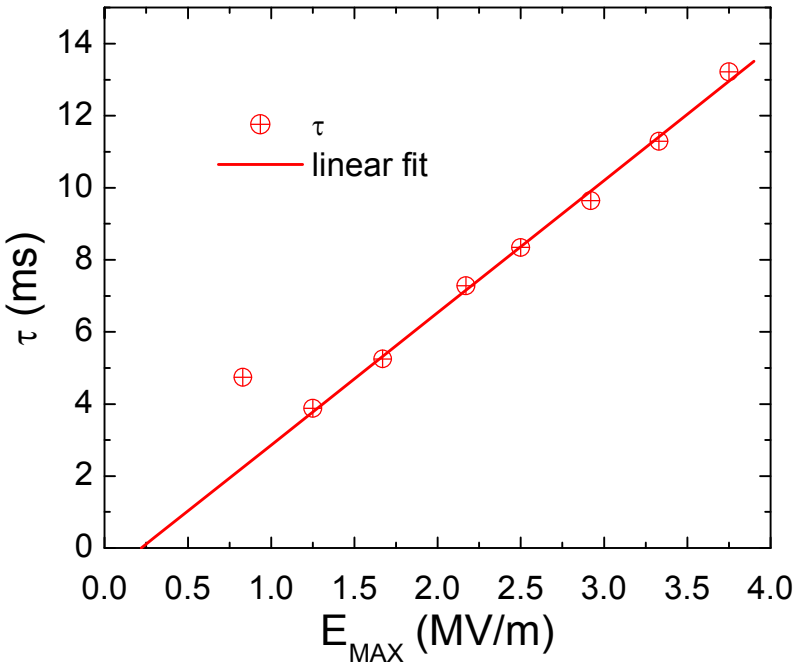

Figure 5-112. The characteristic time constant KWW fitting parameter τ of equation (2-12) with $\beta = 0.5$ is plotted verses the maximum applied field (DT443). The solid red line gives the linear fit to the data.

Table 5-8. Field dependent KWW stretched exponential fitting parameters of fits shown in Figure 5-108. The field dependence of the fitting parameters from the 3rd through 5th column are given in Figure 5-109 in which all three fitting parameters were allowed to vary. The last two columns reflect the fit for a fixed β value of 0.5 (see Figure 5-111) [sample DT443].

V_{max} (V)	E_{max} (MV/m)	A_o (a.u.)	τ (ms)	β		$A_{o\ (\beta=0.5)}$ (a.u.)	$\tau_{(\beta=0.5)}$ (ms)
10	0.83	0.273	3.79	0.42		0.245	4.74
15	1.25	0.398	4.27	0.53		0.416	3.88
20	1.67	0.536	5.52	0.60		0.576	5.25
26	2.17	0.724	7.58	0.56		0.755	7.28
30	2.50	0.803	8.61	0.52		0.819	8.34
35	2.92	0.856	9.66	0.52		0.866	9.64
40	3.33	0.861	11.3	0.54		0.885	11.3
45	3.75	0.947	12.0	0.46		0.905	13.2

From equations (5-76) and (5-70) the probability distributions of relaxation times under for the different values of E_{max} are determined. The resulting Levy α–stable probability density distributions are shown in Figure 5-113, where for clarity they are rendered on both linear and log time or rather τ scales. From Figure 5-113b it is apparent that with increasing E_{max}, the distribution of relaxation times shifts to longer times with the breadth of the distribution scaling with τ_{KWW}. This is consistent with the aforementioned model of Molotskii and Shvebelman which predicts that the domain lifetime upon removal of a poling field increases monotonically with the radius of the domain[149]. The same arguments and observations with regard to the E_{max} dependence of A_o and τ presented in the context of the fitting based on a percolative domain structure likewise hold here.

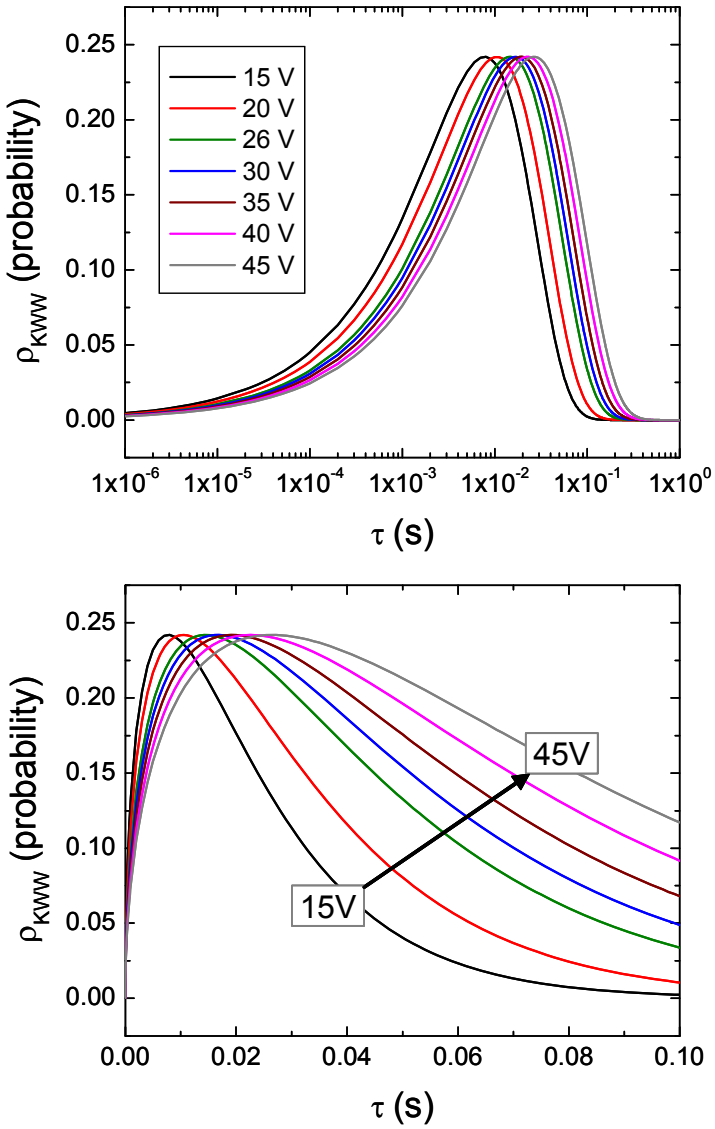

Figure 5-113. Distributions of relaxation times for a range of E_{MAX} amplitudes rendered on both log and linear time scales. In all cases the voltage pulse was applied for 12 ms(DT443).

5.2.4.3 Extrinsic EO effect due to 180° domain flipping

In the previous section the dynamic response of 90° domain switching was examined. Because domains undergoing 90° domain switching are both ferroelectric and ferroelastic their dynamics are expected to be different from that of 180° domain switching, which is purely ferroelectric (no change in strain). In this section the dynamics of 180° domain switching are analyzed. It is qualitatively observed that for equivalent applied field amplitudes, the ratio of the extrinsic to intrinsic contributions to the EO

response is significantly greater under a bipolar driving voltage than under a monopolar driving voltage. This is attributed to 180°-domain reversals occurring upon every cycle of the applied voltage polarity when the sample is driven with a bipolar voltage waveform.

Under a bipolar driving voltage, domains for which some component of the applied field is parallel to the polar axis are susceptible to 180° domain reversal. Unlike the case for 90° domain reversal in a thin film, there is no strain associated with a 180° domain reversal[78,156]. While there are limits on 90° switching due to strain[86] no such limits exist for 180° switching. As a result a substantially larger relative volume fraction of the domains susceptible to 180° reversal will be switched as compared to the switched volume fraction of domains susceptible to 90° reversal. This is evidenced in Figure 5-114 where (a) shows the EO response of sample DT443 when driven by the bipolar ~16 V_{PP} square wave (Figure 5-114b), while (c) shows the EO response of the same sample when driven by a monopolar voltage pulse with the same magnitude of the maximum applied electric field. As the intrinsic EO response is much faster than the measurement system, the degree to which the measured EO response departs from the form of the driving voltage (in this case a square wave) is an indication of the relative magnitude of the extrinsic EO contributions. It is apparent from the figure that the relative transient extrinsic contribution from 180° domain reversal when driven by a bi-polar square-wave bias is appreciably larger than that due to the 90° domain reversal under a monopolar voltage pulse of the same magnitude.

Figure 5-115 shows the KWW fit of the transient EO response of DT443 due to 180° domain reversal using equation (2-12). When all three fitting parameters were left as variables in the fitting, the resulting fit was given by

$$\Phi(t) = 0.21\exp\left[-\left(\left(\frac{t}{8.1\times10^{-4}}\right)^{0.52}\right)\right]$$

A fit with β fixed at 0.5 is likewise show. While the fits with $\beta \sim 0.5$ were optimal, reasonably good fits were realized for β values ranging from 0.35 to 0.6 for which the associated τ values ranged from 0.19 to 1.13 ms.

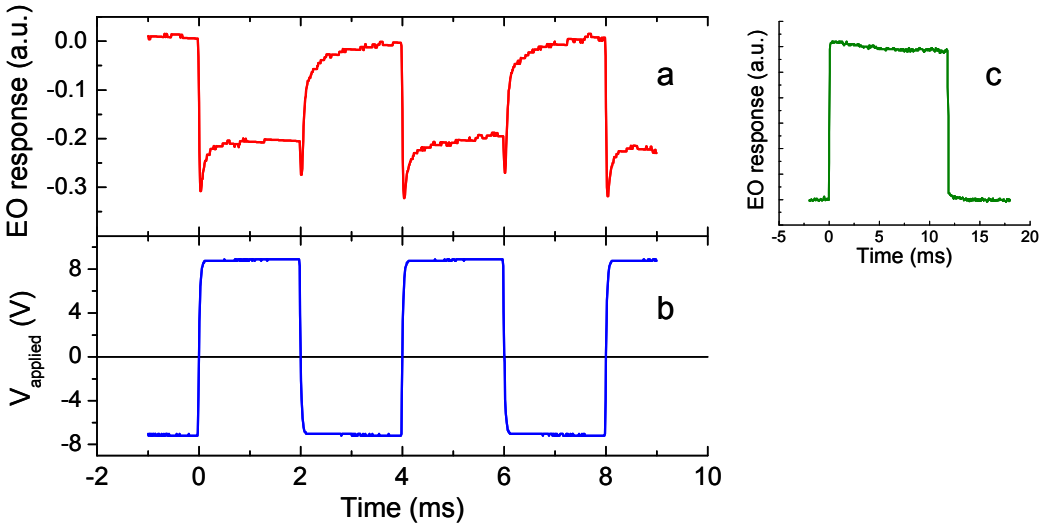

Figure 5-114. a.)EO response of sample DT443 when driven by the bi-polar square wave voltage shown in b. For comparison the EO response of the sample when driven by a mono-polar voltage pulse with the same maximum applied electric field is shown in c.

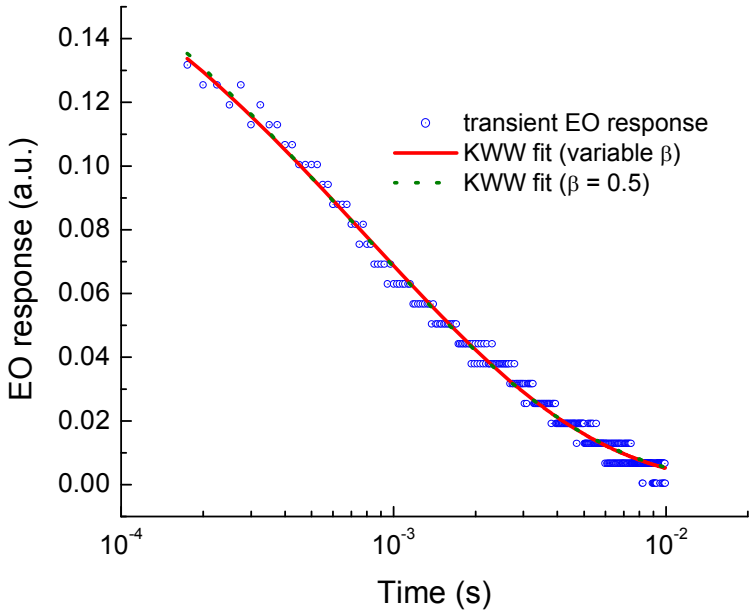

Figure 5-115. KWW stretched exponential fits to the transient EO response due to 180° domain switching (sample DT443)

5.3 Summary of ferroelectric properties of $BaTiO_3$ thin films

In this chapter the dependence of the ferroelectric properties on the domain structure of polydomain epitaxial $BaTiO_3$ thin films was examined. The primary goal was to clarify the dependence of the electro-optic properties of the polydomain thin films on their domain structure. Electronic

polarization was measured in order to provide further insight into the poling properties of the polydomain thin films. The key findings are summarized below.

Electronic polarization:

No in-plane directional dependence of the electronic polarization was observed in the polydomain $BaTiO_3$ thin films. A simple model of the in plane electronic polarization hysteresis loops was developed. The average remnant in-plane polarization of 2.7 $\mu C/cm^2$ is consistent with the theoretically predicted range of the model given the typical 28±8% a-domain volume fractions of the films as determined from x-ray diffraction analysis.

The typical linearity observed in the non-remnant polarization half-loops was attributed to their dominance by linear dielectric contributions. Confirmation of this is found in the nearly identical dielectric constants determined from standard small-signal capacitance measurements and those determined from the linear dP/dE of the non-remnant polarization half-loops.

Electro-optic properties:

Consistent with the earlier work by Hoerman[12] a large dependence of the magnitude of the electro-optic coefficient on the direction of the in-plane electric field is observed. The contrast between the highly anisotropic in-plane EO coefficient and the isotropic in-plane electronic polarization is due the different dependencies of these properties on the direction of the applied electric fields. In contrast to the polarization, large electro-optic coefficients in the polydomain films are only realized when the component of the applied field along the polar axis of a given domain variant is sufficient to pole said variant while also maintaining a sufficient component of the applied field perpendicular to the polar axis of said variant in order to realize an appreciable EO contribution from the large r_{51} electro-optic coefficient.

The measured effective electro-optic coefficients are always dominated by domain variants that make r_{51} or r_{42} contributions to the measured EO response regardless of whether the applied field acts to

pole these variants or not. Evidence for this comes from both the dependence of r_{eff} on bias voltage and the monopolar voltage pulse EO response

A model was developed fro the field-dependent EO response based on the theoretical EO response of the domain variants and the field dependent domain structure within the film. The hysteretic electro-optic response of sample DT443 was effectively fit with the model. By incorporating elasto-optic contributions into the optical response due to strain caused by 90^o domain switching, the attenuation of the EO response at high fields was modeled as well

6 SUMMARY AND CONCLUSIONS

In this study the dependence of the electro-optic (EO) properties on the field-dependent domain structure in epitaxial polydomain $BaTiO_3$ thin films was investigated. A domain-structure-dependent model of both the field-dependent in-plane electronic polarization and the electro-optic response was developed; the measured polarization and electo-optic data was analyzed in the context of the model. The agreement between the model and the measured polarization and EO data demonstrates its efficacy.

The measured domain volume fractions and remnant polarization of the $BaTiO_3$ thin films were both in agreement with those predicted by the in-plane polarization model. The polarization model predicts that the remnant in-plane polarization is proportional to the a-domain volume fraction while the dielectric contributions to the polarization are inversely proportional to the a-domain volume fraction. Consistent with the model, the relatively small a-domain fractions typical of the $BaTiO_3$ thin films (0.28±0.8) result in relatively low remnant polarizations in the films. The remnant polarization of the $BaTiO_3$ thin films ranged from 1.6 to 3.7 $\mu C/cm^2$ with the average value being 2.7 $\mu C/cm^2$. These values are consistent with the upper limit predicted by the model of between 2.6 to 6.6 $\mu C/cm^2$. Similarly the dielectric constants predicted by the model were consistent with the measured dielectric constants of the $BaTiO_3$ thin films.

The hysteretic EO response was well described by an model based on the E-field dependent intrinsic EO response of the individual domains and the E-field dependent domain structure. In the model of the hysteretic EO response, the functional form of the field-dependent domain structure was given by the field-dependent polarization due to ferroelectric switching ($P_{ferro}(E)$). The model extends that developed by Hoerman by including the effects due to $BaTiO_3$'s large off-diagonal r_{51} coefficient. These include the rotation of the indicatrix under an applied field as well as the quadratic field-dependence of the birefringence. At high fields in excess of 1 MV/m evidence of appreciable 90^o domain switching was observed from both EO and x-ray diffraction measurements. Effects due to 90^o domain switching were incorporated into the model by inclusion of elasto-optic contributions to the optical response.

Measurements of the effective electro-optic coefficient were made in waveguide and transmission geometries under both in-plane <110> and <100> E-fields. The field dependence of the electro-optic response (r_{eff}) for both <110> and <100> E-fields is dominated by the r_{51}-contributing domains. The <110> field act to pole these domains, resulting in larger effective electro-optic coefficients (r_{eff}) and a hysteretic response whereas a <100> field does not pole these domains, resulting in a lower r_{eff} and no hysteresis. The 180^o poling of the r_{51}-contributing domains under a <110> E-field results in an increase in r_{eff} with increasing bias voltage. In contrast under a <100> E-field the r_{51}-contributing domains are subject to 90^o domain switching. Subsequent to a 90^o switch the domain no longer makes an r_{51} contribution. As a result for <100> oriented E-fields, r_{eff} decreases with increasing bias field. Average effective electro-optic coefficient (r_{eff}) values at 633 nm under <110> and <100> fields were 247 and 5.6 pm/V, respectively. Average r_{eff} values at 1550 nm under <110> and <100> fields were 132 and 14 pm/V, respectively.

The field-dependent transient EO response due to 90^o domain relaxation was analyzed. The observed non-exponential time decay was attributed to the collective relaxation due to a distribution of Debye-like (exponential) relaxation processes having different relaxation times. The distribution of relaxation times was tentatively attributed to a distribution of domain size in the films. Models based on two different assumptions of the underlying distribution of relaxation times were developed. The assumed distributions of relaxation times used included a Pareto distribution and an Levy α-stable distribution. The Pareto distribution of relaxation times results in a power law relaxation while an Levy α-stable distribution results in a stretched-exponential or Kohlrausch-Watts-Williams (KWW) relaxation. Fits to the transient response using both models indicated that the relaxation time was proportional to the magnitude of the poling field employed. It was proposed that this could be explained by nucleation-limited switching kinetics.

Specific conclusions from this work are as follows:

(1) The measured electro-optic coefficient was highly dependent on the direction of the in-plane electric field. Under in-plane <100> oriented E-fields the median and average measured effective EO coefficient (r_{eff}) were both 12 pm/V with the range of measured r_{eff} of 2 to 25 pm/V. In contrast, under in-plane <110> oriented E-fields the median and average r_{eff} were 153 and 181 pm/V respectively, with a total range of measured r_{eff} of 8 to 424 pm/V.

(2) The effective linear electro-optic coefficient of the polydomain $BaTiO_3$ thin films is always dominated by domain variants that make r_{51} or r_{42} contributions to the measured EO response regardless of whether the applied field acts to pole these variants or not. Evidence for this comes from both the dependence of r_{eff} on bias voltage and the monopolar voltage pulse EO response.

(3) The general attenuation of the measured electro-optic coefficient with increasing bias voltage under in-plane <100> oriented electric fields is consistent with 90^o-domain flipping of the r_{51} and r_{42}-contributing domains. Subsequent to such a flip the domain no longer makes an r_{51} or r_{42} contribution to the EO response. As stated above the r_{51} and r_{42}-contributing domains are not subject to stable 180^o poling by the applied fields. However they are subject to 90^o switching. A similar attenuation of the EO response with increasing applied voltage is observed in the monopolar voltage pulse EO response measurements.

(4) The measured r_{eff} values under in-plane <100> oriented E-fields are significantly smaller than those measured under in-plane <110> E-fields for the following reasons. Only two of the six domain variants in the film make r_{51} or r_{42} contributions to the measured EO response. Because these r_{51} and r_{42}-contributing domains are not subject to poling, cancellations of the EO response from oppositely oriented domains can not be eliminated through poling. Additionally the r_{51} and r_{42}-contributing domains are subject to 90^o-switching under the applied field subsequent to which they do not make an r_{51} or r_{42} contribution to the EO response.

In contrast, for electro-optic measurements under an in-plane <110> oriented electric field all six domain variants can potentially make r_{51} or r_{42} contributions to the EO response. Additionally all four of

the a-domain variants are subject to 180^{o} poling by the applied in-plane <110> oriented electric field. Only the c-domains are subject to 90^{o} domain flipping. Additionally it was shown in chapter 4 that in the waveguide geometry the field induced change in birefringence of the a-domains is optimal for propagation along a <110> direction at 45^{o} to the optic axis of the a-domains.

(5) Through application of the Jones calculus, the hysteretic electro-optic response observed under in-pane <110> E-fields in the monopolar voltage pulse EO measurements was effectively modeled. The model employed the calculated theoretical EO response of the individual domain variants in the $BaTiO_3$ thin film in conjunction with the measured remnant electronic polarization hysteresis loops. The agreement of the model to the measured data demonstrates the quadratic E-field dependence of the EO response of $BaTiO_3$ that results from the large off-diagonal Pockels linear electro-optic coefficient. This represents the first time that the hysteretic electro-optic response has been modeled using the theoretical electro-optic response in conjunction with the component of the measured ferroelectric component of the electronic polarization.

(6) The observed decrease in the EO response at high fields in excess of 1 MV/m was attributed to an elasto-optic contribution to the measured optical response due to E-field driven 90^{o}-domain flipping. E-field dependent surface normal x-ray diffraction measurements provide supporting evidence. By incorporating the theoretical elasto-optic contributions into the theoretical EO response of the $BaTiO_3$ domain variants, the high-field hysteretic EO response was effectively modeled.

(7) The strain-driven transient EO effect due to relaxation of 90^{o}-flipped domains was fit using two relaxation models. In both models the non-exponential time decay was attributed to the collective relaxation due to a distribution of Debye-like (exponential) relaxation times. The distribution was tentatively attributed to a distribution of domain size in the films. Models based on two different assumptions of the underlying distribution of relaxation times were developed. The assumed distributions of relaxation times used included a Pareto distribution and an Levy α-stable distribution. A Pareto distribution of relaxation times results in a power law relaxation while an Levy α-stable distribution

results in a stretched-exponential or Kohlrausch-Watts-Williams (KWW) relaxation. Satisfactory fits to the data were realized with both models. Furthermore, the results in both instances were effectively the same.

The characteristic relaxation time was found to increase linearly with the amplitude of the applied electric field. The dependencies for the two different models were slightly different. For the percolative distribution of relaxation times the field dependence of the characteristic relaxation time constant was $\tau = 2.9E_{\max} - 0.32 \quad (ms)$, while for the Levy distribution of relaxation times it was given by $\tau_{KWW} = 3.7E_{\max} - 0.8 \quad (ms)$ where the field in both cases is in MV/m. The difference in the field dependence of the time constant determined from the tow models is attributed to the differences in the relaxation functions associated with the two models. From the fits to both relaxation models, the field dependent amplitude of the transient response increased with field and was well described by a Weibull cumulative distribution function.

(8) A simple model of the in-plane polarization based on the a-domain volume fraction was developed. The model predicts that the theoretical maximum remnant in-plane polarization is proportional to ½ the a-domain volume fraction. The measured remnant polarizations in the $BaTiO_3$ thin films are consistent with this hypothesis based on the typical a-domain volume fractions observed in the films. The model was used to simulate the measured field-dependent electronic polarization hysteresis of the polydomain $BaTiO_3$ thin films. The model predicts that the in-plane anisotropy of the electronic polarization is inversely proportional to the width of the distribution of coercivities. The coercivity distributions that accurately reproduced the measured hysteresis loops, the theoretical in plane polarization predicted by the model was fairly isotropic, consistent with the measured results.

7 SUGGESTIONS FOR FUTURE WORK

7.1 Effect of point defect structure and oxygen vacancies on the EO response

Electro-optic measurements were made in the <100> transmission and waveguide geometries on $BaTiO_3$ thin films that were annealed at 1100 ^oC for extended periods of time (4 to 10 hours). These samples exhibited effective electro-optic coefficients an order of magnitude larger than any other samples measured under a <100> geometry. It was suggested that a modification of the point defect structure in the thin film might be responsible for the observed improvement in the EO response. In particular the elimination of oxygen vacancies which have been reported to result in domain wall pinning is suspected as the mechanism by which the response was improved.

A defect study of the $BaTiO_3$ films in conjunction with electro-optic measurements would provide insight into the possible relationship between their electro-optic properties and the defect structure in the films. The Wessels group has prior experience in both of these areas. In addition to making standard electro-optic measurements, thermopower, resistivity and transient photocapacitance spectroscopy measurements could be used to characterize the defect structure. Reduction and oxidation anneals on films grown in the same growth run could provide a more controlled method to assess the effect of oxygen vacancies.

7.2 Domain dynamics

In this study the effect of the poling field on the transient domain relaxation was studied. In all cases the poling field was applied for 12 ms and measurements were made at room temperature. There is a wide parameter space of time-(E-field)-temperature that remains to be explored. Examining the effect of temperature on the relaxation process would help clarify if the kinetics are controlled by a temperature dependent nucleation process or a growth process that is independent of temperature.

7.3 Epitaxial Si-integrated $BaTiO_3$ EO modulators

In this study only one result is reported for a Si-integrated $BaTiO_3$ modulator. The measured EO coefficient under a <110> E-field was just 10 pm/V. However a significant supply of high quality Si-integrated MgO buffer layers are available. It would be of interest to deposit $BaTiO_3$ either by MOCVD or MBE on these high quality buffer layers in order to make additional electro-optic measurements.

REFERENCES

[1] N. Setter, D. Damjanovic, L. Eng, G. Fox, S. Gevorgian, S. Hong, A. Kingon, H. Kohlstedt, N. Y. Park, G. B. Stephenson, I. Stolitchnov, A. K. Taganstev, D. V. Taylor, T. Yamada, and S. Streiffer, "Ferroelectric thin films: Review of materials, properties, and applications," J. Appl. Phys. **100** (5) (2006).

[2] M. Dawber, K. M. Rabe, and J. F. Scott, "Physics of thin-film ferroelectric oxides," Rev. Mod. Phys. **77** (4), 1083-1130 (2005).

[3] J. F. Scott, "Applications of modern ferroelectrics," Science **315** (5814), 954-959 (2007).

[4] J. F. Scott, "Nanoferroelectrics: statics and dynamics," Journal of Physics-Condensed Matter **18** (17), R361-R386 (2006).

[5] O. G. Vendik, E. K. Hollmann, A. B. Kozyrev, and A. M. Prudan, "Ferroelectric tuning of planar and bulk microwave devices," Journal of Superconductivity **12** (2), 325-338 (1999).

[6] D. Fuchs, C. W. Schneider, R. Schneider, and H. Rietschel, "High dielectric constant and tunability of epitaxial $SrTiO_3$ thin film capacitors," J. Appl. Phys. **85** (10), 7362-7369 (1999).

[7] C. L. Chen, H. H. Feng, Z. Zhang, A. Brazdeikis, Z. J. Huang, W. K. Chu, C. W. Chu, F. A. Miranda, F. W. Van Keuls, R. R. Romanofsky, and Y. Liou, "Epitaxial ferroelectric $Ba_{0.5}Sr_{0.5}TiO_3$ thin films for room-temperature tunable element applications," Appl. Phys. Lett. **75** (3), 412-414 (1999).

[8] P. Padmini, T. R. Taylor, M. J. Lefevre, A. S. Nagra, R. A. York, and J. S. Speck, "Realization of high tunability barium strontium titanate thin films by RF magnetron sputtering," Appl. Phys. Lett. **75** (20), 3186-3188 (1999).

[9] A. K. Tagantsev, V. O. Sherman, K. F. Astafiev, J. Venkatesh, and N. Setter, "Ferroelectric materials for microwave tunable applications," J. Electroceram. **11** (1-2), 5-66 (2003).

[10] V. Laur, A. Rousseau, G. Tanne, P. Laurent, M. Guilloux-Viry, and F. Huret, "Ferroelectric-based agile devices - Application to tunable filters," International Journal of Rf and Microwave Computer-Aided Engineering **17** (1), 56-62 (2007).

[11] A. Vorobiev, P. Rundqvist, K. Khamchane, and S. Gevorgian, "Silicon substrate integrated high Q-factor parallel-plate ferroelectric varactors for microwave/millimeterwave applications," Appl. Phys. Lett. **83** (15), 3144-3146 (2003).

[12] B. H. Hoerman, Ph.D. Thesis, Northwestern University, 2001.

[13] D. L. Polla and L. F. Francis, "Processing and characterization of piezoelectric materials and integration into microelectromechanical systems," Annual Review of Materials Science **28**, 563-597 (1998).

[14] P. Muralt, "Ferroelectric thin films for micro-sensors and actuators: a review," Journal of Micromechanics and Microengineering **10** (2), 136-146 (2000).

[15] P. Muralt, "PZT thin films for microsensors and actuators: Where do we stand?," Ieee Transactions on Ultrasonics Ferroelectrics and Frequency Control **47** (4), 903-915 (2000).

[16] P. Muralt, "Micromachined infrared detectors based on pyroelectric thin films," Rep. Prog. Phys. **64** (10), 1339-1388 (2001).

[17] A. Sigov, E. Pevtsov, A. Gorelov, and V. Chernokozhin, "Pyroelectric thin films integrated with CCD," Integr. Ferroelectr. **61**, 197-204 (2004).

[18] R. Takayama, Y. Tomita, K. Iijima, and I. Ueda, "Pyroelectric Properties and Application to Infrared-Sensors of $PbTiO_3$, $PbLaTiO_3$ and $PbZrTiO_3$ Ferroelectric Thin-Films," Ferroelectrics **118** (1-4), 325-342 (1991).

[19] G. Nogami, H. Maruyama, and K. Hongo, "Thin-Film Dielectric Ion Sensors," J. Electrochem. Soc. **140** (8), 2370-2373 (1993).

[20] G. G. Mandayo, F. Gonzalez, I. Rivas, I. Ayerdi, and J. Herran, "$BaTiO_3$-CuO sputtered thin film for carbon dioxide detection," Sensors and Actuators B-Chemical **118** (1-2), 305-310 (2006).

[21] J. Yuk and T. Troczynski, "Sol-gel $BaTiO_3$ thin film for humidity sensors," Sensors and Actuators B-Chemical **94** (3), 290-293 (2003).

[22] J. Wang, H. Wan, and Q. H. Lin, "Properties of a nanocrystalline barium titanate on silicon humidity sensor," Meas. Sci. Technol. **14** (2), 172-175 (2003).

[23] T. Ishihara, T. Takagi, M. Ito, H. Nishiguchi, and Y. Takita, "CO_2 sensing property of CuO-$BaTiO_3$ mixed oxide film prepared by self-assembled multibilayer film as a precursor," J. Electroceram. **4** (1), 207-214 (2000).

[24] J. F. Scott and C. A. P. Dearaujo, "Ferroelectric Memories," Science **246** (4936), 1400-1405 (1989).

[25] J. F. Scott, in *Ferroelectric Random Access Memories Fundamentals and Applications* (2004), Vol. 93, pp. 3-16.

[26] T. K. Li, S. T. Hsu, B. Ulrich, and D. Evans, "Integration processes and properties of semiconductive oxide memory transistor," Integr. Ferroelectr. **81**, 27-36 (2006).

[27] R. Ramesh, S. Aggarwal, and O. Auciello, "Science and technology of ferroelectric films and heterostructures for non-volatile ferroelectric memories," Materials Science & Engineering R-Reports **32** (6), 191-236 (2001).

[28] D. R. Lampe, D. A. Adams, M. Austin, M. Polinsky, J. Dzimianski, S. Sinharoy, H. Buhay, P. Brabant, and Y. M. Liu, "Process Integration of the Ferroelectric Memory FETs (FEMFETs) for Ndro FeRAM," Ferroelectrics **133** (1-4), 61-72 (1992).

[29] S. Sinharoy, H. Buhay, D. R. Lampe, and M. H. Francombe, "Integration of Ferroelectric Thin-Films into Nonvolatile Memories," J. Vac. Sci. Technol. A **10** (4), 1554-1561 (1992).

[30] O. Auciello, "Science and technology of thin films and interfacial layers in ferroelectric and high-dielectric constant heterostructures and application to devices," J. Appl. Phys. **100** (5) (2006).

[31] Ramtron International and Fujitsu.

[32] Russ Arensman, "Memory enhancement", Electronic Business (www.edn.com), - 4/1/2003.

[33] M. M. Fejer, G. A. Magel, D. H. Jundt, and R. L. Byer, "Quasi-Phase-Matched 2nd Harmonic-Generation - Tuning and Tolerances," IEEE J. Quantum Electron. **28** (11), 2631-2654 (1992).

[34] V. Gopalan and R. Raj, "Domain structure and phase transitions in epitaxial $KNbO_3$ thin films studied by in situ second harmonic generation measurements," Appl. Phys. Lett. **68** (10), 1323-1325 (1996).

[35] J. P. Meyn and M. M. Fejer, "Tunable ultraviolet radiation by second-harmonic generation in periodically poled lithium tantalate," Opt. Lett. **22** (16), 1214-1216 (1997).

[36] D. J. Towner, Ph.D. Thesis, Northwestern University, 2005.

[37] M. J. Nystrom, Ph.D. Thesis, Northwestern, 1996.

[38] V. Gopalan, Ph.D. Thesis, Cornell University, 1995.

[39] N. Dagli, "Wide-bandwidth lasers and modulators for RF photonics," IEEE Trans. Microw. Theory Tech. **47** (7), 1151-1171 (1999).

[40] Z. M. Xu, M. Suzuki, Y. Tanushi, and S. Yokoyama, "Monolithically integrated optical modulator based on polycrystalline $Ba_{0.7}Sr_{0.3}TiO_3$ thin films," Appl. Phys. Lett. **88** (16) (2006).

[41] V. Fuflyigin, F. Wang, H. Jiang, J. Zhao, and P. Norris, "Electro-optic effect in $Ba_{1-x}Pb_xTiO_3$ films," Appl. Phys. Lett. **76** (13), 1641-1643 (2000).

[42] H. Shima, H. Naganuma, and S. Okamura, "La content dependence of electrooptic properties of polycrystalline $(Pb,La)(Zr_{0.65},Ti_{0.35})O_3$ thick films," Jpn. J. Appl. Phys. Part 1 - Regul. Pap. Brief Commun. Rev. Pap. **45** (9B), 7279-7282 (2006).

[43] D. Y. Wang, Y. Wang, K. H. Wong, K. P. Lor, H. P. Chan, K. S. Chiang, H. L. W. Chan, and C. L. Choy, "Pulsed laser deposition of $Ba_{0.6}Sr_{0.4}TiO_3$ thin films and their optical properties," Integr. Ferroelectr. **69**, 443-+ (2005).

[44] S. H. Choy, D. Y. Wang, J. Y. Dai, H. L. W. Chan, and C. L. Choy, "Barium strontium zirconate titanate (BSZT) thin films for optical waveguide applications," Integr. Ferroelectr. **80**, 107-114 (2006).

[45] R. Thapliya, Y. Okano, and S. Nakamura, "Electrooptic characteristics of thin-film PLZT waveguide using ridge-type Mach-Zehnder modulator," J. Lightwave Technol. **21** (8), 1820-1827 (2003).

[46] P. Tang, A. L. Meier, D. J. Towner, and B. W. Wessels, "High-speed traveling-wave $BaTiO_3$ thin-film electro-optic modulators," Electron. Lett. **41** (23), 1296-1297 (2005).

[47] P. S. Tang, A. L. Meier, D. J. Towner, and B. W. Wessels, "$BaTiO_3$ thin-film waveguide modulator with a low voltage-length product at near-infrared wavelengths of 0.98 and 1.55 μm," Opt. Lett. **30** (3), 254-256 (2005).

[48] P. S. Tang, D. J. Towner, T. Hamano, A. L. Meier, and B. W. Wessels, "Electrooptic modulation up to 40 GHz in a barium titanate thin film waveguide modulator," Opt. Express **12** (24), 5962-5967 (2004).

[49] P. S. Tang, D. J. Towner, A. L. Meier, and B. W. Wessels, "Polarisation-insensitive Si_3N_4 strip-loaded $BaTiO_3$ thin-film waveguide with low propagation losses," Electron. Lett. **39** (23), 1651-1652 (2003).

[50] P. S. Tang, D. J. Towner, A. L. Meier, and B. W. Wessels, "Low-voltage, polarization-insensitive, electro-optic modulator based on a polydomain barium titanate thin film," Appl. Phys. Lett. **85** (20), 4615-4617 (2004).

[51] P. S. Tang, D. J. Towner, A. L. Meier, and B. W. Wessels, "Low-loss electrooptic $BaTiO_3$ thin film waveguide modulator," IEEE Photonics Technol. Lett. **16** (8), 1837-1839 (2004).

[52] A. Petraru, J. Schubert, M. Schmid, and C. Buchal, "Ferroelectric $BaTiO_3$ thin-film optical waveguide modulators," Appl. Phys. Lett. **81** (8), 1375-1377 (2002).

[53] A. Petraru, J. Schubert, M. Schmid, O. Trithaveesak, and C. Buchal, "Integrated optical Mach-Zehnder modulator based on polycrystalline $BaTiO_3$," Opt. Lett. **28** (24), 2527-2529 (2003).

[54] D. M. Gill, C. W. Conrad, G. Ford, B. W. Wessels, and S. T. Ho, "Thin-film channel waveguide electro-optic modulator in epitaxial $BaTiO_3$," Appl. Phys. Lett. **71** (13), 1783-1785 (1997).

[55] R. W. Boyd, *Nonlinear Optics*. (Elsevier Science, Academic press, New York, 2003).

[56] M. Zgonik, P. Bernasconi, M. Duelli, R. Schlesser, P. Gunter, M. H. Garrett, D. Rytz, Y. Zhu, and X. Wu, "Dielectric, Elastic, Piezoelectric, Electrooptic, and Elasto-Optic Tensors of $BaTiO_3$ Crystals," Phys. Rev. B **50** (9), 5941-5949 (1994).

[57] K. Atsuki and E. Yamashita, "Transmission-Line Aspects of the Design of Broad-Band Electrooptic Traveling-Wave Modulators," J. Lightwave Technol. **5** (3), 316-319 (1987).

[58] V. Vaithyanathan, J. Lettieri, W. Tian, A. Sharan, A. Vasudevarao, Y. L. Li, A. Kochhar, H. Ma, J. Levy, P. Zschack, J. C. Woicik, L. Q. Chen, V. Gopalan, and D. G. Schlom, "c-axis oriented epitaxial $BaTiO_3$ films on (001) Si," J. Appl. Phys. **100** (2) (2006).

[59] A. R. Meier, F. Niu, and B. W. Wessels, "Integration of $BaTiO_3$ on Si (001) using MgO/STO buffer layers by molecular beam epitaxy," J. Cryst. Growth **294** (2), 401-406 (2006).

[60] A. L. Glebov, M. G. Lee, L. Huang, S. Aoki, K. Yokouchi, M. Ishii, and M. Kato, "Electrooptic planar deflector switches with thin-film PLZT active elements," Ieee Journal of Selected Topics in Quantum Electronics **11** (2), 422-430 (2005).

[61] B. W. Wessels, "Ferroelectric oxide epitaxial thin films: synthesis and non-linear optical properties," J. Cryst. Growth **195** (1-4), 706-710 (1998).

[62] J. Li, B. Nagaraj, H. Liang, W. Cao, C. H. Lee, and R. Ramesh, "Ultrafast polarization switching in thin-film ferroelectrics," Appl. Phys. Lett. **84** (7), 1174-1176 (2004).

[63] M.E Lines and A.M Glass, *Principles and Applications of Ferroelectric and Related Materials*. (Oxford University Press, Oxford, 2001), p.680.

[64] F. Jona and G. Shirane, *Ferroelectric Crystals*. (Pergamon Press Inc., New York, 1962), p.402.

[65] B. H. Hoerman, B. M. Nichols, M. J. Nystrom, and B. W. Wessels, "Dynamic response of the electro-optic effect in epitaxial $KNbO_3$," Appl. Phys. Lett. **75** (18), 2707-2709 (1999).

[66] B. H. Hoerman, B. M. Nichols, and B. W. Wessels, "Dynamic response of the dielectric and electro-optic properties of epitaxial ferroelectric thin films," Phys. Rev. B **65** (22) (2002).

[67] M. Melnichuk and L. T. Wood, "Time-resolved optical transients in tetragonal $BaTiO_3$," J. Opt. Soc. Am. A-Opt. Image Sci. Vis. **22** (4), 734-744 (2005).

[68] Y. Barad, J. Lettieri, C. D. Theis, D. G. Schlom, and V. Gopalan, "Domain rearrangement in ferroelectric Bi4Ti3O12 thin films studied by in situ optical second harmonic generation," J. Appl. Phys. **90** (7), 3497-3503 (2001).

[69] B. Dickens, E. Balizer, A. S. Dereggi, and S. C. Roth, "Hysteresis Measurements of Remanent Polarization and Coercive Field in Polymers," J. Appl. Phys. **72** (9), 4258-4264 (1992).

[70] R. Waser, U. Bottger, and M. Grossmann, in *Ferroelectric Random Access Memories Fundamentals and Applications* (2004), Vol. 93, pp. 31-45.

[71] D. Bolten, U. Bottger, and R. Waser, "Reversible and irreversible piezoelectric and ferroelectric response in ferroelectric ceramics and thin films," J. Eur. Ceram. Soc. **24** (5), 725-732 (2004).

[72] O. Lohse, D. Bolten, M. Grossmann, and R. Waser, in *Ferroelectric Thin Films VI - Proceedings from MRS Fall Meeting 1998* (1998-1999), pp. 267-278.

[73] I. W. Chen and Y. Wang, "Activation field and fatigue of (Pb, La)(Zr, Ti)O-3 thin films," Appl. Phys. Lett. **75** (26), 4186-4188 (1999).

[74] J. T. Evans, "What happens to ferroelectric materials under a test?" Radiant Technologies, Inc., (electronic report - www.ferrodevices.com), 2003.

[75] J. T. Evans and J. A. Bullington, presented at the Applications of Ferroelectrics, 1990., IEEE 7th International Symposium on, 1990.

[76] RT6000S Operating Manual, Radiant Technologies Inc., RT6000S, Albuquerque, NM.

[77] P. Gerber, C. Kugeler, U. Bottger, and R. Waser, "Effects of reversible and irreversible ferroelectric switchings on the piezoelectric large-signal response of lead zirconate titanate thin films," J. Appl. Phys. **98** (12) (2005).

[78] D. Damjanovic, "Ferroelectric, dielectric and piezoelectric properties of ferroelectric thin films and ceramics," Rep. Prog. Phys. **61** (9), 1267-1324 (1998).

[79] K. A. Demarest, *Engineering Electromagnetics*. (Prentice Hall, Upper Saddle River, 1998).

[80] D. J. Jung, K. Kim, and J. F. Scott, "Switching kinetics in nanoferroelectrics," Journal of Physics-Condensed Matter **17** (30), 4843-4852 (2005).

[81] D. Y. Wang and C. Y. Chang, "Switching current study: Hysteresis measurement of ferroelectric capacitors using current-voltage measurement method," Jpn. J. Appl. Phys. Part 1 - Regul. Pap. Brief Commun. Rev. Pap. **44** (4A), 1857-1861 (2005).

[82] D. Damjanovic, in *The Science of Hysteresis, Volume 3*, edited by I. Mayergoyz and G. Bertotti (Elsevier, 2005), Vol. Volume 3, pp. 337-465.

[83] D. D. Glower and D. L. Hester, "Hysteresis Studies of Reactor-Irradiated Single-Crystal Barium Titanate," J. Appl. Phys. **36** (7), 2175-& (1965).

[84] T. Granzow, A. B. Kounga, E. Aulbach, and J. Rodel, "Electromechanical poling of piezoelectrics," Appl. Phys. Lett. **88** (25) (2006).

[85] K. Lee and S. Baik, "Ferroelastic domain structure and switching in epitaxial ferroelectric thin films," Annual Review of Materials Research **36**, 81-116 (2006).

[86] W. W. Cao, "Ferroelectrics - The strain limits on switching," Nat. Mater. **4** (10), 727-728 (2005).

[87] G. D. Hu, "Orientation dependence of ferroelectric and piezoelectric properties of $Bi_{3.15}Nd_{0.85}Ti_3O_{12}$ thin films on $Pt(100)/TiO_2/SiO_2/Si$ substrates," J. Appl. Phys. **100** (9) (2006).

[88] C. Duran, "Processing and ferroelectric behavior of textured KSr2Nb5O15 ceramics," J. Mater. Sci. **41** (22), 7620-7627 (2006).

[89] P. X. Yang, H. M. Deng, M. R. Shi, and Z. Y. Tong, "Properties of $SrBi_2Ta_{0.8}Nb_{1.2}O_9$ thin films deposited by plasma-assisted pulsed-laser deposition," Journal of Vacuum Science & Technology A **25** (1), 148-152 (2007).

[90] M. Tsukada, H. Yamawaki, M. Kondo, J. S. Cross, and K. Kurihara, "Polarization switching in (100)/(001) oriented epitaxial $Pb(Zr,Ti)O_3$ thin films," J. Electroceram. **13** (1-3), 29-33 (2004).

[91] O. Nakao, K. Tomomatsu, S. Ajimura, A. Kurosaka, and H. Tominaga, "Influence of 180-Degrees Domains on Ferroelectric Properties of $BaTiO_3$ Single-Crystal," Appl. Phys. Lett. **61** (14), 1730-1732 (1992).

[92] T. S. Benedict and J. L. Durand, "Dielectric Properties of Single Domain Crystals of $BaTiO_3$ at Microwave Frequencies," Phys. Rev. **109** (4), 1091-1093 (1958).

[93] W. J. Merz, "The Dielectric Behaviour of $BaTiO_3$ Single-Domain Crystals," Phys. Rev. **75**, 687 (1949).

[94] A. V. Turik and N. B. Shevchenko, "Dielectric Spectrum of $BaTiO_3$ Single-Crystals," Phys. Status Solidi B-Basic Solid State Phys. **95** (2), 585-592 (1979).

[95] Y. Tominaga and T. Nakamura, "Temperature-Dependence of Dispersion-Relation of Over-Damped E-Polariton in $BaTiO_3$," J. Phys. Soc. Jpn. **39** (3), 746-752 (1975).

[96] L. Merten, "Directional Dispersion of Optical Phonons of Tetragonal $BaTiO_3$ at Room Temperature," Phys. Status Solidi **25** (1), 125-& (1968).

[97] W. J. Merz, "The Electric and Optical Behaviour of $BaTiO_3$ Single-Domain Crystals," Phys. Rev. **76** (8), 1221 (1949).

[98] A. F. Devonshire, "Theory of Ferroelectrics - part 2," Philosophical Magazine (series 7) **42**, 1065 (1951).

[99] Y. Ishibashi and Y. Takagi, "Ferroelectric Domain Switching," J. Phys. Soc. Jpn. **31** (2), 506-& (1971).

[100] R. Abe, "Theoretical Treatment of the Movement of 180^o Domain in $BaTiO_3$ Single Crystal," J. Phys. Soc. Jpn. **14** (5), 633-642 (1959).

[101] W.J. Merz, "Domain formation and domain wall motions in ferroelectric $BaTiO_3$ single crystals," Phys. Rev. **95** (3), 690 (1954).

[102] E. A. Little, "Dynamic Behavior of Domain Walls in Barium Titanate," Phys. Rev. **98** (4), 978-984 (1955).

[103] R. Abe, "Theoretical Study of the Properties of Coercive Field of $BaTiO_3$ Single Crystal," J. Phys. Soc. Jpn. **15** (5), 795-801 (1960).

[104] E. Fatuzzo, "Theoretical Considerations on Switching Transient in Ferroelectrics," Phys. Rev. **127** (6), 1999-& (1962).

[105] J. Fousek and L. E. Cross, "Open issues in application aspects of domains in ferroic materials," Ferroelectrics **293**, 43-60 (2003).

[106] E. V. Sinyakov, E. F. Dudnik, and Fondurok.Va, "Action of a Constant Electric Field on Domain Structure of $BaTiO_3$ Single Crystals," Soviet Physics Crystallography, Ussr **13** (6), 887-& (1969).

[107] R. Landauer, "Electrostatic Considerations in $BaTiO_3$ Domain Formation During Polarization Reversal," J. Appl. Phys. **28** (2), 227-234 (1957).

[108] C. S. Ganpule, A. L. Roytburd, V. Nagarajan, B. K. Hill, S. B. Ogale, E. D. Williams, R. Ramesh, and J. F. Scott, "Polarization relaxation kinetics and 180 degrees domain wall dynamics in ferroelectric thin films," Phys. Rev. B **65** (1) (2002).

[109] A. Roelofs, N. A. Pertsev, R. Waser, F. Schlaphof, L. M. Eng, C. Ganpule, V. Nagarajan, and R. Ramesh, "Depolarizing-field-mediated 180 degrees switching in ferroelectric thin films with 90 degrees domains," Appl. Phys. Lett. **80** (8), 1424-1426 (2002).

[110] A. Grigoriev, D. H. Do, D. M. Kim, C. B. Eom, B. Adams, E. M. Dufresne, and P. G. Evans, "Nanosecond domain wall dynamics in ferroelectric $Pb(Zr,Ti)O_3$ thin films," Phys. Rev. Lett. **96** (18) (2006).

[111] D. J. Jung, M. Dawber, J. F. Scott, L. J. Sinnamon, and J. M. Gregg, "Switching dynamics in ferroelectric thin films: An experimental survey," Integr. Ferroelectr. **48**, 59-68 (2002).

[112] A. Jiang, M. Dawber, J. F. Scott, C. Wang, P. Migliorato, and M. Gregg, "Studies of switching kinetics in ferroelectric thin films," Jpn. J. Appl. Phys. **42** (11), 6973-6982 (2003).

[113] H. Orihara, S. Hashimoto, and Y. Ishibashi, "A Theory of D-E Hysteresis Loop Based on the Avrami Model," J. Phys. Soc. Jpn. **63** (3), 1031-1035 (1994).

[114] C. Jullian, J. F. Li, and D. Viehland, "Investigation of polarization switching in (001)(c), (110)(c), and (111)(c) oriented $Pb(Zn_{1/3}Nb_{2/3})O_{3\text{-}4.5\%}PbTiO_3$ crystals," J. Appl. Phys. **95** (10), 5671-5678 (2004).

[115] X. F. Du and I. W. Chen, "Model experiments on fatigue of $Pb(Zr_{0.53}Ti_{0.47})O_3$ ferroelectric thin films," Appl. Phys. Lett. **72** (15), 1923-1925 (1998).

[116] A. K. Tagantsev, I. Stolichnov, N. Setter, J. S. Cross, and M. Tsukada, "Non-Kolmogorov-Avrami switching kinetics in ferroelectric thin films," Phys. Rev. B **66** (21) (2002).

[117] M. Ozgul, E. Furman, S. Trolier-McKinstry, and C. A. Randall, "Polarization relaxation anisotropy in $Pb(Zn_{1/3}Nb_{2/3})O_3$-$PbTiO_3$ single-crystal ferroelectrics as a function of fatigue history," J. Appl. Phys. **95** (5), 2631-2638 (2004).

[118] D. S. Fu, K. Ishikawa, M. Minakata, and H. Suzuki, "Observation of piezoelectric relaxation in ferroelectric thin films by continuous charge integration," Jpn. J. Appl. Phys. Part 1 - Regul. Pap. Brief Commun. Rev. Pap. **40** (9B), 5683-5686 (2001).

[119] A. Gruverman, H. Tokumoto, A. S. Prakash, S. Aggarwal, B. Yang, M. Wuttig, R. Ramesh, O. Auciello, and T. Venkatesan, "Nanoscale imaging of domain dynamics and retention in ferroelectric thin films," Appl. Phys. Lett. **71** (24), 3492-3494 (1997).

[120] J. W. Hong, W. Jo, D. C. Kim, S. M. Cho, H. J. Nam, H. M. Lee, and J. U. Bu, "Nanoscale investigation of domain retention in preferentially oriented $PbZr_{0.53}Ti_{0.47}O_3$ thin films on Pt and on $LaNiO_3$," Appl. Phys. Lett. **75** (20), 3183-3185 (1999).

[121] K. Matyjasek and R. Z. Rogowski, "Polarization relaxation in $(CH_3NH_3)_{(5)}Bi_2Br_{11}$ ferroelectric crystals," Cryst. Res. Technol. **41** (6), 570-575 (2006).

[122] K. Matyjasek and R. Z. Rogowski, "Slow polarization relaxation in non-uniform telluric acid ammonium phosphate crystals," Journal of Physics-Condensed Matter **18** (32), 7687-7701 (2006).

[123] K. Matyjasek and R. Z. Rogowski, "Effect of internal bias field on domain switching in $(CH_3NH_3)_{(5)}Bi_2Br_{11}$ crystal," J. Appl. Phys. **99** (7) (2006).

[124] V. Koval, M. J. Reece, and A. J. Bushby, "Relaxation processes in dielectric and electromechanical response of PZT thin films under nanoindentation," Ferroelectrics **318**, 55-61 (2005).

[125] Y. J. Oh, J. H. Lee, and W. Jo, "Dynamics of space and polarization charges of ferroelectric thin films measured by atomic force microscopy," Ultramicroscopy **106** (8-9), 779-784 (2006).

[126] T. K. Song, J. G. Yoon, and S. I. Kwun, "Microscopic polarization retention properties of ferroelectric $Pb(Zr,Ti)O_3$ thin films," Ferroelectrics **335**, 61-68 (2006).

[127] V. Nagarajan, S. Aggarwal, A. Gruverman, R. Ramesh, and R. Waser, "Nanoscale polarization relaxation in a polycrystalline ferroelectric thin film: Role of local environments," Appl. Phys. Lett. **86** (26) (2005).

[128] A. A. Bokov and Z. G. Ye, "Giant electrostriction and stretched exponential electromechanical relaxation in $_{0.65}Pb(Mg_{1/3}Nb_{2/3})O_{3-0.35}PbTiO_{(3)}$ crystals," J. Appl. Phys. **91** (10), 6656-6661 (2002).

[129] V. Shvartsman, A. Tyunina, J. Levoska, and A. Kholkin, "Local electromechanical properties of $PbMg_{1/3}Nb_{2/3}O_3$ thin films studied by piezoelectric force microscopy," Ferroelectrics **302**, 569-572 (2004).

[130] P. Lehnen, W. Kleemann, T. Woike, and R. Pankrath, "Ferroelectric nanodomains in the uniaxial relaxor system $Sr_{0.61-x}Ba_{0.39}Nb_2O_6 : Ce_{x(3+)}$," Phys. Rev. B **64** (22) (2001).

[131] B. Tadic, "Switching current noise and relaxation of ferroelectric domains," Eur. Phys. J. B **28** (1), 81-89 (2002).

[132] D. C. Lupascu, S. Fedosov, C. Verdier, J. Rodel, and H. von Seggern, "Stretched exponential relaxation in perovskite ferroelectrics after cyclic loading," J. Appl. Phys. **95** (3), 1386-1390 (2004).

[133] D. S. Fu, K. Suzuki, K. Kato, M. Minakata, and H. Suzuki, "Investigation of domain switching and retention in oriented $PbZr_{0.3}Ti_{0.7}O_3$ thin film by scanning force microscopy," Jpn. J. Appl. Phys. Part 1 - Regul. Pap. Brief Commun. Rev. Pap. **41** (11B), 6724-6729 (2002).

[134] D. S. Fu, K. Ishikawa, Y. Yoshimi, and H. Suzuki, "Long-time piezoelectric relaxation in lead zirconate titanate thin film," Jpn. J. Appl. Phys. **41** (5B), L580-L582 (2002).

[135] D. S. Fu, K. Suzuki, K. Kato, and H. Suzuki, "Dynamics of nanoscale polarization backswitching in tetragonal lead zirconate titanate thin film," Appl. Phys. Lett. **82** (13), 2130-2132 (2003).

[136] H. Y. Guo, J. B. Xu, Z. Xie, E. Z. Luo, I. H. Wilson, and W. L. Zhong, "Ferroelectric relaxation of $(Pb_{0.76}Ca_{0.24})TiO_3$ thin film," Solid State Commun. **121** (11), 603-607 (2002).

[137] H. T. Huang, T. S. Zhang, J. T. Oh, and P. Hing, "Stress- and strain-relaxation in lead zirconate titanate based ceramics," Mater. Chem. Phys. **75** (1-3), 186-189 (2002).

[138] B. S. Kang, J. G. Yoon, T. W. Noh, T. K. Song, S. Seo, Y. K. Lee, and J. K. Lee, "Polarization dynamics and retention loss in fatigued $PbZr_{0.4}Ti_{0.6}O_3$ ferroelectric capacitors," Appl. Phys. Lett. **82** (2), 248-250 (2003).

[139] T. Volk, D. Isakov, L. Ivleva, and M. Wohlecke, "Ferroelectric switching of strontium-barium-niobate crystals in pulsed fields," Appl. Phys. Lett. **83** (11), 2220-2222 (2003).

[140] J. R. Macdonald, "Linear Relaxation - Distributions, Thermal-Activation, Structure, and Ambiguity," J. Appl. Phys. **62** (11), R51-R62 (1987).

[141] N. L. Johnson, S. Kotz, and N. Balakrishnan, *Continuous Univariate Distributions*. (Wiley-Interscience, New York, 1994), p.2.

[142] C. P. Lindsey and G. D. Patterson, "Detailed comparison of the Williams-Watts and Cole-Davidson functions," J. Chem. Phys. **73** (7), 3348 (1980).

[143] K. Weron and M. Kotulski, "On the equivalence of the parallel channel and the correlated cluster relaxation models," J. Stat. Phys. **88** (5-6), 1241-1256 (1997).

[144] E. Perez-Enciso, N. Agrait, and S. Vieira, "Experimental evidence of nonactivated creep in $Pb(Zr_xTi_{1-x})O_3$ ceramics at low temperatures," Phys. Rev. B **56** (6), R2900-R2903 (1997).

[145] C.J.F.; Bottcher and P. Bordevijk, *Theory of Electric Polarization*. (Elsevier, Amsterdam, 1978).

[146] P. Hetman, B. Szabat, K. Weron, and D. Wodzinski, "On the Rajagopal relaxation-time distribution and its relationship to the Kohlrausch-Williams-Watts relaxation function," J. Non-Cryst. Solids **330** (1-3), 66-74 (2003).

[147] F. Brouers, O. Sotolongo-Costa, and K. Weron, "Burr, Levy, Tsallis," Physica A **344** (3-4), 409-416 (2004).

[148] M.M. Somoza, KWW distribution functions, made with Mathematica July 16, 2006, Physik-Department E14,Technische Universität München, Germany

[149] M. I. Molotskii and M. M. Shvebelman, "Decay of ferroelectric domains formed in the field of an atomic force microscope," J. Appl. Phys. **97** (8) (2005).

[150] Y. Kan, X. M. Lu, X. M. Wu, and J. S. Zhu, "Domain reversal and relaxation in $LiNbO_3$ single crystals studied by piezoresponse force microscope," Appl. Phys. Lett. **89** (26) (2006).

[151] A. Agronin, M. Molotskii, Y. Rosenwaks, G. Rosenman, B. J. Rodriguez, A. I. Kingon, and A. Gruverman, "Dynamics of ferroelectric domain growth in the field of atomic force microscope," J. Appl. Phys. **99** (10) (2006).

[152] K. Bhattacharya and G. Ravichandran, "Ferroelectric perovskites for electromechanical actuation," Acta Mater. **51** (19), 5941-5960 (2003).

[153] E. Burcsu, G. Ravichandran, and K. Bhattacharya, "Large strain electrostrictive actuation in barium titanate," Appl. Phys. Lett. **77** (11), 1698-1700 (2000).

[154] Eric N. Burcsu, Guruswaminaidu Ravichandran, and Kaushik Bhattacharya, presented at the Smart Structures and Materials 2000: Active Materials: Behavior and Mechanics, Newport Beach, CA, USA, 2000.

[155] Eric N. Burcsu, Guruswaminaidu Ravichandran, and Kaushik Bhattacharya, presented at the Smart Structures and Materials 2001: Active Materials: Behavior and Mechanics, Newport Beach, CA, USA, 2001.

[156] E. Burcsu, G. Ravichandran, and K. Bhattacharya, "Large electrostrictive actuation of barium titanate single crystals," J. Mech. Phys. Solids **52** (4), 823-846 (2004).

[157] K. Nashimoto, S. Nakamura, T. Morikawa, H. Moriyama, M. Watanabe, and E. Osakabe, "Electrooptical properties of heterostructure (Pb, La)(Zr,Ti)O_3 waveguides on Nb-$SrTiO_3$," Jpn. J. Appl. Phys. **38** (9B), 5641-5645 (1999).

[158] F. L. Wang, E. Furman, and G. H. Haertling, "Electrooptic Measurements of Thin-Film Materials by Means of Reflection Differential Ellipsometry," J. Appl. Phys. **78** (1), 9-15 (1995).

[159] M. Ishida, H. Matsunami, and T. Tanaka, "Electro-Optic Effects of PLZT Thin-Films," Appl. Phys. Lett. **31** (7), 433-434 (1977).

[160] H. Adachi, T. Kawaguchi, K. Setsune, K. Ohji, and K. Wasa, "Electrooptic Effects of (Pb, La)(Zr, Ti)O_3 Thin-Films Prepared by Rf Planar Magnetron Sputtering," Appl. Phys. Lett. **42** (10), 867-868 (1983).

[161] D. H. Reitze, E. Haton, R. Ramesh, S. Etemad, D. E. Leaird, T. Sands, Z. Karim, and A. R. Tanguay, "Electrooptic Properties of Single-Crystalline Ferroelectric Thin-Films," Appl. Phys. Lett. **63** (5), 596-598 (1993).

[162] K. D. Preston and G. H. Haertling, "Comparison of Electrooptic Lead-Lanthanum Zirconate Titanate Films on Crystalline and Glass Substrates," Appl. Phys. Lett. **60** (23), 2831-2833 (1992).

[163] P. F. Thacher, "Linear Electrooptic Effect in Ferroelectric Ceramics - PLZT 12/40/L0," Ferroelectrics **3** (2-3-), 147-& (1972).

[164] P. D. Thacher, "Linear Electrooptic Effect in Ferroelectric Ceramics - PLZT 12/40/60," Ieee Transactions on Sonics and Ultrasonics **SU19** (2), 147-& (1972).

[165] B. G. Potter, M. B. Sinclair, and D. Dimos, "Electrooptical Characterization of Pb(Zr,Ti)O_3 Thin-Films by Wave-Guide Refractometry," Appl. Phys. Lett. **63** (16), 2180-2182 (1993).

[166] C. E. Land, "Longitudinal Electrooptic Effects and Photosensitivities of Lead Zirconate Titanate Thin-Films," J. Am. Ceram. Soc. **72** (11), 2059-2064 (1989).

[167] W. Jo, H. J. Cho, T. W. Noh, B. I. Kim, D. Y. Kim, Z. G. Khim, and S. I. Kwun, "Structural and Electrooptic Properties of Pulsed-Laser Deposited $Bi_4Ti_3O_{12}$ Thin-Films on Mgo," Appl. Phys. Lett. **63** (16), 2198-2200 (1993).

[168] J. W. Li, F. Duewer, C. Gao, H. Y. Chang, X. D. Xiang, and Y. L. Lu, "Electro-optic measurements of the ferroelectric-paraelectric boundary in $Ba_{1-x}Sr_xTiO_3$ materials chips," Appl. Phys. Lett. **76** (6), 769-771 (2000).

[169] D. Y. Kim, S. E. Moon, E. K. Kim, S. J. Lee, J. J. Choi, and H. E. Kim, "Electro-optic characteristics of (001)-oriented $Ba_{0.6}Sr_{0.4}TiO_3$ thin films," Appl. Phys. Lett. **82** (9), 1455-1457 (2003).

[170] C. Hubert, J. Levy, A. C. Carter, W. Chang, S. W. Kiechoefer, J. S. Horwitz, and D. B. Chrisey, "Confocal scanning optical microscopy of $Ba_xSr_{1-x}TiO_3$ thin films," Appl. Phys. Lett. **71** (23), 3353-3355 (1997).

[171] D. H. Kim and H. S. Kwok, "Pulsed-Laser Deposition of $BaTiO_3$ Thin-Films and Their Optical-Properties," Appl. Phys. Lett. **67** (13), 1803-1805 (1995).

[172] Y. W. Liu, Z. H. Chen, C. L. Li, D. F. Cui, Y. L. Zhou, and G. Z. Yang, "Electrical and electro-optical properties of Ce-doped barium titanate thin films prepared by pulsed laser deposition," J. Appl. Phys. **81** (9), 6328-6331 (1997).

[173] T. M. Graettinger, S. H. Rou, M. S. Ameen, O. Auciello, and A. I. Kingon, "Electrooptic Characterization of Ion-Beam Sputter-Deposited $KNbO_3$ Thin-Films," Appl. Phys. Lett. **58** (18), 1964-1966 (1991).

[174] V. Gopalan, K.L. Schepler, V. Dierolf, and I. Biaggio, in *The Handbook of Photonics*, edited by M.C. Gupta and J. Ballato (CRC Press, 2006).

[175] M. Aillerie, N. Theofanous, and M. D. Fontana, "Measurement of the electro-optic coefficients: description and comparison of the experimental techniques," Appl. Phys. B-Lasers Opt. **70** (3), 317-334 (2000).

[176] D. G. Sun, Z. F. Liu, Y. Y. Huang, S. T. Ho, D. J. Towner, and B. W. Wessels, "Performance simulation for ferroelectric thin-film based waveguide electro-optic modulators," Opt. Commun. **255** (4-6), 319-330 (2005).

[177] F. Abdi, M. D. Fontana, M. Aillerie, and G. Godefroy, "Strongly Temperature-Dependent Electrooptic Coefficients in $BaTiO_3$," Ferroelectrics **133** (1-4), 175-180 (1992).

[178] Amnon Yariv, *Optical Electronics in Modern Communications*. (Oxford University Press, Oxford, 1997).

[179] B.E.A.; Saleh and M.C. Teich, *Fundamentals of photonics*. (John Wiley & Son, Inc., New York, 1991).

[180] D. Y. Chen and J. D. Phillips, in *Proceedings of SPIE* (San Diego, CA, USA, 2005), Vol. 5867, pp. 63-69.

[181] P. S. Theocaris and E. E. Gdoutos, *Matrix Theory of Photoelasticity*. (Springer, Berlin, Heidelberg, 1979).

[182] M DiDomenico and S. H. Wemple, "Oxygen-Octahedra Ferroelectrics .I. Theory of Electro-Optical and Nonlinear Optical Effects," J. Appl. Phys. **40** (2), 720-& (1969).

[183] D. J. Towner, J. Ni, T. J. Marks, and B. W. Wessels, "Effects of two-stage deposition on the structure and properties of heteroepitaxial $BaTiO_3$ thin films," J. Cryst. Growth **255** (1-2), 107-113 (2003).

[184] S. Gevorgian, H. Berg, H. Jacobsson, and T. Lewin, "Basic parameters of coplanar-strip waveguides on multilayer dielectric/semiconductor substrates, part 1: High permittivity substrates," IEEE Microw. Mag. **4** (2), 60-+ (2003).

[185] O. G. Ramer, "Integrated Optic Electrooptic Modulator Electrode Analysis," IEEE J. Quantum Electron. **18** (3), 386-392 (1982).

[186] T. Hamano, D. J. Towner, and B. W. Wessels, "Relative dielectric constant of epitaxial $BaTiO_3$ thin films in the GHz frequency range," Appl. Phys. Lett. **83** (25), 5274-5276 (2003).

[187] D. Eimerl, "Crystal Symmetry and the Electrooptic Effect," IEEE J. Quantum Electron. **23** (12), 2104-2115 (1987).

[188] C. C. Teng and H. T. Man, "Simple Reflection Technique for Measuring the Electrooptic Coefficient of Poled Polymers," Appl. Phys. Lett. **56** (18), 1734-1736 (1990).

[189] Y. L. Li, S. Y. Hu, Z. K. Liu, and L. Q. Chen, "Effect of substrate constraint on the stability and evolution of ferroelectric domain structures in thin films," Acta Mater. **50** (2), 395-411 (2002).

[190] R. A. Silverman, *Calculus with analytic geometry*. (Prentice Hall, Englewood Cliffs, 1985).

[191] W. L. Warren, D. Dimos, G. E. Pike, B. A. Tuttle, M. V. Raymond, R. Ramesh, and J. T. Evans, "Voltage Shifts and Imprint in Ferroelectric Capacitors," Appl. Phys. Lett. **67** (6), 866-868 (1995).

[192] R. Bouregba, G. Le Rhun, and G. Poullain, "Polarization offsets of non graded and graded ferroelectric films," Integr. Ferroelectr. **70**, 67-78 (2005).

[193] K. Abe, N. Yanase, T. Yasumoto, and T. Kawakubo, "Voltage shift phenomena in a heteroepitaxial $BaTiO_3$ thin film capacitor," J. Appl. Phys. **91** (1), 323-330 (2002).

[194] D. Wu, A. D. Li, and N. B. Ming, "Structure and electrical properties of $Bi_{3.15}Nd_{0.85}Ti_3O_{12}$ ferroelectric thin films," J. Appl. Phys. **95** (8), 4275-4281 (2004).

[195] H. H. Wieder, "Ferroelectric Hysteresis in Barium Titanate Single Crystals," J. Appl. Phys. **26** (12), 1479-1482 (1955).

[196] W.D.; Kingery, H.K.; Bowen, and D.R.; Uhlmann, *Introduction to ceramics*. (John Wiley & Sons, New York, 1976).

[197] P. C. Joshi and S. B. Desu, "Structural, electrical, and optical studies on rapid thermally processed ferroelectric $BaTiO_3$ thin films prepared by metallo-organic solution deposition technique," Thin Solid Films **300** (1-2), 289-294 (1997).

[198] Y. P. Guo, K. Suzuki, K. Nishizawa, T. Miki, and K. Kato, in *Electroceramics in Japan IX* (2006), Vol. 320, pp. 77-80.

[199] K. J. Choi, M. Biegalski, Y. L. Li, A. Sharan, J. Schubert, R. Uecker, P. Reiche, Y. B. Chen, X. Q. Pan, V. Gopalan, L. Q. Chen, D. G. Schlom, and C. B. Eom, "Enhancement of ferroelectricity in strained $BaTiO_3$ thin films," Science **306** (5698), 1005-1009 (2004).

[200] K. Abe, N. Yanase, and T. Kawakubo, "Asymmetric switching of ferroelectric polarization in a heteroepitaxial $BaTiO_3$ thin film capacitor," Jpn. J. Appl. Phys. **39** (7A), 4059-4063 (2000).

[201] H. H. Wieder, "Electrical Behavior of Barium Titanate Single Crystals at Low Temperatures," Phys. Rev. **99** (4), 1161-1165 (1955).

[202] A. L. Meier, A. Y. Desai, L. Wang, T. J. Marks, and B. W. Wessels, "Phase stability of heteroepitaxial polydomain $BaTiO_3$ thin films," J. Mater. Res. **(accepted for publication Feb. 2007)** (2007).

[203] S. Bhattacharyya, S. Saha, and S. B. Krupanidhi, "Investigation of reversible and irreversible polarizations in thin films of $SrBi_2(Ta_{0.5},Nb_{0.5})_{(2)}O_9$," Thin Solid Films **422** (1-2), 155-160 (2002).

[204] L. Cima and E. Laboure, "A model of ferroelectric behavior based on a complete switching density," J. Appl. Phys. **95** (5), 2654-2659 (2004).

[205] D. Bolten, U. Bottger, and R. Waser, "Reversible and irreversible polarization processes in ferroelectric ceramics and thin films," J. Appl. Phys. **93** (3), 1735-1742 (2003).

[206] A. K. Soh, Y. C. Song, and Y. Ni, "Phase field simulations of hysteresis and butterfly loops in ferroelectrics subjected to electro-mechanical coupled loading," J. Am. Ceram. Soc. **89** (2), 652-661 (2006).

[207] V. Nagarajan, A. Roytburd, A. Stanishevsky, S. Prasertchoung, T. Zhao, L. Chen, J. Melngailis, O. Auciello, and R. Ramesh, "Dynamics of ferroelastic domains in ferroelectric thin films," Nat. Mater. **2** (1), 43-47 (2003).

[208] S. Poykko and D. J. Chadi, "Ab initio study of dipolar defects and 180 degrees domain walls in $PbTiO_3$," J. Phys. Chem. Solids **61** (2), 291-294 (2000).

[209] M. Calleja, M. T. Dove, and E. K. H. Salje, "Trapping of oxygen vacancies on twin walls of $CaTiO_3$: a computer simulation study," Journal of Physics-Condensed Matter **15** (14), 2301-2307 (2003).

[210] B. L. Cheng, M. Gabbay, and G. Fantozzi, in *Defects and Diffusion in Ceramics: An Annual Retrospective Iv* (2002), Vol. 206-2, pp. 143-146.

[211] C. Wang, Q. F. Fang, Y. Shi, and Z. G. Zhu, "Internal friction study on oxygen vacancies and domain walls in $Pb(Zr,Ti)O_3$ ceramics," Mater. Res. Bull. **36** (15), 2657-2665 (2001).

[212] R. J. Harrison and S. A. Redfern, "The influence of transformation twins on the seismic-frequency elastic and anelastic properties of perovskite: dynamical mechanical analysis of single crystal $LaAlO_3$," Phys. Earth Planet. Inter. **134** (3-4), 253-272 (2002).

[213] Q. Zhang and R. W. Whatmore, "Low fatigue lead zirconate titanate-based capacitors modified by manganese for nonvolatile memories," Mater. Sci. Eng. B-Solid State Mater. Adv. Technol. **109** (1-3), 136-140 (2004).

[214] X. B. Ren, "Large electric-field-induced strain in ferroelectric crystals by point-defect-mediated reversible domain switching," Nat. Mater. **3** (2), 91-94 (2004).

[215] Lawrence R Lawson and John E. Hilliard, *Physics: Measurement Techniques/ Instruments: Stereology and Stochastic Geometry*. (Springer, Boston, 2004).

[216] S. C. Hwang, C. S. Lynch, and R. M. McMeeking, "Ferroelectric/Ferroelastic Interactions and a Polarization Switching Model," Acta Metall. Mater. **43** (5), 2073-2084 (1995).

[217] J. F. Nye, *Physical Properties of Crystals - Their Representation by Tensors and Matrices*. (Oxford University Press, Oxford, 1957).

[218] P. Bernasconi, M. Zgonik, and P. Gunter, "Temperature-Dependence and Dispersion of Electrooptic and Elasto-Optic Effect in Perovskite Crystals," J. Appl. Phys. **78** (4), 2651-2658 (1995).

[219] B.D. Cullity, *Elements of x-ray diffraction*. (Addison-Wesley Publishing Company, Inc., Reading, 1978).

[220] L. Pintilie, I. Boerasu, and M. J. M. Gomes, "Simple model of polarization offset of graded ferroelectric structures," J. Appl. Phys. **93** (12), 9961-9967 (2003).

[221] P. U. Sastry, "Linear electro-optical properties of tetragonal $BaTiO_3$," Pramana-J. Phys. **59** (3), 547-552 (2002).

[222] C. C. Shih and A. Yariv, "A Theoretical-Model of the Linear Electrooptic Effect," Journal of Physics C-Solid State Physics **15** (4), 825-846 (1982).

[223] M. D. Fontana, K. Laabidi, B. Jannot, M. Maglione, and P. Jullien, "Relationship between Electrooptic, Vibrational and Dielectric-Properties in $BaTiO_3$," Solid State Commun. **92** (10), 827-830 (1994).

[224] L. X. Zhang and X. Ren, "In situ observation of reversible domain switching in aged Mn-doped BaTiO3 single crystals," Phys. Rev. B **71** (17) (2005).

[225] X. B. Ren, "Large electric-field-induced strain in ferroelectric crystals by point-defect-mediated reversible domain switching (Supplement)," Nat. Mater. **3** (2), 91-94 (2004).

[226] H. L. Stadler, "Thickness Dependence of $BaTiO_3$ Switching Time," J. Appl. Phys. **33** (12), 3487-& (1962).

[227] H. L. Stadler, "Ferroelectric Switching Time of $BaTiO_3$ Crystals at High Voltages," J. Appl. Phys. **29** (10), 1485-1487 (1958).

APPENDIX I

Device Fabrication Process

Transmission EO device:

The $BaTiO_3$ thin film sample is first cleaned in hot acetone for ~5 minutes followed by ~ 2 minutes in a hot methanol bath. After blowing the sample dry with an N_2 gun, the sample is placed on a hot plate at 105 ^oC to desiccate for 10 minutes after which the sample is ready for device fabrication. In preparation for device fabrication, MicroPrime MP-90 hexamethyl-disilazane (HMDS) adhesion promoter and Shipley AZ1518 photo-resist are loaded into pipettes which have first been blown cleaned with an N_2 gun to remove any dust particles. The adhesion promoter is then spun on the sample at 4000 rpm for 30 seconds. Next the AZ1518 photoresist is spun on at 4000 rpm for 30 seconds. To improve mask contact, the photoresist edge bead is removed at the corners of the sample. This is accomplished as follows. A Texwipe polypropylene foam swab is wetted with acetone. The swab is then daubed on a filter paper to remove the excess acetone. Finally, the swab is carefully drawn across the corners of the sample while moving away from the sample. This removes the photoresist edge bead, leaving small regions in the corners of the sample free of resist. After spinning on the resist, it is "soft baked" by placing the sample on a 105 ^oC hot plate for 60 seconds.

Subsequent to the soft bake the sample is ready for patterning. The sample is loaded on the vacuum chuck of the Q-4000 and brought into pressure contact with the clean photolithography mask, and then exposed to the UV source. Exposure times varied from 3.0 to 5.5 seconds depending on the intensity of the UV source. The intensity decreases somewhat over the lifetime of the bulb. Subsequent to exposure the sample is developed in a 1:4 solution of AZ400K developer and DI water. Typically an initial develop time of 30 seconds is employed. This is immediately followed by a 30 second rinse in a DI water bath to arrest the development process. The sample is then inspected under the microscope to check for the completeness of the development process. The green illumination filter on the microscope

is used to avoid exposure of the sample. If the exposure time was insufficient for the given source intensity anywhere from 30 seconds to 5 minutes of additional development time may be required.

Once the development is complete and the pattern is clear, a 60 second O_2 plasma clean "ash" is performed using the Oxford Plasmalab80 reactive ion etcher (RIE) to remove any residual resist from the pattern. For the RIE ash, a 50 sccm flow rate of O_2, and a 300 mTorr throttle pressure are employed. The RF power employed is 75 W.

After The O_2 ash in the RIE the electrodes are deposited by electron beam evaporation. As shown in Figure 3-1, a 10 – 30 nm adhesion layer of either titanium or chromium is first deposited followed by 250 – 600 nm of gold. The final step in the process involves lift-off to remove the resist pattern and the overlying metal layers leaving just the deposited electrodes. The sample is placed in an acetone bath and ultrasonically cleaned to remove the resist. After a final acetone and methanol rinse, the samples were blown dry with an N_2 gun completing the device fabrication process.

Waveguide EO device:

The first step in the process is the deposition of a 70 to 120 nm Si_3N_4 layer on the $BaTiO_3$ thin film. The Si_3N_4 layer is deposited using plasma enhanced chemical vapor deposition (PECVD) in an Oxford Plasmalab80. The PECVD Si_3N_4 process parameters are given in Table AI-1.

Table AI-1. Si_3N_4 PECVD deposition parameters on Oxford Plasmalab80 RIE/PECVD

PECVD Si_3N_4 deposition parameters	Value
SiH_4 flow rate (sccm)	100
NH_3 flow rate (sccm)	40
Bottom electrode Temperature (^oC)	300
Throttle pressure (mTorr)	320
RF power (W)	12
Deposition rate (nm/min)	4.7

After deposition of the Si_3N_4 layer, contact photolithography is used to pattern the waveguides. The lithography process for the patterning of the waveguides is identical to that used to pattern the electrodes

for the transmission electro-optic device described for the transmission device. Subsequent to the waveguide patterning and the O_2 plasma descum described in the transmission device process flow, the Si_3N_4 strip loaded waveguides are fabricated by a reactive ion etch of the Si_3N_4. Parameters for the Si_3N_4 RIE etch are given in Table AI-2. After RIE etching the Si_3N_4 strip-loaded waveguides, the sample is

Table AI-2. Si_3N_4 RIE etch recipe parameters on Oxford Plasmalab80 RIE/PECVD

RIE Si_3N_4 etch parameters	Value
CF_4 flow rate (sccm)	35
O_2 flow rate (sccm)	12
Throttle pressure (mTorr)	75
RF power (W)	150
Etch rate (nm/min)	355

cleaned in an acetone bath to remove the photoresist. At this juncture, if desired, an SiO_2 buffer layer of between 100 nm to 1 μm is deposited by electron beam evaporation.

With the waveguides and optional buffer layer completed, the sample is cleaned as before in preparation for patterning of the electrodes by photolithography. The electrode lithography involves negative-tone processing using the resist AZ5214, which can be used as an image reversal resist. In negative tone processing the region exposed through the photolithography mask remains on the sample after developing while those areas not exposed in the initial exposure are cleared of resist after developing. Through the initial exposure of the sample, the electrode photolithography process is the same as that outlined in the transmission device process flow with the exception that the AZ5214 is used rather than the AZ1518 resist. Additionally, the electrode mask must be carefully aligned with the waveguides on the sample using the Q-4000's translation and rotation capabilities.

After the initial exposure, the sample is placed on a 120 ^oC hot plate for 60 seconds. This "post-exposure bake" triggers the chemistry in the resist that allows for image reversal. The post-exposure bake is followed by a 60 second UV "flood" exposure of the sample on the Q-4000 without any mask. The remainder of the process, which includes developing the pattern, an O_2 plasma descum, e-beam

deposition of the electrodes and lift-off, is the same as that described in the transmission device process flow.

APPENDIX II

The intrinsic EO response with elasto-optic effect included

When the elasto-optic contributions are included the change in the impermeability tensor is written as

$$\Delta\eta_{ij} = r_{ijk}E_k + \rho_{ijrs}\varepsilon_{rs} \tag{II-1}$$

where ρ_{ijrs} are the elasto-optic coefficients and ε_{rs} are the components of the strain tensor. The terms of the impermeability tensor are given by

$$\begin{aligned}
\Delta\eta_{11} &= r_{113}E_3 + \rho_{1111}\left(\varepsilon_{22}+\varepsilon_{11}\right) + \rho_{1133}\varepsilon_{33} \\
\Delta\eta_{22} &= r_{113}E_3 + \rho_{1111}\left(\varepsilon_{22}+\varepsilon_{11}\right) + \rho_{1133}\varepsilon_{33} \\
\Delta\eta_{33} &= r_{333}E_3 + \rho_{3311}\left(\varepsilon_{22}+\varepsilon_{11}\right) + \rho_{3333}\varepsilon_{33} \\
\Delta\eta_{23} &= r_{133}E_2 \\
\Delta\eta_{13} &= r_{133}E_1 \\
\Delta\eta_{12} &= 0
\end{aligned} \tag{II-2}$$

The unitless values used of the elasto-optic coefficients of $BaTiO_3$ taken from Zgonik et al.[56] were

$$\begin{aligned}
\rho_{1111} &= 0.50 \quad & \rho_{1133} &= 0.20 \\
\rho_{3333} &= 0.77 \quad & \rho_{3311} &= 0.07
\end{aligned} \tag{II-3}$$

The surface normal strain (ε_{22}) was measured from x-ray diffraction analysis while the in-plane strains perpendicular (ε_{11}) and parallel (ε_{33}) to the polar axis are given in terms of the surface normal strain as

$$\begin{aligned}
\sigma_{11} = \sigma_{33} &= \frac{\varepsilon_{22}}{s_{1122}+s_{1133}} \\
\varepsilon_{11} &= \sigma_{11}\left(s_{1111}+s_{1133}\right) \\
\varepsilon_{33} &= \sigma_{11}\left(s_{1133}+s_{3333}\right)
\end{aligned} \tag{II-4}$$

The components of the diagonalized impermeability tensor are given by

$$\begin{bmatrix} \eta_1'' \\ \eta_2'' \\ \eta_3'' \end{bmatrix} = \begin{bmatrix} \frac{1}{2}\left(\eta_3' + \eta_1' - \Theta\right) \\ \eta_2' \\ \frac{1}{2}\left(\eta_3' + \eta_1' + \Theta\right) \end{bmatrix} \tag{II-5}$$

where the η_i' represent the components of the un-diagonalized impermeability tensor under field and the term Θ is given by

$$\Theta = \sqrt{\eta_3'^2 - 2\eta_1'\eta_3' + \eta_1'^2 + 4\eta_5'^2} \tag{II-6}$$

From the components of the diagonalized impermeability tensor under field in equation (II-5) the indices of refraction under field are plotted in Figure 116 and given by

$$\begin{aligned} n_1' &= \eta_1'^{-\left(\frac{1}{2}\right)} \\ n_3' &= \eta_3'^{-\left(\frac{1}{2}\right)} \end{aligned} \tag{II-7}$$

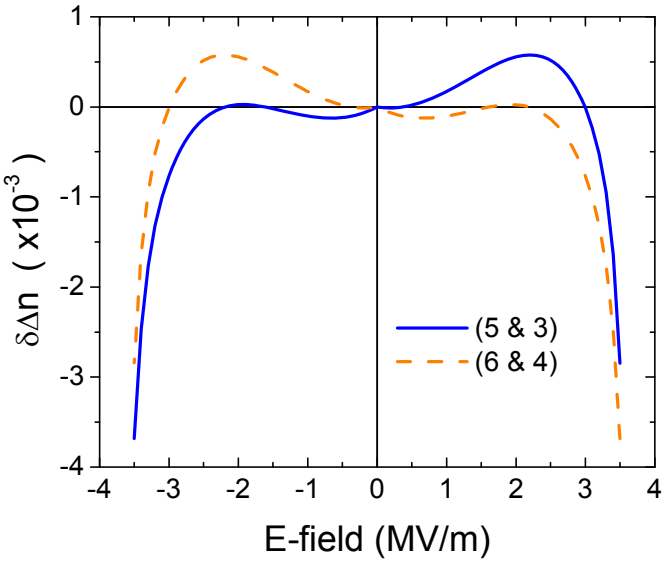

Figure 116 The field dependent change in birefringence of the a-domain variants when the elasto-optic as well as electro-optic effects are included is shown

The change in transmitted intensity through the polariscope is likewise effected by the field induced rotation of the indicatrix which is plotted in Figure 117 and given by

$$\alpha_{ij} = \frac{1}{2}\arctan\left[\frac{2\eta'_{ij}}{\eta'_{ii} - \eta'_{jj}}\right] \qquad \text{(II-8)}$$

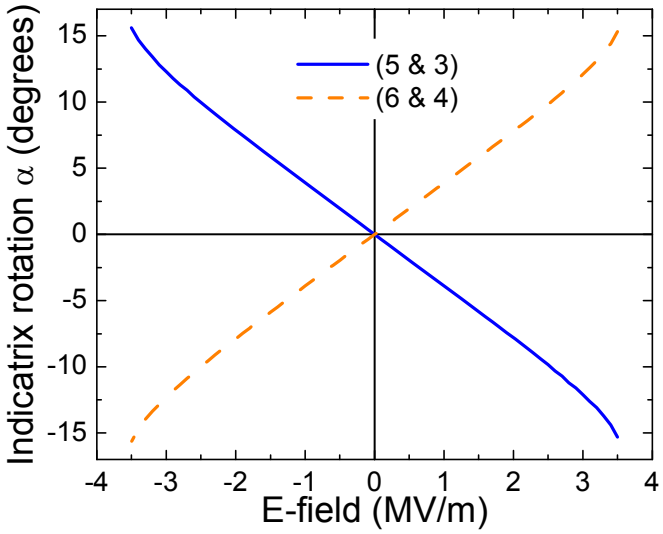

Figure 117. Field induced rotation of the indicatrix of the a-domains when both EO and elasto-optic contributions are considered.

The change in the transmitted intensity is calculated using the Jones calculus. The Jones matrix of the EO sample, which shall be referred to as ***R***, is given by

$$\begin{bmatrix} e^{-i(\delta/2)}\cos^2(\theta+\alpha) + e^{i(\delta/2)}\sin^2(\theta+\alpha) & -i\sin\left(\delta/2\right)\sin\left(2(\theta+\alpha)\right) \\ -i\sin\left(\delta/2\right)\sin\left(2(\theta+\alpha)\right) & e^{-i(\delta/2)}\sin^2(\theta+\alpha) + e^{i(\delta/2)}\cos^2(\theta+\alpha) \end{bmatrix} \qquad \text{(II-9)}$$

where δ is the retardation induced by the birefringence and $(\theta+\alpha)$ is the azimuthal angle of the slow axis with respect to the x-axis. With no E-field applied α is set to zero and δ is proportional to the natural birefringence $\Delta n = n_o - n_e$. The Jones matrix of the quarter waveplate with its fast axis parallel to the x-axis is given by

$$Q = \begin{bmatrix} i & 0 \\ 0 & 1 \end{bmatrix} \qquad \text{(II-10)}$$

and that of the analyzer with its transmission axis at an azimuthal angle β to the x-axis, is given by

$$A=\begin{bmatrix} \cos^2(\beta) & \sin(\beta)\cos(\beta) \\ \sin(\beta)\cos(\beta) & \sin^2(\beta) \end{bmatrix} \tag{II-11}$$

The normalized optical field at the output of the PSCA polariscope is thus given by

$$\begin{bmatrix} E_x' \\ E_z' \end{bmatrix} = A \cdot Q \cdot R \cdot \begin{bmatrix} 0 \\ 1 \end{bmatrix} \tag{II-12}$$

where the last term on the right is the z-polarized input optical field with incident intensity normalized to 1. The output optical field given by (4-23) is of the form

$$\begin{bmatrix} E_x' \\ E_z' \end{bmatrix} = \begin{bmatrix} \cos^2(\beta)\cdot\Delta + \nabla \\ \sin(\beta)\cos(\beta)\cdot\Delta + \nabla \end{bmatrix} \tag{II-13}$$

where Δ and ∇ are given by

$$\begin{aligned} \Delta &= \sin\left(\delta/2\right)\sin\left(2(\theta+\alpha)\right) \\ \nabla &= \sin(\beta)\cos(\beta)\left[e^{-i\delta/2}\sin^2(\theta+\alpha) + e^{i\delta/2}\cos^2(\theta+\alpha)\right] \end{aligned} \tag{II-14}$$

The transmitted intensity is then given by

$$I = E_x' \cdot \left(E_x'\right)^* + E_z' \cdot \left(E_z'\right)^* \tag{II-15}$$

By evaluating equation (4-26) both with and without an applied field the theoretical change in the transmitted intensity shown in

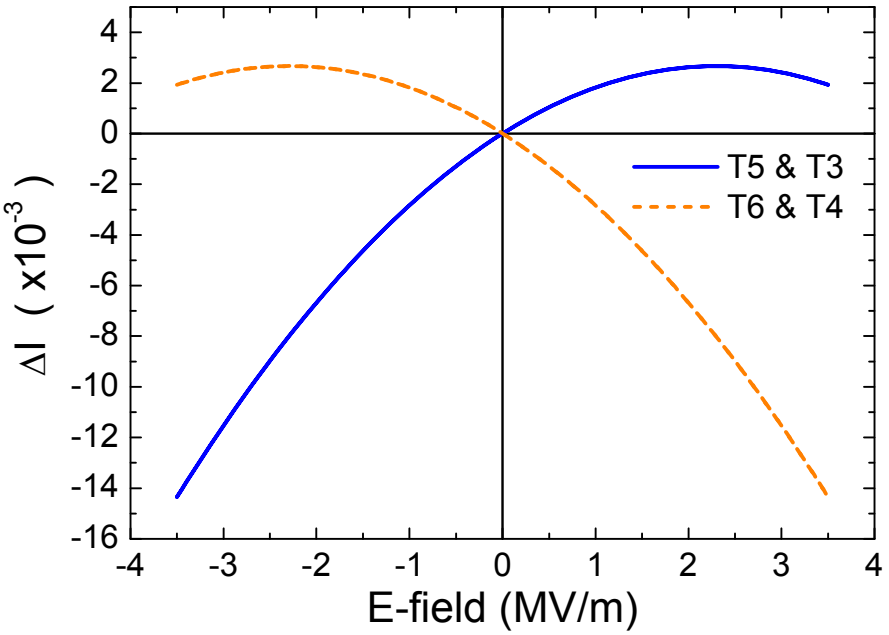

Figure 118. The theoretical change in the transmitted intensity of the a-domains when both the electro-optic and elasto-optic effects are considered.

Finally it should be noted that because there is no a priori theoretical relationship between the strain and the applied field it must be determined empirically. It will depend upon the domain structure in the film, the zero-field strain state and the coercivities for 90^{o} domain reversal.